



MINISTÉRIO DA CIÊNCIA, TECNOLOGIA, INOVAÇÕES E COMUNICAÇÕES
INSTITUTO NACIONAL DE PESQUISAS ESPACIAIS

sid.inpe.br/mtc-m21b/2017/03.30.17.37-TDI

**AEROSOL AND THERMODYNAMIC EFFECTS ON
THE FORMATION AND EVOLUTION OF AMAZONIAN
CLOUDS AS OBSERVED FROM AIRCRAFT
MEASUREMENTS**

Micael Amore Cecchini

Doctorate Thesis of the Graduate
Course in Meteorology, guided by
Dr. Luiz Augusto Toledo Machado,
approved in April 28, 2017.

URL of the original document:

<<http://urlib.net/8JMKD3MGP3W34P/3NKDGFS>>

INPE
São José dos Campos
2017

PUBLISHED BY:

Instituto Nacional de Pesquisas Espaciais - INPE

Gabinete do Diretor (GB)

Serviço de Informação e Documentação (SID)

Caixa Postal 515 - CEP 12.245-970

São José dos Campos - SP - Brasil

Tel.:(012) 3208-6923/6921

E-mail: pubtc@inpe.br

**COMMISSION OF BOARD OF PUBLISHING AND PRESERVATION
OF INPE INTELLECTUAL PRODUCTION (DE/DIR-544):**

Chairperson:

Maria do Carmo de Andrade Nono - Conselho de Pós-Graduação (CPG)

Members:

Dr. Plínio Carlos Alvalá - Centro de Ciência do Sistema Terrestre (CST)

Dr. André de Castro Milone - Coordenação de Ciências Espaciais e Atmosféricas (CEA)

Dra. Carina de Barros Melo - Coordenação de Laboratórios Associados (CTE)

Dr. Evandro Marconi Rocco - Coordenação de Engenharia e Tecnologia Espacial (ETE)

Dr. Hermann Johann Heinrich Kux - Coordenação de Observação da Terra (OBT)

Dr. Marley Cavalcante de Lima Moscati - Centro de Previsão de Tempo e Estudos Climáticos (CPT)

Silvia Castro Marcelino - Serviço de Informação e Documentação (SID) **DIGITAL LIBRARY:**

Dr. Gerald Jean Francis Banon

Clayton Martins Pereira - Serviço de Informação e Documentação (SID)

DOCUMENT REVIEW:

Simone Angélica Del Ducca Barbedo - Serviço de Informação e Documentação (SID)

Yolanda Ribeiro da Silva Souza - Serviço de Informação e Documentação (SID)

ELECTRONIC EDITING:

Marcelo de Castro Pazos - Serviço de Informação e Documentação (SID)

André Luis Dias Fernandes - Serviço de Informação e Documentação (SID)



MINISTÉRIO DA CIÊNCIA, TECNOLOGIA, INOVAÇÕES E COMUNICAÇÕES
INSTITUTO NACIONAL DE PESQUISAS ESPACIAIS

sid.inpe.br/mtc-m21b/2017/03.30.17.37-TDI

**AEROSOL AND THERMODYNAMIC EFFECTS ON
THE FORMATION AND EVOLUTION OF AMAZONIAN
CLOUDS AS OBSERVED FROM AIRCRAFT
MEASUREMENTS**

Micael Amore Cecchini

Doctorate Thesis of the Graduate
Course in Meteorology, guided by
Dr. Luiz Augusto Toledo Machado,
approved in April 28, 2017.

URL of the original document:

<<http://urlib.net/8JMKD3MGP3W34P/3NKDGFS>>

INPE
São José dos Campos
2017

Cataloging in Publication Data

Cecchini, Micael Amore.

C322a Aerosol and thermodynamic effects on the formation and evolution of Amazonian clouds as observed from aircraft measurements / Micael Amore Cecchini. – São José dos Campos : INPE, 2017.

xxvi + 173 p. ; (sid.inpe.br/mtc-m21b/2017/03.30.17.37-TDI)

Thesis (Doctorate in Meteorology) – Instituto Nacional de Pesquisas Espaciais, São José dos Campos, 2017.

Guiding : Dr. Luiz Augusto Toledo Machado.

1. Amazon. 2. Cloud microphysics. 3. Aerosol-cloud interactions. 4. Gamma DSD. I.Title.

CDU 551.576:504.5



Esta obra foi licenciada sob uma Licença [Creative Commons Atribuição-NãoComercial 3.0 Não Adaptada](https://creativecommons.org/licenses/by-nc/3.0/).

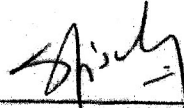
This work is licensed under a [Creative Commons Attribution-NonCommercial 3.0 Unported License](https://creativecommons.org/licenses/by-nc/3.0/).

Aluno (a): **Micael Amore Cecchini**

"AEROSOL AND THERMODYNAMIC EFFECTS ON THE FORMATION AND EVOLUTION OF AMAZONIAN CLOUDS AS OBSERVED FROM AIRCRAFT MEASUREMENTS"

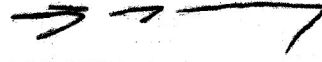
Aprovado (a) pela Banca Examinadora
em cumprimento ao requisito exigido para
obtenção do Título de **Doutor(a)** em
Meteorologia

Dr. Gilberto Fernando Fisch



Presidente / IAE/DCTA / SJCampos - SP

Dr. Luiz Augusto Toledo Machado



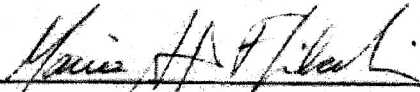
Orientador(a) / INPE / Cachoeira Paulista - SP

Dr. Daniel Alejandro Vila



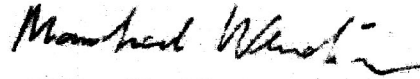
Membro da Banca / INPE / Cachoeira Paulista - SP

Dra. Maria Assunção Faus da Silva Dias



Convidado(a) / IAG/USP / São Paulo - SP

Dr. Manfred Wendisch



Convidado(a) / Leipzig University / Germany - GER

Este trabalho foi aprovado por:

maioria simples

unanimidade

São José dos Campos, 26 de abril de 2017.

ACKNOWLEDGMENTS

To my parents, Marco and Zita, who gave me birth.

To my wife, Luciana, an infinite source of love and understanding.

To my brothers, David and Mário, my lifetime friends.

To my advisor, Luiz Augusto, for bearing with me all those years and for dedicating his time and effort to make this work possible.

To my international advisor, Manfred, for the attention given to me and for opening international cooperation possibilities.

To my friends Rômulo, Ramon, and Enrique for all the help in practical and academic matters, including housing when I needed.

To my friends at CPTEC/INPE, especially Izabelly, Vinicius, Valesca, Cristiano, Lia, and Bruno, for making the academic activities more fun.

To all my colleagues at INPE for the support and the happy memories.

To my professors for providing all the necessary background for the development of this work.

To all GoAmazon2014/5, IARA, and ACRIDICON-CHUVA teams for the efforts in deploying field experiments and collecting the data that allowed this study.

To the secretaries, in particular Juliana, Luana and Isabel, which were always there when I needed.

To CAPES for the initial financial funding.

To FAPESP for the remainder of the financial funding, under grant number 2014/08615-7 (and BEPE number 2014/21189-7).

To FAPESP for funding the associated thematic project CHUVA (grant number 2009/15235-8).

ABSTRACT

Convective clouds over the Amazon are a key component of the South America and global climate systems. Nonetheless, they are poorly understood and models struggle to represent them appropriately. One of the primary reasons for that is the lack of data available for this type of cloud. Satellite retrievals have high underlying uncertainties for continental regions, especially considering the variability of surface reflectance between forested and deforested regions. The inherent lack of infrastructure also hampers the deployment of continuous field experiments. Additionally, the underlying physical processes in tropical clouds and their relation to aerosols is an open scientific question. This study aims at contributing to filling this gap by reporting on recent aircraft measurements over the Amazon, encompassing forested, deforested, urbanized, and maritime regions. One of the focus was on studying the interactions between the pollution plume generated by Manaus, a 2-million-inhabitant city surrounded by hundreds of km of rainforest, and the surrounding clouds. This was achieved by a low-altitude research aircraft that continuously penetrated the plume region and its surrounding cleaner air downwind from Manaus. Another research aircraft performed long range flights from remote regions on northern and northwestern Amazon, to the biomass-burning-polluted Arc of Deforestation in the south, and off the coast of Amapá State for the maritime reference. Both small and large scale approaches showed a primary role of aerosols on the warm-phase microphysical characteristics of Amazonian clouds regardless of thermodynamic conditions. Sensitivity calculations demonstrated that when aerosol number concentrations increase by 100%, there is an +84% and -25% response on cloud droplet number concentration and effective diameter, respectively. On the other hand, when updraft speeds strengthen by the same amount, droplet number concentrations increase by 43% and almost no effect is seen on the effective diameter. It shows that aerosols have significant impacts on the clouds microphysical structure, while updrafts modulate the amount of condensed water. In this study, it is proposed that the aerosol-cloud interactions can be studied by using the Gamma droplet size distribution (DSD) parameterization and its phase state. The phase state is defined by the three parameters that define the Gamma curve and can be visualized in an 3D plot. Polluted and clean clouds were found to populate different regions in this space, where each point represents one DSD measurement. By sequentially connecting points associated to increasing altitudes, it was possible to infer the DSD evolution during the clouds development and define trajectories in the phase space. The trajectories of polluted and clean clouds were substantially different given the different balance between condensational and collection growth mechanisms. It is suggested that those growth processes can be represented by pseudo-forces in the 3D phase space because they are able to generate displacements. The pseudo-force balance in clean clouds were found to favor their development into the phase space region favorable for fast glaciation, while polluted clouds remained outside of it. As a consequence, clean clouds readily glaciate above the 0 °C isotherm while supercooled droplets persist in polluted system. This was confirmed by

hydrometeor sphericity measurements. Overall, this work contributes to the understanding of Amazonian clouds by both providing statistics of their microphysical properties and by suggesting a new way to study the underlying physical processes in the Gamma phase space. The two approaches can be useful to infer specific modeling weaknesses regarding tropical clouds as well as steer the development of new parameterizations.

Keywords: Amazon. Cloud microphysics. Aerosol-cloud interactions. Gamma DSD.

EFEITOS DA TERMODINÂMICA E DOS AEROSSÓIS NA FORMAÇÃO E EVOLUÇÃO DE NUVENS SOBRE A AMAZÔNIA OBSERVADOS POR AERONAVES

RESUMO

As nuvens convectivas sobre a Amazônia são uma importante componente do sistema climático global e da América do Sul. No entanto, o seu conhecimento científico é limitado e, conseqüentemente, são mal representadas pelos modelos. Uma das principais razões para isto é a falta de dados a respeito deste tipo de nuvem. Estimativas por satélite apresentam grandes incertezas sobre regiões continentais, especialmente se considerarmos que a região amazônica apresenta significativa variabilidade na refletância de superfície entre regiões florestadas e desmatadas. A inerente falta de infraestrutura na floresta também dificulta a execução de experimentos de campo. Adicionalmente, os processos físicos nas nuvens tropicais e sua relação com os aerossóis é ainda uma questão científica em aberto. Este estudo tem como objetivo contribuir para esta lacuna de conhecimento através da análise de dados recentes coletados sobre a Amazônia em regiões florestadas, desmatas, urbanizadas e marítimas. Um dos focos foi o estudo dos efeitos da pluma de poluição emitida por Manaus, uma cidade de 2 milhões de habitantes cercada por centenas de quilômetros de floresta, nas nuvens próximas. Para isto, foram analisados dados coletados por aeronave de baixa altitude que penetrou repetidamente a pluma de poluição e o ar mais limpo ao seu redor. Outra aeronave realizou voos de longo alcance, desde regiões remotas no Norte e Noroeste da Amazônia, ao Arco de Desmatamento altamente poluído pela queima de biomassa mais ao Sul e até região oceânica próxima à costa do estado do Amapá. Ambas abordagens mostraram o papel primário dos aerossóis na formação das características microfísicas da fase quente das nuvens amazônicas independente das condições termodinâmicas. Cálculos de sensibilidade mostraram que aumentos de 100% na concentração de aerossóis geram uma resposta de +84% e -25% na concentração de gotas e no diâmetro efetivo, respectivamente. Por outro lado, quando as correntes ascendentes são intensificadas na mesma proporção, o aumento nas concentrações de gotas é de apenas 43% enquanto que o diâmetro efetivo se mantém praticamente inalterado. Isto mostra que os aerossóis são capazes de alterar a estrutura microfísica das nuvens, enquanto que as correntes ascendentes modulam o conteúdo de água condensada. Neste estudo é proposto que as interações entre os aerossóis e as nuvens podem ser estudadas através do uso da parametrização Gamma das distribuições de tamanho de gotas (DSDs) e o seu espaço de fase. Tal espaço de fase é caracterizado pelos três parâmetros que definem a curva Gamma e pode ser visualizado em gráficos tridimensionais. Detectou-se que as nuvens poluídas e limpas ocupam diferentes

regiões desse espaço, onde cada ponto representa uma medida de DSD. Ao conectar sequencialmente os pontos associados a crescentes altitudes, foi possível obter a evolução das DSDs ao longo do desenvolvimento das nuvens e definir trajetórias no espaço de fase. Neste sentido, foi observado que as nuvens poluídas e limpas apresentam trajetórias significativamente diferentes devido ao diferente balanço entre os processos de crescimento por condensação ou colisão-coalescência. Uma vez que os processos de crescimento das gotas geram movimentos no espaço, foi proposto que tais mecanismos podem ser representados por pseudo-forças. O balanço das pseudo-forças nas nuvens limpas contribui para a sua evolução para a região favorável aos processos de glaciação, enquanto que nuvens poluídas se mantiveram fora desta. Conseqüentemente, as nuvens limpas glaciam rapidamente ao ultrapassar a isoterma de 0 °C, enquanto que gotas super-resfriadas persistem em nuvens poluídas. Isto foi confirmado por medidas da esfericidade dos hidrometeoros. De modo geral, este trabalho contribui para o entendimento das nuvens da Amazônia tanto do ponto de vista estatístico de suas características microfísicas quanto do ponto de vista físico ao propor o estudo dos processos no espaço de fase Gamma. As duas abordagens podem ser úteis para identificar falhas específicas em modelos numéricos, assim como auxiliar no desenvolvimento de novas parametrizações.

Palavras-chave: Amazônia. Microfísica de nuvens. Interações aerossóis-nuvens. DSD Gamma.

FIGURES LIST

	<u>Page</u>
Figure 2.1: chain of events in an ideal scenario for cloud invigoration	15
Figure 2.2: schematic representation of the conditions favoring convection invigoration or suppression.....	18
Figure 2.3: location of the campaigns sites within (a) South America (black square) and (b) the State of Rondônia	21
Figure 2.4: main characteristics of the updrafts and hydrometeors in clean Amazonian clouds	24
Figure 2.5: LWC size distributions for the different types of clouds and at different altitudes	27
Figure 2.6: vertical D_L profiles for clouds subject to varying aerosol conditions	29
Figure 2.7: relation between effective radius r_e and adiabatic fraction (ratio between the observed LWC and the calculated adiabatic LWC) for (a) Blue Ocean, (b) Green Ocean, (c) Transitional Regime, and (d) Polluted Regime clouds.....	30
Figure 2.8: relative dispersion ε as function of the specific water content	32
Figure 3.1: ground-based site locations during GoAmazon2014/5.....	34
Figure 3.2: G-1 flight trajectories during IOP1 (February-March 2014)	36
Figure 3.3: trajectories of the 14 HALO flights during ACRIDION-CHUVA (GoAmazon2014/5 IOP2).....	39
Figure 3.4 – Physical aspect and principles of operation of the FCDP instrument	43
Figure 4.1 – Conceptual schematic for the flight patterns planning	55
Figure 4.2 - Trajectories for all G-1 flights during GoAmazon2014/5 IOP1	57
Figure 4.3 – N_{CN} around Manaus for March 10, 2014	61
Figure 4.4 - The same as Figure 4.3, with the coloring representing the plume classification	62
Figure 4.5 – N_{CCN} as function of supersaturation.....	63

Figure 4.6 - Normalized histograms of cloud droplet properties affected and unaffected by the Manaus pollution plume	65
Figure 4.7 - Mean (a) LWC values for different log-spaced w intervals and mean D_{eff} (b) and N_d (c) for log-spaced LWC intervals.....	69
Figure 4.8 - Averaged DSDs for three different cloud layers of bottom, mid and top of the warm layer.....	73
Figure 4.9 - Averaged DSDs as function of altitude, presence of up/downdrafts and aerosol conditions	75
Figure 5.1 - Locations where cloud profiles have been collected for different HALO flights	80
Figure 5.2 - Droplet size distributions as function of altitude above cloud base, aerosol particle number concentration, and vertical wind speed, W	86
Figure 5.3 – Same as Figure 5.2 but for flight AC19 only.....	87
Figure 5.4 - Same as Figure 5.2 but for flights (a) AC9 and (b) AC18 only	88
Figure 5.5 – Same as Figure 5.2 but for flights (a) AC7, (b) AC11, and (c) AC20 only.....	89
Figure 5.6 – Same as Figure 5.2 but for flights (a) AC12 and (b) AC13 only ...	90
Figure 5.7 - Variations of the sensitivities of Λ and ε with (a) N_{CN} and (b) H .	100
Figure 6.1 - Profile locations and trajectories of interest to this study.....	107
Figure 6.2 - GOES-13 visible images for flights (a) AC19, (b) AC9, (c) AC18, (d) AC7, (e) AC12, and (f) AC13.....	108
Figure 6.3 - Conceptual drawing of the properties of the Gamma phase-space in the warm-layer of the clouds	112
Figure 6.4 - Average vertical profiles of (a) potential temperature and (b) relative humidity for flights over the Atlantic coast, remote Amazon and Arc of Deforestation	114
Figure 6.5 - Gamma phase space for flight AC19 over the coastal region	117
Figure 6.6 - Similar to Figure 6.5, but for flights AC9 and AC18 over the remote Amazon	118

Figure 6.7 - Similar to Figure 6.5, but for flights AC7, AC12 and AC13 over the Arc of Deforestation.....	119
Figure 6.8 - Observed trajectories for the clouds measured over the remote Amazon during flight AC9 (continuous line) and over the Arc of Deforestation during flight AC12 (dashed line).....	122
Figure 6.9 - Averaged DSDs and their respective Gamma fittings for some points in the trajectories of clouds measured over (a) the remote Amazon (flight AC9) and (b) the Arc of Deforestation (flight AC12)	123
Figure 6.10 - Surfaces of constant N_d as calculated by the inversion of Equation 3.3.6	125
Figure 6.11 - Vertical profiles of the 1 Hz measurements of N_d , LWC , D_{eff} and ε for background clouds over the remote Amazon (a, c, e, g) and polluted clouds over the Arc of Deforestation (b, d, f, h).....	130
Figure 6.12 - Frequency of occurrence of NIXE-CAPS sphericity classifications for (a) the remote Amazon and (b) the Arc of Deforestation.....	132

TABLE LIST

	<u>Page</u>
Table 2.1: CO, CN, and CCN concentrations of the different types of clouds identified by Andreae et al. (2004).....	26
Table 3.1: list of instruments carried by G-1	37
Table 3.2: overall characteristics and mission types of the 14 HALO research flights.....	38
Table 3.3: instrumentation carried by the HALO aircraft during ACRIDICON-CHUVA – part 1.....	40
Table 3.4: instrumentation carried by the HALO aircraft during ACRIDICON-CHUVA – part 2.....	41
Table 4.1 - Dates and times for all G-1 flights during GoAmazon2014/5 IOP1	54
Table 4.2 - Averaged bulk DSD properties for the three warm-phase layers and the respective standard deviations	71
Table 5.1 – N_{CN} and N_{CCN} at cloud base for each flight considered in this study	82
Table 5.2 - N_d and D_{eff} averaged sensitivities to N_{CN} , w , and H	93
Table 5.3 - Same as Table 5.2, but for the sensitivities in Λ , ϵ , and LWC	98
Table 6.1 - General characteristics of the cloud profiling missions of interest to this study	109
Table 6.2 - Properties of the points highlighted in Figure 6.8 for flight AC9....	126
Table 6.3 - Properties of the points highlighted in Figure 6.8 for flight AC12..	128
Table A.1 - sensitivities of D_{eff} to N_{CN}	165
Table A.2 - sensitivities of D_{eff} to w	166
Table A.3 - sensitivities of D_{eff} to H	166
Table A.4 - sensitivities of N_d to N_{CN}	167
Table A.5 - sensitivities of N_d to w	167
Table A.6 - sensitivities of N_d to H	168
Table A.7 - sensitivities of LWC to N_{CN}	168
Table A.8 - sensitivities of LWC to w	169

Table A.9 - sensitivities of LWC to H	169
Table A.10 - sensitivities of Λ to N_{CN}	170
Table A.11 - sensitivities of Λ to w	170
Table A.12 - sensitivities of Λ to H	171
Table A.13 - sensitivities of ϵ to N_{CN}	171
Table A.14 - sensitivities of ϵ to w	172
Table A.15 - sensitivities of ϵ to H	172
Table A.16. number of 1 Hz DSD data for the sensitivities to N_{CN}	172
Table A.17 - number of 1 Hz DSD data for the sensitivities to w	173
Table A.18 - number of 1 Hz DSD data for the sensitivities to H	173

ACRONYMS AND ABBREVIATIONS LIST

CN	Condensation Nuclei
CCN	Cloud Condensation Nuclei
GCCN	Giant Cloud Condensation Nuclei
S	Supersaturation
IN	Ice Nuclei
DSD	Droplet Size Distribution
PSD	Particle Size Distribution
CAPE	Convective Available Potential Energy
DCC	Deep Convective Cloud
SAMS	South America Monsoon System
SACZ	South America Convergence Zone
VOC	Volatile Organic Compound
WBF	Wegener-Bergeron-Findeisen
LWP	Liquid Water Path
LWC	Liquid Water Content
RH	Relative Humidity
LBA	Large-scale Biosphere-Atmosphere Experiment in Amazônia
SMOCC	Smoke, Aerosols, Clouds, Rainfall, and Climate
WETAMC	Wet Season Atmospheric Mesoscale Campaign
GoAmazon2014/5	Observations and Modeling of the Green Ocean Amazon
IARA	Intensive Airborne Research in the Amazon
ACRIDICON- CHUVA	Aerosol, Cloud, Precipitation, and Radiation Interactions and Dynamics of Convective Cloud Systems - Cloud Processes of the Main Precipitation Systems in Brazil: A Contribution to Cloud Resolving Modeling and to the GPM (Global Precipitation Measurement)
T0, T0k, T0l, T0e, T1, T2, and T3	GoAmazon2014/5 ground sites

INPA	Instituto Nacional de Pesquisas da Amazônia
UND	University of North Dakota
UECE	Universidade Estadual do Ceará
MPI	Max Planck Institute
IPA	Institute for Atmospheric Physics (Mainz, Germany)
DMT	Droplet Measurement Technologies
IOP	Intensive Operations Period
IOP1	GoAmazon2014/5 first IOP
IOP2	GoAmazon2014/5 second IOP
DLR	German Aerospace Center
FCDP	Fast Cloud Droplet Probe
TRMM	Tropical Rainfall Measuring Mission
A-Train	Afternoon Constellation (satellites)
PFC	Perfluorocarbons
AC7 to AC20	Names of HALO research flights during ACRIDICON-CHUVA, in order
ARM	Atmospheric Radiation Measurement
DOE	Department of Energy (USA)
HALO	High Altitude and Long Range Research Aircraft
G-1	G-159 Gulfstream I aircraft
CCP	Cloud Combination Probe
CDP	Cloud Droplet Probe
CIPgs	Cloud Imaging Probe Greyscale
FSSP	Forward-Scattering Spectrometer Probe
2D-C	Two-dimensional cloud probe
1D-P	One-dimensional precipitation probe
HVPS	High-Volume Particle Sampler
CPI	Cloud Particle Imager
CSIRO	Commonwealth Scientific and Industrial Research Organization

NIXE-CAPS	New Ice eXpEriment - Cloud and Aerosol Particle Spectrometer
AMETYST	Aerosol MEAsurement sYSTem
CCNC	Cloud Condensation Nuclei Counter
CPC	Condensation Particle Counter
AIMMS-20	Aircraft-Integrated Meteorological Measurement System
OPC	Optical Particle Counter
PSAP	Particle Soot Absorption Photometer
DMA	Differential Mobility Analyzer
HASI	HALO sub-micrometer aerosol inlet
CAS-Depol	Cloud and Aerosol Spectrometer
BAHAMAS	Basic HALO Measurement and Sensor System
PCASP	Passive Cavity Aerosol Spectrometer
2D-S	Two-dimensional Stereo Probe
GOES-13	Geostationary Operational Environmental Satellite 13
ACP	Atmospheric Chemistry and Physics
ACPD	Atmospheric Chemistry and Physics Discussions

SYMBOLS LIST

N_{CN}	Number concentration of condensation nuclei
N_{CCN}	Number concentration of cloud condensation nuclei
N_0	Intercept parameter of a Gamma distribution
μ	Shape parameter of a Gamma distribution
Λ	Curvature parameter of a Gamma distribution
T	Temperature
θ	Potential temperature
r_e	Effective radius
D_e	Effective diameter
N_d	Droplet number concentration
D_L	Modal diameter of the liquid water content size distribution
ε	DSD relative dispersion parameter
S	Supersaturation
D	Diameter
$N(D)$	Number concentration of droplets in a given diameter interval
M_p	Moment of order p of a DSD
G	Non-dimensional ratio, given by $\frac{M_2^3}{M_3^2 M_0}$
ρ_w	Density of water = 1000 g m ⁻³
σ	Droplet size distribution standard deviation
D_g	Mean geometric diameter
w	Updraft speed (always positive)
W	Vertical wind speed (positive or negative)
H	Altitude above cloud base
H_{base}	Cloud base altitude
$H_{0^\circ\text{C}}$	Altitude of the 0 °C isotherm
$S_Y(X_i)$	Sensitivity of the dependent variable Y to the independent variable X_i
D_a	Mean areal diameter
t_x	Time interval x

- \vec{P}_1, \vec{P}_2 Position vectors in the Gamma phase space
- \vec{F} Generic pseudo-force in the Gamma phase space
- \vec{F}_{cd} Condensational pseudo-force in the Gamma phase space
- \vec{F}_{cl} Collisional pseudo-force in the Gamma phase space

SUMMARY

	<u>Page</u>
1 INTRODUCTION	1
1.1. Objectives	6
2 LITERATURE REVIEW	7
2.1. Aerosol effects on warm clouds	7
2.2. Aerosol effects on mixed-phase clouds	10
2.3. Convection invigoration or suppression by aerosols	14
2.4. Previous aircraft campaigns in the amazon	19
2.4.1. TRMM-LBAWETAMC.....	20
2.4.2. LBA-SMOCC	24
3 METHODS.....	33
3.1. Experimental campaigns.....	33
3.1.1. GoAmazon2014/5	33
3.1.2. IARA.....	35
3.1.3. ACRIDICON-CHUVA	37
3.2. Instruments description.....	42
3.2.1. G-1	42
3.2.1.1. FCDP	42
3.2.1.2. CPC.....	43
3.2.1.3. AIMMS-20	44
3.2.2. HALO	45
3.2.2.1. CCP.....	45
3.2.2.2. AMETYST-CPC.....	46
3.2.2.3. CCNC.....	46
3.2.2.4. NIXE-CAPS.....	47
3.2.2.5. BAHAMAS.....	48
3.3. Gamma parameterization	48

4	IMPACTS OF THE MANAUS POLLUTION PLUME ON THE MICROPHYSICAL PROPERTIES OF AMAZONIAN WARM-PHASE CLOUDS IN THE WET SEASON.....	51
4.1.	Background.....	51
4.2.	Flight characteristics	53
4.3.	Plume classification	57
4.4.	Bulk DSD properties for polluted and background clouds.....	63
4.5.	Vertical DSD development and the role of the vertical wind speed.....	69
4.6.	Closing remarks	76
5	SENSITIVITIES OF AMAZONIAN CLOUDS TO AEROSOLS AND UPDRAFT SPEED	77
5.1.	Background.....	77
5.2.	Campaign and methodology	79
5.3.	Sensitivity calculation.....	81
5.4.	Cloud droplet size distributions related to different aerosol and thermodynamic conditions.....	85
5.5.	Comparing the main drivers of bulk microphysical properties of Amazonian clouds.....	90
5.6.	Effects on DSD shape and relation between sensitivities	95
5.7.	Closing remarks	101
6	ILLUSTRATION OF MICROPHYSICAL PROCESSES OF AMAZONIAN DEEP CONVECTIVE CLOUDS IN THE GAMMA PHASE SPACE: INTRODUCTION AND POTENTIAL APPLICATIONS	103
6.1.	Background.....	103
6.2.	Flight characterization.....	106
6.3.	Introducing the Gamma phase space	109
6.4.	Aerosol and thermodynamic conditions in different Amazonian regions	112
6.5.	Observed trajectories in the Gamma phase space	115
6.6.	Contrasts between clean and polluted trajectories.....	120
6.7.	Observations of the mixed-phase formation	128
6.8.	Closing remarks	133

7	CONCLUSIONS.....	135
7.1.	Future perspectives	140
	REFERENCES.....	141
	APPENDIX A – SUPPLEMENT MATERIAL TO CHAPTER 5.....	165
	Sensitivities for individual intervals	165

1 INTRODUCTION

The Amazon is a key component of the global climate system. According to Keller et al. (2009), the Amazon can be understood as a giant biogeochemical reactor, where it serves as both source and sink of quantities that determine the climate. The forest emits high amounts of water vapor through evapotranspiration as well as the particles necessary for cloud formation (CCN, cloud condensation nuclei), thus maintaining an intense hydrological cycle (SILVA DIAS et al., 2002; BETTS et al., 2004). Gandu and Silva Dias (1998) identified the Amazon as one of the primary heat sources of the global climate due to the latent heat release by the condensing water vapor in the clouds. Regarding South America, the strong latent heat release by Amazonian convection is one of the primary mechanisms supporting the Bolivian High, which is a key component of the South America Monsoon System (SAMS, ZHOU; LAU, 1998; VERA et al., 2006).

Human activities involved in the management of agriculture, logging, and urbanization significantly affect the land use and surface characteristics of the Amazonian region (SOARES-FILHO et al., 2006). As of 2005, Ometto et al. (2005) estimates that deforestation reached 18% of the original forest area, primarily in the southern and western regions. This activity has not only regional effects on the ecosystem, but may also contribute to the global climate change. Malhi et al. (2008) estimate that the forest stores around 200 Pg of carbon, which can be released into the atmosphere during deforestation. Additionally, the deforestation that converts forest into pasture has a drying effect and alters the energy partitioning in favor of sensible heat (FISCH et al., 2004). Feedback between the perturbed climate and the biome response further favor regional and global climate change (DAVIDSON et al., 2012; HUNTINFORD et al., 2013). Boisier et al. (2015) identified an overall drying trend for the Amazon, especially in the eastern region, which is a major concern as deforestation tends to intensify during relatively dry periods because the trees are easier to burn. The changing characteristics of the forest and the overall climate also result in more frequent

extreme events such as the droughts during 2005 and 2010 (MARENGO et al., 2008; MARENGO et al., 2011).

Beyond the biome, the Amazon also contains an extensive river system that is responsible for around 20% of the world's freshwater discharge, which was found to be sensible to climate change (NOBRE et al., 2009). Both the biome and the river system interact with the clouds and maintain the hydrological cycle in balance. In that regard, aerosol particles play an important role, as they are responsible for activating cloud formation, allowing for the water evaporated from the rivers and emitted by the forest via evapotranspiration to return to the surface through precipitation. The aerosol particles over the Amazon can have both natural, emitted by the forest or transported from other regions, and anthropogenic sources. According to Andreae (2007), the natural aerosols in the Amazon most likely maintain similar characteristics as in the preindustrial era because of the vast unpopulated areas in the forest. The fraction of the natural aerosols that serve as CCN were found to be primarily secondarily generated through the oxidation of the volatile organic compounds (VOCs) emitted by the forest (PÖSCHL et al., 2010). Primary biogenic particles from the forest were identified as the primary source of ice nuclei (IN), complemented by the occasional Saharan dust transport (PRENNI et al., 2009).

One of the primary ways human impact cloud formation over the Amazon is through the increase of CCN number concentrations (N_{CCN}) caused by pollution. In that sense, biomass burning is the activity that most contributes to pollution in the Amazon (CRUTZEN; ANDREAE, 1990; BOWMAN et al., 2011), being more active during the dry season (ARTAXO et al., 2002). Although there are some natural-occurring biomass burning events, the vast majority is caused by human activities. The southern and southeastern Amazon is a region where the deforestation and biomass burning events are frequent. The smoke produced by the burning vegetation is carried upwards by convection (ANDREAE et al., 2001) while also spreading horizontally. Additionally, the aerosol particles are also subject to long range transport and can potentially affect clouds as far as in the

La Plata Basin (CAMPONOGARA et al., 2014). The frequency of biomass burning events in southern and southeastern Amazon contrasts sharply with the other regions (as it is closer to more densely urbanized regions), which is the reason why it is commonly referred to as “arc of deforestation” (FUZZI et al., 2007).

Clouds that form under Amazonian background conditions can present significantly different properties compared to clouds that develop over polluted regions such as the arc of deforestation. Andreae et al. (2007) and Martin et al. (2010) report that aerosol particles number concentrations (N_{CN}) reach up to several hundred per cm^{-3} under background conditions. By contrast, N_{CN} is an order of magnitude higher when biomass burning events are widespread (MARTIN et al., 2010; ARTAXO et al., 2013), especially during the dry season when precipitation is less frequent. A tenfold increase in N_{CN} , which is usually followed by a similar increase in N_{CCN} , can have deep impacts in cloud formation and development (MCFIGGANS et al., 2006; REUTTER et al., 2009; KOREN et al., 2014). Andreae et al. (2004) presented a pioneer study comparing microphysical properties of clouds that develop over biomass burning events to those under Amazonian background or even maritime conditions. They show that polluted clouds present much higher droplet number concentrations, with suppression of the growth processes in the warm layer ($T > 0\text{ }^{\circ}\text{C}$). As pointed out by Rosenfeld et al. (2008), the warm-phase suppression does not necessarily lead to suppression of the cloud as a whole. Given the smaller droplets in polluted clouds, they take longer to precipitate by warm mechanisms and end up participating in and intensifying the mixed and glaciated layers. In fact, Lin et al. (2006) report increased rainfall amounts, cloud cover and cloud top hydrometeor effective radius for polluted regions in the Amazon. Gonçalves et al. (2015) report that biomass-burning aerosols may suppress or enhance convective systems depending on the atmospheric instability. They found aerosol-enhanced rainfall in systems developing under high CAPE (Convective Available Potential Energy) conditions. Given that pollution affects the layer distribution in the clouds, it is also

possible to observe a relation between biomass burning pollution and electrical activity in clouds (ALTARATZ et al., 2010).

Even though the interaction between aerosols, clouds, and precipitation has received significant attention in recent years (see the reviews by TAO et al., 2012; ROSENFELD et al., 2014; FAN et al., 2016), there are still unknown features regarding the feedback mechanisms involved. One difficulty in this type of study is the isolation of the aerosol effect, as opposed to the thermodynamic and meteorology differences. In the Amazon, the analysis of the aerosol effect is usually studied by comparing clouds that develop over remote Amazonian or polluted regions. However, the polluted regions usually present different local meteorology given the land use change and the consequent different energy partitioning (FISCH et al., 2004). One possibility in that regard is to analyze clouds that develop in the same region, and the underlying thermodynamic conditions, but are subject to different aerosol conditions. One example is by studying the surroundings of cities in the Amazon such as Manaus. This city is located in the center of the Amazon (3° 6' S, 60° 1' W), with a population of approximately 2 million people (IBGE, 2017), being surrounded by hundreds or even thousands of km of forest in all directions. The pollution plume emitted from the city usually disperse to the southwest direction (Kuhn et al., 2010) and interact with the clouds in its way. By comparing the clouds in and around the plume, it is possible to infer the aerosol effect where the thermodynamic conditions are relatively similar. This will be addressed in this thesis, with more details in Chapter 4.

The uncertainties related to the aerosol-cloud-precipitation interactions in the Amazon are only one aspect of the unknowns surrounding tropical continental clouds as a whole. This type of cloud, despite their importance to the regional and global climate, is still poorly represented by models (BETTS, 2002; DAI, 2006; KIDD et al., 2013). According to Kidd et al. (2013), although the bias between model and observations of rainfall amounts in the tropics can be as low as 4%, there are still major misrepresentations such as the spatial distribution and daily cycle of the precipitation. In specific to the daily cycle, the modelled

clouds usually precipitate earlier than in the observations. This is a result of misrepresentation of the evolving cloud microphysics, which includes the aerosol effect and the representation of the droplet size distribution (DSD) of the hydrometeors. Therefore, in order to better understand and model Amazonian clouds, with the broader goal of improving our global climate knowledge, more studies are needed highlighting the details of the clouds microphysical properties and their sensitivity to changes in aerosol number concentrations and thermodynamic conditions.

The main goal of this work is to take advantage of new measurements of microphysical properties of Amazonian clouds in order to further our knowledge on their evolving characteristics and relation to different aerosol and thermodynamic conditions. The analyzes are developed based on the measurements of several field campaigns as part of the GoAmazon2014/5, IARA, and ACRIDICON-CHUVA experiments (see descriptions in Chapter 3). Specific subjects to be addressed are 1) the relation between Manaus pollution plume and the microphysical properties of surrounding clouds, 2) quantification of the sensitivities of Amazonian clouds to changes in aerosol and thermodynamic conditions, and 3) the use of the Gamma DSD and its phase space to represent the evolution of the clouds microphysical properties.

Chapter 2 provides a general review of the associated literature, while Chapter 3 presents the overall methods used. The results are segregated into three chapters (Chapters 4, 5, and 6), each one related to either submitted or accepted papers. At the time of writing (May 2017), the first paper (described in Chapter 4) is already published in final form in the Atmospheric Chemistry and Physics (ACP) journal. The second and third papers (Chapters 5 and 6) are submitted to the same journal and are currently under review. Finally, Chapter 7 presents the main conclusions from this thesis.

1.1. Objectives

The specific objectives of this study can be listed as (unless specified, the results are focused on the warm layer of the clouds):

- 1) Acquire statistics of Amazonian clouds microphysical properties as function of region within the forest, aerosol, and thermodynamic conditions.
- 2) Develop a methodology to infer the Manaus pollution plume effect on Amazonian clouds microphysics.
- 3) Quantify the clouds sensitivity to aerosol and thermodynamic conditions by expanding the methodologies found in the literature.
- 4) Understand how microphysical properties evolve throughout the clouds life cycle.
- 5) Demonstrate new ways to analyze cloud microphysics using the Gamma DSD and its phase space.
- 6) Study the transition from the warm to the mixed phase.

2 LITERATURE REVIEW

In this Chapter, a general overview of the fundamental processes of importance to this work is presented. Chapters 4, 5, and 6 contain additional specific background information and references.

2.1. Aerosol effects on warm clouds

Aerosol particles in the atmosphere are a determinant factor for cloud formation, as they can serve as cloud condensation nuclei (CCN). The process in which the dry particle grows by condensation and becomes a cloud droplet was initially studied by Köhler (1936). The author notes that the dry particles must grow to a critical radius, with a corresponding critical supersaturation, to become cloud droplets. This critical radius is reached by increased water vapor pressure around the particle, which can be achieved, for instance, in arising parcels. For water vapor pressure below the critical threshold, the dry particle grows and shrinks according to the fluctuations in relative humidity. When the critical value is reached, the droplet will grow spontaneously regardless of further fluctuations in the humidity around it. At this point, the aerosol particle is activated and becomes a CCN. The Köhler theory has been recently revised (PETTERS; KREIDENWEIS, 2007, 2008, 2013), but the main concepts remain the same.

The presence of aerosol particles able to act as CCN allows for cloud formation in the atmosphere. In the absence of such particles, the necessary supersaturation for homogeneous nucleation would be unrealistic. Therefore, aerosol population aspects such as number concentration and chemical composition are determinant for the initial cloud formation. The early characteristics of the cloud microphysics as function of aerosol conditions has been extensively studied and is considered as the first indirect aerosol effect on climate, or the Twomey effect (TWOMEY, 1977). The author states that, given two clouds with the same liquid water path (LWP), the one subject to higher N_{CCN} will have more droplets with reduced size. This can be understood by the water

vapor competition concept, where the same amount of water is being distributed into more droplets, therefore reducing their size.

In actual observations, even though clouds present diverse LWP values, it is possible to observe a correlation between aerosol particles and cloud droplets concentrations. Ramanathan et al. (2001) combine results from different studies and show a clear correlation between N_{CN} and N_d for several regions with diverse aerosol conditions. With aircraft measurements, Martin et al. (1994) showed that marine stratocumulus clouds presented higher droplet concentrations and lower effective radius (r_e) with increasing pollution. Because the rate of growth by collision-coalescence is proportional to $r_e^{4.8}$ (FREUD; ROSENFELD, 2012), collection growth is rather ineffective for small droplets but intensifies quite quickly when $r_e \gtrsim 14 \mu\text{m}$. In this way, increased pollution tends to suppress warm rain formation. Indeed, Rosenfeld et al. (1999) used the TRMM satellite to analyze precipitation in the tropics and found significant suppression of warm rain related to increased pollution. They estimate that the polluted clouds would need to grow to the altitude where $T = -10 \text{ }^\circ\text{C}$ to efficiently produce rain by the warm mechanisms. Of course, this is just a theoretical estimation given that other processes take place with negative temperatures. Shrivastava et al. (2013) also confirm the first aerosol indirect effect by using coupled atmospheric-chemistry model for short-lived shallow cumuli.

When a higher number of small droplets is formed, the condensation rate should be intensified as it is inversely proportional to droplet size. Additionally, small droplets have enhanced area-to-volume ratio that also contributes to the condensation. One result is quicker consumption of the supersaturation and, given favorable conditions, may induce higher amounts of water in the clouds. Beyond that, the warm rain suppression allows for the water to remain longer in the cloud. Xue and Feingold (2006) use large-eddy simulations of trade wind clouds and note that increased aerosol pollution leads to higher LWP. This quantity is proportional not only to vertical LWC profile, but also to cloud depth. Therefore, both effects should be analyzed in order to comprehend the aerosol

effect on LWP. This effect, however, is complex because of the feedback mechanisms involved and frequently vary depending on the meteorological conditions. Some contrasting results are found in the literature. Liu et al. (2003) found that LWC remained relatively constant between polluted and clean clouds in the Indian Ocean, while Cecchini et al. (2016) reported on increased LWC for polluted clouds in the Amazon. The feedback mechanisms will be discussed in more detail in the next sections, but it seems that pollution significantly affects cloud vertical development in the Amazon, therefore favoring higher LWP values (ANDREAE et al., 2004). Andreae et al. (2004) analyzed Amazonian clouds forming directly over biomass burning events and compared to cleaner systems. Given that biomass burning also emit heat, it is difficult to appoint the specific role of the aerosols in that case.

Another consequence of the first indirect effect are narrower DSDs in the warm phase, given that the condensational growth is favored. However, one usual assumption is that the dry aerosol size distribution does not change much from clean to polluted conditions. In fact, when the ambient aerosol population includes particles with radii $r > 5 \mu\text{m}$, the effects might be different. This type of particle is known as giant CCN (GCCN) and is common in maritime regions as the sea salt (O'DOWD et al., 1997) and can also be present in the Amazon because biological particles are known to be GCCN too (MÖHLER et al., 2007). Nevertheless, Johnson (1982) showed that GCCN presence may enhance warm rain formation. The primary reason is that the bigger particle size prompts an early formation of rain embryos, favoring the collection growth. Cheng et al. (2007) modeled the role of GCCN, noting that they increase droplet size and therefore precipitation amounts. However, the presence of GCCN is not a sufficient condition for rain formation. It is necessary that smaller CCN are also available to maximize the GCCN efficacy. Feingold et al. (1999) use a varied modeling framework and note that the GCCN efficiency grows as the CCN concentrations increase. The explanation is that the bigger droplets formed via GCCN need to have smaller ones to grow by collection. When CCN are too low (e.g. 50 cm^{-3} or lower),

precipitation will likely form regardless of the GCCN presence. However, when CCN concentrations are in the range 50-250 cm⁻³, Feingold et al. (1999) notes that the GCCN might be responsible by the transition from non-precipitating to precipitating condition. On the other hand, if CCN concentrations are too high (e.g. 1000 cm⁻³), warm rain formation will be suppressed and GCCN may not be enough to produce precipitation. Amazonian background CCN concentrations are in the range 200-300 cm⁻³ (ROBERTS et al., 2001, 2002; ANDREAE et al., 2004; GUNTHER et al., 2009), which is in the range sensitive to GCCN.

Some studies also suggest that, under certain circumstances, warm clouds may be invigorated by added CCN. This happens relatively rarely and in very pristine clouds subject to moderate increases in CCN. Yuan et al. (2011b), Christensen and Stephens (2011) and Chen et al. (2015) note that maritime clouds have higher cloud tops and therefore allow for more time for the warm precipitation to occur. However, if too much pollution is added to the systems, the precipitation will be suppressed. Koren et al. (2014) reports on positive correlations between rainfall rates and aerosol concentration/cloud top height. Nonetheless, this effect is probably not determinant in the studies proposed here as biomass burning and/or the Manaus pollution plume often increase CCN concentrations by an order of magnitude (ANDREAE et al., 2004; KUHN et al., 2010; MARTIN et al., 2010; ARTAXO et al., 2013).

2.2. Aerosol effects on mixed-phase clouds

Aerosols can impact the mixed phase by directly serving as IN, or by changing the warm layer as CCN and then impacting the further development of the cloud. The study of the role of mixed and ice processes in clouds is crucial, given that they are responsible for most of the precipitation in the tropics (LAU; WU, 2003). Additionally, DeMott et al. (2010) showed that global climate simulations, including the aerosol indirect effect, are sensitive to the model's representation of the glaciation process. If aerosols can significantly impact the mixed and ice

processes, then it is imperative that the interactions are understood and well represented in models.

For the Amazon, most of the IN population comes from biological particles emitted by the forest itself, with occasional contributions from Saharan dust transport (PRENNI et al., 2009). This long-range dust transport is favored during the wet season (January-May). Contrary to CCNs, IN particles participate later in the cloud lifecycle, when the temperature reach values low enough for the activation process. Under IN-free conditions, the ice can be activated homogeneously when the temperatures fall below $-38\text{ }^{\circ}\text{C}$, but some biological particles emitted by the Amazon, such as bacteria, may increase this limit to temperatures as high as $-4\text{ }^{\circ}\text{C}$ (MORRIS et al., 2004). Fan et al. (2010a) notes that increases in IN concentrations does not significantly affect convective strength, but can significantly increase ice concentrations in the cloud's anvil given enough humidity. Ice particles not only participate in rain formation but also scatter solar radiation differently than liquid droplets. Therefore, if anthropogenic emissions can enhance IN concentrations, the liquid-ice proportion in clouds will be different and will affect rain amounts at the surface and the clouds radiative forcing.

Lohmann and Feichter (2005) summarize the aerosol indirect effects in clouds, noting that there are three primary mechanisms in mixed-phase clouds. The first one is known as the thermodynamic indirect effect, where the smaller droplets formed in polluted clouds have lower probability of collecting IN and therefore take longer to freeze. If IN concentrations are enhanced, the clouds may glaciate quickly and form precipitation more efficiently. This is the second mechanism, known as the glaciation effect. Finally, the third effect is related to ice growth by collection of supercooled water, a process known as rimming. The smaller droplets in polluted systems may slow down the growth by rimming. However, the interactions involved in the effects summarized by Lohmann and Feichter (2005) are still poorly understood and newer studies are trying to piece together all the moving parts.

Perhaps the easiest process to comprehend is the heterogeneous ice activation, given that it does not rely on interactions between liquid droplets and ice particles. van den Heever et al. (2006) simulated deep convective clouds (DCCs) and showed that increased IN concentrations produced ice in warmer temperatures, resulting in deeper anvils. However, IN increases were not the most efficient process to increase overall ice concentrations. CCN enhancements proved to be more effective in that regard, where the smaller droplets in the warm phase did not precipitate and were carried upwards to participate in the ice processes. Increased CCN concentrations also lead to increased supercooled water mixing ratios, given the thermodynamic effect, which were responsible for higher hail mixing ratios as well.

The aerosol effect in mixed-phase clouds by first acting as CCN and then affecting the mixed layer was also studied by Cheng et al. (2010). The authors found that increased CCN concentrations lead to more cloud droplets and ice, but the effects on precipitation were non-linear. The amount of precipitation formed is the result of several competing mechanisms that depend on cloud microphysics and dynamics. The increased droplet concentration, which favors the persistence of supercooled droplets above the 0 °C isotherm, can enhance ice growth in cloud layers sub-saturated with regards to liquid water but supersaturated with regards to ice. In such layers the water of the supercooled droplets evaporates and sublimates into the ice particles, in the process known as the Wegener-Bergeron-Findeisen mechanism (WBF, WEGENER, 1911; BERGERON, 1935; FINDEISEN, 1938). However, updraft cores in mixed-phase clouds frequently produce water vapor pressure above the liquid water limit (FAN et al., 2011), making both liquid droplets and ice particles grow concomitantly. In that case, the growth of the ice particles is slowed down given the competition with the supercooled droplets. Therefore, ice growth in polluted systems may be enhanced especially in the downdraft regions of the clouds, where the supercooled droplets are continually evaporated until depleted. On the other hand, supercooled droplets persist in the updraft cores, sometimes even reaching

the homogeneous freezing limit (ROSENFELD; WOODLEY, 2000). Graupel particles growth by rimming may be either enhanced or suppressed depending on the total amount of supercooled water and the size of the droplets. Rimming is favored by higher amounts of supercooled water, but may also be suppressed because of the smaller droplet size (CHENG et al., 2010). The ultimate result will depend on the number of CCN available and the dynamics within the cloud.

One additional source of complexity to the ice processes stems from the observations that there are secondary ice generation mechanisms. Hobbs and Rangno (1985) found that the ice concentration in clouds can be significantly higher than IN concentrations. Therefore, there are mechanisms that multiply ice concentrations. One of such mechanisms was described by Hallett and Mossop (1974). The basic concept is that freezing droplets may emit ice splinters which then act as nuclei for further ice formation. Note that this process has a cascading effect, where each new ice particle formation may release multiple splinters. More recently, Lawson et al. (2015) describe a similar secondary ice generation mechanism that is active in updraft cores of maritime clouds. In this process, the big supercooled droplets in the maritime system collect the ice splinters and quickly freeze. The authors note that the splinter release is favored in big droplets, making the glaciation process rather effective in maritime clouds. Given the similarities between Amazonian background and maritime clouds, this process may also occur over the rainforest. This is further supported by the observations of Heymsfield and Willis (2014), which note that secondary ice generation is favored by low LWC, low updraft speed, and low concentrations of supercooled droplets. All three factors are expected in Amazonian background clouds given the relatively low CCN concentrations. Smaller droplets can also contribute to the multiplication of ice particles, therefore contributing to the glaciation of the cloud, by the rime splintering process. This occurs when supercooled droplets are collected by bigger ice particles (being graupel, hail, frozen drops, or snowflakes), releasing splinters in the process. However, rime splintering is expected to be of secondary importance to this study, given the focus on growing convective clouds

at early stages of their life cycle. A review of secondary ice production processes is given in Field et al. (2017).

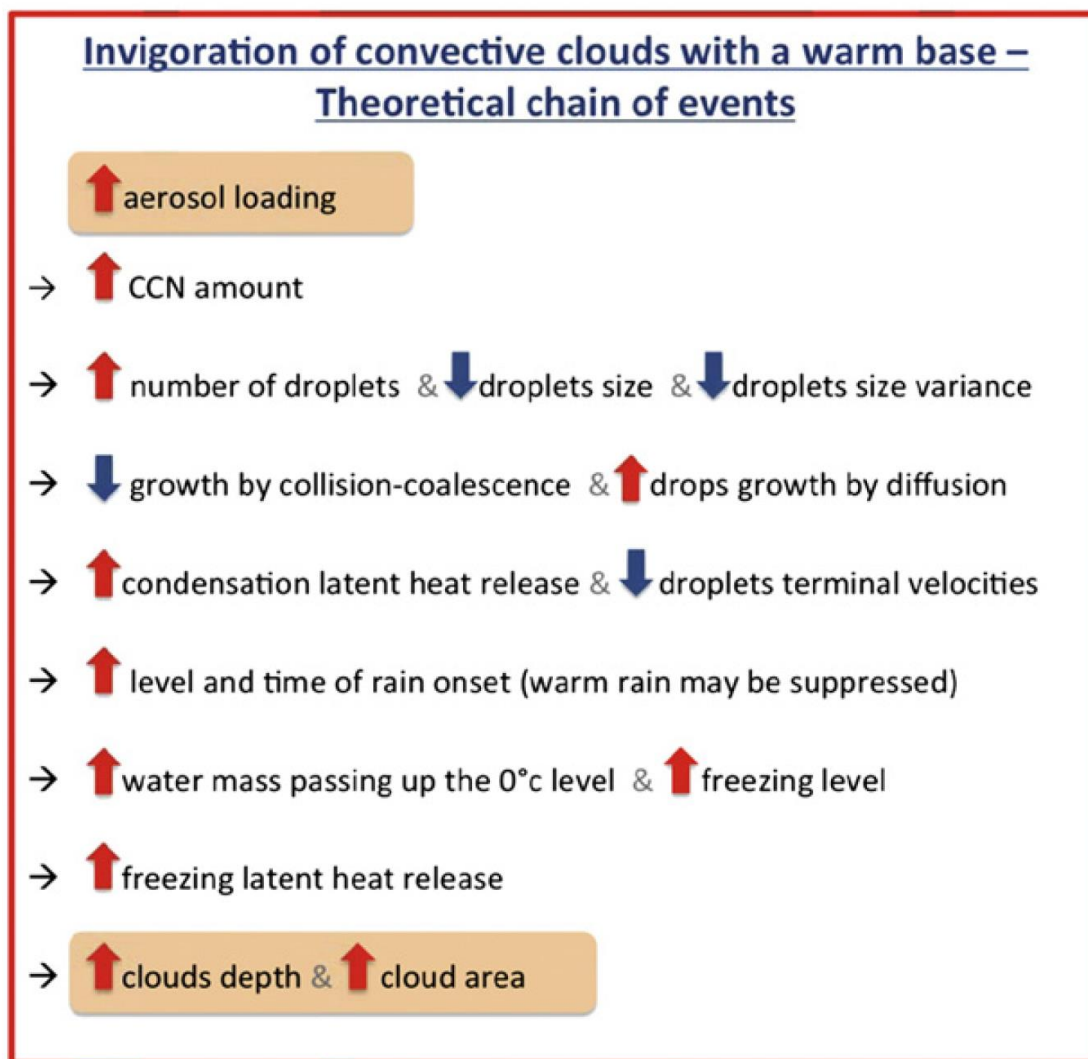
2.3. Convection invigoration or suppression by aerosols

Clouds that develop above the 0 °C isotherm can have its convective intensity altered by increased pollution. This effect occurs due to the microphysics-dynamics feedback, i.e. the ability of microphysical processes to affect cloud dynamics and vice-versa. One of the primary mechanisms by which aerosols can affect cloud dynamics is by impacting the updrafts. As modeled by van den Heever (2006), increases in pollution lead to stronger updrafts as the condensation rates are increased. Additionally, by increasing the level of the precipitation onset, the peak of the latent release is higher in the cloud, favoring further vertical development (KHAIN et al., 2005). When the cloud droplets start to freeze, they release even further latent heat, favoring further cloud development. This cycle was consolidated into the conceptual model proposed by Rosenfeld et al. (2008). However, several processes may occur and the convection invigoration is not always straightforward.

Altaratz et al. (2014) notes that convection invigoration occurs when the processes in the cloud core (condensate gain) dominate over the processes in the cloud margins (condensate loss). Following this distinction, the authors propose an ideal scenario for cloud invigoration that follow the chain of events expressed in Figure 2.1. The scenario can be described as follows: 1) increase in aerosol loading lead to increased CCN concentrations; 2) more and smaller liquid droplets are formed in a narrower DSD; 3) collection growth is suppressed, while condensation is enhanced; 4) more latent heat is released and the droplets have lower terminal velocity; 5) the rain initiation is delayed and occurs higher in the cloud; 6) more water go through the 0 °C isotherm and the droplets freeze at higher altitudes; 7) more latent heat is released by freezing; and 8) cloud depth and area are increased. More details about each step and the corresponding references can be found in Altaratz et al. (2014). With the ideal scenario

established, it is important to understand which meteorological and dynamical aspects favor deviations from it.

Figure 2.1: chain of events in an ideal scenario for cloud invigoration. Source: Altaratz et al. (2014).



Xue and Feingold (2006) studied the effects of aerosols on warm trade wind cumuli. They note that the smaller droplet size favor not only higher condensation rates but also their faster evaporation. Therefore, the relatively high area-to-volume ratio of warm clouds favor evaporation, resulting in shallower and smaller clouds with enhanced aerosol loading. In that case, the margin-based processes (entrainment mixing) dominate over the core-based ones. In case the

surrounding air is dry, the suppression can be even stronger (KHAIN et al., 2008). Storer et al. (2010) simulated clouds under different CAPE and aerosol conditions. The convection suppression may occur under low CAPE conditions given that the clouds tend to be shallower. Alternatively, high CAPE conditions favor convective invigoration by aerosols. The authors also quantitatively compared the effects of altered CAPE and aerosol conditions on the cloud development. They found that the aerosol effect can be equal or even stronger than changes in thermodynamic conditions.

The vertical wind shear was also found to modulate the aerosol effect on convective strength. Fan et al. (2009) analyzed this issue and found that strong wind shear favor convective suppression by aerosols because of the increased area-to-volume ratio. On the other hand, weak vertical wind shear favors the core-based processes and thus the convective strength. Clouds that have cold bases (e.g. $< 15\text{ }^{\circ}\text{C}$) are also less susceptible to the aerosol invigoration mechanism given that there is less time for the latent heat release during the warm phase (LI et al., 2011; FAN et al., 2012b).

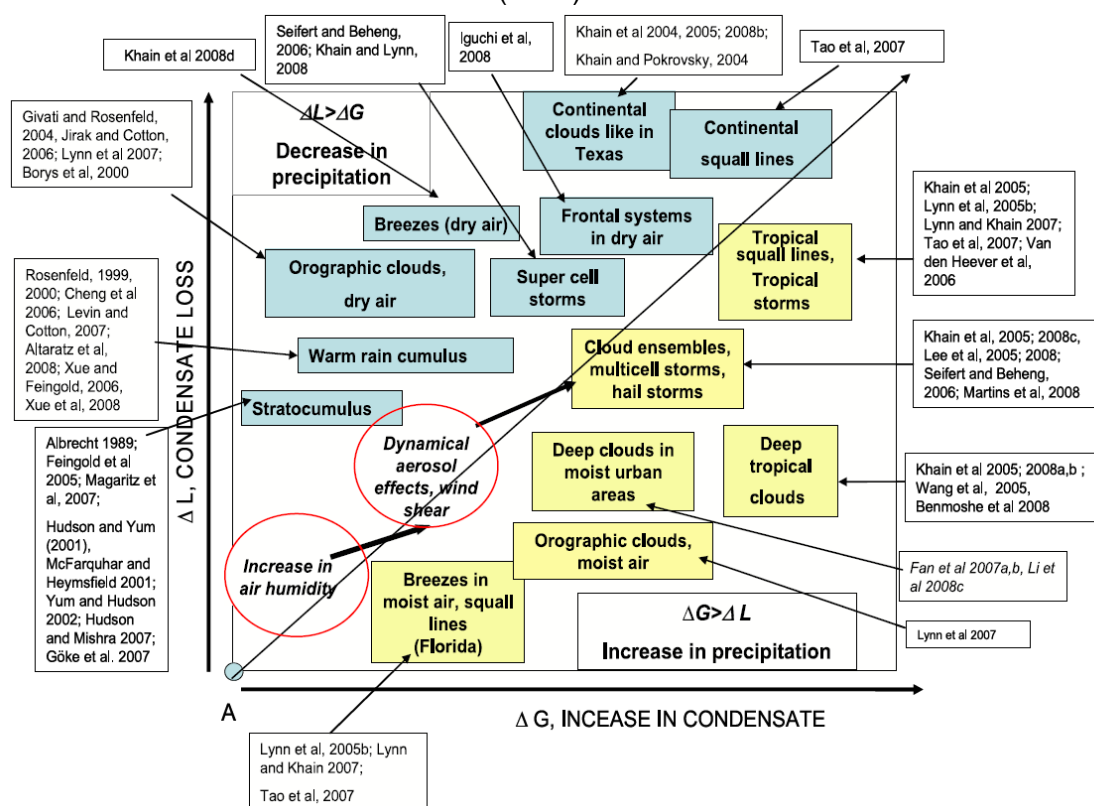
Fan et al. (2013) argues that the concept of convection invigoration by the increased latent heat release is dominant only at the growing stage of the cloud lifecycle. Later in the cloud development, the polluted clouds reach higher altitudes with larger area because the anvil ice particles are smaller and therefore sediment slower. Enhancements in the updraft strength are also subject to two competing mechanisms. On one hand, the increased latent heat release during the growth stage favor stronger updrafts, but increased ice mass higher in the cloud hampers ascending movements (LEBO; SEINFELD, 2011). Storer and van den Heever (2013) modeled clouds with the same thermodynamic conditions and varied CCN concentrations. They found that polluted systems present stronger updrafts initially, but the average vertical speeds are lower further in the life cycle and above 6 km.

The aerosol effect on deep convective clouds also has complex consequences for secondary convection and cloud field organization. If the convection is invigorated, the stronger updrafts and evaporative cooling also produce stronger downdrafts. The relatively small rain droplets will evaporate quickly during their descent and will generate stronger cold pool below the clouds (TAO et al., 2007). The stronger cold pool favors low level convergence, favoring secondary convection formation. Additionally, this process may even organize the secondary convection into squall lines (KHAIN et al., 2005). However, if the clouds are suppressed (due to low CAPE or high vertical wind shear, for instance), then the reduced precipitation results in weaker cold pools and less organized convection (HEIBLUM et al., 2016b). Additional aerosol effects on cloud cover and atmospheric stability occur when the particles are efficient at absorbing radiation. Ackerman et al. (2000) found that soot particles suppressed cloud cover over the tropics given the warming of the aerosol layer. Over the Amazon, Koren et al. (2008) note that for very high concentrations of biomass burning aerosols the convection is suppressed. The main reasons are two-fold. On one hand, the absorbing aerosols evaporate cloud droplets by warming the air around them, favoring condensate loss. On the other hand, the warming of the injection layer induces atmospheric stability and hampers the vertical development of the clouds.

With the aim of synthesizing the studies related to convection invigoration/suppression by aerosols, Khain (2009) produced the sketch shown in Figure 2.2. The authors consider the invigoration/suppression as the balance between condensate gain or loss that generate precipitation enhancement or suppression, respectively. Note that a wide variety of scenarios are possible, but there is enough consistency to substantiate conclusions for the Amazon region. Note that deep tropical clouds and squall lines are in the precipitation enhancement region, which suggests that this is the primary aerosol effect for the Amazonian region. Indeed, the atmosphere over the forest is humid, with usually high CAPE values and relatively low vertical wind shear. All those characteristics

favor the core-based mechanisms pointed out by Altaratz et al. (2014) and favor convection invigoration by aerosols. Nonetheless, it is important to note that relatively shallow warm-based precipitating cumuli are frequent in the Amazon, especially during the wet season. For those systems that do not have a significant portion above the 0 °C isotherm, the suppression of the warm processes most likely dominates.

Figure 2.2: schematic representation of the conditions favoring convection invigoration or suppression. The specific citation shown can be found in the source material. Source: Khain (2009).



Given that the aerosols can impact different types of clouds in different ways, it is expected that they impact the precipitation histogram of a given region. For instance, Qian et al. (2009) found that aerosols specifically suppressed light rain over eastern China. Conversely, for the same region, Fan et al. (2012a) that aerosols also enhance stronger precipitating systems. For the tropic, subtropics, and mid-latitudes, Koren et al. (2012), using TRMM data, found that aerosols enhanced heavy precipitation. Other studies also found that aerosols

concomitantly suppress light precipitation while enhancing heavy rainfall (LI et al., 2011; GUO et al., 2014). However, it is interesting to contrast aerosol regional effects with their effects on larger scale. Van den Heever et al. (2011) studied this issue and concluded that, for larger domains, there are compensating mechanisms that smooth the local aerosol effects. One example is the lower frequency of occurrence of light rain with higher frequency of heavy precipitation. Those two factors, when averaged over a large region, will result in relatively weak aerosol effect on the domain-averaged rainfall. This type of observation, where one pathway of the aerosol effect has minimizing effects on other pathways, prompted Stevens and Feingold (2009) to call the aerosol-cloud interactions a buffered system. The authors chose the “buffered” name because inputs in the aerosol-cloud interactions system are minimized by secondary processes resulting in smoother outputs. Additionally, they argue that the buffer processes are not limited to large scales. One microphysical example is the relation between the number of droplets and the supersaturation during the CCN activation. When only a few droplets are formed (as in a clean atmosphere), the supersaturation remain high and partially compensates the lower condensation rates of the big droplets. This could partly explain the sublinear relation between CCN and cloud droplet number concentration found in the literature (STEVENS; FEINGOLD, 2009).

For further details on the aerosol effects on clouds, precipitation, and climate, see the reviews by Tao et al. (2012), Altaratz et al. (2014), Rosenfeld et al. (2014), and Fan et al. (2016).

2.4. Previous aircraft campaigns in the amazon

The Amazon has been recognized as a key entity in the global climate. Therefore, a large-scale, multinational, and multidisciplinary experiment was set to study the internal processes in the Amazon and their relationship with the climate. This experiment is called Large-scale Biosphere-Atmosphere Experiment in Amazônia (LBA), is led by Brazil and operated by Instituto Nacional de Pesquisas

da Amazônia (INPA). As part of this large-scale experiment, several smaller field campaigns took place in the Amazon. Here we will describe the main findings of two campaigns that used aircraft to probe clouds. This will provide the background understanding of Amazonian clouds, putting the results of this work into historical perspective.

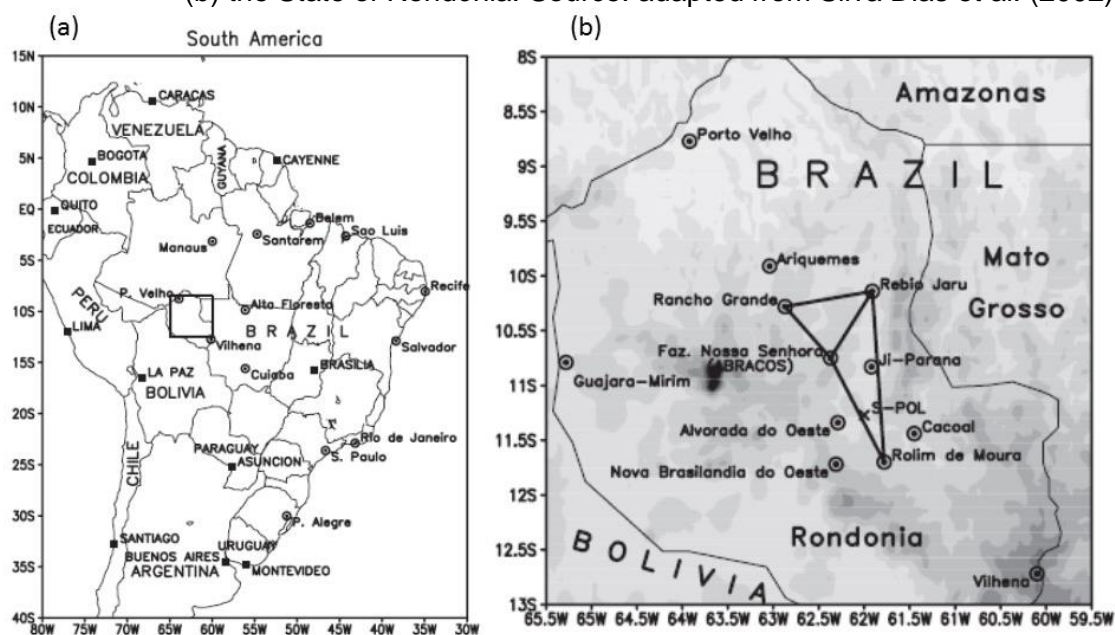
2.4.1. TRMM-LBA/WETAMC

During January and February 1999, two collaborating campaigns took place at the same time in the Amazon as part of the LBA program. Those were the wet season atmospheric mesoscale campaign (WETAMC) and the Tropical Rainfall Measuring Mission validation campaign (TRMM-LBA). At the time of the campaigns, little was known about the rain formation mechanisms in the Amazon such as natural CCN sources and cloud microphysics evolution. The overall aim of the campaigns was to understand the feedback between the forest and its hydrological cycle. More specifically, the heat, moisture, CO₂, trace gases and VOCs exchanges and the dynamics of clouds over forested and deforested regions. By using ground-based instrumentation that included radar and aircraft measurements, it was possible to compare with TRMM overpasses for validation and cross-calibration purposes (SILVA DIAS et al., 2002).

The campaigns were based on the southwestern Amazon, in the state of Rondônia (Figure 2.3). A multitude of surface-based instruments were deployed, including radars, rain gauges, wind profilers, micrometeorological and chemistry towers, among others. For a complete list of the instrumentation see Silva Dias et al. (2002). For the purposes of this work, the focus will be on the measurements performed by the University of North Dakota (UND) Citation II and UECE's (Universidade Estadual do Ceará) Bandeirante EMB 110 aircrafts. Silva Dias et al. (2002) report on the first overall results of the campaigns, highlighting several processes of the biosphere-atmosphere interaction. The authors note that there are two main regimes for cloud formation in the region, associated to westerlies and easterlies winds. The latter is usually associated to isolated and deep

systems, while the former has larger scale forcing from the South America Convergence Zone (SACZ) that induces the westerly flow. When the SACZ are active in the region, the clouds tend to be shallower with increased stratus occurrence.

Figure 2.3: location of the campaigns sites within (a) South America (black square) and (b) the State of Rondônia. Source: adapted from Silva Dias et al. (2002).



Silva Dias et al. (2002) found that shallow clouds over forest form 30 minutes earlier than over pasture, while mesoscale systems tend to be initiated over higher terrain. There was also indication that deforestation increased rainfall. Finally, the authors identified a relation between the downdrafts and the ozone budget. Although the forest acts as a sink for ozone, its concentration is resupplied by downdrafts generated by clouds. This feedback is different over pasture, given its lower efficiency to remove ozone from the atmosphere. The recent study of Gerken et al. (2016) provides more details about the feedback between clouds and low-level ozone concentrations. Wang et al. (2016) report on similar feedback mechanism for downdrafts and aerosol concentration and CCN formation. They note that the downdrafts not only carry ozone downwards but also reestablish the nanoparticles concentrations close to the surface (that were previously washed-out by precipitation), which may later grow into active CCN.

For cloud measurements, the UND's Citation aircraft carried a forward-scattering spectrometer probe (FSSP-100, measuring cloud DSDs), a two-dimensional cloud probe (2D-C, measuring drizzle DSDs and ice PSDs), a one-dimensional precipitation probe (1D-P, measuring precipitation DSDs and ice PSDs), a high-volume particle sampler (HVPS, measuring precipitation DSDs and ice PSDs), a cloud particle imager (CPI), and a Commonwealth Scientific and Industrial Research Organization (CSIRO) King-type hot wire probe. This instrumentation is capable of measuring cloud and precipitation DSDs and ice PSDs, together with the bulk water content (CSIRO). Additionally, CPI takes very precise pictures of ice particles. Stith et al. (2002) report on the results from several cloud penetrations in different altitude and temperatures. They show several aspects of the clouds over the Amazon, providing comparisons to clouds measured over the ocean at another campaign. The authors note that the clean Amazonian clouds have similar microphysical properties to systems over the ocean. In shallow clouds with weak updrafts, the warm processes dominate the rain formation and precipitation-sized droplets are formed by the 0 °C isotherm level. In deeper clouds, the precipitation is primarily formed by the ice processes.

Stith et al. (2002) also shows that the updrafts contained high concentrations of relatively small droplets (e.g. < 50 μm), while the biggest droplets are found in the downdraft regions. Therefore, the intersection between up- and downdraft regions permits high growth rates by collection mechanisms. In terms of updraft characteristics, Anderson et al. (2005) shows that updraft cores are usually 1 km wide, with average upwards speed of approximately 2.5 m s^{-1} . Over the ocean, the authors note that the updraft cores are around 200 m wider. Regarding the average mass flux of the updraft cores, Anderson et al. (2005) estimates around $10^3 \text{ kg m}^{-1} \text{ s}^{-1}$. Stith et al. (2006) further notes that the updraft speeds are higher than the downdrafts', which is consistent with clouds at the growing stage. According to Stith et al. (2004), the vertical structure of the up- and downdraft is similar between clean Amazonian and oceanic clouds. However, Giagrande et al. (2016) recently pointed out that the overall characteristics of the updrafts change

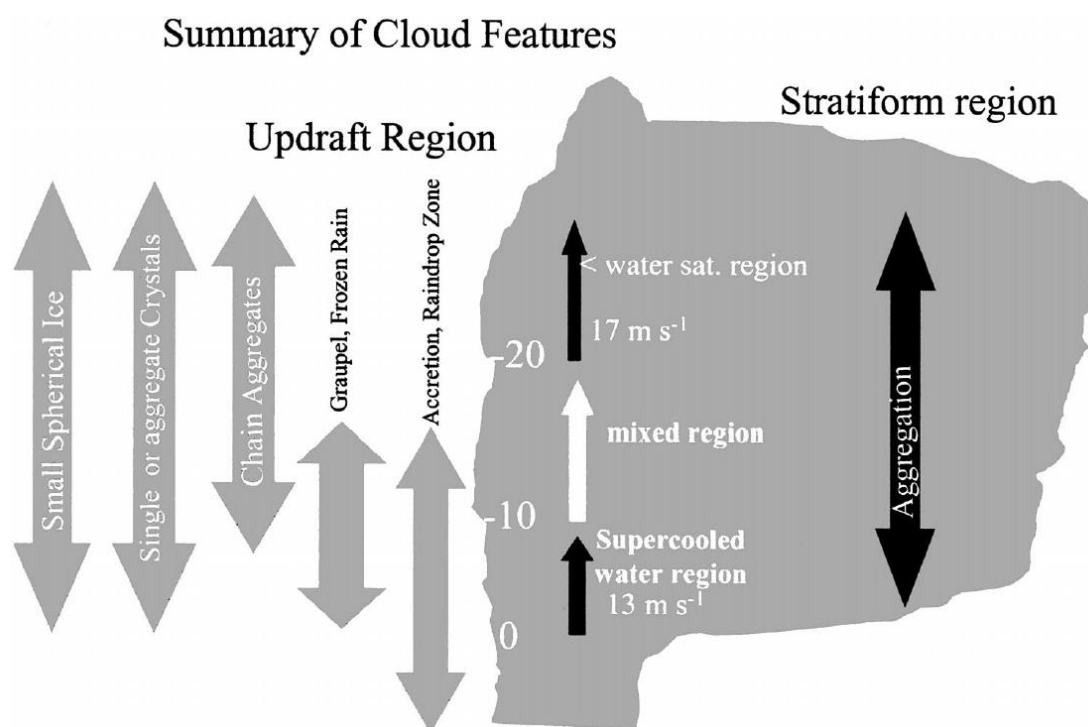
from the wet to dry seasons. They note that the averaged vertical mass flux is higher during the wet season when convection is more frequent but weaker.

There seems to be a relation between updraft characteristics and graupel (or other ice particles) formation. Stith et al. (2002) only found significant presence of supercooled droplets up to the level of $-7\text{ }^{\circ}\text{C}$ in convective systems. For stratiform clouds, where the updrafts are weaker, they found no supercooled droplets. Conversely, some graupel particles were observed in the weak updraft regions of the convective clouds. When the updrafts are strong (e.g. $> 5\text{ m s}^{-1}$), supercooled drizzle droplets may be carried up to the level of $-17\text{ }^{\circ}\text{C}$ (STITH et al., 2004). Possible reasons for those observations are threefold. The first one is that stronger updrafts can physically sustain and carry the droplets upwards. The fast ascension rates also leave less time for the droplets to evaporate. Finally, high updraft speed can lead to enhanced supersaturations, which may overcome both the liquid water and ice thresholds. Therefore, the droplets are not evaporated in favor of ice particles as in the WBF mechanism. Nonetheless, Stith et al. (2004) found supercooled droplets near unrimmed ice particles, suggesting that the evaporation followed by sublimation probably occurred in the intersection between them. This most likely happens when the updrafts are not so strong and the supersaturation is between the liquid water and ice thresholds.

Stith et al. (2004) summarized their findings in Figure 2.4. The supercooled region is limited for the layer below the $-10\text{ }^{\circ}\text{C}$ level, where they also found graupel, frozen and unfrozen rain, and ice crystals. The maximum updraft speeds measured in this region was 13 m s^{-1} . For temperatures below $-17\text{ }^{\circ}\text{C}$, the peak updraft speed was 17 m s^{-1} . This layer is likely subsaturated with respect to liquid water and most of the hydrometeors are frozen. The stratiform region of the systems was characterized exclusively by ice particles that grow by aggregation. Heymsfield et al. (2002) reported on the measurements of the Citation spiral descents (1 m s^{-1} average speed, roughly corresponding to snow fall speeds) in those stratiform regions, also confirming aggregation as the primary mechanism. From cloud top to the $0\text{ }^{\circ}\text{C}$ isotherm, the ice particles lower than 0.1 cm are

depleted and the biggest ice particles were measured close to the melting layer. Following this growth, the ice PSDs also get broader from cloud top to the melting layer.

Figure 2.4: main characteristics of the updrafts and hydrometeors in clean Amazonian clouds. Those properties are most likely representative of moderate-intensity systems, given that the aircraft usually avoided stronger convection for safety reasons. Source: Stith et al. (2004).



2.4.2. LBA-SMOCC

The aircraft measurements during the Large-Scale Biosphere-Atmosphere Experiment in Amazonia – Smoke, Aerosols, Clouds, Rainfall, and Climate (LBA-SMOCC) experiment took place in the south-western Amazon between September and November 2002. The experiment was based in Ji-Paraná, Rondônia State. Two aircrafts were deployed, one focusing on aerosols and the other on clouds measurements. Here we will focus on the measurements made UECE’s Bandeirante aircraft that performed cloud penetrations. The instrumentation carried by the aircraft was similar to the TRMM-LBA experiment.

The first results of the LBA-SMOCC experiment were published by Andreae et al. (2004), where they developed a conceptual model of Amazonian clouds as function of the aerosol loading. They note that clouds developing over the ocean are subject to very low CCN concentrations and usually present few and big droplets. The warm rain formation in those clouds is effective given the weak water vapor competition and slow updrafts. They classified those clouds as Blue Ocean. Over undisturbed portions of the Amazon, the CCN concentrations are not much higher than those over the ocean and the authors found similarities between clean clouds over the forest and the maritime case. Those clouds were grouped as the Green Ocean case. Widespread biomass burning in southern Amazon generates a smoky layer that contains enhanced CCN concentrations. The clouds that develop in this disturbed atmosphere, named Smoky cloud, present more and smaller droplets that take longer to form precipitation. Therefore, there is less rainout of aerosol particles below the clouds and less drag force hampering the updrafts. In this way, more water is carried upwards in stronger updrafts and the ice processes are enhanced. The latent release profile is extended vertically and the clouds have the potential to produce hail and lightning. Pyro clouds were classified as the ones that develop directly above biomass burning events. They are not only subject to extreme aerosol loading, but also enhanced heating from the fires. Therefore, updrafts are further accelerated and the droplets have even less time to grow by the warm mechanisms. However, ash particles may serve as GCCN and it can partly compensate the precipitation suppression. The following results will further detail the characteristics of each type of cloud.

Given the difficulty to disentangle the aerosol from the thermodynamic effects, Andreae et al. (2004) chose to analyze data for flights that presented similar meteorological conditions. The low-level wind field indicated that most of the flights were subject to the easterly regime identified by Silva Dias et al. (2002), which typically coincides with isolated convective cells formation and/or squall lines. The authors note that the flights analyzed were subject to similar

thermodynamic conditions but varying aerosol concentrations. Table 2.1 shows the different aerosol properties for the four flight classifications. Green Ocean CCN concentrations were only slightly higher than over the ocean, but increased by an order of magnitude for Smoky Cb. The Pyro-Cb clouds were subject to extreme aerosol loading where N_{CCN} may have reached values as high as $23 \times 10^4 \text{ cm}^{-3}$.

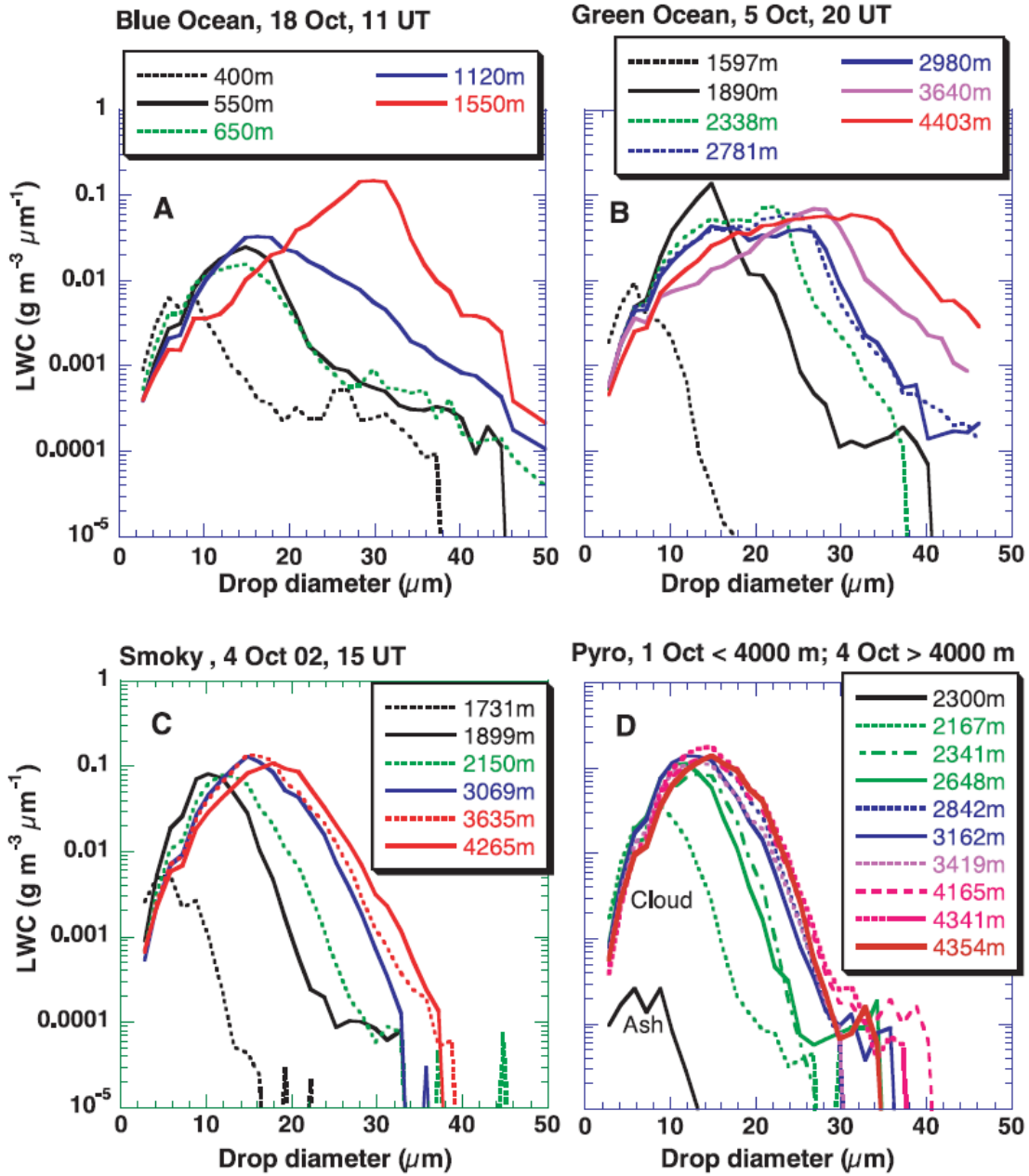
Table 2.1: CO, CN, and CCN concentrations of the different types of clouds identified by Andreae et al. (2004).

	CO (ppb)	CN (cm^{-3})	CCN at 1% SS (cm^{-3})
Blue ocean	120	100-350	320
Green ocean	140	500	340
Smoky Cb	200-650	2000-8000	1000-4000
Pyro-Cb	$1 \times 10^4 - 2.2 \times 10^4$	$20 \times 10^4 - 44 \times 10^4$	$10 \times 10^4 - 23 \times 10^4$

Source: adapted from Andreae et al. (2004).

Figure 2.5 shows the *LWC* size distributions for the different types of clouds, discerning by altitude. The small amount of CCN over the ocean favored the quick formation of few and big droplets, which was also facilitated by sea salt acting as GCCN. When CCN concentrations get progressively higher, the size distributions get narrower and the droplets grow less efficiently with altitude. Note that there are similarities between the Green Ocean and Blue Ocean size distributions. However, the slightly higher CCN concentrations over the forest slightly slows down droplet growth. The Pyro clouds showed the slowest growth with altitude. However, when comparing to the Smoky clouds, it is possible to see a second mode of droplets bigger than $30 \mu\text{m}$. This was attributed to the ability of ash particles emitted by biomass burning to act as GCCN (note the ash size distribution in Figure 2.5d). Differently from previous studies, Andreae et al. (2004) did not find a CCN saturation level where increased aerosol loadings have almost no effect on the clouds. They suggested that the enhanced updraft speeds by the fire forcing was responsible for such observation.

Figure 2.5: LWC size distributions for the different types of clouds and at different altitudes. The measurements for Pyro clouds is a composite between two flights. Source: Andreae et al. (2004).

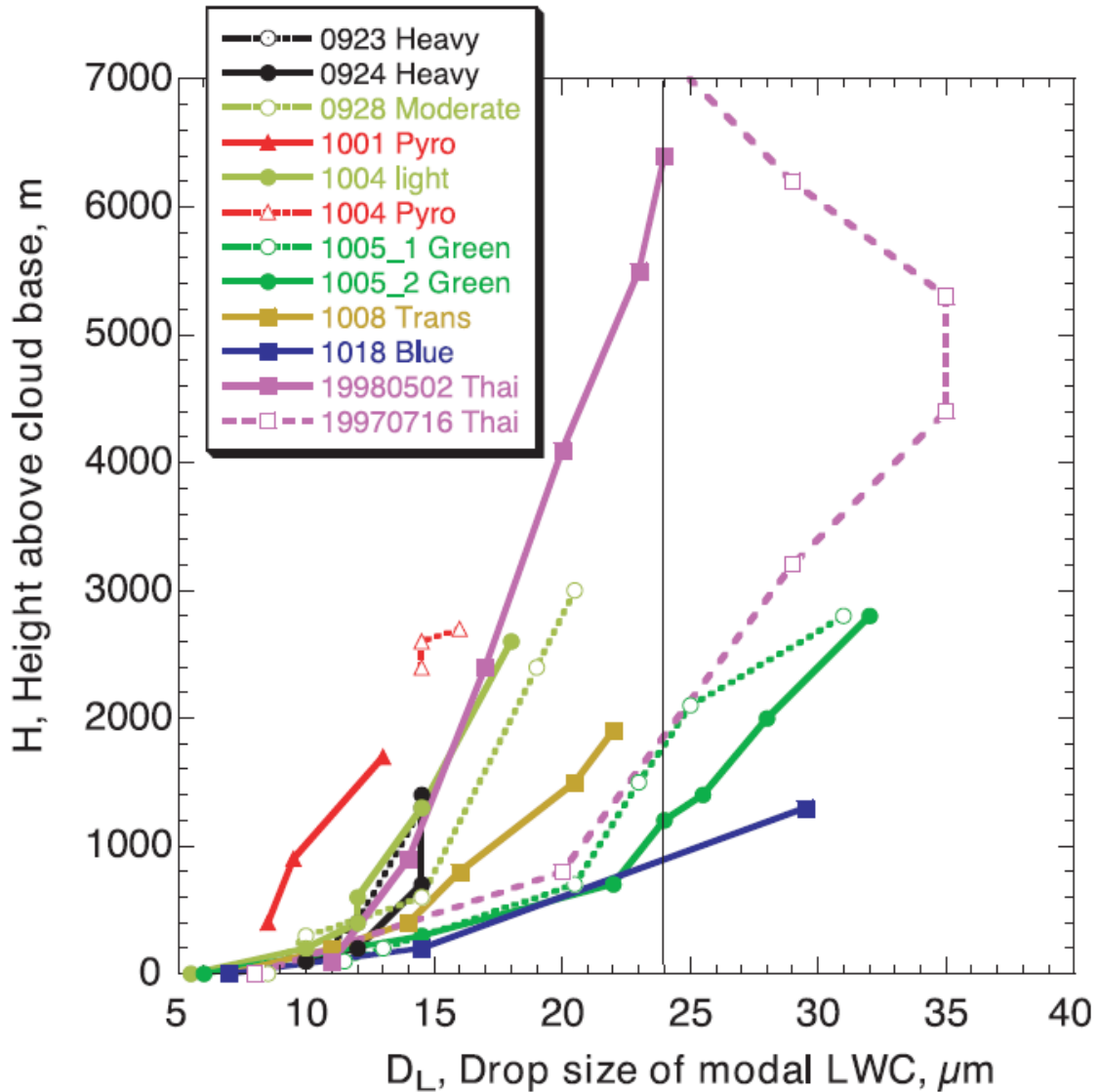


Andreae et al (2004) point out that the less efficient droplet growth in polluted clouds leads to the delay of the onset of precipitation, which occurs higher in the clouds. They suggest that a measure of the level of onset of precipitation can be obtained from the modal diameter of the LWC distributions, D_L . When this parameter reaches $24 \mu\text{m}$, the collection growth is efficient and precipitation

droplets are efficiently produced. Therefore, the height in which $D_L = 24 \mu\text{m}$ can be used as an estimate to the altitude of the precipitation onset. Figure 2.6 shows vertical D_L profiles for several flights under different CCN conditions. It is possible to see that aerosols play a major role on the characteristics of those profiles, where the $D_L = 24 \mu\text{m}$ level gets progressively higher with increasing CCN loading. Although the aircraft did not fly above 4300 m, satellite estimates showed that the Smoky and Pyro clouds would have to reach respectively 6700 m and 7800 m in order to efficiently produce rain by warm processes. However, this is above the freezing level (usually around 5 km) and other processes take place at this altitude. Both the less efficient rain production and the fire forcing resulted in more intense ice processes in the polluted clouds that even produced hail precipitation. The less efficient rain production was also not able to completely washout the smoke, which was detrained at the lower stratosphere.

The relationship between CCN and the height of the precipitation onset was also observed by Freud et al. (2008). The authors additionally showed that the effective radius r_e does not change much with adiabatic fraction, i.e. between cloud edges and core at the same altitude (Figure 2.7). Therefore, they validated satellite retrievals of the vertical r_e profiles such as the one proposed by Rosenfeld and Lensky (1998). This type of retrieval assumes that the cloud-top r_e of different cloud cells can be combined into a single profile representative of one deep cloud. Given that the adiabatic fraction does not effectively affect r_e , the characteristics of the cloud tops of growing convective elements can be used to represent the core of deep convection. As shown in Figure 2.7, r_e is tightly linked to altitude and aerosol loading, while being almost insensitive to adiabatic fraction. Freud et al. (2011) notes that the patterns observed in Figure 2.7 are consistent to the extreme inhomogeneous mixing process.

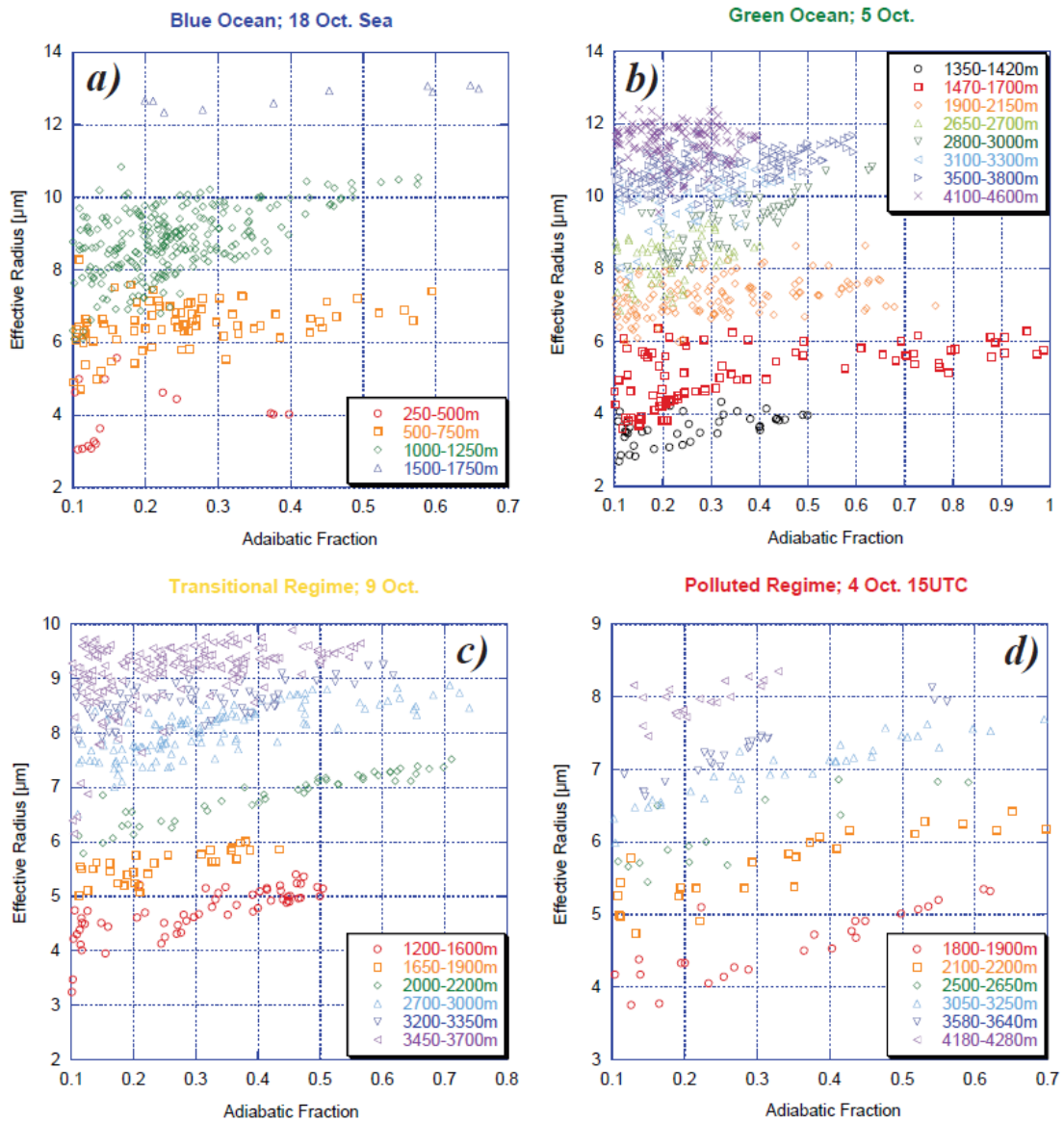
Figure 2.6: vertical D_L profiles for clouds subject to varying aerosol conditions. Source: Andreae et al. (2004).



When the surrounding air penetrates the cloud during mixing, there are typically two possible outcomes. If the entrainment is quick, the cloud-edge DSDs will be partially evaporated throughout its size range and the effective radius will diminish. The drier the air, the bigger will be the effect on r_e . However, if the process is slow, the smallest droplets at the cloud edge can completely evaporate while the biggest ones diminish only slightly in size. Therefore, there is almost no effect in r_e . The results shown in Figure 2.7 suggest that extreme inhomogeneous mixing processes dominate in the Amazon. Given the relative insensitivity of r_e to

the adiabatic fraction, Freud and Rosenfeld (2012) showed that the vertical r_e can be reproduced by adiabatic assumptions.

Figure 2.7: relation between effective radius r_e and adiabatic fraction (ratio between the observed LWC and the calculated adiabatic LWC) for (a) Blue Ocean, (b) Green Ocean, (c) Transitional Regime, and (d) Polluted Regime clouds. Source: Freud et al. (2008).

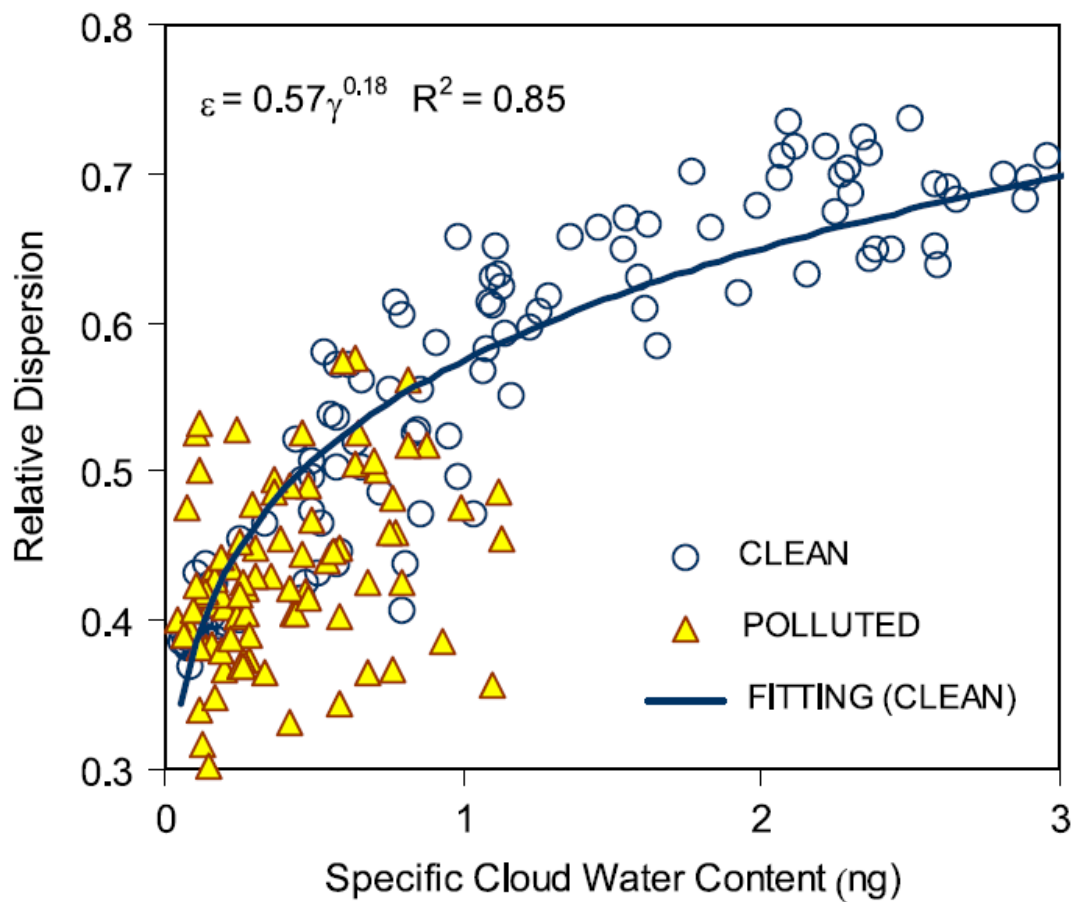


Martins and Silva Dias (2009) show that the Amazonian biomass burning aerosols also affect the cloud DSD shape. They analyzed the effects of aerosols on the parameter ϵ , which is defined as the ratio between the DSD mean size

and standard deviation. This parameter is known as the relative dispersion and provides an estimate of the DSD width where high values indicate broad distributions. For every clean and polluted flight, they calculated the overall average value of ϵ and compared it to the specific water content (LWC/N_d) as in Figure 2.8. They show that the relative dispersion is proportional to the specific water content, which is proportional to the droplets effective size. Therefore, the reduced droplet size in the polluted clouds caused reductions on the average ϵ .

Previous studies suggested an opposite aerosol effect on ϵ . Liu and Daum (2002) suggested that aerosol pollution increased the DSDs relative dispersion and this process would partially compensate the Twomey effect in terms of climate forcing. This contradiction can be understood by considering the aerosol effect on cloud evolution and droplet growth. The clean atmosphere over the Amazon presents a limited aerosol population in terms of size variety. Therefore, the cloud base DSD in clean systems tend to be narrower than in polluted cases where the added aerosols produce wider dry-particles size distributions. In that case, increased CCN concentrations induces higher ϵ . However, the situation is different higher in the cloud where the droplets have already gone through growth mechanisms. In a clean cloud, the collision-coalescence is effective and induces DSD broadening. The suppressed collision growth in polluted systems slows down this process. Therefore, the effect of enhanced CCN concentrations on ϵ will change in signal higher in the clouds. The averaged results obtained by Martins and Silva Dias (2009) suggest that the latter prevailed in the LBA-SMOCC measurements. This point will be further discussed in Chapter 5.

Figure 2.8: relative dispersion ε as function of the specific water content. Source: Martins and Silva Dias (2009).



3 METHODS

3.1. Experimental campaigns

The study presented here was made possible by collaborating efforts of several national and international institutions and researchers. During the execution of this study, several experiments took place in the Amazon, with the overall goal of increasing our knowledge on the interactions between atmospheric chemistry, aerosol properties, clouds, and radiation, with a specific goal of understanding the anthropogenic role. Here the experiments are briefly described, with the appropriate references for further details.

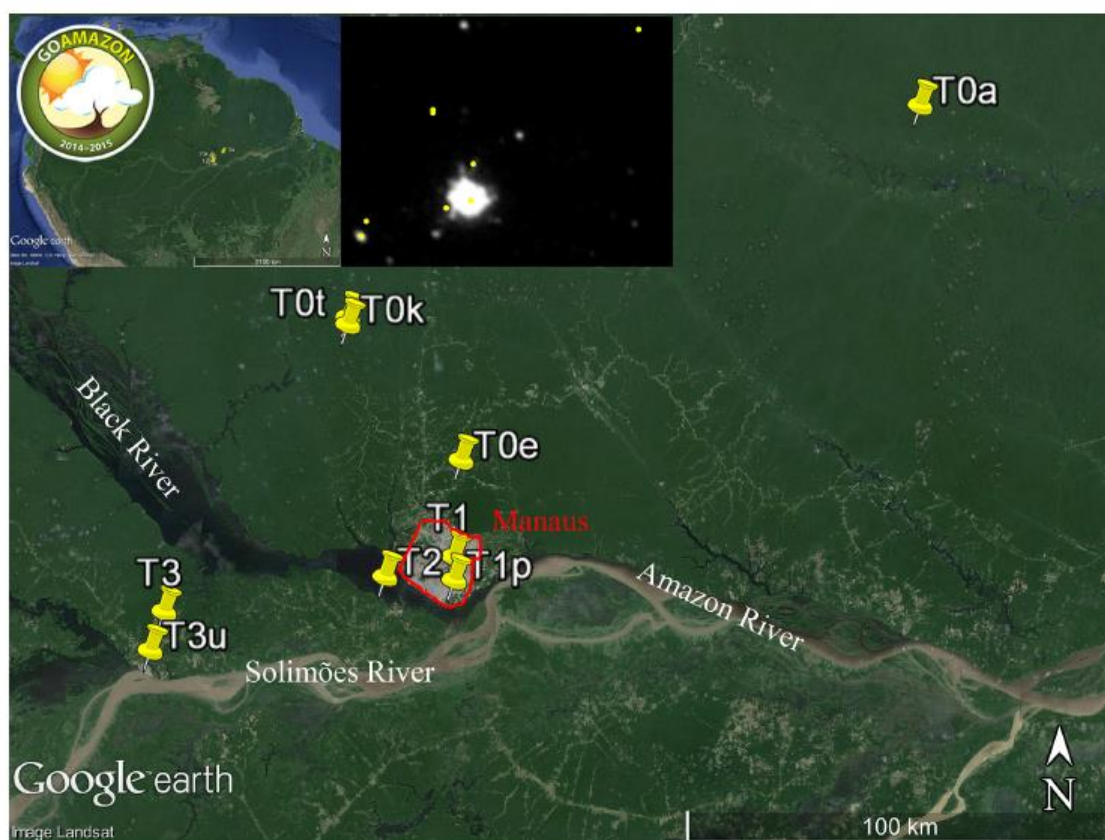
3.1.1. GoAmazon2014/5

The data presented here were collected in a total of four experiments. The GoAmazon2014/5 (Observations and Modeling of the Green Ocean Amazon, MARTIN et al., 2016) operated in Manaus, Brazil, located in the center of the Amazon. The experiment lasted a total of two years, from 1 January 2014 to 31 December 2015. The overall intent of the experiment is to contribute to our understanding of the complex relations between the forest, atmospheric chemistry, aerosols, clouds, precipitation, and the anthropogenic role. The region chosen for the experiment represents a natural laboratory where both the background (undisturbed) and the pollution-affected atmosphere can be assessed. The city produces a pollution plume that is transported by the prevailing easterly winds and interacts with the natural atmosphere downwind. Therefore, it is possible to obtain the background reference by measuring atmospheric properties in the plume-free regions, while the anthropogenic effects can be evaluated by studying the interactions between the natural atmosphere and the pollution.

The location for the ground-based instrumentation was chosen to capture both the background conditions upwind from Manaus and the characteristics of the pollution downwind. Figure 3.1 shows the location of the sites, where T0 stands

for the sites upwind, T1 for sites in Manaus, T2 right at the pollution outflow, and T3 further away in the usual plume dispersion direction. From the inserts in Figure 3.1, it is clear that, aside from biomass burning, Manaus is the only major pollution source for the region. A list of the complete ground-based instrumentation can be found in Martin et al. (2016).

Figure 3.1: ground-based site locations during GoAmazon2014/5. The left insert shows the location of the sites within South America, while on its right the nighttime lights are shown (as of 2010). Source: Martin et al. (2016).



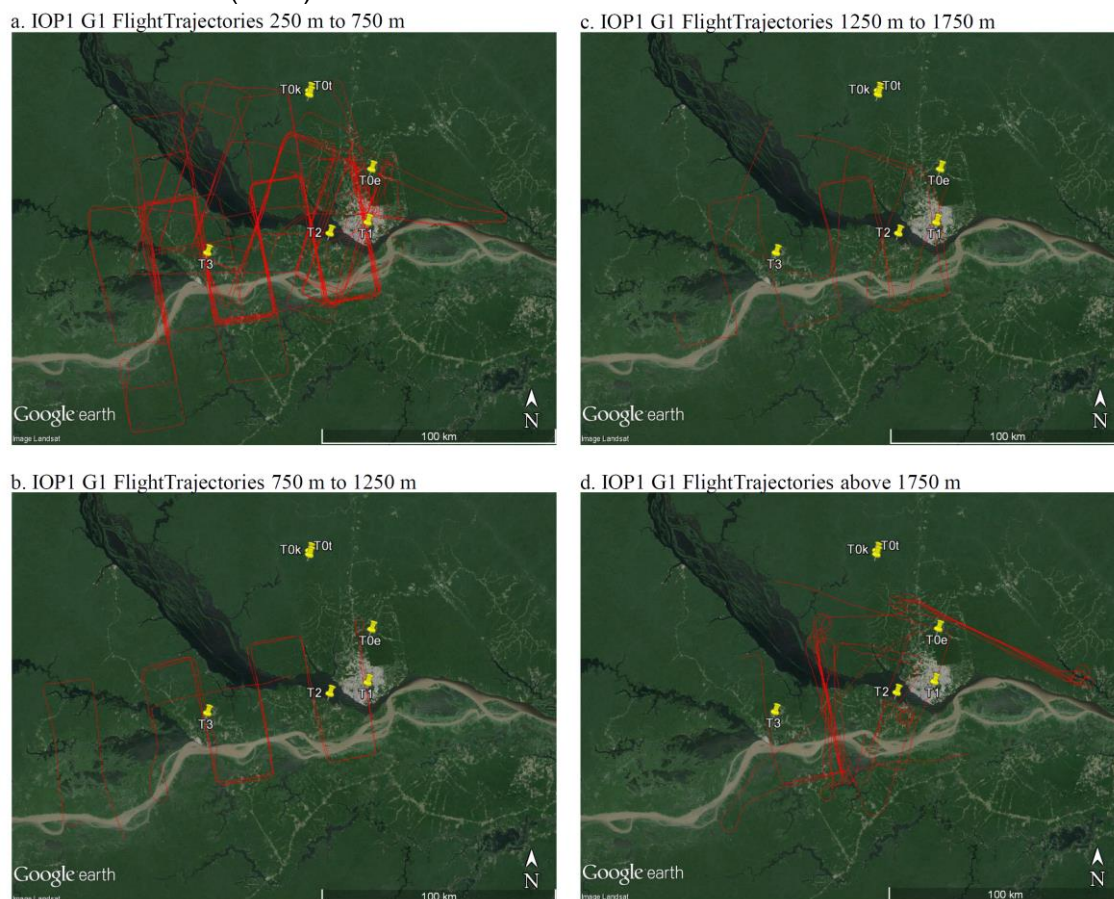
As part of the GoAmazon2014/5, two Intensive Operations Periods (IOP1 and IOP2) took place in February-March 2014 and September-October 2014, respectively. During the IOP1, a low-altitude G-159 Gulfstream I (G-1) aircraft, described in detail by Schmid et al. (2014) and owned by the Department of Energy (DOE) Atmospheric Radiation Measurement (ARM) program, was deployed to measure Manaus' plume and its interactions with the natural atmosphere and clouds. During the second IOP, both the G-1 and a high-altitude

G550 (HALO, or High Altitude and Long Range Research Aircraft, WENDISCH et al., 2016) operated at the same time, including coordinated flights where the G-1 probed the lower parts of the clouds and HALO measured the system's upper characteristics. HALO is owned by the German Aerospace Center (DLR) – see more information at <http://www.halo.dlr.de/>. The G-1 flights were part of the Intensive Airborne Research in the Amazon (IARA) campaign, while HALO flights were made possible by the ACRIDICON-CHUVA campaign. ACRIDICON stands for “Aerosol, Cloud, Precipitation, and Radiation Interactions and Dynamics of Convective Cloud Systems” and CHUVA means “Cloud Processes of the Main Precipitation Systems in Brazil: A Contribution to Cloud Resolving Modeling and to the GPM (Global Precipitation Measurement)”. The ACRIDICON and CHUVA represent the German and Brazilian sides of collaborating campaigns, respectively. The IARA and ACRIDICON-CHUVA campaigns are described in the next sections.

3.1.2. IARA

The overall aim of the IARA campaign was to obtain extensive data regarding the interactions between Manaus pollution plume and the surrounding natural atmosphere and clouds. For that purpose, G-1 performed 16 flights during IOP1 and 19 flights during IOP2. This study will focus on the measurements made during IOP1 to analyze the pollution plume effects in the clean wet season clouds. Figure 3.2 shows the G-1 flight trajectories for the IOP1, segregated by altitude. Note that most of the flight legs were in the low levels and performed perpendicular transects in the plume. During the transects, clouds were also probed both in and out of the plume region, allowing the study of local aerosol effects on clouds. Most flights took place at late morning or early afternoon (local time).

Figure 3.2: G-1 flight trajectories during IOP1 (February-March 2014). The trajectories are segregated by the altitude intervals: (a) 250 m to 750 m, (b) 750 m to 1250 m, (c) 1250 m to 1750 m, and (d) above 1750 m. Source: Martin et al. (2016).



The G-1 aircraft carried several instruments to measure atmospheric chemistry, aerosols, clouds, and radiation. A list of the instruments can be seen in Table 3.1. This study will focus on the cloud DSD measurements by the Fast Cloud Droplet Probe (FCDP) and on the aerosol number concentrations measured by the Ultrafine Condensation Particle Counter. More details about those instruments are given in Section 3.2.1 and the specific methodologies in Sections 4.2 and 4.3.

Table 3.1: list of instruments carried by G-1.

Instrument	Abbreviation	Data Available	
		IOP1	IOP2
Global Positioning System (DSM 232)	GPS	Yes	Yes
Temperature (Rosemount E102AL)		Yes	Yes
Pressure (Rosemount 1201F1)		Yes	Yes
Gust Probe: Rosemount 1221F2 (3 units)		Yes	Yes
Chilled-mirror hygrometer (GE-1011B)		Yes	Yes
Tunable Diode Laser Hygrometer	TDL-H	Yes	Yes
Aircraft Integrated Meteorological Measurement System	AIMMS-20	Yes	Yes
Video Camera P1347 (forward looking)		Yes	Yes
Video Camera P1344		Yes	Yes
Ultrafine Condensation Particle Counter (Model 3025A)	UCPC	Yes	Yes
Condensation Particle Counter (Model 3010)	CPC	Yes	Yes
Fast Integrated Mobility Spectrometer	FIMS	Yes	Yes
Ultra High Sensitivity Aerosol Spectrometer - Airborne	UHSAS-A	Yes	Yes
Passive Cavity Aerosol Spectrometer	PCASP	Yes	Yes
Particle/Soot Absorption Photometer	PSAP	Yes	Yes
Three-Wavelength Integrating Nephelometer (Model 3563)		Yes	Yes
High Resolution Aerosol Mass Spectrometer	HR-ToF-AMS	Yes	Yes
Cloud Condensation Nuclei Counter	CCN Counter	Yes	Yes
Optical Particle Counter (Model CI-3100)	OPC	Yes	Yes
Quadrupole Proton-Transfer-Reaction Mass Spectrometer	PTR-MS	Yes	Yes
N ₂ O and CO concentrations (Los Gatos 23r)		Yes	Yes
Oxides of Nitrogen (Nox)		Yes	Yes
Ozone (Thermo Scientific Model 49i)		Yes	Yes
Picarro Cavity Ring Down System (Model G1301-m)	CRD	Yes	Yes
Multi Element Water content System (SEA WCM-2000)		Yes	Yes
High Volume Precipitation Spectrometer (Version 3)	HVPS-3	Yes	Yes
Two-Dimensional Stereo Probe	2D-S	Yes	Yes
Fast Cloud Droplet Probe	Fast-CDP	Yes	Yes
Cloud Droplet Probe (version 2)	CDP ver2	Yes	Yes
Cloud Particle Imager (version 2)	CPI ver2	Yes	Yes
Sunshine Pyranometer, shaded	SPN-1	Yes	Yes
Sunshine Pyranometer, unshaded (up and down looking)	SPN-1	Yes	Yes

Source: Martin et al. (2016).

3.1.3. ACRIDICON-CHUVA

Given the HALO capabilities, the ACRIDICON-CHUVA campaign could perform longer range and higher flights. HALO can reach up to 15 km and endure 8 h-long flights. As described in Wendisch et al. (2016), there was five different mission types, with one or more being focused on each flight. The types were: (a) cloud profiling, in which HALO made several cloud penetrations from cloud base to cloud top; (b) aerosol and trace gases processing by clouds, in which HALO determined the atmospheric characteristics at the cloud inflow (cloud base) and outflow (cloud anvils); (c) satellite and radar validation, in which HALO

performed trajectories in the range of the X-band radar installed at T3 or above clouds synchronized with A-Train overpasses; (d) tracer experiment, in which perfluorocarbons (PFCs) were released below clouds to study its dispersion and processing by clouds - HALO flew in the estimated direction of PFCs dispersion; and (e) forest/deforested contrast, in which HALO probed clouds above the forest and over pasture for comparison.

In order to cover all five mission types and the associated research interests, HALO performed 14 flights over different regions in the Amazon. Table 3.2 shows the overall characteristics of each flight, highlighting the mission types covered, while the trajectories are shown in Figure 3.3. This study will focus primarily on the flights that performed the cloud profiling mission type (a), that focused on different regions in the Amazon with contrasting pollution levels. The cloud profiling during flight AC19 took place over the Atlantic Ocean, flights AC9 and AC18 focused on the remote and clean Amazon, while flights AC7, AC12, and AC13 probed clouds over the polluted southern Amazon (Figure 3.3). Some cloud penetrations are also available in the other flights, which will also be considered in this study.

Table 3.2: overall characteristics and mission types of the 14 HALO research flights. The research flights were numbered from AC07 to AC20.

No.	Date in 2014	Research topic	Ceiling altitude (km)	Time span	Remark
AC07	6 Sep	a	13.9	7 h, 35 min	Test of flight strategy
AC08	9 Sep	a	13.8	5 h, 30 min	Coordinated with GI
AC09	11 Sep	a	12.6	6 h, 10 min	Clean conditions
AC10	12 Sep	c	14.4	7 h, 25 min	Along A-Train path
AC11	16 Sep	b, d	12.9	7 h, 25 min	Tracer experiment
AC12	18 Sep	a	13.8	6 h, 15 min	Polluted conditions
AC13	19 Sep	a	12.9	6 h, 30 min	Polluted conditions
AC14	21 Sep	c	15.2	7 h, 15 min	Coordinated with GI; Along A-Train path
AC15	23 Sep	c, b	13.8	7 h, 20 min	Along A-Train path
AC16	25 Sep	b, d	13.2	6 h, 50 min	Tracer experiment
AC17	27 Sep	e	8.1	6 h, 40 min	Comparison with GPM
AC18	28 Sep	a	14.4	6 h, 50 min	Clean conditions
AC19	30 Sep	a	13.8	7 h, 15 min	Marine conditions
AC20	1 Oct	b, a	14.4	7 h, 5 min	Coordinated with GI

Source: Wendisch et al. (2016).

HALO carried several instruments focusing on different aspects of the mission types. A complete list of the instruments can be seen in Tables 3.3-4. In this study, we will focus on the cloud measurements of the CCP and NIXE-CAPS probes, and aerosol measurements by the AMETYST-CPC and CCN-200 (referred here as CCNC).

Figure 3.3: trajectories of the 14 HALO flights during ACRIDION-CHUVA (GoAmazon2014/5 IOP2). Source: Wendisch et al. (2016).

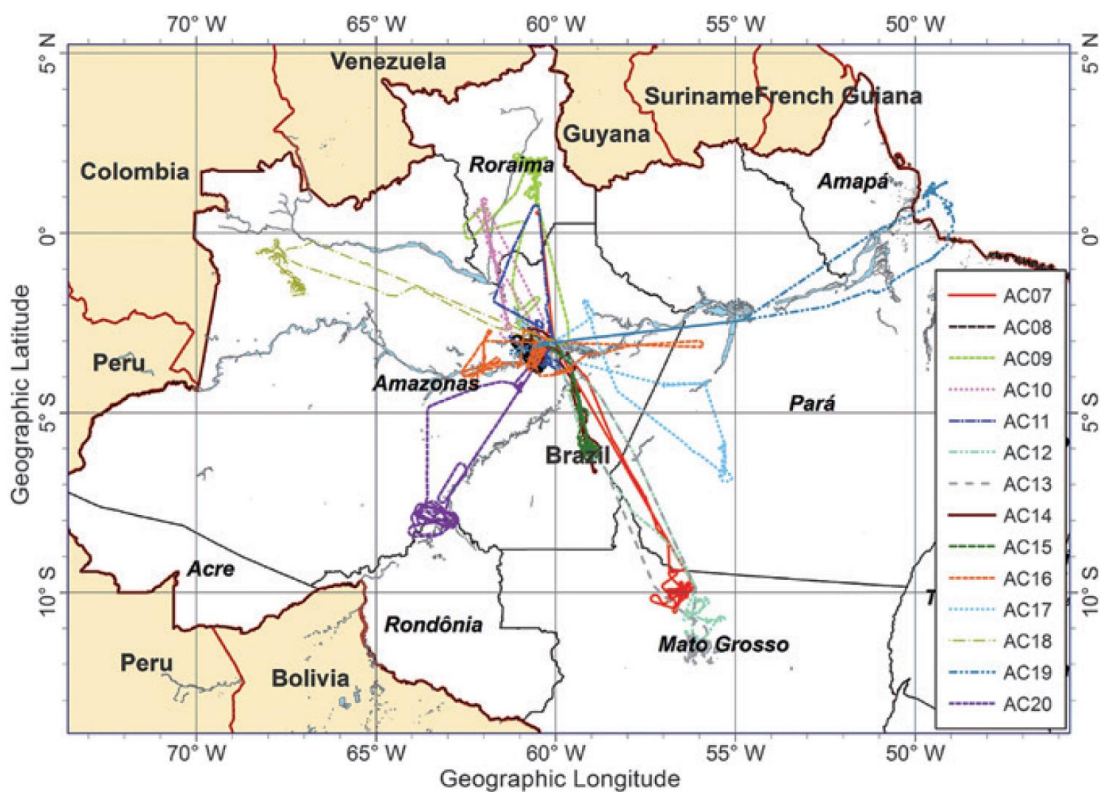


Table 3.3: instrumentation carried by the HALO aircraft during ACRIDICON-CHUVA – part 1. The references highlighted in the Table can be found in Wendisch et al. (2016).

Instrument acronym [Additional reference]	Measured quantity	R: range of measurement P: precision, A: accuracy	Time resolution in Hz
INLETS			
HALO-CVI	Inlet for cloud particles and residues	$D_p = 5-50 \mu\text{m}$	
HASI	HALO aerosol submicrometer inlet	D_p up to a few mm (analysis ongoing)	
TGI	Trace gas inlet		
METEOROLOGY			
BAHAMAS	Pressure, temperature, wind, humidity, TAS aircraft position, attitude, heading, altitude		Up to 100
BAHAMAS-SHARC	H ₂ O mixing ratio (gas phase)	R: 20–60,000, A: <10%	1
MTP	Microwave radiances for temperature profiles	R: $\nu = 56.363, 57.612, 58.363 \text{ GHz}$	0.1
HAI [1, 2]	H ₂ O gas phase concentration	R: 1–40,000 ppmv (vapor)	Up to 120
	Four channels: 2 × open path, 2 × closed path	A: 4.3%	
CHEMISTRY			
Aerosol impactor	Collects aerosol particles for microspectroscopy	R: >100 nm	Offline analysis
C-ToF-AMS [3, 4]	Nonrefractory particle composition (organics, sulfate, nitrate, ammonium, chloride)	R: $D_p = 40 \text{ nm} - 1 \mu\text{m}$, A and P: $\approx 30\%$	0.03
AMTEX	CO, O ₃ concentrations	P: 2 ppb; A: 5%	1
	PFCs (C ₆ F ₁₂ , C ₇ F ₁₄)	P: 1 ppq; A: 3%	1
ITMS	PAN (peroxyacetyl nitrate), SO ₂ — concentration	P: 5 ppt; A: 7%	1
	HNO ₃ , HONO concentrations	P: 30 ppt; A: 10%	1
PERTRAS	PFCs: perfluorocarbons		
AENEAS	NO, NO _y	R: 5 pmol mol ⁻¹ –60 nmol mol ⁻¹ NO: A: $\sim 8\%$ at 50 nmol mol ⁻¹ NO _y : A: $\sim 7\%$ at 450 nmol mol ⁻¹	1
miniDOAS [5]	Spectral radiance to derive trace gas concentrations: HCHO, BrO, IO, ClO ₂ , C ₂ H ₂ O ₂ , CH ₄	R: $\lambda = 310-1,680 \text{ nm}$; $\Delta\lambda = 0.7-7 \text{ nm}$	10
	BrO ₂ , I ₂ , O ₂ , O ₃ , O ₄ , NO ₂ , HONO, H ₂ O, CO ₂		
MICROPHYSICS			
Aerosol particles			
SNOOPY (SP2) [6]	rBC mass/number concentration, aerosol PSD	R: rBC, mass: 0.26–125 fg (65–510 nm)	1

Source: Wendisch et al. (2016).

Table 3.4: instrumentation carried by the HALO aircraft during ACRIDICON-CHUVA – part 2.

TABLE 1. Continued.			
Instrument acronym [Additional reference]	Measured quantity	R: range of measurement P: precision, A: accuracy	Time resolution in Hz
AMETYST			
CPC	Particle number concentration	R: $D_v = 5 \text{ nm} - 1 \mu\text{m}$	1
PSAP	Particle absorption coefficient	R: $\lambda = 467, 530, 660 \text{ nm}$	1
DMPS and OPC	Aerosol PSD	R: $D_v = 5 - 350 \text{ nm}$ and $250 \text{ nm} - 3 \mu\text{m}$	1
Permanently behind CVI			
CPC	Residual particle number concentration	R: $D_v = 10 \text{ nm} - 3 \mu\text{m}$	0.33
PSAP	Residual particle absorption coefficient	R: $\lambda = 567 \text{ nm}$	0.33
UHSAS	Residual PSD	R: $D_v = 100 \text{ nm} - 1 \mu\text{m}$	0.33
Electrometer	Drop charge		0.33
UHSAS-A	Aerosol PSD	R: $D_v = 60 \text{ nm} - 1 \mu\text{m}$	1
PCASP-100X	Aerosol PSD	R: $D_v = 0.12 - 3.5 \mu\text{m}$	1
CCN and IN			
CCN-200	CCN concentration	R: $S = 0.13\% - 0.53\%$	1
FINCH	Total and biological IN concentrations	R: $T \geq -40^\circ\text{C}$, saturation ratio wrt ice ≤ 2	0.1
SP2 [6]	rBC mass concentration, aerosol PSD	R: $D_v = 120 - 360 \text{ nm}$	1
Cloud particles			
CAS-DPOL	Cloud PSD and shape, liquid water content	R: $D_v = 0.5 - 50 \mu\text{m}$	1
PHIPS-HALO	Cloud PSD, stereoscopic particle imaging	R: $D_v = 10 \mu\text{m} - 1 \text{ mm}$	1
	Single particle scattering phase function		
SID-3	Cloud PSD, ice particle shape,	R: $D_v = 5 - 50 \mu\text{m}$	1
	surface roughness		
NIXE-CAPS			
CAS-DPOL	Cloud PSD, asphericity	R: $D_v, D_v = 0.6 - 50 \mu\text{m}$	1
CIPgs	Cloud PSD	R: $D_v = 15 - 950 \mu\text{m}$; $\Delta D_v = 15 \mu\text{m}$	1
CCP			
CDP	Cloud PSD	R: $D_v = 3 - 50 \mu\text{m}$; $\Delta D_v = 1 - 2 \mu\text{m}$	1
CIPgs	Cloud PSD	R: $D_v = 15 - 950 \mu\text{m}$; $\Delta D_v = 15 \mu\text{m}$	1
Precipitation			
PIP	Precipitation PSD	R: $D_v = 100 - 6,400 \mu\text{m}$; $\Delta D_v = 100 \mu\text{m}$	1
RADIATION			
specMACS [7]	Spectral radiance	R: $\lambda = 400 - 2,500 \text{ nm}$; $\Delta\lambda = 5 - 10 \text{ nm}$	30-100
SMART [8, 9, 10]	Spectral irradiance (upward and downward)	R: $\lambda = 350 - 2,200 \text{ nm}$; $\Delta\lambda = 2 - 16 \text{ nm}$	2
	Spectral radiance (upward, FOV = 2.1°)	R: $\lambda = 350 - 2,200 \text{ nm}$; $\Delta\lambda = 2 - 16 \text{ nm}$	2

Source: Wendisch et al. (2016).

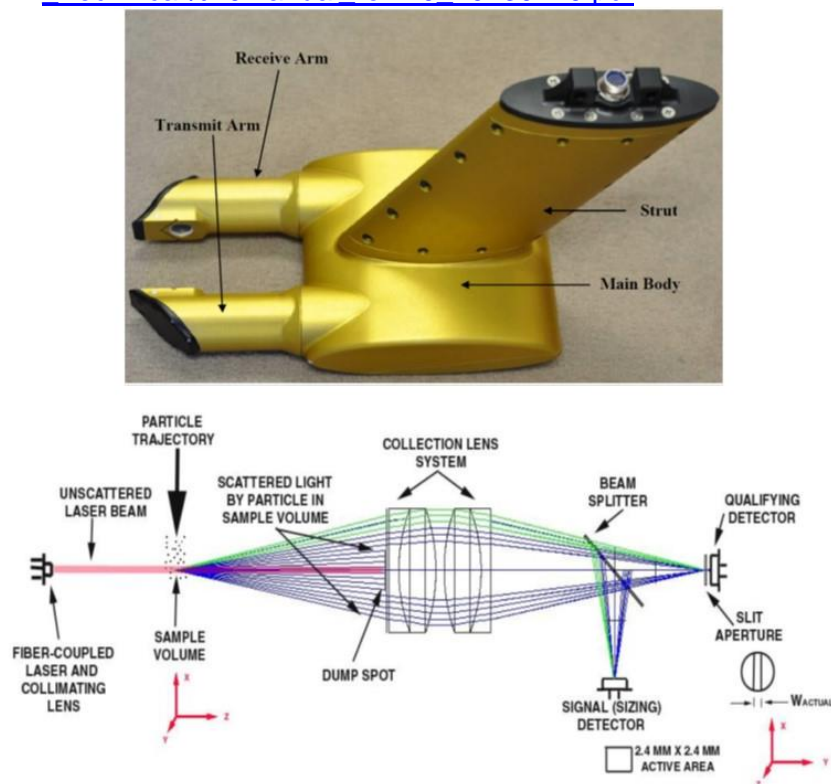
3.2. Instruments description

3.2.1. G-1

3.2.1.1. FCDP

The Fast Clouds Droplet Probe (FCDP) is an instrument focused on the measurements of hydrometeor (especially cloud droplets) DSDs on the range between 1 μm and 50 μm , developed by SPEC Inc. Figure 3.4 presents the physical aspect and a schematic representation of its principles of operation. The instrument contains two arms, with one of them continuously emitting a focused laser signal. When droplets enter the sampling volume, they scatter the laser light, which is redirected to two sensors by a lens system. One of the sensors detects the quality of the scattered signal, comparing it to the background, droplet free, reference. In case the signal-to-noise ratio is in the proportion of 70:30, the droplets are sized by the other sensor. Bin sizes were calibrated using glass beads at several sizes in the total range. The FCDP was mounted on the right wing of the G-1 aircraft. Shattering effects were filtered from the FCDP-measured DSDs, which is a built-in feature of the provider software. Additionally, measurements with low number concentration ($< 0.3 \text{ cm}^{-3}$) and low water contents ($< 0.02 \text{ g m}^{-1}$) were excluded.

Figure 3.4 – Physical aspect and principles of operation of the FCDP instrument. Source: instrument manual, available at: http://www.specinc.com/sites/default/files/software_and_manuals/FCDP_Technical%20Manual_rev1.0_20130120.pdf.



3.2.1.2. CPC

The CPC (Condensation Particle Counter) instrument, model 3025 and manufactured by TSI, measures number concentration of aerosols between 3 nm and 3 μm using an optical detector after a supersaturated vapor condenses onto the particles, growing them into larger droplets. Particle concentrations can be detected between 0 and 10^5 cm^{-3} with an accuracy of 10 %. Coincidence is less than 2% at 10^4 cm^{-3} concentration and corrections are automatically applied for concentrations between 10^4 and 10^5 cm^{-3} . The CPC was mounted in a rack inside the cabin and connected to an isokinetic inlet and an aerosol flow diluter and was operated using an external pump. The isokinetic inlet has an upper limit of 5 μm for particle diameter, with penetration efficiency higher than 96 %. A 1.5 L min^{-1} flow rate was maintained using a critical orifice. The dilution factor varied between one and five.

The internal quality flag of the CPC instrument was used to correct the concentration measurements. Whenever an observation was flagged as “bad”, it was substituted by an interpolation between the closest measurements before and after it that were either “questionable” or “good”. For “good” measurements, which represent 59% of all the measurements, the uncertainty is less than 10 %. The interpolation weights decayed exponentially with the time difference between the current observation and the reference ones. If the reference observations were more than 10 s apart, these data were excluded. Sixteen percent of the data were interpolated in that manner, while only 0.02 % had to be excluded. This process was required not only to smooth out the bad measurements but was also important for maintaining significant sample sizes (instead of simply excluding “bad” measurements). No averaging was applied to the 1 Hz CPC data. However, tests were made in order to check the impact that the sample frequency had on the results. The results were not sensible to moving averages of up to 10 s, which corresponds to roughly 1 km displacement given that the G-1 flew around 100 m s⁻¹ in speed. Given this observation, the analyses are based on the 1 Hz CPC measurements.

3.2.1.3. AIMMS-20

Complementary measurements of meteorological conditions were obtained from the Aventech Research Inc. AIMMS-20 instrument (Aircraft-Integrated Meteorological Measurement System, BESWICK et al., 2008). This instrument combines temperature, humidity, pressure, and aircraft-relative flow sensors in order to provide the atmospheric conditions during the measurements. From the aircraft measurements of relative flow, the vertical wind speed was obtained and was used herein to compare cloud properties in the up- and downdraft regions. The precision of vertical wind speeds is 0.75 m s⁻¹ at 75 m s⁻¹ true airspeed.

3.2.2. HALO

For the studies regarding the GoAmazon2014/4 IOP2, the focus is on the HALO aircraft measurements. Five instruments, described below, are used for the analyses, focusing on aerosol and CCN number concentrations and hydrometeor size distributions and sphericity. For further details on the HALO instrumentation and the relevant references, see Wendisch et al. (2016). For a comprehensive description of the airborne instrumentation introduced below, see Wendisch et al. (2013).

3.2.2.1. CCP

For the cloud droplet size distribution measurements, a modified Cloud Combination Probe (CCP, manufactured by Droplet Measurement Technologies, Inc., Boulder, CO, USA) was adopted on HALO covering an overall size diameter range from 3 μm to 950 μm . The probe consists of two separate instruments, the CDP (Cloud Droplet Probe; LANCE et al., 2010; MOLLEKER et al., 2014) and a grayscale optical array imaging probe (CIPGs, Cloud Imaging Probe, KOROLEV, 2007). By means of a two-dimensional shadowcast technique the CIPGs detects cloud particles with size diameters ranging from 15 μm to 2000 μm . The in-house developed analysis algorithm from MPI and IPA in Mainz sizes and sorts the recorded images into bins of roughly 15 μm bin width in dependency on particle shapes and dimensions. The CDP is an optical particle counter detecting scattered laser light (in forward direction) arising from individual particles passing through the illuminated optical sample area (LANCE et al., 2010; MOLLEKER et al., 2014). The optical sample area has a cross section of 0.2 mm^2 ($\pm 15\%$) perpendicular to the flight direction. The CDP detects particles with sizes from 3 μm to 50 μm , and classifies these into size histograms of bin widths between 1 and 2 μm . In addition to size histograms recorded at 1Hz frequency, the CDP stores single particle data (signal amplitude and μs -resolved detection time) of continuous intervals with up to 256 particles every second. This feature can be used to assess the spatial distribution of the droplets in case of multi modal size

distributions (KLINGEBIEL et al., 2015). The main uncertainties for the CCP size distributions are due to the uncertainty of the sample area (and thus the scanned air volume), as well as counting statistics. We applied a filter to eliminate DSDs with concentrations lower than 1 cm^{-3} for $D < 50 \text{ }\mu\text{m}$ or lower than 0.1 cm^{-3} for $D > 50 \text{ }\mu\text{m}$.

3.2.2.2. AMETYST-CPC

The aerosol concentrations used in the GoAmazon2014/5 IOP2 studies refer to the total concentration of particles measured with a butanol-based condensation particle counter (CPC). Four CPCs were deployed on HALO as part of the new basic aerosol instrument package for HALO named AMETYST (Aerosol Measurement sYSTem), described in detail by D. Fütterer (DLR, PhD thesis in preparation) and which also includes two Grimm 1.129 OPC (Optical Particle Counters), a two-channel thermal denuder operated at $250 \text{ }^\circ\text{C}$, a Radiance Research 3-wavelength PSAP (Particle Soot Absorption Photometer), and optionally two DMAs (Differential Mobility Analyzers). AMETYST is operated behind the HALO sub-micrometer aerosol inlet (HASI). The CPCs are Grimm 5.410 models, operating at two different flow rates. The CPC internal butanol saturation setting is user-selectable to vary minimum detectable particle sizes. Data used in the studies were obtained from 0.6 L min^{-1} flow rate, set to a nominal lower cut-off size of 10 nm . Concentrations reported are normalized to standard temperature and pressure conditions. Original data are recorded at 1 Hz temporal resolution. In-cloud data at altitudes below 9 km were removed from the dataset based on cloud probe data (here CAS-DPOL instrument of DLR) to exclude apparent sampling artefacts of the inlet in the presence of liquid droplets in clouds.

3.2.2.3. CCNC

A Cloud Condensation Nuclei Counter (CCNC) was used to obtain CCN number concentrations. The instrument has two columns with continuous flow longitudinal thermal-gradient where the aerosol particles are subject to controlled

supersaturation (S) conditions. When particles travel longitudinally in the center of each column, they grow by water condensation (depending on their physical and chemical compositions) and are counted as CCN if they reach $1\ \mu\text{m}$ in size (1 Hz sampling rate). It is manufactured by Droplet Measurement Technologies (DMT) – Roberts and Nenes (2005). At one column, S was set to be relatively constant at $S \approx 0.55\%$, while the other was subject to 100-s stepping variations between 0.2% and 0.55%.

3.2.2.4. NIXE-CAPS

Cloud hydrometeor sphericity was analyzed by the NIXE-CAPS probe (New Ice eXperiment – Cloud and Aerosol Particle Spectrometer, LUEBKE et al., 2016, COSTA et al., 2017). NIXE-CAPS also contains two instruments, a CIPgs as the CCP and the CAS-Depol for particle measurements in the size range $0.6\ \mu\text{m}$ to $50\ \mu\text{m}$. The sizing principle of CAS-Depol is similar to the CDP, the difference is the particle probing: while CAS-Depol has an inlet tube (optimized with respect to shattering), CDP is equipped with an open path inlet. In addition to the sizing, CAS-Depol is equipped with a detector to discriminate between spherical and aspherical particles by measuring the change of the polarized components of the incident light. Spherical particles do not strongly alter the polarization state, in contrast to non-spherical ice crystals. The cloud particle phase of the whole cloud particle size spectrum was analyzed from the combination of phase determination in the size ranges $< 50\ \mu\text{m}$ (from the CAS-Depol polarization signal) and $> 50\ \mu\text{m}$ (from visual inspection of the CIPgs images - for details, see COSTA et al., 2017). Here, the phase states are defined as follows: “Sph (liquid)” stands for many only spherical ($D < 50\ \mu\text{m}$) and predominantly spherical ($D > 50\ \mu\text{m}$) hydrometeors, “Asph small (mixed phase)” for many predominantly spherical ($D < 50\ \mu\text{m}$) and only aspherical ($D > 50\ \mu\text{m}$), “Asph large (ice)” for only very few aspherical ($D < 50\ \mu\text{m}$) and only aspherical ($D > 50\ \mu\text{m}$).

3.2.2.5. BAHAMAS

Meteorological conditions, including three-dimensional (3D) winds, were obtained by the Basic HALO Measurement and Sensor System (BAHAMAS) located at the nose of the aircraft. The wind components were calibrated according to Mallaun et al. (2015), with an uncertainty of 0.2 m s^{-1} and 0.3 m s^{-1} for the horizontal and vertical directions, respectively. All probes were synchronized with BAHAMAS and operated at a frequency of 1 Hz.

3.3. Gamma parameterization

In a portion of the studies shown here, the cloud DSDs were fitted to Gamma distributions. This method aims at representing the DSDs as the function given by (ULBRICH, 1983):

$$N(D) = N_0 D^\mu \exp(-\Lambda D) \quad (3.3.1)$$

where $N(D)$ is the number concentration of droplets in the diameter range $D + \delta D$. N_0 ($\text{cm}^{-3} \mu\text{m}^{-1-\mu}$), μ (dimensionless), and Λ (μm^{-1}) are the intercept, shape, and curvature parameters, respectively. The Gamma parameters were obtained by matching the zeroth, second and third moments between the observed and fitted DSDs. Those moments were chosen in order to favor the study of the DSD properties of interest to this study (e.g. droplet number concentration, liquid water content and effective diameter), but they also coincided with the properties usually predicted by bulk microphysics models (zeroth and third moments in two-moment schemes). The Gamma parameters are calculated by:

$$\mu = \frac{6G - 3 + \sqrt{1 + 8G}}{2(1-G)} \quad (3.3.2)$$

$$\Lambda = \frac{(\mu+3)M_2}{M_3} \quad (3.3.3)$$

$$N_0 = \frac{\Lambda^{\mu+1} M_0}{\Gamma(\mu+1)} \quad (3.3.4)$$

where M_p is the p -th moment of the DSD. The symbol G is a non-dimensional ratio, given as follows:

$$G = \frac{M_2^3}{M_3^2 M_0} \quad (3.3.5)$$

The three parameters N_0 , μ , and Λ define the Gamma distribution in Equation 3.3.1; they are used to construct the phase-space described in Chapter 6. The DSD bulk properties, such as droplet number concentration (N_d), liquid water content (LWC), effective droplet diameter (D_{eff}), and relative dispersion (ε), can be derived from the Gamma parameters N_0 , μ , and Λ by taking into account the complete Gamma function integral properties:

$$N_d = \int_0^\infty N(D) dD = N_0 \frac{\Gamma(\mu+1)}{\Lambda^{\mu+1}} \quad (3.3.6)$$

$$LWC = 10^{-9} \frac{\pi}{6} \rho_w \int_0^\infty N(D) D^3 dD = 10^{-9} \frac{\pi}{6} \rho_w N_0 \frac{\Gamma(\mu+4)}{\Lambda^{\mu+4}} \quad (3.3.7)$$

$$D_{eff} = \frac{\int_0^\infty N(D) D^3 dD}{\int_0^\infty N(D) D^2 dD} = \frac{\mu+3}{\Lambda} \quad (3.3.8)$$

$$\varepsilon = \frac{\sigma}{D_g} = \frac{1}{\sqrt{\mu+1}} \quad (3.3.9)$$

where $\rho_w = 1000 \text{ g m}^{-3}$ represents the density of liquid water and σ and D_g are the DSD standard deviation and mean geometric diameter, respectively. N_d , LWC and D_{eff} are given in cm^{-3} , g m^{-3} and μm , respectively. Given the choice of the conserved moments, they exactly match the respective characteristics of the observed DSDs. ε is described in detail in Tas et al. (2015). The relative dispersion of the Gamma DSD may differ from the observations. Our measurements show that the Gamma and observed ε are closely related by $\varepsilon_{Gamma} = 0.95 \varepsilon_{Observed}$ ($R^2 = 0.93$), showing that the Gamma DSDs are narrower on average. We focus on ε as obtained by the Gamma parameters and do not use subscripts.

4 IMPACTS OF THE MANAUS POLLUTION PLUME ON THE MICROPHYSICAL PROPERTIES OF AMAZONIAN WARM-PHASE CLOUDS IN THE WET SEASON

This Chapter consists of the first paper written as part of the thesis studies. It is already published in final form in ACP (available at <http://www.atmos-chem-phys.net/16/7029/2016/>).

4.1. Background

The natural atmosphere of the Amazon is a system where the forest itself provides the nuclei for clouds, which in turn activate the hydrological cycle and help distribute the water that maintains the local flora. Under undisturbed conditions the aerosol particles that serve as CCN are mainly secondarily generated from the oxidation of biogenic gases (PÖSCHL et al., 2010). Primary aerosols emitted directly from the forest may also contribute to the overall CCN population and are especially active as IN (PRENNI et al., 2009). A review of the cloud-active aerosol properties and sources in general is provided by Andreae and Rosenfeld (2008) and specifically for the Amazon by Martin et al. (2010). The results presented herein relate to the local wet season, which presents a relatively clean atmosphere compared to the local dry season when biomass burning is more frequent (ARTAXO et al., 2002).

Given such an environment it is interesting to study the impacts that a city like Manaus has on the atmospheric conditions. Manaus is in the Brazilian Amazonas state, in the middle of the forest, and has a population of about 2 million people. The human activities associated with the city produce air pollution, which interacts with the natural background gases and particles. Several studies found that city pollution enhanced atmospheric oxidation (LOGAN et al., 1981; THOMPSON, 1992; KANAKIDOU et al., 2000; LELIEVELD et al., 2008), which not only impacts human health but also may interact with biogenic gases to increase secondary aerosol formation. Another example is the interaction between volatile organic compounds (VOCs) with the urban NO_x, which leads to enhanced ozone

concentrations through a photochemical process (TRAINER et al 1987, CHAMEIDES et al., 1992; BIESENTHAL et al. 1997; STARN et al. 1998; ROBERTS et al. 1998; WIEDINMYER et al., 2001).

The effects that the Manaus city has on the chemical properties of the local atmosphere potentially alter the way in which clouds are formed. Not only the human activities can change particles chemical properties, they also can increase the number concentration available for droplet formation. Most of this additional particulate matter is tied to emissions from traffic and power plants in the case of Manaus. Previous studies regarding the effects of anthropogenic aerosols on Amazonian cloud generally focused on biomass-burning related occasions (e.g. ROBERTS et al., 2003; ANDREAE et al., 2004; FREUD et al., 2008, MARTINS; SILVA DIAS, 2009) in the dry or transition seasons. However, very few studies evaluated the urban aerosol interaction with clouds over the rain forest during the wet season, when biomass-burning is strongly reduced given the frequent rain showers that leave the forest wet and more difficult to burn. In this case, the effects of the Manaus plume can be studied separately and in detail. Polluted clouds over the Amazon usually present more numerous but smaller droplets that grow inefficiently by collision-coalescence and therefore delay the onset of precipitation to higher altitudes within clouds (ROSENFELD et al., 2008).

The results presented herein are based on data sets collected between February and March 2014 during the first Intensive Operations Period (IOP1) of The Observations and Modeling of the Green Ocean Amazon (GoAmazon2014/5) experiment (MARTIN et al., 2016). The period is in the wet season, which presents a clean atmosphere due to the reduction in biomass burning. The pristine characteristic of the background air provides the opportunity for contrasting the microphysics of natural and urban pollution-affected clouds. The large-scale wind field is rather stable over the region for the campaign period, with prevailing northeasterly winds that advect the pollution plume southwestward. This scenario allows for the direct comparison between clouds

formed under background conditions and those affected by pollution in the wet season.

Clouds in the wet season differ from those in the dry and transition periods both because of aerosol conditions and large-scale meteorology (MACHADO et al, 2004). Although there is not a complete reversal of the mean wind directions intra-annually, the wet season clouds can be related to a monsoon system, usually referred as South American Monsoon System (SAMS). Zhou and Lau (1998) suggest that the monsoon-like flow can be understood when analyzing monthly anomalies on the wind fields. During the austral summer months, the winds tend to have a stronger northeastern component over Manaus area, while at austral winter time the stronger wind component is from the southeast. More details on the SAMS, including comparisons with other monsoon systems, can be found in Vera et al. (2006).

The main objective of this work is to understand the effects that anthropogenic urban pollution has on cloud droplets properties and development in the Amazon during the wet season. Specifically, the focus is on the comparison between warm-phase properties of clouds affected and not affected by the pollution emitted from Manaus city. The urban aerosol effect will be analyzed as function of height above the cloud base and vertical velocity.

4.2. Flight characteristics

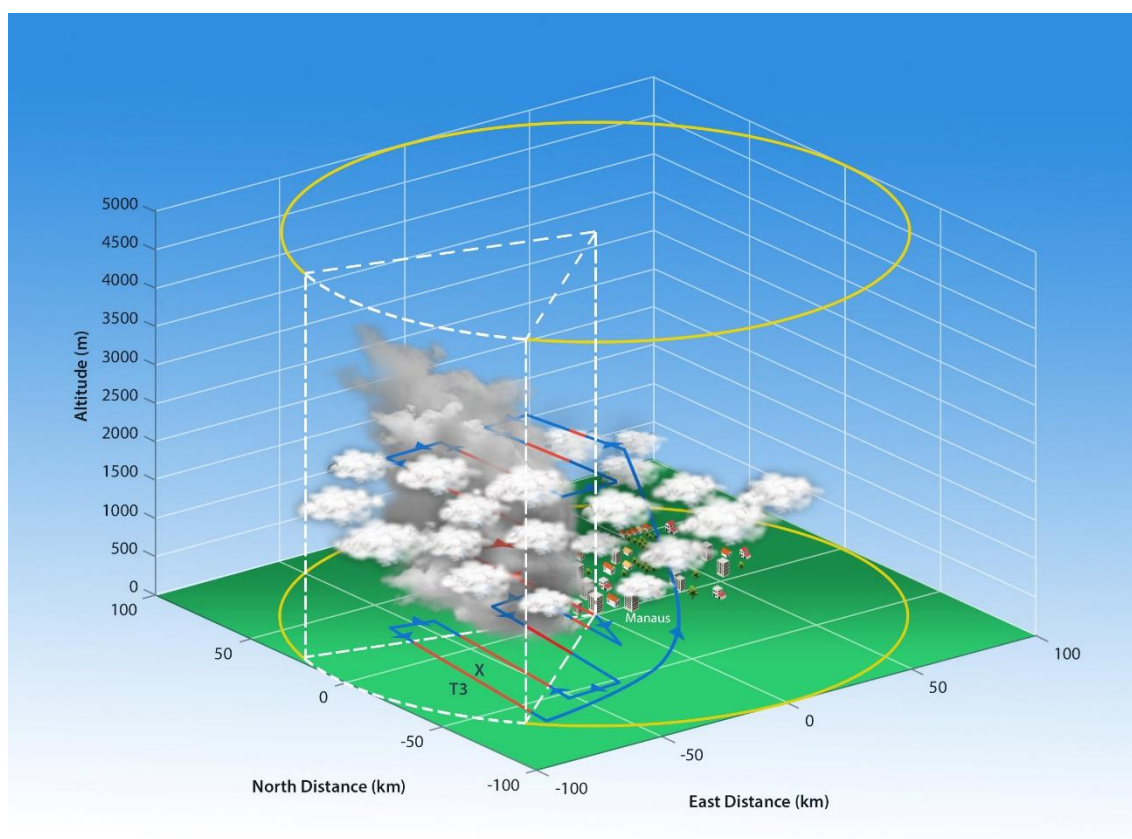
Sixteen research flights took place near Manaus in the Amazon forest between February and March 2014. Manaus coordinates are 3°06'S, 60°01'W and the dates and time periods of the flights are listed in Table 4.1, with times in UTC (local time is UTC-4). The U.S. Department of Energy Atmospheric Radiation Measurement program Gulfstream-1 (G-1) airplane (SCHMID et al., 2014) performed 16 flights while measuring aerosol concentrations and composition, radiation quantities, gas-phase chemistry and cloud microphysical properties.

Table 4.1 - Dates and times for all G-1 flights during GoAmazon2014/5 IOP1. Local time for Manaus is UTC-4. All flights were carried out in the year 2014.

Flight Number	Date	Start Time (UTC)	End Time (UTC)
1	February 22	14:38:27	17:25:26
2	February 25	16:32:06	18:40:07
3	March 1	13:35:37	15:27:35
4	March 1	17:18:48	18:47:07
5	March 3	17:46:34	19:11:57
6	March 7	13:09:51	15:35:25
7	March 10	14:26:37	17:09:35
8	March 11	14:42:23	17:51:08
9	March 12	17:21:25	19:29:42
10	March 13	14:16:09	17:21:27
11	March 14	14:18:54	16:48:23
12	March 16	14:40:17	17:26:32
13	March 17	16:24:40	19:26:36
14	March 19	14:26:38	17:17:48
15	March 21	16:33:47	18:56:07
16	March 23	14:59:05	17:43:34

The G-1 aircraft performed mostly short-ranged flights from Manaus, with most of the observations being within 100 km from Manaus. The flight patterns were mainly focused on measuring properties in and around the city pollution plume. A schematic for the concepts of the flight planning is shown in Figure 4.1. The actual patterns varied daily depending on the weather forecast and plume dispersion prediction (Figure 4.2). Additionally, other patterns were performed such as a run upwind from Manaus in order to probe a background air reference, or cloud profiling missions (vertical slices of the cloud field). However, the kind of pattern shown in Figure 4.1 was the most used and is the determinant to assess the interaction between the urban plume with the background atmosphere.

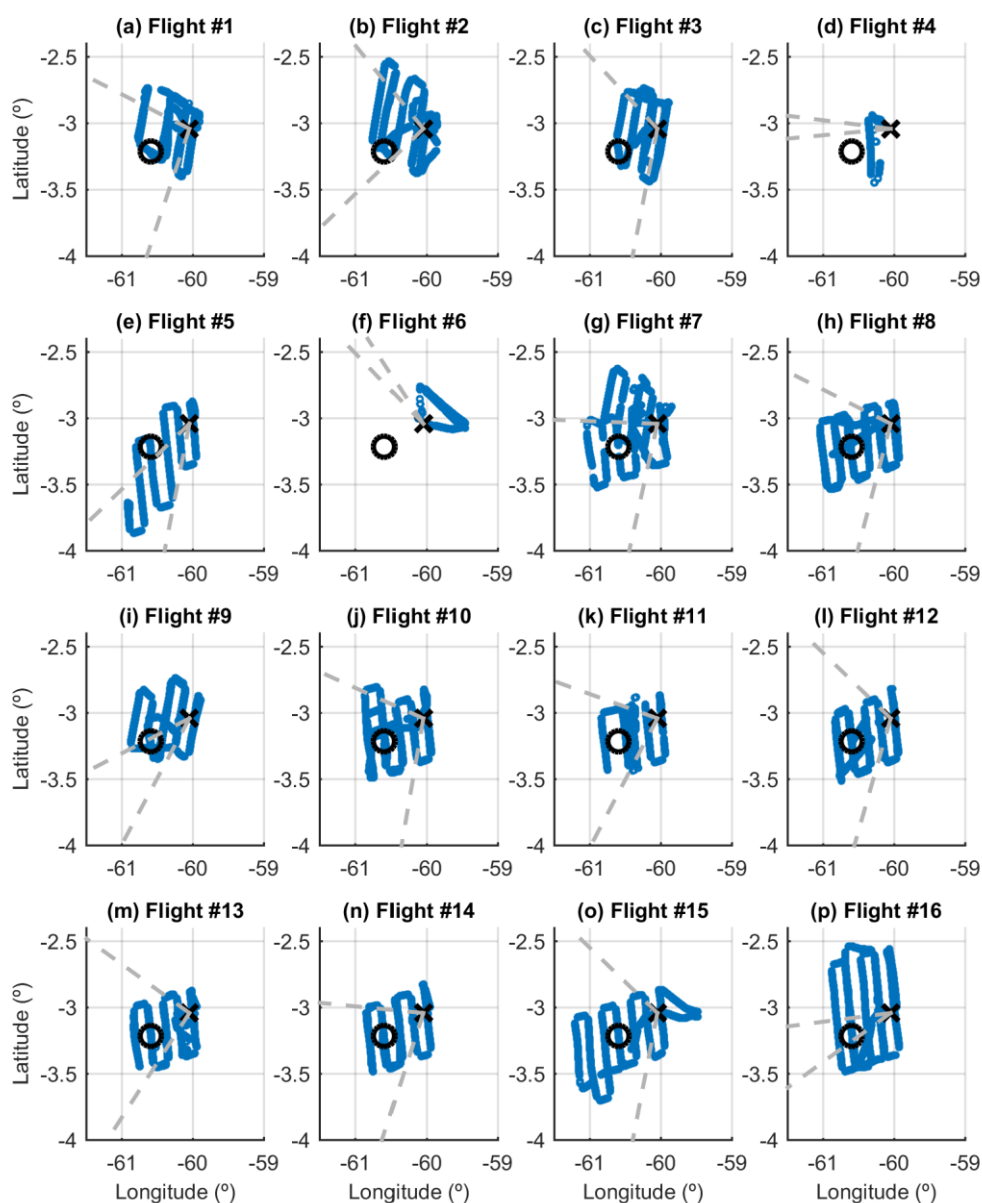
Figure 4.1 – Conceptual schematic for the flight patterns planning. It shows Manaus city and its pollution plume dispersing over the surrounding Amazon forest. The Cu field shown is very common during the wet season and is representative for most of the cloud conditions during the flights. The yellow circles indicate a 100-km radius from Manaus airport, although the figure is not meant to be quantitatively accurate. The lines with arrow heads show the most common flight plan used, where blue regions are possible locations for the background air measurements and the red ones indicate measurements inside the plume section (dashed white lines). T3 is a GoAmazon site to the north of Manacapuru.



During the wet season, it is very common to observe cumulus clouds as exemplified in Figure 4.1 and the G-1 cloud measurements consisted mostly of quick penetrations in those types of systems. From Manaus airport, the aircraft performed several legs perpendicular (or as close to as possible) to the plume direction while moving away from the city. At the end of the pattern, the aircraft started over in a different altitude and performed the same flight legs. In this way, it was possible to collect not only data regarding the plume but also on the surrounding background air. During the local wet season, the background

atmosphere is rather clean and the effects of the plume can be readily observed. The pollution-aerosols in this situation are almost only urban and biomass-burning contribution is very exceptional. The main idea to compare the background and polluted clouds is to accumulate statistics inside and outside the plume sections as shown in Figure 4.1. By concatenating the observations for the different flights, it was possible to obtain a dataset of background and polluted droplet size distributions (DSDs), which can then be used to look at aerosol impacts in different ways. All G-1 flights were used in order to obtain the highest sample size possible. Figure 4.2 shows the trajectories for all flights, where the dashed grey lines represent the plume angular section considered from the airplane data. Note that the plume usually disperses from Manaus to the T3 site, with relatively small variations on the direction based on the wind field. Two flights (4 and 6) had low sampling on the plume given the trajectories and the grey lines may not represent the overall region of the plume. However, the directions identified presented higher N_{CN} than the other ones.

Figure 4.2 - Trajectories for all G-1 flights during GoAmazon2014/5 IOP1. Manaus is located close to the $\{-60, -3\}$ point, marked with an "X", while the T3 site is marked with the black circle.



4.3. Plume classification

In order to compare two different populations of clouds, namely those formed under background conditions compared to those affected by pollution, a

classification scheme was developed. The most discernible and readily observable difference between a polluted and background atmosphere is the number concentration of aerosol particles per unit volume. Urban activities such as car traffic emit large quantities of particles to the atmosphere, which are then transported by atmospheric motions and can participate in cloud formation, especially when they grow, age and become more effective droplet activators. Their number concentration and sizes primarily determine their role on the initial condensational growth of cloud droplets through the aerosol activation mechanism. Even though the urban aerosols have a lower efficiency to become CCN, their number concentrations are high enough to potentially produce a higher number of cloud droplets (see, for example, KUHN et al., 2010). By affecting the initial formation of the droplets, increased aerosol concentrations due to urban activities can alter the cloud microphysical properties throughout its whole life cycle. It will be considered here that a simple, yet effective, classification scheme should consider primarily aerosol number concentrations to discriminate polluted and background conditions with respect to cloud formation environments. The intent of the classification scheme is not to quantify specifically the aerosols concentrations available for cloud formation under background and polluted conditions. Rather, it is a way to identify atmospheric sections that presented urban or natural aerosol characteristics.

Aerosol particles number concentrations (N_{CN}) measured by the CPC instrument were used to identify the plume location. The first procedure required is the elimination of possible artifacts related to measurements while the aircraft was inside a cloud. For that purpose, a cloud mask must be considered. The data are considered to be in-cloud by examining particle concentrations detected by several aircraft probes. The aircraft probes used to determine the presence of cloud are the Passive Cavity Aerosol Spectrometer (PCASP, SPEC Inc.), the 2D-Stereo Probe (2D-S), and the Cloud Droplet Probe (CDP, Droplet Measurement Technologies). The thresholds for detection of cloud are when either the PCASP bins larger than $2.8 \mu\text{m}$ have a total concentration larger than 80 cm^{-3} , the 2D-S

total concentration is larger than 0.05 cm^{-3} , or the CDP total concentration is larger than 0.3 cm^{-3} . Thresholds were determined by examining the sensitivity of each instrument. Assuming that the presence of clouds can affect the N_{CN} measurements, the concentrations inside clouds were related to those in clear air. Whenever an in-cloud observation is detected, the N_{CN} value is substituted by the closest cloud-free measurement (given that they are not more than 15 s apart, in which case the data are excluded from the analysis). In this way, possible cloud and rain effects on aerosols concentrations, such as rainout or washout, can be mitigated on the analysis.

A simple and fixed threshold to separate the background and polluted observations is not enough because the altitude of the measurements should also be considered. For that purpose, all CPC data were used to compute vertical profiles of particle number concentrations in 800-m altitude bins. This resolution was chosen in order to result in significant amounts of data in each vertical bin. A background volume is identified whenever the measured particle concentration is below the 25% quartile profile. The polluted ones are considered to be the ones above the 90% profile. Additionally, it is required that the measurement is located in the general direction of the urban pollution dispersion in order to be considered a plume volume. Similarly, the background measurements are limited to the section outside the plume location only. It is important to note that, while the CPC data are available for the whole duration of the flights, in-cloud observations are limited to the times of actual penetrations. The choice of asymmetric 25% and 90% profiles result in similar sample sizes for the classified polluted and background in-clouds measurements (305 s and 424 s, respectively), while maximizing the differences between the populations.

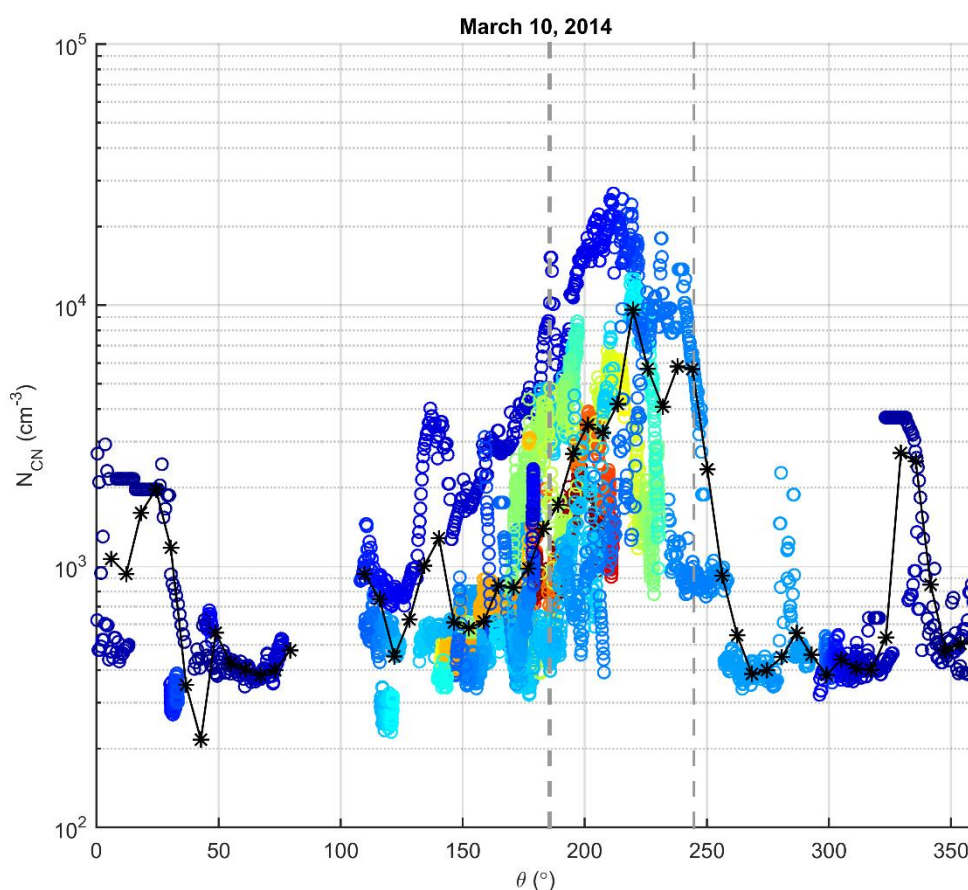
Given the daily variations of meteorological characteristics, the plume direction, width, and overall particle concentrations may vary. For that reason, the plume angular section must be obtained for each day individually. Figure 4.3 shows an example of plume classification for the flight on 10 March 2014. The N_{CN} is shown as a function of the azimuth angle with respect to Manaus airport (0° is east,

grows counterclockwise), irrespective of altitude. The color represents the horizontal distance (km) from the airport. Note that there is an angular section where the concentrations are high not only close to the city but also as far as 70 km. This section is defined to be affected by Manaus pollution plume (delimited by grey dashed lines in Figure 4.3). Note that the coordinate system is centered on Manaus' airport, where the G-1 took off, and not on the center of the city or other point of interest. For this reason, it is also possible to observe relatively high N_{CN} close to the origin and to the northeast and southeast directions. This corresponds to high N_{CN} over the city. By keeping those directions outside the plume angular section, this data is not considered as plume. This is intentional because other aspects occur over the city that may contribute to the cloud formation. For instance, the heat island effect may contribute to the convection, changing the thermodynamic conditions compared to those over the forest. By keeping the origin point as the airport, which is located on the west section of the city, this problem is avoided.

The final result of the classification scheme for March 10 is shown in Figure 4.4. A visual inspection of radiosonde (released from the Ponta Pelada airport located on southern Manaus) trajectory plots confirmed the overall direction of the plume for each flight. Given the nature of the meteorology in the Amazonian wet season, i.e. its similarities with oceanic conditions concerning horizontal homogeneity, there should be no significant difference between the thermodynamic conditions inside and outside the plume region for the G-1 flights. In this way, differences observed in pollution-affected clouds are primarily due to the urban aerosol effects. It should be noted that even though the plume classification is defined from the N_{CN} measurements, there are also observable differences regarding N_{CCN} . The in-plume N_{CCN} (for altitudes lower than 1000 m) averages 257 cm^{-3} for a 0.23% supersaturation, while the respective background concentration is 107 cm^{-3} (Figure 4.5). Note the overall low concentrations representative of the wet season. In that case, the plume increases N_{CCN} by more than a factor of 2. For higher supersaturation conditions (which can be achieved in strong updrafts), the

differences are even more pronounced. At 0.5% supersaturation, average N_{CCN} inside the plume is 564 cm^{-3} , while outside it is 148 cm^{-3} . This shows that the plume increases the concentration of aerosol particles that are able to form cloud droplets under reasonable supersaturation conditions, even though they are less efficient than the particles in the background air.

Figure 4.3 – N_{CN} around Manaus for March 10, 2014. θ is the azimuth angle and is zero for East direction and grows counterclockwise. Colors are proportional to the horizontal distance (km) between Manaus airport and the aircraft. The black dots represent the angular mean N_{CN} for each one of the 60 bins (azimuth). The vertical dashed lines represent the limits of the plume location.



In addition to the plume, the river breeze also plays a role on the convection characteristics over the region and the respective microphysics. The clouds directly above the rivers are usually suppressed given the subsidence from the

breeze circulation. This was addressed by comparing the DSDs under plume and background conditions only for measurements over land and it showed a similar picture to what will be shown in the next section. In this way, it is possible to confirm that the results presented here reflects the effect of Manaus pollution plume and not the river breeze, even though the clouds over land were indeed more vigorous. The results shown on the next section consists of the data probed both above rivers and above land.

Figure 4.4 - The same as Figure 4.3, with the coloring representing the plume classification. The green-colored dots represent unclassified points, red is for plume, and cyan is for background conditions. The inset shows the median (cyan) and the 25% (blue) and 90% (red) percentiles profiles of N_{CN} .

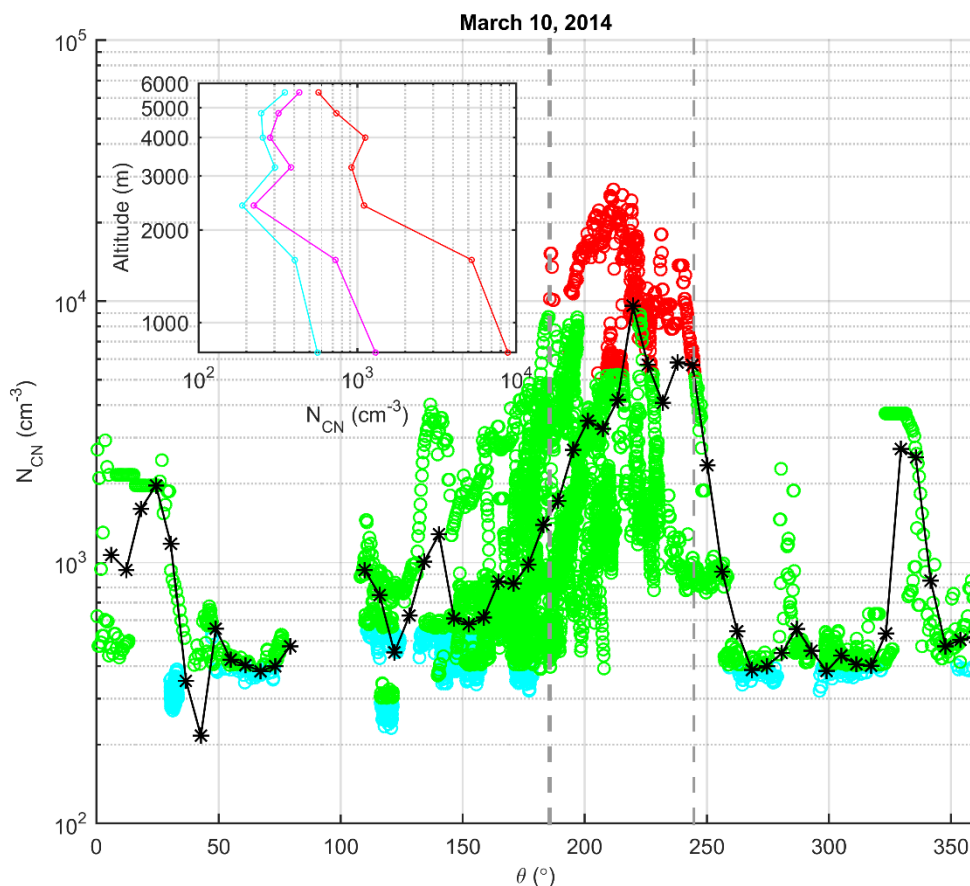
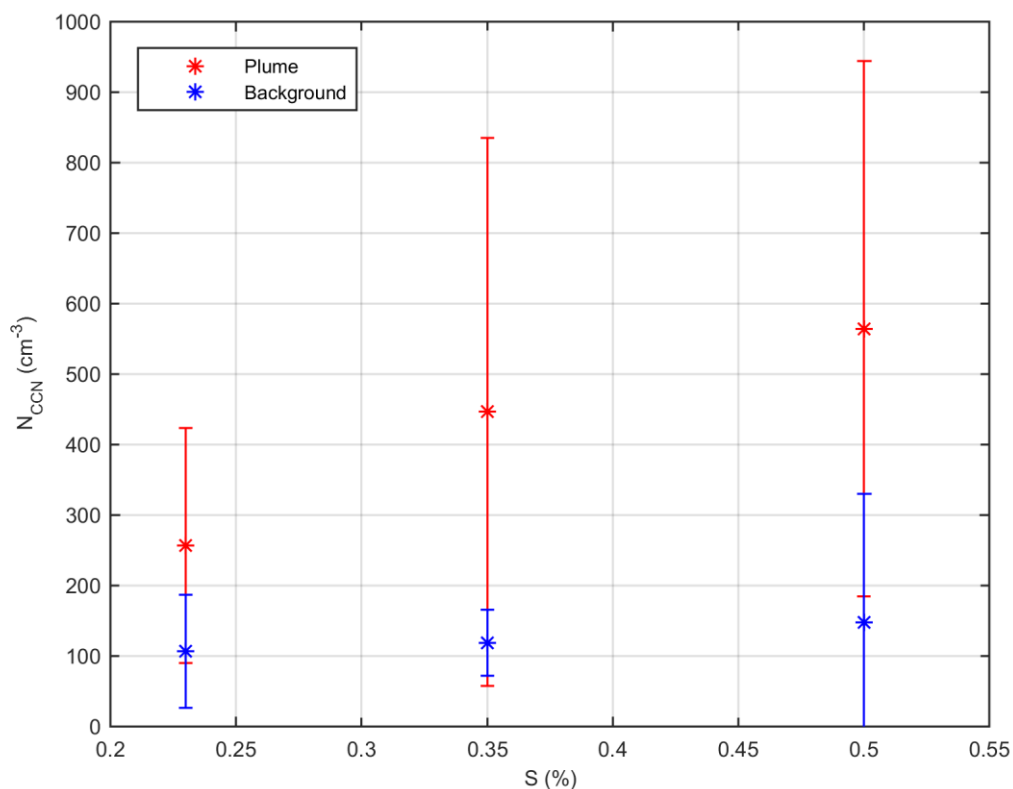


Figure 4.5 – N_{CCN} as function of supersaturation. Measurements inside the plume are shown in red, while background conditions are represented in blue.



4.4. Bulk DSD properties for polluted and background clouds

Given that the aerosol population directly affects cloud formation during the CCN activation process, bulk DSD properties under polluted and background conditions may differ. Figure 4.6 shows the frequency distribution of the droplet number concentrations (N_d), liquid water content (LWC), and effective diameter (D_{eff}) for all measurements inside the plume and under background conditions, irrespective of altitude. Those bulk properties were obtained from the FCDP-measured DSDs. The background clouds presented droplet number concentrations below 200 cm^{-3} for most cases, while being more dispersed for the polluted DSDs. It shows that it is much more likely to find higher N_d under polluted conditions than on background air. This observation may be tentatively justified as an increase in the water vapor competition, which leads to the formation of a higher number of droplets with smaller diameters. However, the

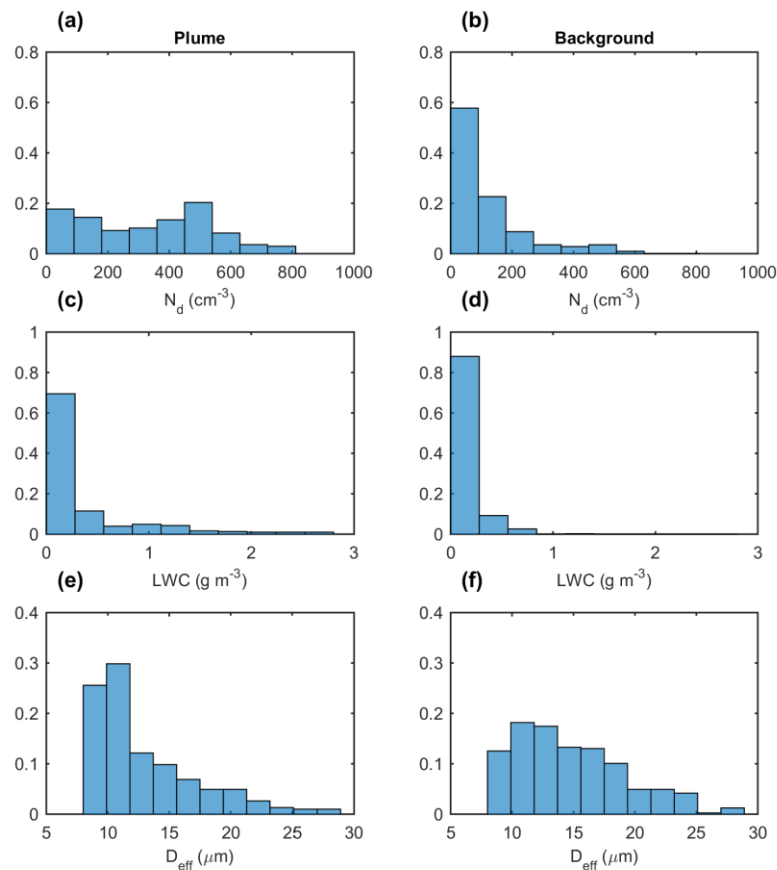
water vapor competition is usually discussed for a fixed LWC , which is not the case for the statistics shown here. The background clouds measured presented lower water contents overall, which could also partly justify the lower concentrations observed.

The effective diameter histograms show distinct droplet sizes distributions for both populations. While around 50% of droplets in the polluted clouds have D_{eff} between 8 and 12 μm , the frequency distribution for the background clouds shows more frequent occurrence of $D_{eff} > 12 \mu\text{m}$, even though they peak at similar diameters. This factor shows that, despite condensing lesser amounts of total liquid water, the background clouds are able to produce bigger droplets than their polluted counterparts. Overall, Figure 4.6 shows a picture consistent with the water vapor competition concept. However, the DSD formation under a water vapor competition scenario depends on two factors. One is commonly cited on the literature (e.g. ALBRECHT, 1989) and is related to the impacts on effective droplet sizes as function of aerosol number concentrations. The other factor is how much bulk water the systems are able to condense while the vapor competition is ongoing. Figure 4.6 suggests that the Manaus pollution plume affects both mechanisms, which are more complex than the water vapor competition process.

An interesting question to address is why LWC is lower for background clouds, i.e., why this type of cloud is relatively inefficient to convert water vapor to liquid droplets. One possible answer is related to total particle surface area in a given volume. Considering a constant aerosol size distribution, when their total number concentration is increased, the total particle surface area per unit volume also increases. In this way, there is a wider area for the condensation to occur, leading to higher liquid water contents. Additionally, if there is higher competition for the water vapor, the more numerous and smaller droplets formed under polluted conditions will grow faster by condensation than their background counterparts (because the condensation rate is inversely proportional to droplet size) and will readily reach the threshold for detection by the FCDP (around 1 μm). One point

to remember is the high amount of water vapor available during the wet season. Those differences in the bulk condensational growth under polluted or background conditions may explain in part the differences observed in Figures 4.6c-d, even if the aerosol size distribution changes from the background to the polluted sections. If the bulk condensation is more effective in a polluted environment, it should also lead to increased latent heat release and stronger updrafts. In a stronger updraft, the supersaturations tend to be higher, which feeds back into an even higher condensation rate.

Figure 4.6 - Normalized histograms of cloud droplet properties affected and unaffected by the Manaus pollution plume. (a-b) Total droplet number concentrations N_d (cm^{-3}), (c-d) liquid water content LWC (g m^{-3}), and (e-f) effective diameter D_{eff} (μm).



Other possible physical explanations for the higher LWC in polluted clouds include processes associated with precipitation-sized droplets (i.e., outside the

FCDP size range) and aerosol characteristics. If the aerosol-rich plume is able to reduce the effective sizes of the liquid droplets, it will also be able to delay the drizzle formation. In this way, the liquid water would remain inside the cloud instead of precipitating. On the other hand, the fast-growing droplets in the background clouds may grow past the FCDP upper threshold, effectively removing water from the instrument size range. However, the clouds penetrated were predominantly non-precipitating cumulus at early stages of their life cycle. Therefore, the warm-phase was not completely developed and the condensational growth plays a major role in determining the overall DSD properties. The second process identified (i.e. suppressed precipitation staying longer inside the clouds) probably has a lesser impact. The averaged ratio between second moment of the polluted and background DSDs is around 2, which shows that the former has around twice of the total area for condensation than their background counterparts. In this way, the increase in the bulk condensation efficiency is probably significant. Further studies are encouraged in order to detail and quantify the processes that lead to the observed *LWC* amount. However, based on Koren et al. (2014), the most determinant factor contributing for the high amount of cloud water under polluted conditions seems to be related to the condensation process. In the referred paper, it is shown that the amount of total condensed water tends to grow with aerosol concentration in a pristine atmosphere.

In order to detail the pollution effects on the total condensation rate and on the DSD properties, averaged properties for different water content and updraft speeds are analyzed. Firstly, given that the *LWC* is a measure of the total amount of water condensed onto the aerosol population, its correlation with the updrafts should be assessed. The updraft speed at cloud base can be understood as a proxy for the thermodynamic conditions, as it is a result of the meteorological properties profiles in lower levels. In this way, it is possible to disentangle the aerosol and thermodynamic effects by averaging the *LWC* data at different updraft speed levels. Figure 4.7a shows the result of this calculation for only the

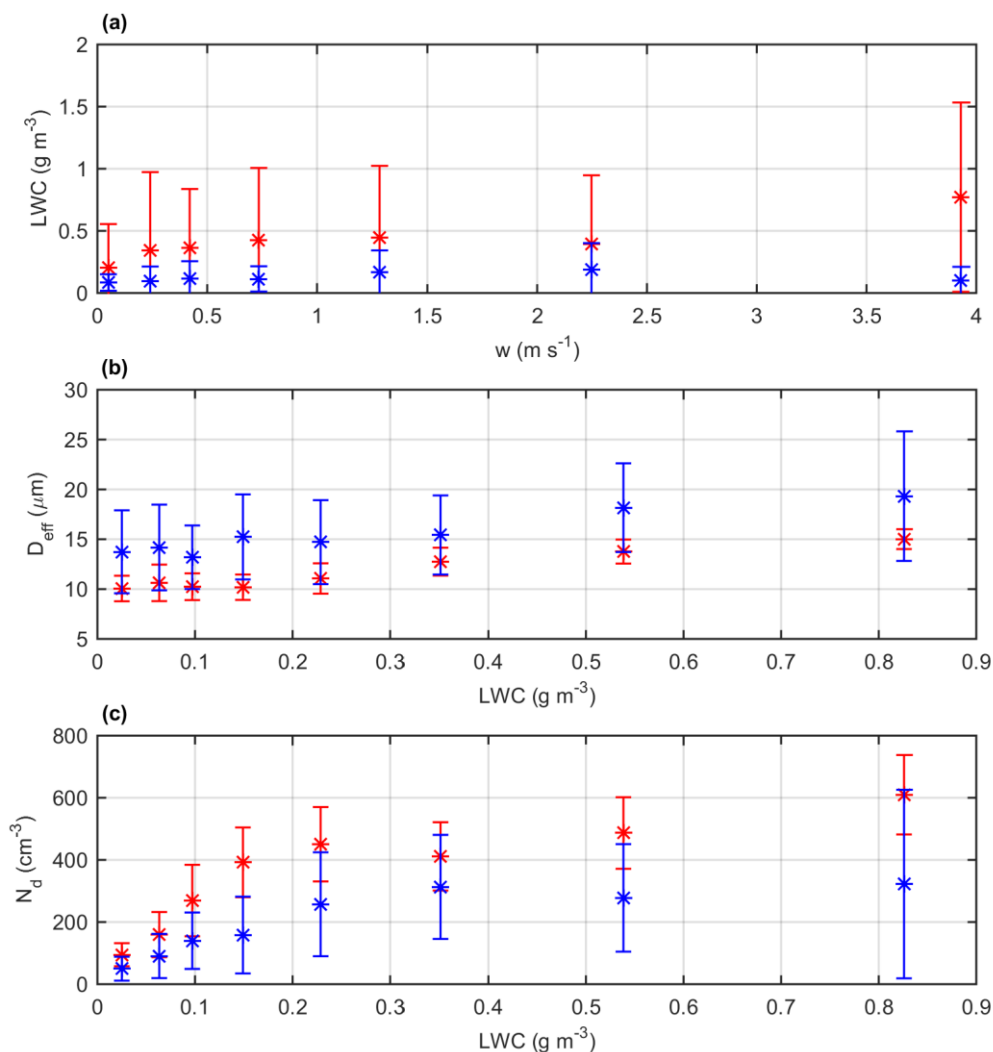
lower 1000 m of the clouds, while also differentiating between polluted and background clouds. The 1000m limit is chosen for both maximizing statistics and also capturing the layer in which the aerosol activation takes place. That layer is possibly thicker under polluted conditions, given the higher availability of nuclei. For similar updraft conditions, i.e., similar thermodynamics, the averaged total liquid water is always higher for polluted clouds. By eliminating the dependence on the thermodynamic conditions, it is possible to conclude that the *LWC* values are significantly influenced by the aerosol population. This figure shows that, on average, not only are the polluted clouds more efficient at the bulk water condensation but also the resulting *LWC* scales with updraft speed (linear coefficients, considering the error bars, are 0.13 g s m^{-2} for plume measurements and 0.033 g s m^{-2} for background clouds). In a background atmosphere, most of the aerosols have been activated, and increasing updraft strength does not result in further condensation. On the other hand, the higher availability of aerosols inside the plume allows for more condensational growth as long as enough supersaturation is generated, especially considering that the critical dry diameter for activation is inversely proportional to supersaturation and, consequently, to the updraft speed. However, a deeper analysis in a bigger dataset would be required to assess the statistical significance. The enhanced condensation efficiency and the possible *LWC* scaling with updraft strength at least partly explain the higher liquid water contents in the plume-affected clouds. The standard deviation bars in Figure 4.7a indicate that while there is high variability for the *LWC* in polluted clouds, the clean ones are rather consistent regarding the condensation efficiency.

The water vapor competition effect can be observed by examining droplet effective diameter and number concentrations at a certain *LWC* interval, as shown in Figures 4.7b and 4.7c. In this way, the polluted and background DSD properties can be evaluated irrespective of the bulk efficiency of the cloud to convert water vapor into liquid water. It is clear that, even with the dispersion observed, the two DSD populations present consistently different average

behaviors for all LWC intervals. For similar LWC, the averaged effective diameter is always larger on background clouds, with lower droplet number concentrations on average. Those results show a picture clearly consistent with enhanced water vapor competition in polluted clouds. It shows that, given a bulk water content value, droplet growth is more efficient in background clouds. This process should make background clouds more efficient to produce rain from the warm-phase mechanisms because of the early initiation of the collision-coalescence growth.

Another noteworthy point shown in Figure 4.7 is the difference between the relationships of D_{eff} and LWC, and of N_d and LWC. While the average effective diameter varies linearly with LWC ($R^2=0.95$ for plume and $R^2=0.92$ for background DSDs), there seems to be a capping on N_d . This means that for low LWC ($< 0.4 \text{ g m}^{-3}$), increases in the total water content are reflected in increased droplet concentrations. For higher LWC values, the averaged N_d remains relatively constant while the effective diameter grows with the water content. This suggests that at low water content levels, i.e., at the early stages of cloud formation, the formation of new droplets has a relatively higher impact on the overall LWC. As the cloud develops, the LWC is tied to the effective diameter of the droplets, as the impact of new droplet formation is weaker at this point. This effect is clearer in background clouds given the limited aerosol availability.

Figure 4.7 - Mean (a) LWC values for different log-spaced w intervals and mean D_{eff} (b) and N_d (c) for log-spaced LWC intervals. Error bars are the standard deviation for each interval. Blue points indicate background measurements, while red ones are relative to the polluted ones. The points are located at the middle of the respective bin intervals. Those results are limited to the first 1000 m of the clouds.



4.5. Vertical DSD development and the role of the vertical wind speed

The analysis of bulk DSD properties indicates a clear difference between the polluted and background cloud microphysics. However, it is desirable to further detail those differences. As most of the aerosol activation takes place close to cloud base (HOFFMANN et al., 2015), the direct effects of enhancements in

particle concentrations should be limited to this region. However, the aerosol effect can carry over to later stages of the cloud life cycle given that it will develop under perturbed initial conditions. One proxy for the cloud DSD evolution in time is to analyze its vertical distribution. For a statistical comparison, a relative altitude for all flights is defined. This relative altitude is calculated as follows: firstly, the closest radiosonde is used in order to obtain the cloud base altitude (as the lifting condensation level) and the freezing level. In case the airplane reached high enough altitudes, its data is instead used to obtain the altitude of the 0 °C isotherm. From those two levels, the relative altitude is calculated as percentages where 0 % represents the cloud base and 100 % is the freezing level. The altitudes of the cloud base and freezing levels range, respectively, from 100 m to 1200 m and from 4670 m to 5300 m approximately. Three layers are then defined: 1) bottom layer in which relative altitudes vary between 0 % and 20 %; 2) mid layer for 20 % to 50 %; and 3) top layer, where the altitude is above 50 %. Those specific relative altitude intervals were chosen in order to capture the physics of the cloud vertical structure and to minimize the differences in sample sizes for each layer, as there are more measurements for lower levels. Despite probing individual clouds, the DSD measurements can be combined into the three layers defined and interpreted as representative of a single system. It is conceptually similar to satellite retrievals of vertical profiles of droplets effective radii (e.g. ROSENFELD; LENSKY, 1998), where the cloud top radius is measured for different clouds with distinct depths and combined into one profile. This approach was validated with in-situ measurements for the Amazon region by Freud et al (2008).

Figure 4.8 shows statistical results for the DSDs in the three warm layers defined, while Table 4.2 shows the respective mean bulk properties. The altitude-averaged values show that the polluted clouds present higher number concentrations and water contents and lower diameters for all layers. Additionally, N_d decays much slower with altitude and droplet growth is

significantly suppressed. Those observations point to enhanced collisional growth in the background clouds.

Table 4.2 - Averaged bulk DSD properties for the three warm-phase layers and the respective standard deviations. The bottom (Bot) layer is defined by relative altitudes between 0 % and 20 %, the mid layer (Mid) between 20 % and 50 % and the top (Top) between 50 % and 100 %. The abbreviation “Bckgrnd” stands for “Background”.

Layer	N_d (cm ⁻³)		D_{eff} (μm)		LWC (g m ⁻³)	
	Plume	Bckgrnd	Plume	Bckgrnd	Plume	Bckgrnd
Bot	317 ±	127 ±	11.3 ±	14.2 ±	0.206 ±	0.114 ±
	190	131	2.00	4.19	0.216	0.122
Mid	360 ±	81.6 ±	17.7 ±	18.4 ±	0.848 ±	0.183 ±
	276	77.4	4.12	6.18	0.788	0.218
Top	191 ±	7.64 ±	15.5 ±	31.7 ±	0.522 ±	0.0766
	203	14.9	5.28	4.12	0.703	± 0.151

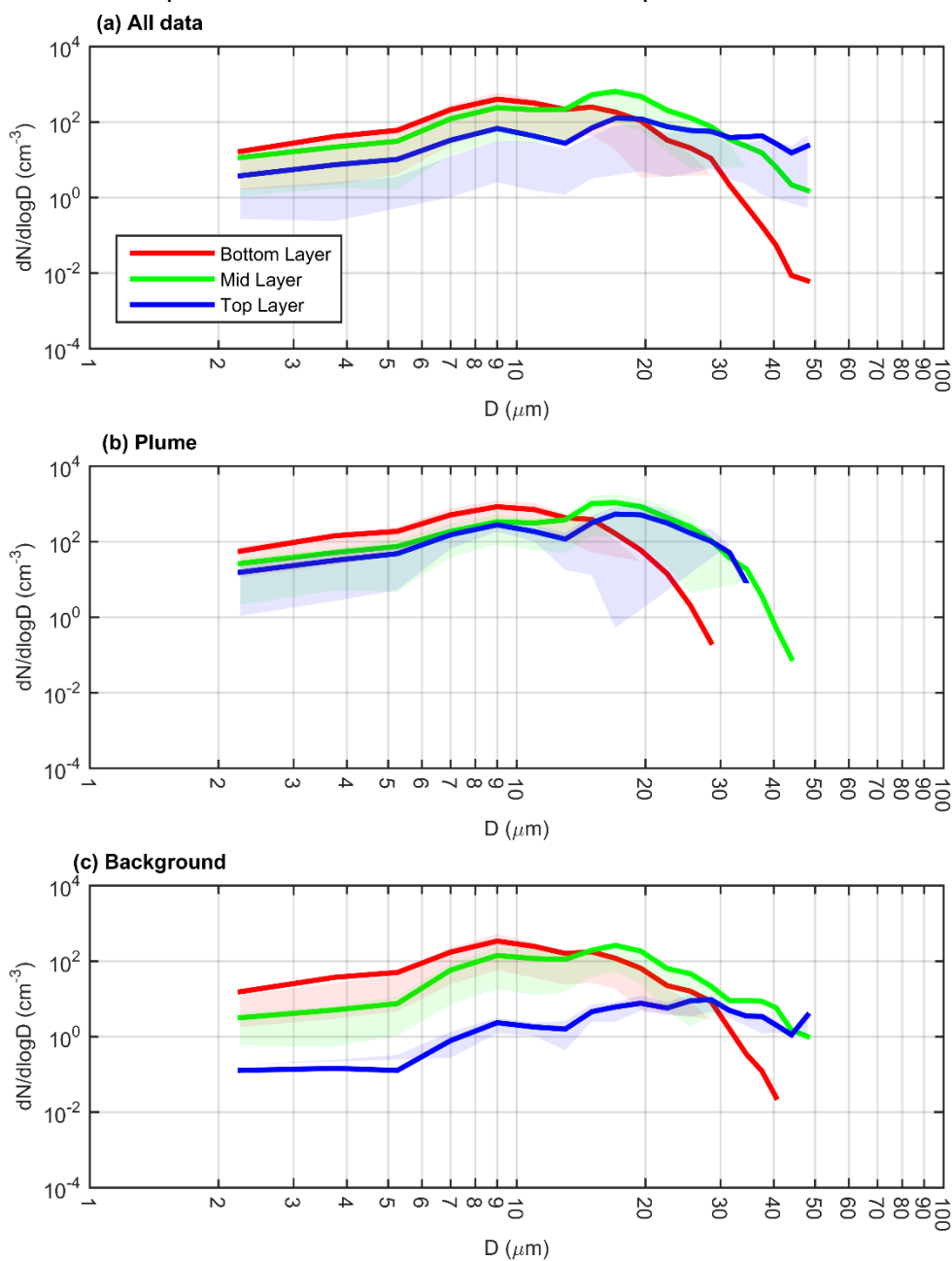
The overall picture of cloud DSD vertical evolution can be seen in Figure 4.8a. The most discerning feature between the DSDs at different altitudes is related to the concentrations of droplets greater than 25 μm. The concentrations in this size range grow with altitude on average. On the other hand, the concentrations of droplets smaller than 15 μm tend to diminish from the bottom to the top layer. Considering that the vertical dispersion of the DSDs represents at least in part its temporal evolution, this feature is associated with droplet growth where the bigger droplets grow in detriment of the smaller ones. This growth mechanism is the collision-coalescence process, where the bigger droplets collect the smaller ones and acquire their mass. The shaded areas on the figure show that this is not only an average feature, but is also visible in the quantiles.

The statistical results of the vertical evolution of the DSDs are discriminated for the measurements inside the plume and in background regions in Figures 4.8b-c. At first glance, it is quite clear that the two DSD populations present different

behaviors with altitude, meaning that the droplets grow differently depending on the aerosol loading. The plume DSDs present a high concentration on the bottom layer and shows weak growth with altitude. The concentration of small droplets ($< 15 \mu\text{m}$) does not change much with altitude and the top layer DSD is relatively similar to the middle one. On the other hand, the DSDs in the background clouds show a stronger growth with altitude (Figure 4.8c). The bottom layer DSD presents lower concentrations of small droplets but higher concentrations of bigger droplets than its polluted counterpart does. This coexistence of relatively big and small droplets readily activates the collision-coalescence process, accelerating droplet growth. Comparing both polluted and background DSDs with the overall averages (Figure 4.8a), it is clear that enhanced aerosol loading leads to less-than-average growth rates and the opposite is true for background clouds. The average growth rate for D_{eff} is $2.90 \mu\text{m km}^{-1}$ and $5.59 \mu\text{m km}^{-1}$ for polluted and background clouds, respectively.

The vertical speed inside the cloud is a critical factor as it helps determine the supersaturation and, consequently, the condensation rates in the updrafts. The interaction between the updraft speeds and aerosol loadings ultimately determines the initial DSD formations at cloud base. As mentioned before, the characteristics of the initial DSD may have impacts on the whole cloud life cycle, making the study of the vertical velocities critical for understanding the system development. Figure 4.9 shows averaged DSDs for different cloud layers and vertical velocities conditions, discriminating between the plume and background cases. The first row shows results for the bottom layer under (a) plume and (b) background conditions. The mid and top layer results are shown together in the second row, for (c) plume and (d) background conditions. “Strong” and “Mod” are references to the up- or downdraft speed (strong or moderate). The mid and top layers are considered in conjunction in order to increase the sample size.

Figure 4.8 - Averaged DSDs for three different cloud layers of bottom, mid and top of the warm layer. Graph (a) shows the results for all DSDs irrespective of classification, while (b) is for polluted DSDs only and (c) for background. Lines represent averages, while the shaded areas represent the dispersion between the 25 % and 75 % quantiles.



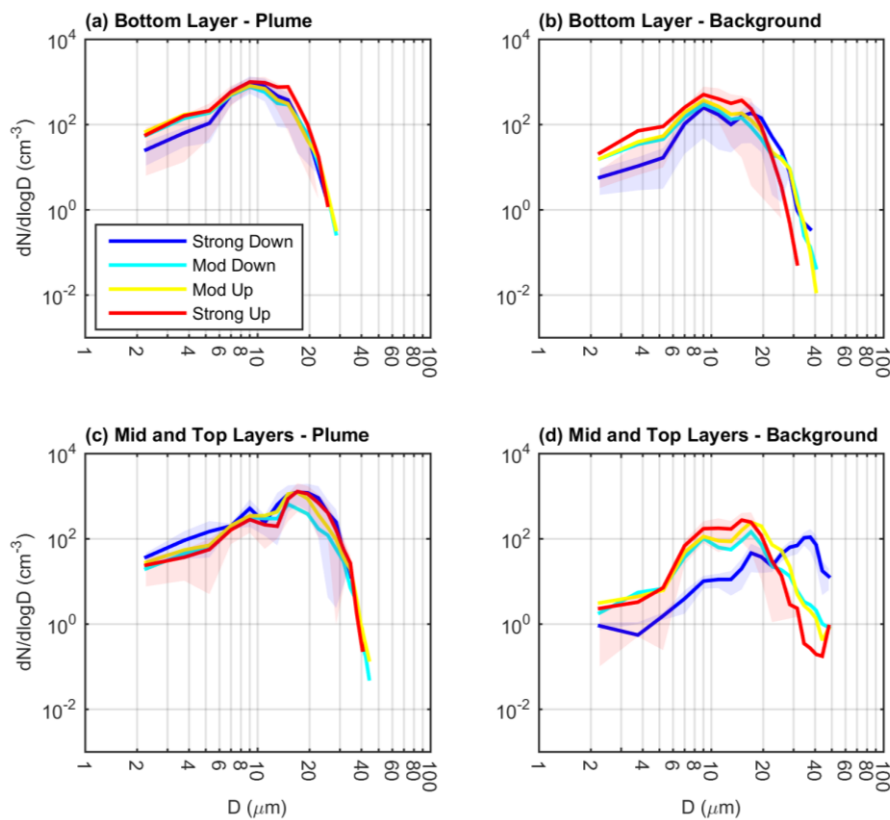
For the bottom layer, the vertical velocity has an impact mainly on the concentration of small droplets on polluted DSDs in the range $D < 5 \mu\text{m}$. The regions that presented updrafts are associated with higher concentrations of such

droplets because of new droplets nucleated under supersaturation. The downdraft regions mainly contain droplets that already suffered some processing in the cloud system and have relatively lower concentrations of small droplets that were probably collected by bigger ones. Additionally, small droplets ascend readily with the updrafts given their low mass, which is also a factor that can contribute to the differences between up- and downdraft DSDs. However, the dispersion shown in the shaded areas shows that the populations of DSDs in up- and downdrafts are relatively similar, suggesting a homogeneous layer with respect to DSD types. The DSDs shown on Figure 4.9a indicate single-mode distributions, which hampers collection processes and explains the similarities between the different vertical velocity regions. On the other hand, the background clouds have a second mode, especially in the downdrafts given the additional cloud processing, which favor the collision-coalescence process. The particles associated with background air in the Amazon are not only less numerous but also bigger overall compared to the urban pollution, and both of those features favor faster growth by condensation because of less vapor competition and larger initial sizes. It is interesting to note that the background DSDs in the strong updraft regions are narrower when compared to their polluted counterpart. In a polluted environment, there is not only the natural background aerosol population but also the urban particles emitted from Manaus. The mixture of the two, with the consequent physicochemical interactions, permits the formation of droplets over a wider size range, with a prolonged tail towards the lower diameters. The shaded areas show that the differences between the DSDs in the up- and downdraft regions are statistically relevant for the background clouds and are not a mere averaging feature.

Cloud droplets keep growing as they move to higher altitudes, but the way in which it occurs is rather different in a background or plume-affected environment. For polluted DSDs, there are two modes at the higher altitudes: one reminiscent of the lower levels and the other is probably mainly a result of additional condensational growth. In those systems, the additional processing does not

seem to be effective to produce bigger droplets, as shown by the blue line and shaded area in Figure 4.9c. For the background clouds, DSDs in the updraft regions show similar modes to their polluted counterparts, one close to 10 μm and the other at around 18 μm . However, there are appearances of droplets bigger than 30 μm that contribute to the formation of a third mode in the mid and top layers. This mode appears on the strong downdraft regions, which suggests it appears after in-cloud processing.

Figure 4.9 - Averaged DSDs as function of altitude, presence of up/downdrafts and aerosol conditions. The first row shows results for the bottom layer under (a) polluted and (b) background conditions. The mid and top layers' results are shown together in the second row for (c) plume and (d) background conditions. "Strong Down" means the presence of strong downdrafts, with vertical velocities lower than -2 m s^{-1} . "Mod Down" is moderate downdrafts, with $-2 \text{ m s}^{-1} < w \leq 0$. "Mod Up" and "Strong Up" are the equivalents for updrafts. Their velocities ranges are, respectively, $0 < w \leq 2 \text{ m s}^{-1}$ and $w > 2 \text{ m s}^{-1}$. The shaded areas represent the dispersion between the 25% and 75% percentiles for the strong downdrafts (in blue) and updrafts (in red).



4.6. Closing remarks

This study focused on the analysis of microphysics of warm-phase clouds in Amazonia during the wet season, with a specific emphasis on interactions with the pollution emitted by Manaus city. A statistical approach was used to compare several clouds probed in different flights on different days. Polluted clouds were found to have smaller (10%-40%) and more numerous (up to 1000%) cloud droplets. Additionally, they usually presented higher values of LWC , which can be attributed to favorable aerosol area-to-volume ratio and faster condensation rates over the smaller droplets. Despite the lower amount of water condensed in background DSDs, bigger droplets readily form given the early start of the collision-coalescence process (which does not increase LWC).

The smaller droplets in the plume-affected clouds hampered their growth rate with altitude, being approximately half of the clean case. Background clouds present relatively high concentrations of droplets greater than $20\ \mu\text{m}$ near cloud base that contributed to the growth rates, especially taking into account the non-linear nature of the collection process. With respect to warm-phase cloud DSDs, the updraft strength does not seem to be the major driving force for effective droplet growth, especially beyond the $20\ \mu\text{m}$ range. The most important features to produce such big droplets are weak water vapor competition (usually observed in background clouds) and the existence of bi-modality at the lower levels of the cloud. However, the thermodynamic role of the updraft speeds should not be underestimated. It is responsible for transporting hydrometeors beyond the freezing level, activating the cold processes. Those processes are known to be associated to thunderstorms and intense precipitation. Nevertheless, the main feature that determines warm-phase DSD shapes seems to be the aerosol conditions, with the vertical velocities playing a role in the modulation of the distributions.

5 SENSITIVITIES OF AMAZONIAN CLOUDS TO AEROSOLS AND UPDRAFT SPEED

This Chapter consists of the second paper written as part of this thesis. It is currently under review for ACP and can be accessed in the ACPD (Atmospheric Chemistry and Physics Discussions) website at <http://www.atmos-chem-phys-discuss.net/acp-2017-89/>.

5.1. Background

The Amazon basin can serve as a natural laboratory to study anthropogenic effects on cloud microphysical and radiative properties. In its remote parts, an absence of pollution similar to the pre-industrial era still prevail (ANDREAE et al., 2007), while in other regions, cities and biomass burning emit high amounts of aerosol particles into the atmosphere. This is especially important during the dry season, when rainout is less frequent (ARTAXO et al., 2002; KUHN et al., 2010; MARTIN et al., 2010). The natural CCN formed by the oxidation of VOCs can interact with anthropogenic emissions, enhancing the oxidation process, leading to increased CCN concentrations (KANAKIDOU et al., 2000; HALLQUIST et al., 2009). Even though aerosol particles can be scavenged by precipitation, nanoparticles produced in the upper troposphere can be transported downwards by deep convective systems, approximately reestablishing the surface aerosol concentration (WANG et al., 2016).

These processes illustrate the complex feedback between the vegetation, the aerosols serving as CCN, and the clouds providing water to the vegetation. There are, however, still plenty of open questions. The main difficulty is the quantitative comparison of the aerosol effect to other processes, given that the anthropogenic influences alter more than just aerosol particle concentrations. Human activities associated with urbanization and agriculture change the local landscape and the Earth's surface properties, also altering the energy budget (FISCH et al., 2004) and consequently the thermodynamic conditions for cloud formation. According to Fisch et al. (2004), the convective boundary layer is deeper over pasture during

the dry season because of the increased sensible heat fluxes. This effect results in greater cloud base heights with potentially stronger updrafts, which should also be considered when analyzing the aerosol effect.

One possible way to compare different effects on cloud microphysical properties is through a sensitivity calculation. It can provide specific quantifications of aerosol and thermodynamic effects on cloud microphysical quantities. One such sensitivity study was proposed by Feingold (2003), where the author calculates cloud droplet number concentration (N_d) sensitivities to several aerosol and thermodynamic drivers, such as total aerosol particle concentration (N_{CN}), updraft speed (w), and liquid water content (LWC). However, this analysis was limited to adiabatic stratocumulus clouds where collision-coalescence was not considered. Another modeling study was proposed by Reutter et al. (2009), where they identified three regimes that modulate the N_d sensitivity. The regimes are aerosol-limited, updraft-limited, and the transition between them. The authors highlight that the N_d dependence on N_{CN} and w may vary given their relative magnitudes. This study is limited to cloud base, therefore not addressing cloud evolution. The Reutter et al. (2009) study was extended by Chang et al. (2015), who took into account the evolution of the systems by considering the sensitivities on precipitation and ice phase, but was relatively limited in terms of representativeness because of the use of a 2D model. Satellite studies (e.g., BRÉON 2002; QUAAS et al. 2004; BULGIN et al. 2008) have an intrinsic limitation given the characteristics of the remote sensors. This kind of study usually deals with vertically-integrated quantities and frequently focuses on oceanic regions because of the favorable surface contrast.

The main goal of this study is to expand the sensitivity calculations usually found in the literature to include: 1) aerosol and thermodynamic effects on cloud droplet number concentration, size, and shape of the size distribution; 2) comparison with the effect of cloud evolution, i.e., in-cloud processing; and 3) in-situ observations of the less frequently studied convective clouds over tropical continental regions. For this purpose, we report on recent measurements over the Amazon rainforest

during the ACRIDICON-CHUVA campaign (WENDISCH et al. 2016), where a wide variety (in terms of aerosol concentrations and thermodynamic conditions) of cloud types were measured. We quantify the aerosol-induced changes in cloud microphysical properties and compare them to the effects of updraft intensity, which are related to thermodynamic properties, over different regions in the Amazon. Both processes are analyzed with a focus on cloud evolution. Our methodology should prove useful for better understanding aerosol-cloud interactions over the Amazon, which is a region, as are the tropics as a whole, with poor forecasting skill (KIDD et al., 2013).

5.2. Campaign and methodology

During the years 2014 and 2015, the GoAmazon2014/5 campaign took place in the Amazon to improve our understanding regarding aerosol particles, atmospheric chemistry, clouds, radiation, and their interactions (MARTIN et al., 2016). In conjunction with the second Intensive Operations Period (IOP2) of this experiment, the ACRIDICON-CHUVA campaign took place during September-October 2014 (WENDISCH et al., 2016). It included 14 research flights with the German HALO (High Altitude and Long Range Research Aircraft). A previous campaign dedicated to study aerosol-cloud interactions took place in the Amazon in 2002 (LBA-SMOCC, ANDREAE et al., 2004), but it had been relatively limited in terms of range and ceiling of the aircraft measurements. The high endurance of the HALO aircraft, which carried sophisticated microphysical, aerosol and solar radiation instrumentation, allowed for long-range flights from remote areas in northern Amazon, to the deforestation arc in the south and to the Atlantic coast in the eastern part (Figure 5.1). The flights were planned to cover five different mission types focusing on different cloud, aerosol, chemistry and radiation processes (see WENDISCH et al., 2016 for details). The flights were numbered chronologically as ACXX, where XX varies from 07 to 20. For this study, the cloud profiling missions are of particular interest and their respective locations are shown in Figure 5.1. In this study, we take advantage of HALO's capabilities to compare different types of clouds formed over different Amazonian regions,

focusing on their warm microphysics. In addition to the HALO measurements, ground-based equipment was also operated in and near Manaus city (MACHADO et al., 2014; MARTIN et al., 2016).

The results shown here were obtained from the measurements of four different instruments (for a list of all HALO instruments, see WENDISCH et al., 2016), covering aerosol, cloud and meteorological properties. We will focus on aerosol and CCN number concentrations, cloud droplet size distributions (DSD), and updraft speed. The instruments are described in Section 3.2.

Figure 5.1 - Locations where cloud profiles have been collected for different HALO flights. Clouds formed over southern Amazonia and in the Manaus region are subject to higher aerosol loadings due to the presence of the deforestation arc and urban emissions. Clouds formed over the northern and northwestern Amazon are driven by background conditions with low aerosol concentration. During the GoAmazon2014/5 IOP2, maritime clouds were also profiled on the Atlantic coast.



5.3. Sensitivity calculation

Several earlier studies calculated cloud sensitivity to aerosols and/or updrafts (FEINGOLD, 2003; MCFIGGANS et al, 2006; KAY; WOOD, 2008; REUTTER et al, 2009; SOROOSHIAN et al, 2009; KARDYS et al, 2012; CHANG et al, 2015), but they were usually limited in scope by not considering the factors that contribute to the cloud microphysics individually. This study aims to expand the sensitivity methodology by concurrently considering cloud evolution, updraft speed, and aerosol effects on clouds and by taking advantage of the comprehensive ACRIDICON-CHUVA dataset to represent different kinds of clouds and thermodynamic conditions. As pointed out by Seinfeld et al. (2016), major field campaigns provide a key opportunity for improving our knowledge of the aerosol-cloud-climate interactions, further motivating the results to be presented here.

Three factors will be considered as the main drivers of cloud microphysical properties, each representative at least partially of thermodynamic and aerosol conditions and cloud evolution. For the aerosol characterization, we will use averaged concentrations measured by the AMETYST-CPC (referred here as N_{CN} - see Table 5.1) at the cloud base level. This level was obtained from the CCP-CDP measurements as the lowest level where the LWC is higher than 0.01 g m^{-3} . As the profiles always started by cloud base penetrations, this ensures a precise estimation of cloud base altitude. Table 5.1 also shows that cloud condensation nuclei (CCN) concentrations were proportional to N_{CN} for the chosen instrument supersaturation. A linear fit between the two concentrations results in $R^2=0.96$, with angular and linear coefficients equal to 1.57 and 243 cm^{-3} , respectively. For the purposes of the sensitivity calculations, we will use N_{CN} instead of N_{CCN} because they are not dependent on instrument or cloud supersaturations. The sensitivity calculation (see below) uses derivatives of the concentrations, so the choice of N_{CN} or N_{CCN} should have no significant impact on the results to be presented here. The most pristine clouds are observed near the coast (AC19), followed by the ones measured over the forest. The flights AC7,

AC12, and AC13 each showed increasing aerosol concentrations as the flights moved towards the southern Amazon. For the flights closer to Manaus city, the aerosol loading of the clouds depends on localized aspects such as small-scale biomass burning and the pollution plume from urban/industrial activities (CECCHINI et al., 2016).

Table 5.1 – N_{CN} and N_{CCN} at cloud base for each flight considered in this study. * N_{CCN} for flight AC20 showed pronounced scaling with S . The value shown is for the measurements where $S > 0.52$ %. This value is closer to the maximum droplet concentration measured at the base of the clouds ($=1422 \text{ cm}^{-3}$).

Flight	$N_{CN} (\text{cm}^{-3})$	$N_{CCN} (\text{cm}^{-3})$	$S (\%)$
AC19	465	119	0.52
AC18	744	408	0.50
AC9	821	372	0.51
AC20	2331	1155*	0.55
AC7	2498	1579	0.50
AC11	2691	1297	0.49
AC12	3057	2017	0.44
AC13	4093	2263	0.44

The second factor that affects cloud microphysics is the updraft intensity (w). It, along with the aerosol population, defines the supersaturation inside the clouds and thus affects the droplets condensational growth. The intensity of the updrafts depends both on meteorological conditions (e.g., temperature and humidity profiles) and on the latent heat release of condensing water. Aerosols may indirectly affect the amount of latent heat released (smaller droplets in polluted clouds have favorable area-to-volume ratio), but the speed of the ascending air

can be understood as a response to the thermodynamic conditions in the clouds. Therefore, w can be used as a benchmark to compare different clouds subject to similar cloud-microphysics-relevant thermodynamic conditions.

Lastly, it is important to have an estimate of how cloud microphysical properties evolve throughout the system evolution. More importantly, how to detect similar cloud stages over the different flights for comparison. The HALO cloud profiling missions were planned to capture growing convective clouds in the different Amazonian regions. The aircraft penetrated the systems first at cloud base and then at ascending altitudes in the cloud tops of the growing convective elements. This strategy allows the use of altitude above cloud base (herein referred as H , in meters, also known as cloud depth) as proxy for cloud evolution. Measurements at higher altitudes reflect later stages of the cloud lifecycle as the systems develop upward. We use the derivatives of the microphysical properties with respect to H , which can be understood as variations during the cloud evolution. This will put the sensitivities to N_{CN} and w into perspective, highlighting the importance to detect cloud stage.

The sensitivities are calculated as partial derivatives on a natural log scale. In this way, they are normalized for quantitative comparison. Based on the terminology in the literature (e.g., FEINGOLD 2003; CHANG et al., 2015), we consider the sensitivities as follows:

$$S_Y(X_i) = \left. \frac{\partial \ln Y}{\partial \ln X_i} \right|_{X_j, X_k} \quad (5.3.1)$$

where X is the independent variable, i.e., w , N_{CN} and H , and Y is the cloud microphysical property of interest. For the sensitivity calculation, we will focus firstly (Section 5.5) on cloud droplet number concentration (N_d) and effective droplet diameter (D_{eff}) of cloud DSD with $D < 50 \mu\text{m}$. In Section 5.6 we also consider the sensitivities in (LWC), relative dispersion (ϵ) and curvature parameter (Λ , see respective text for details). The three factors chosen for X in this study are not necessarily independent; therefore, in order to follow the partial

derivative formalism, we include the criteria expressed by the vertical line (Equation 5.3.1). The subscript in X identifies the different independent variables considered. This notation means that two independent variables remain constant while the sensitivity to the third is being calculated. As an example, the sensitivity of N_d to N_{CN} , w , and H can be expressed as:

$$S_{N_d}(N_{CN}) = \left. \frac{\partial \ln N_d}{\partial \ln N_{CN}} \right|_{w,H}, \quad S_{N_d}(w) = \left. \frac{\partial \ln N_d}{\partial \ln w} \right|_{N_{CN},H}, \quad S_{N_d}(H) = \left. \frac{\partial \ln N_d}{\partial \ln H} \right|_{w,N_{CN}} \quad (5.3.2)$$

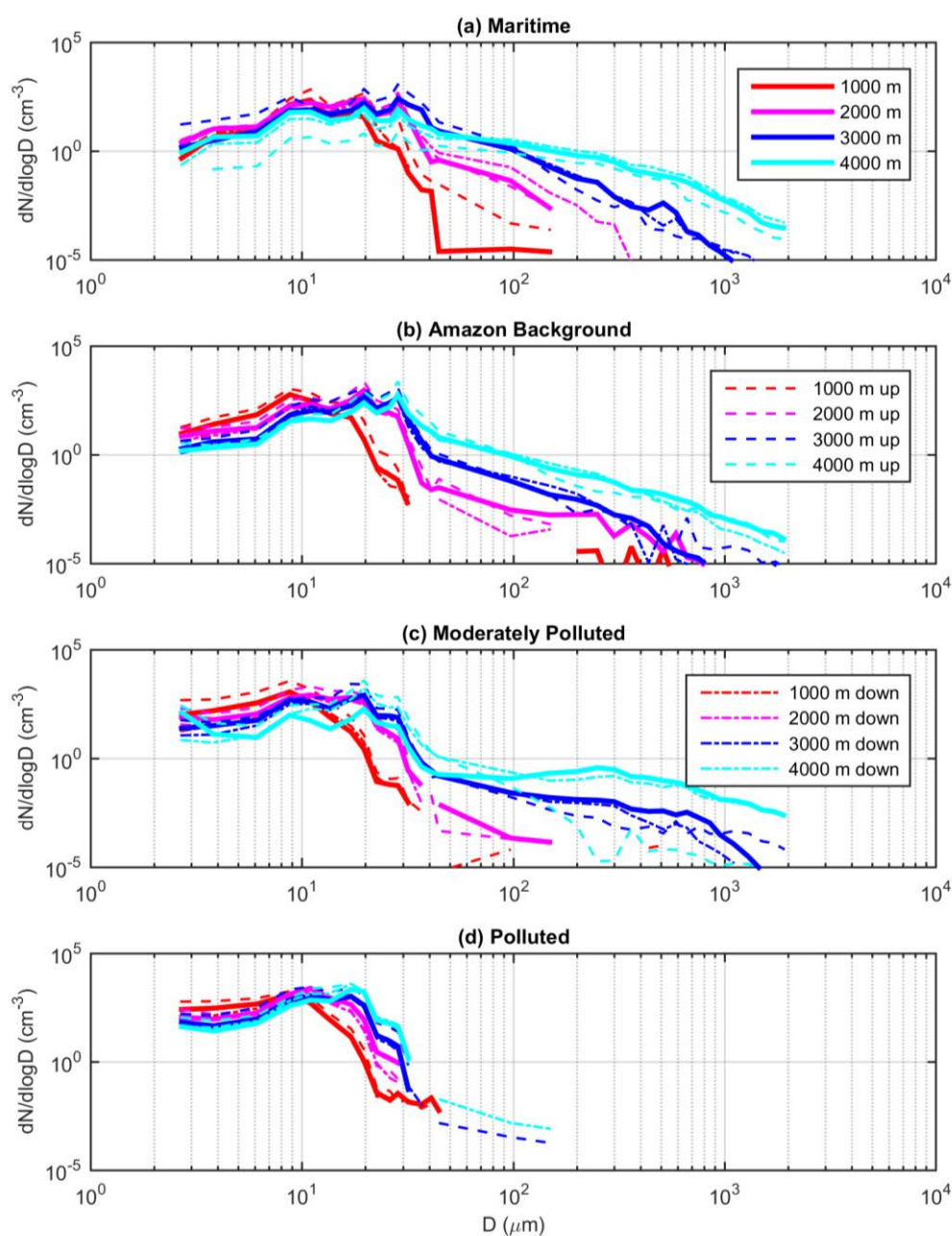
Equation 5.3.2 recognizes that several parameters can affect N_d , and they should be analyzed individually. Other sensitivities, such as $S_{D_{eff}}(N_{CN})$ or $S_{D_{eff}}(w)$, are obtained analogously.

As it is not feasible to analyze the sensitivities under exactly constant conditions as in Equation 5.3.2, we decided to use N_{CN} , w and H intervals instead. These quantities were binned into $\{0 \text{ cm}^{-3}, 500 \text{ cm}^{-3}, 1000 \text{ cm}^{-3}, 3000 \text{ cm}^{-3}, 4500 \text{ cm}^{-3}\}$, $\{0 \text{ m s}^{-1}, 0.5 \text{ m s}^{-1}, 1 \text{ m s}^{-1}, 2 \text{ m s}^{-1}, 4 \text{ m s}^{-1}, 8 \text{ m s}^{-1}\}$, and $\{0 \text{ m}, 200 \text{ m}, 500 \text{ m}, 950 \text{ m}, 1625 \text{ m}, 2637 \text{ m}, 4156 \text{ m}\}$, respectively. In this way, there are 4, 5, and 6 N_{CN} , w , and H intervals, respectively. The values of the bins were chosen in order to maximize the amount of data in each interval, which required growing spacing in w and H . We use constant N_{CN} values for each profile and the respective bins effectively group different flights according to the pollution level. Note that flight AC19 falls in the first interval, flights AC9 and AC18 in the second, AC7, AC11, and AC20 in the third and AC12 and AC13 in the fourth (see Table 5.1). We then produce 4-by-5-by-6 matrices containing averaged N_d and D_{eff} values for the combined intervals, covering all variations possible. By fixing two dimensions and varying the third, we obtain the average variation of the microphysical property to the independent variable of choice. The sensitivity is calculated as linear fits in the natural logarithm scale.

5.4. Cloud droplet size distributions related to different aerosol and thermodynamic conditions

The first qualitative indication of the effect of N_{CN} , w , and H on cloud microphysical properties can be seen in Figure 5.2. This figure shows DSDs grouped into four categories according to the aerosol concentration (N_{CN}) at cloud base: 1) Maritime clouds, with $N_{CN} \leq 500 \text{ cm}^{-3}$ (only flight AC19); 2) Clouds under Amazonian background conditions, with $500 \text{ cm}^{-3} < N_{CN} \leq 1000 \text{ cm}^{-3}$ (flights AC9 and AC18); 3) Moderately polluted clouds, with $1000 \text{ cm}^{-3} < N_{CN} \leq 3000 \text{ cm}^{-3}$ (flights AC7, AC11, and AC20); and 4) Polluted clouds, with $N_{CN} > 3000 \text{ cm}^{-3}$ (flights AC12 and AC13). Solid lines in Figure 5.2 represent DSDs for neutral vertical speed ($-1 \text{ m s}^{-1} \leq W \leq 1 \text{ m s}^{-1}$) while the DSDs with dashed and dot-dashed lines indicate the up- and downdraft regions, respectively ($|W| > 1 \text{ m s}^{-1}$; note that we use W to differentiate from w which refers only to the updraft portion). They represent averages for all profiles matching the aerosol intervals chosen (1 maritime, 2 Amazonian background conditions, 3 moderated pollution and 2 polluted). Individual profiles can be found in Figures 5.3-6. It is evident that aerosols and updrafts affect the droplet size distribution and its evolution in different ways and magnitudes. Clouds that develop under similar aerosol conditions tend to have similar DSDs not only at cloud base but also higher in the warm layer. The individual profiles shown in Figures 5.3-6 confirm the pattern that is evident in Figure 5.2. On the other hand, the updraft effect is limited to modulations of the DSDs, especially in the $D < 10 \text{ }\mu\text{m}$ range. Note that DSDs subject to similar w can be widely different depending on the respective pollution. The resulting vertical evolution of the clouds is dependent of the N_{CN} value, being more pronounced the cleaner the clouds are. We only observed significant concentrations of precipitation-sized droplets (e.g., $> 100 \text{ }\mu\text{m}$) for $N_{CN} < 3000 \text{ cm}^{-3}$.

Figure 5.2 - Droplet size distributions as function of altitude above cloud base, aerosol particle number concentration, and vertical wind speed, W . Four 1000-m-thick layers are considered in the vertical, where the legends in the graphs show the respective upper limit of each one. Solid lines represent averaged DSDs for $-1 \text{ m s}^{-1} \leq W \leq 1 \text{ m s}^{-1}$, i.e., for relatively neutral vertical movements. Dashed lines represent averaged DSDs for the updraft regions where $W > 1 \text{ m s}^{-1}$, and dot-dashed lines represent the downdrafts ($W < -1 \text{ m s}^{-1}$). There is only one Maritime flight (AC19), two in the Amazonian Background (AC9 and AC18), three with moderate pollution (AC7, AC11, and AC20), and two polluted (AC12 and AC13).



The main motivation for calculating sensitivities is to quantify and compare the role of N_{CN} , w , and H in the formation and evolution of the DSDs as seen in Figure 5.2. In this way, it will be possible to check the magnitudes of the effects of aerosols, thermodynamics (as seen from the updrafts), and cloud evolution in the determination of the warm-phase characteristics. Note, however, that we are focusing on only one portion of the updraft effects, i.e., the condensation and collision-coalescence effects. For instance, Heymsfield et al. (2009) showed that small droplets carried up by updrafts can significantly participate in the cold processes of the clouds, which are not addressed here. This study considers the first stage of the cumulus clouds just before the formation of ice particles. Regardless, Figure 5.2 evidences that all three chosen independent variables have specific roles in determining cloud DSDs characteristics. Together they explain most of the warm-phase properties.

Figure 5.3 – Same as Figure 5.2 but for flight AC19 only.

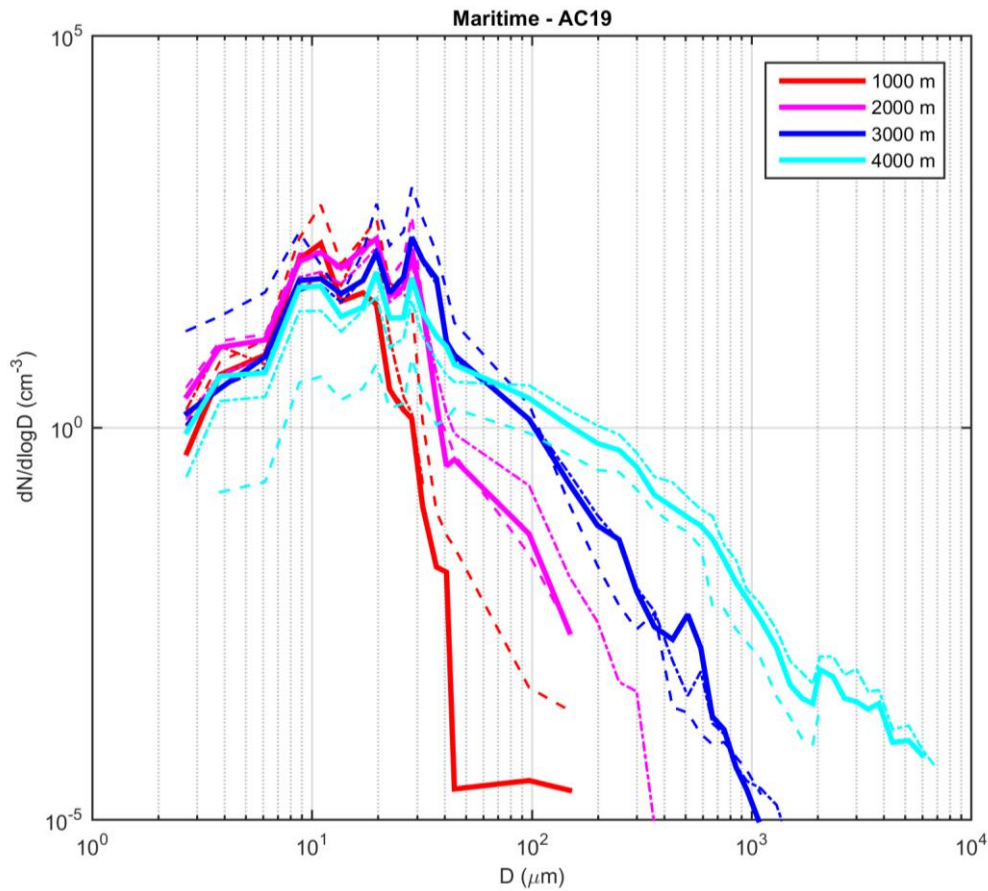


Figure 5.4 - Same as Figure 5.2 but for flights (a) AC9 and (b) AC18 only.

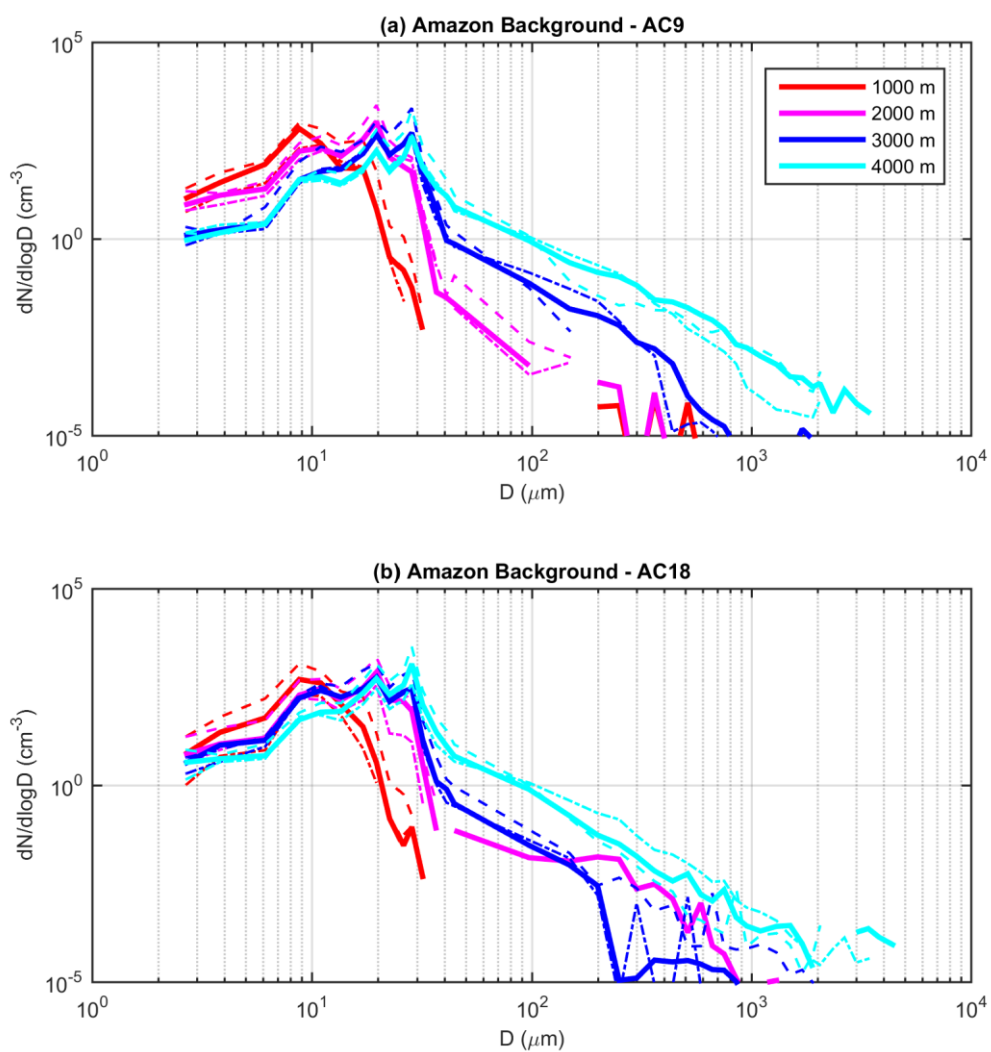


Figure 5.5 – Same as Figure 5.2 but for flights (a) AC7, (b) AC11, and (c) AC20 only.

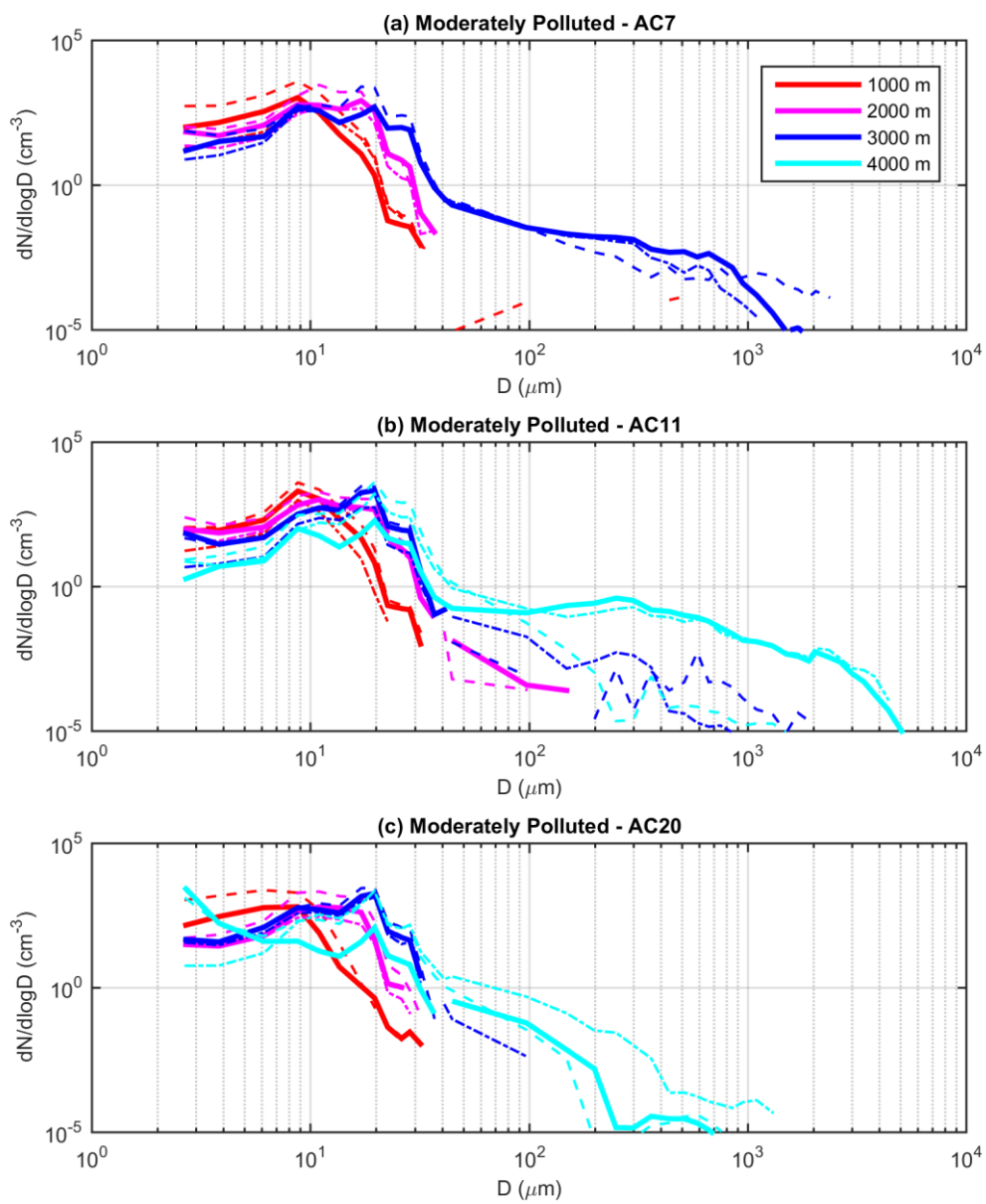
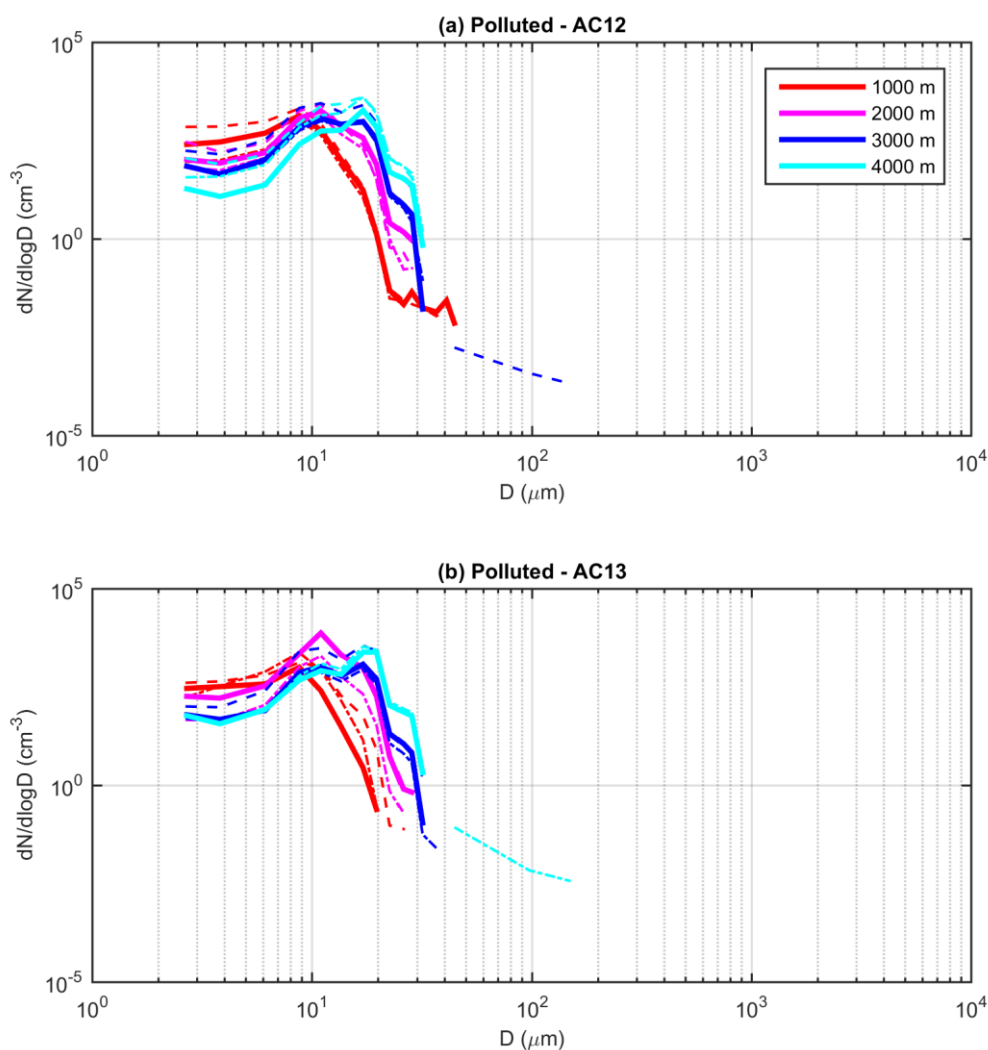


Figure 5.6 – Same as Figure 5.2 but for flights (a) AC12 and (b) AC13 only.



5.5. Comparing the main drivers of bulk microphysical properties of Amazonian clouds

For quantitative comparisons, it is interesting to consider bulk DSD properties such as N_d and D_{eff} instead of the whole DSD as in Figure 5.2. We will quantify the influence of N_{CN} , w , and H in these properties as a means to understand the effects on the overall DSD. This analysis will be complemented by the study of

the DSD shape in next section. By comparing the sensitivities of cloud droplet concentration and size to N_{CN} and w , it is possible to make a comparison that represents, at least partially, the contrasts between the importance of aerosols and thermodynamics on cloud characteristics. A significant portion of the previous work in this field was dedicated to understand the processes that lead to the observed N_d . Twomey (1959) provides theoretical considerations of N_{CN} and w effects on the supersaturation, which ultimately defines N_d for a given CCN spectra. More recent studies report on observations and modeling efforts to portray these processes in different regions of the world, calculating cloud sensitivities to both updraft speed and aerosol conditions. By analyzing aerosol and updraft conditions around the globe, Sullivan et al. (2016) note that w can be the primary driver of N_d in some regions. Reutter et al. (2009), using an adiabatic cloud model, argue that N_d sensitivities to aerosol concentrations and w can vary depending on their relative magnitudes. Adiabatic clouds are not highly sensitive to w (at cloud base) when N_{CCN} is low and vice-versa. Some studies also consider sensitivities in droplet size, such as Feingold (2003). However, cloud evolution is rarely put into perspective representing a limitation of previous studies. In the following, we will show our extended calculations of the sensitivities, where we consider the effects of aerosols, updraft speed, and H on N_d and D_{eff} .

Based on Equation 5.3.2, it is evident that there exist several values for each sensitivity. As an example, $S_{N_d}(N_{CN})$ has different values depending on the chosen pair of $\{w, H\}$. However, given the nature of in-situ measurements, individual $S_{N_d}(N_{CN})$ values are associated with reduced sample sizes and, therefore, compromise the statistical confidence. In this case, we present averaged values and the respective standard deviation for all $\{w, H\}$ pairs considered, applying the same calculation to the other sensitivities as well. The intervals chosen for N_{CN} , w , and H imply that those averages are representative of the lower ~ 4 km of the clouds, with updrafts up to 8 m s^{-1} and aerosol concentrations ranging from 500 to 4500 cm^{-3} .

The results of the N_d and D_{eff} averaged sensitivities (Table 5.2) reflect the patterns observed in Figure 5.2. The effective diameter shows strong association to the aerosol concentration and H while being almost independent of w . Specifically regarding N_{CN} , the sensitivities calculated represent the first step in the parameterization of the aerosol indirect effect for climate models, i.e., its relation to cloud microphysical properties. Multiple studies have focused on this issue from several observational setups such as satellite/surface remote sensing and in situ measurements. Pandithurai et al. (2012) provide a compilation of this type of calculation (see their Table 2), showing a high variability among the sources. According to Schmidt et al. (2015), the differences are due to not only the measurement setup but also to the region (ocean/land), the types of clouds, and differences in the methodologies. Remote sensing techniques often retrieve vertically integrated quantities at relatively rough horizontal resolution, which can smooth the results, meaning lower sensitivities. On the other hand, in-situ airborne measurements are closer to the process scale and may result in more accurate estimates of the aerosol effect (WERNER et al., 2014). However, the studies reviewed in Pandithurai et al. (2012) and Schmidt et al. (2015) are mostly for stratus or cumulus clouds over ocean. Additionally, measurements of w were either not available or were not differentiated in most of the previous analyzes, while the results are often integrated in altitude or limited to a specific cloud layer (e.g., cloud top in satellite retrievals). Our study focuses on tropical convection over the Amazon and takes into account both the updraft speed and altitude of the measurements.

The values of the sensitivities with regard to N_{CN} presented here are among the highest reported in literature. They are not far from the theoretical limit of $S_{N_d}(N_{CN}) = 1$ ($N_d \leq N_{CN}$) and $S_{D_{eff}}(N_{CN}) = -0.33$, which is quite common for in-situ airborne studies (WERNER et al., 2014). The limit for D_{eff} is an approximation and stems from the relation (if LWC is held constant) $D_{eff} \propto \left(\frac{LWC}{N_d}\right)^{1/3}$ (e.g. MARTIN et al., 1994). Given the precautions taken here to isolate the aerosol effects, these values show that Amazonian clouds are highly sensitive to

pollution. Human-emitted particles affect not only the DSDs close to cloud base but also over at least the lower 4 km of the warm-phase domain.

Table 5.2 - N_d and D_{eff} averaged sensitivities to N_{CN} , w , and H . Standard deviations are also shown. R^2 values are averages of the individual fits. The total variations for N_{CN} , w , and H are 500 cm^{-3} to 4500 cm^{-3} , 0 m s^{-1} to 8 m s^{-1} and 0 m to 4156 m , respectively. Intervals grows logarithmically (or close to) for w and H .

	$\overline{S_{N_d}}$	$\overline{S_{D_{eff}}}$
N_{CN}	0.84 ± 0.21	-0.25 ± 0.074
	$R^2 = 0.91$	$R^2 = 0.89$
w	0.43 ± 0.28	0.028 ± 0.058
	$R^2 = 0.81$	$R^2 = 0.46$
H	-0.13 ± 0.16	0.28 ± 0.058
	$R^2 = 0.38$	$R^2 = 0.93$

The sensitivities to the updraft speed have a distinct behavior when compared to the aerosol effect. Not only does it show lower values overall but it shows different behaviors for N_d and D_{eff} . It shows that even strong updrafts are not able to significantly increase the effective droplet size by enhancing condensation. In fact, this sensitivity oscillates around zero with slightly negative and positive values (see Table A.2) and with relatively low R^2 . This finding is similar to what Berg et al. (2011) observed in Oklahoma City. Close to cloud base, they found a significant relation between N_d and w , and a low correlation between D_{eff} and w . Here we show that this feature is not limited to cloud base but persists with altitude on average. Feingold et al. (2003), using an adiabatic cloud parcel model, found a negative value for $S_{D_{eff}}(w)$, with a higher absolute value for polluted clouds. The result could be explained by activation of smaller aerosol particles with increasing updraft speed, leading to higher concentrations of small droplets

that skewed the mean diameter to lower values. Although we observed slightly negative sensitivity for highly polluted clouds at their base (Table A.2), our measurements show that the overall averaged D_{eff} is nearly independent of w for the Amazonian clouds.

Freud et al. (2011) and Freud and Rosenfeld (2012) showed similar observations in the Amazon, India, California, and Israel. They provide theoretical formulations that support some of those observations. These authors showed that the vertical evolution of D_{eff} behaves almost adiabatically because of the predominance of inhomogeneous mixing in convective clouds. In this way, droplet effective size can be obtained from cloud base N_d , pressure, and temperature. In fact, this is the framework for a new technique developed to obtain CCN retrievals from satellites (ROSENFELD et al., 2016). Our study provides a new look at those observations and theoretical considerations by specifically quantifying, without any adiabatic assumption, each process with our formulation of sensitivity.

Comparisons of the sensitivities to w and N_{CN} can be used to infer the roles of the aerosols and thermodynamic conditions on the DSD characteristics. Not only do the aerosols primarily determine the size of the droplets but they also have the biggest impact on the number concentration, high variability in $S_{N_d}(w)$ notwithstanding. This result shows that in terms of the warm layer aerosols play a primary role in determining DSD characteristics.

The sensitivities to H are calculated in order to put the aerosol and updraft effects into perspective regarding cloud evolution. This calculation shows that, on average, droplet growth with cloud evolution is comparable in absolute value and opposite to the aerosol effect. For this reason, studies should take into account the altitude of the measurements. Polluted Amazonian clouds show slower droplet growth with altitude (CECCHINI et al., 2016) and $S_{D_{eff}}(H)$ may vary with N_{CN} . With lower $S_{D_{eff}}(H)$, $S_{D_{eff}}(N_{CN})$ possibly increase with altitude. The most important factor evident in Table 5.2 for D_{eff} is that it shows strong relations with

N_{CN} and H , while being independent of w . This result is of great value for parameterizations or other analyses of cloud droplet size.

Whereas D_{eff} shows a clear relation to N_{CN} and H , being relatively constant at fixed altitude, N_d displays a highly variable behavior. The averaged $S_{N_d}(H)$ has a slightly negative value with high standard deviation. There can be either droplet depletion or production with altitude, but the former prevails on average. New droplet activation should be expected in polluted clouds, where not all aerosols are activated at cloud base. In fact, Table A.6 shows that $S_{N_d}(H)$ is positive for the most polluted clouds probed when updraft speeds are $> 0.5 \text{ m s}^{-1}$, although R^2 values are quite low. Droplet depletion with altitude can be a result of evaporation and/or collection growth. Cecchini et al. (2016) showed that Amazonian background clouds present rather effective collision-coalescence growth, which would suggest a negative $S_{N_d}(H)$ for those clouds. This mechanism is difficult to observe in the present study, with relatively low R^2 in the individual $S_{N_d}(H)$ (Table A.6). Overall, the highly variable relation between N_d and H suggest that droplet concentration is not closely tied to altitude above cloud base, as it is the case for D_{eff} . On the other hand, droplet concentration has significant horizontal variation given different mixture and w conditions, while the effective diameter remains similar at constant altitude levels.

5.6. Effects on DSD shape and relation between sensitivities

The use of a parametric function to represent the DSDs can be of interest in order to understand the sensitivities in the overall shape of the DSDs. One function widely adopted in many applications and especially in models (KHAIN et al. 2015) is the Gamma function. One of the forms of the Gamma function represents the DSDs as in Equation 3.3.1. The advantage of using this function is that it can be analytically integrated, providing relatively simple equations for the DSD parameters. N_d , D_{eff} , and LWC can be calculated from the moments of the Gamma DSD (units are cm^{-3} , μm , and g m^{-3} , respectively):

$$N_d = M_0 \quad (5.6.1)$$

$$D_{eff} = \frac{M_3}{M_2} \quad (5.6.2)$$

$$LWC = 10^{-9} \rho_w \frac{\pi}{6} M_3 \quad (5.6.3)$$

Where ρ_w is the density of liquid water (considered as 1000 kg m⁻³ here) and M_p is the pth moment of the DSD, given by:

$$M_p = \int_0^{\infty} D^p N(D) dD = N_0 \frac{\Gamma(\mu+p+1)}{\Lambda^{\mu+p+1}} \quad (5.6.4)$$

By substituting Equation 5.6.4 into Equation 5.6.2 it is possible to write D_{eff} as a function of N_d and LWC :

$$D_{eff} = 10^9 \frac{6}{\pi \rho_w} \gamma \frac{LWC}{N_d} \quad (5.6.5)$$

Where γ is a parameter that depends on the DSD shape and droplet size. It can be written as a function of ε , defined as the ratio between the DSD standard deviation and its average, which is much more common in the literature (e.g. LIU; DAUM 2002; TAS et al. 2015):

$$\gamma = \frac{\Lambda^2}{(\mu+2)(\mu+1)} = \frac{\Lambda \varepsilon^2}{D_a} \quad (5.6.6)$$

D_a is the mean diameter resulting from the ratio between the 2nd and 1st order moments. By substituting Equation 5.6.6 into Equation 5.6.5, applying the natural logarithm and the partial derivative to $\ln X_i$ (as in Equation 5.3.1), it is possible to write:

$$\frac{\partial \ln N_d}{\partial \ln X_i} = \frac{\partial \ln \Lambda}{\partial \ln X_i} + 2 \frac{\partial \ln \varepsilon}{\partial \ln X_i} + \frac{\partial \ln LWC}{\partial \ln X_i} - 2 \frac{\partial \ln D_{eff}}{\partial \ln X_i} \quad (5.6.7)$$

which is an explicit representation of the relation between the sensitivities. Note that $\frac{\partial \ln D_{eff}}{\partial \ln X_i} = \frac{\partial \ln D_a}{\partial \ln X_i}$ because of the similarities in the equations of both diameters.

The first two terms in the right-hand side of Equation 5.6.7 represent the DSD shape, where Λ is related to the curvature of the Gamma curve and ε is the relative dispersion around the DSD mean geometric diameter. Lower (higher) Λ and higher (lower) ε are associated to broader (narrower) DSDs. Equation 5.6.7 shows that, in order to compare the sensitivities in N_d , D_{eff} , and LWC , the DSD shape has to be taken into account.

Several aspects of the aerosol-cloud-interaction physics can be illustrated by Equation 5.6.7. The Twomey effect states that clouds subject to high aerosol concentrations have enhanced albedo because of the more numerous droplets with increasing aerosol loading (Twomey,1974). This effect is defined when comparing clouds with the same LWC . Translating it into Equation 5.6.7 (with $X_i = N_{CN}$), it means the LWC derivative is neglected, which defines a relation between droplet concentration, effective diameter, and DSD shape. By comparing to the expression $\overline{S_{D_{eff}}(N_{CN})} = -\frac{1}{3}\overline{S_{N_d}(N_{CN})}$ often found in the literature, we can conclude that the sensitivity in N_d is offset by DSD shape alteration. In other words, two thirds of the N_d sensitivity is allocated into DSD narrowing or broadening, while the remainder is effectively altering D_{eff} .

The effects of enhanced aerosol concentrations on the DSD shape is of great interest to the climate change community, given that it contributes to the aerosol indirect effect. Liu and Daum (2002) report that pollution, besides lowering droplet size, tends to broaden the DSDs, which would result in weaker cooling forcing compared to previous calculations. They show that the previous estimations of the aerosol indirect effect considered a fixed ε , possibly overestimating the cooling forcing. Recently, Xie et al. (2017) reports improved model comparisons with satellites when better estimating the relative dispersion. Therefore, it is important to understand the relation between ε (and Λ) not only to aerosols, but also to updraft speed and height above cloud base. The overall averages presented in Table 5.3 show that the DSD curvature (Λ) is sensitive to N_{CN} and H , but the values are rather small for ε . This results from the not-so-simple relation

between DSD shape and N_{CN} , w and H . Figure 5.7 shows the variations of the sensitivities of Λ and ε with N_{CN} and H (no significant variations were found for w), where it is clear that the overall averages in Table 5.3 must be analyzed with caution for DSD shape. The ε sensitivities have significantly different behavior for clean and polluted clouds and also change sign along H . Both features result in a low overall average as presented in Table 5.3, but this does not mean that the ε sensitivity is negligible. Instead, a more detailed analysis should be considered.

Table 5.3 - Same as Table 5.2, but for the sensitivities in Λ , ε , and LWC .

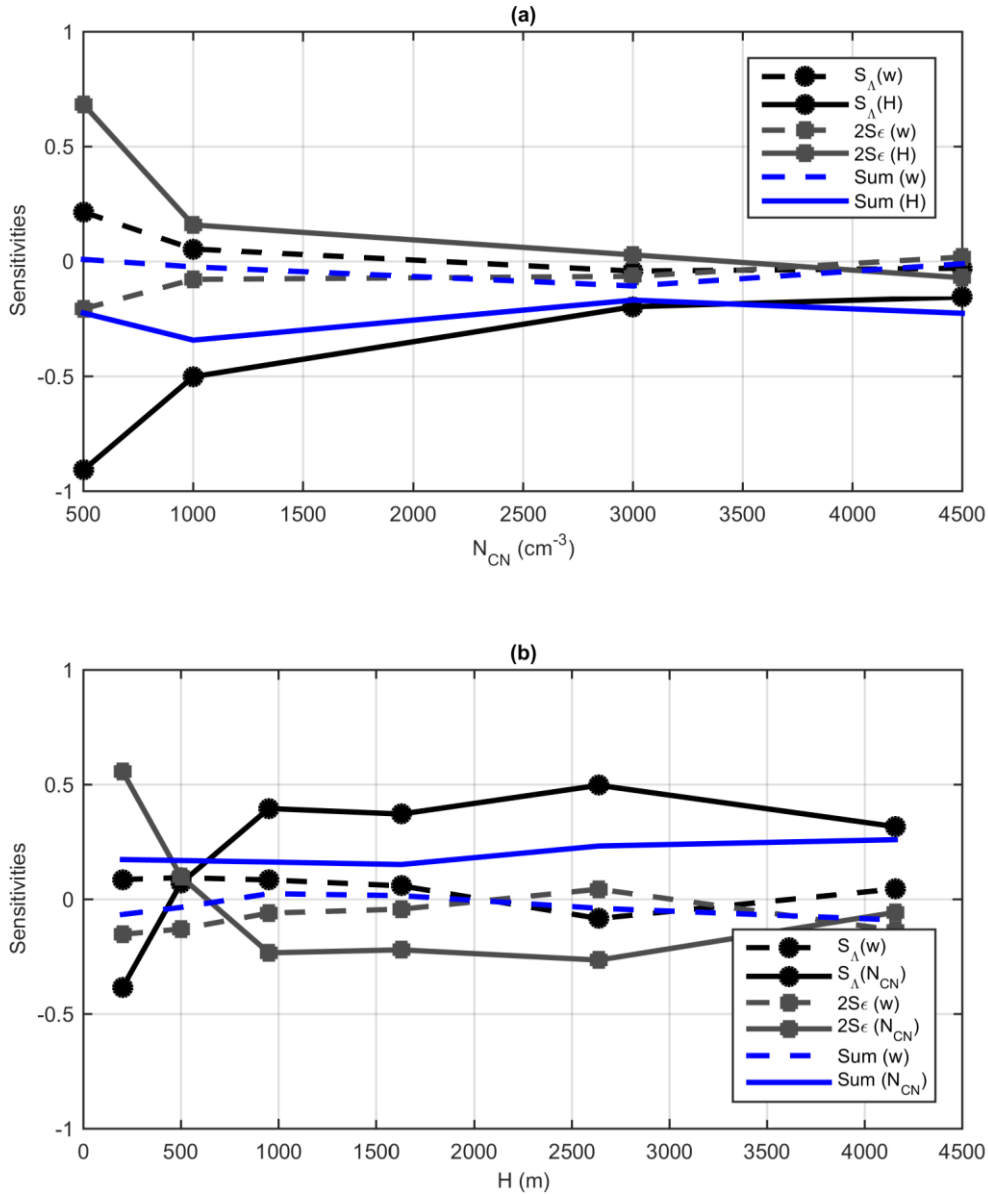
	$\overline{S_{\Lambda}}$	$\overline{S_{\varepsilon}}$	$\overline{S_{LWC}}$
N_{CN}	0.23 \pm 0.34	-0.015 \pm 0.16	0.078 \pm 0.34
	$R^2 = 0.64$	$R^2 = 0.54$	$R^2 = 0.34$
w	0.046 \pm 0.17	0.039 \pm 0.094	0.49 \pm 0.34
	$R^2 = 0.49$	$R^2 = 0.46$	$R^2 = 0.77$
H	-0.43 \pm 0.32	0.094 \pm 0.16	0.67 \pm 0.21
	$R^2 = 0.64$	$R^2 = 0.42$	$R^2 = 0.76$

The sensitivities in Λ and ε usually have opposite signs, given their relation to DSD shape – broader DSDs tend to have higher ε but lower Λ . Nevertheless, their relation with N_{CN} and H are conceptually similar and illustrate interesting processes. Figure 5.7a shows that the DSD shape variation with altitude is much more pronounced in cleaner clouds, which is a result of a strong collision-coalescence process. The higher the aerosol concentration, the lower is the sensitivity of ε to H . For the most polluted clouds measured by HALO, the relative dispersion parameter is almost insensible to H , meaning that it does not change much as the cloud grows. There is, however, still some effect on the DSD curvature, making the summation of the first two terms in the right-hand side of

Equation 5.6.7 non-negative in this case (see solid blue line in Figure 5.7a). For the sensitivities of Λ and ε to w , the same summation (dashed line in Figure 5.7a) is basically null, meaning that these two terms have no contribution in Equation 5.6.7. Nevertheless, stronger updrafts tend to produce narrower DSDs in the maritime clouds where the aerosol population is limited in terms of number concentration and particle type/chemistry.

The patterns along H of the DSD shape sensitivities (Figure 5.7b) pose an interesting question for the parameterization of the aerosol indirect effect in Amazonian clouds. There are significant changes in ε tendencies as the clouds evolve. Note that aerosols induce broader DSDs up to $H \sim 500$ m, but the opposite happens above that point. In fact, for our higher altitude bin ($2637 \text{ m} < H \leq 4156 \text{ m}$), the average ε is lowest for the most polluted clouds (= 0.28, while clouds over the forest and Atlantic Ocean show values of 0.32 and 0.42, respectively). In other words, the effect of broader DSDs under polluted conditions may not directly apply for convective clouds over the Amazon, where growth processes in the cloud can significantly change this pattern. This highlights the need to take cloud evolution into account and there is no direct relation between aerosols and cloud relative dispersion in the warm phase of Amazonian clouds. For satellite retrievals, where integrated quantities are of likely interest, the relative dispersion will depend not only on the aerosol concentration but also on cloud depth and lifecycle stage.

Figure 5.7 - Variations of the sensitivities of Λ and ε with (a) N_{CN} and (b) H . Note that the sensitivities of ε are multiplied by 2 in order to be consistent with Equation 5.6.7. The curves are averaged over all values of the third dependent variable. For instance, the curve $S_{\Lambda}(w)$ in a) is averaged over all H values. Blue curves represent the sum of the sensitivities of Λ and ε , equivalent to the first two terms in the right-hand side of Equation 5.6.7.



Regarding the sensitivities to w , Figure 5.7 and Tables 5.2 and 5.3 show that updraft speed has little impact on DSD shape or droplet size. The result in terms of Equation 5.6.7 is the equality between the sensitivities in N_d and LWC , which is generally the case when we compare the averages shown in Tables 5.2 and

5.3. In other words, the updraft effect is limited to increases in the droplet concentration and water content, modulating both N_d and LWC in the same proportion. Overall, the observations shown here should help understand which cloud properties are affected by aerosols, cloud evolution and thermodynamic conditions. The latter was found to be associated to bulk water contents in the clouds, while the overall shape of the DSDs are determined by the aerosol condition during cloud formation and the subsequent evolution.

5.7. Closing remarks

The ACRIDICON-CHUVA campaign and the capabilities of the HALO aircraft allowed, for the first time, analyzing the sensitivities of Amazon tropical convective clouds to aerosol number concentrations and updraft speed while also considering cloud evolution. The sensitivity formulation identified that aerosol number concentrations play a primary role in the formation of the warm phase of convective clouds, determining not only droplet concentration but also diameter and overall DSD shape. On the other hand, the thermodynamic conditions, as represented by the updraft intensity, affect primarily DSD bulk properties such as water content and droplet concentration. It was shown that the altitude above cloud base is critical when analyzing aerosol and updraft impacts on clouds, given that the DSD properties evolve with further processing in the system.

It was observed that an increase of 100% in aerosol concentration results in an 84% increase in droplet number concentration on average, while the same relative increase in updraft wind speed results in only 43% change. Regarding mean droplet size, we found it to be effectively independent of the updraft speed. Roughly, the effective droplet diameter decreases 25% when aerosol concentration doubles. The comparison between the aerosol and the thermodynamic effects shows that the aerosol concentration is the primary driver for DSD, whereas the updrafts mainly affect droplet number concentration and liquid water content. During cloud evolution, droplet number concentration is depleted while the diameter sensitivity to the growth processes is quantitatively

similar to the aerosol effect. Additionally, the aerosol effect on DSD shape inverts in sign with altitude, favoring broader droplet distributions close to cloud base but narrower higher in the clouds. This highlights the importance of differentiating the analysis by altitude above cloud base, which is an appropriate proxy for DSD lifetime for our measurements.

6 ILLUSTRATION OF MICROPHYSICAL PROCESSES OF AMAZONIAN DEEP CONVECTIVE CLOUDS IN THE GAMMA PHASE SPACE: INTRODUCTION AND POTENTIAL APPLICATIONS

This Chapter consists of the third paper written as part of this thesis. It is currently under review for ACP and can be found in the ACPD website at <http://www.atmos-chem-phys-discuss.net/acp-2017-185/>.

6.1. Background

Tropical deep convective clouds (DCCs) constitute an important source of precipitation (LIU, 2011), they interact with atmospheric solar and terrestrial radiation, dynamical processes and the hydrological cycle (ARAKAWA, 2004). Deep tropical convection is responsible for transporting energy upwards, and thus sustaining the Hadley circulation that redistributes heat to higher latitudes (RIEHL; MALKUS, 1958; RIEHL; SIMPSON, 1979; FIERRO et al., 2009, 2012). Therefore, understanding the processes that impact the characteristics of tropical DCCs is crucial in order to comprehend and model the Earth's climate.

DCCs over the Amazon are of particular interest. Given the homogeneity of the surface and the pristine air over undisturbed portions of the rainforest, Amazonian DCCs can have similar properties to maritime systems (ANDREAE et al., 2004). At the same time, their daily persistence and the considerable latent heat release have a noticeable impact on the South America climate by, for instance, maintaining the Bolivian High, which is a key component of the South America monsoon system (ZHOU; LAU, 1998; VERA et al., 2006).

Clouds and aerosol particles interact in a unique way in the Amazon. Low concentrations of natural aerosols derived from the forest are the major source of natural cloud condensation nuclei (CCN) and ice nuclei (IN) population under undisturbed conditions (PÖSCHL et al., 2010; PRENNI et al., 2009). Other sources of aerosol particles over the Amazon include long range Saharan dust and sea salt transport, biomass burning (either naturally-occurring or human-

induced) and urban pollution downwind from cities and settlements (CECCHINI et al., 2016; MARTIN et al., 2010).

Human-emitted pollution can significantly alter cloud properties by enhancing CCN number concentrations (N_{CCN}). Since the work of Twomey (1974), analyzing the effects of enhanced N_{CCN} on cloud albedo, large attention has been given to aerosol-cloud-precipitation interactions. The effects of aerosol particles on warm-phase precipitation formation is fairly well understood, where enhanced N_{CCN} leads to the formation of more numerous but smaller droplets delaying the onset of rain (ALBRECHT, 1989; SEIFERT; BEHENG, 2006; VAN DEN HEEVER et al., 2006; ROSENFELD et al., 2008). However, in mixed-phase clouds, the drizzle suppression by pollution can enhance ice formation leading to stronger updrafts and convective invigoration (ANDREAE et al., 2004; KHAIN et al., 2005; VAN DEN HEEVER et al., 2006; FAN et al., 2007; VAN DEN HEEVER; COTTON, 2007; LEE et al., 2008; ROSENFELD et al., 2008; KOREN et al., 2010; LI et al., 2012; GONÇALVES et al., 2015). Aerosol effects on clouds are reviewed by Tao et al. (2012), Rosenfeld et al. (2014) and Fan et al. (2016). By changing cloud properties, aerosol particles have an indirect impact in the thermodynamics of local cloud fields through, for instance, the suppression of cold pools and the enhancement of atmospheric instability (HEIBLUM et al., 2016b).

Clouds that develop above the freezing level are harder to model given the complexity of the processes involving ice particles. One aspect of the aerosol effects on clouds is their ability to alter the way in which ice is formed in the mixed-phase of convective clouds. Contact freezing is possibly the dominant process by which the first ice is formed (COOPER, 1974; YOUNG, 1974; LAMB et al., 1981; HOBBS; RANGNO, 1985). As pointed out by Lohmann and Hoose (2009), anthropogenic aerosol particles can either enhance or hinder cloud glaciation due to black carbon emission (increasing IN concentrations) and aerosol particle coating (decreasing IN effectiveness), respectively. After the initial ice formation, secondary ice generation can be triggered by the release of ice splinters from freezing droplets (HALLET; MOSSOP, 1974; HUANG et al., 2008; SUN et al.,

2012; LAWSON et al., 2015). Rather big (larger than 23 μm) cloud and drizzle droplets favor secondary ice generation (MOSSOP, 1978; SAUNDERS; HOSSEINI, 2001; HEYMSFIELD; WILLIS, 2014). Consequently, the smaller droplets found in polluted Amazonian clouds (ANDREAE et al., 2004; CECCHINI et al., 2016; WENDISCH et al., 2016) may slow down secondary ice generation.

In order to model aerosol effects on clouds and the thermodynamic feedback processes involved, it is crucial to understand their effects on hydrometeor size distributions. The first step is the study of aerosol impacts on liquid droplet size distributions (DSDs) in the cloud's warm-phase. Operational models that require fast computations usually adopt a Gamma curve (ULBRICH, 1983) to parameterize the DSDs (Equation 3.3.1). However, even though this function is widely adopted in models (KHAIN et al., 2015), there is almost no study regarding its phase space for checking DSD predictions between parameterization schemes.

The phase space of cloud micro- and macro-physical properties has received recent attention because of the considerable gain of information accessible by relatively simple analysis tools. Heiblum et al. (2016a, b) studied cumulus fields in a two-dimensional (2D) phase-space consisting of cloud center of gravity versus water mass. The authors were able to evaluate several processes in this sub-space, including the aerosol effect. McFarquhar et al. (2015) studied the Gamma phase space for improving ice particle size distributions (PSD) fitting and parameterization. They showed that the inherent uncertainty of Gamma fittings result in multiple solutions for a single ice PSD, corresponding to ellipsoids rather than points in the phase-space. However, there is no study regarding the representation of warm-phase cloud DSDs in the Gamma phase-space and its evolution.

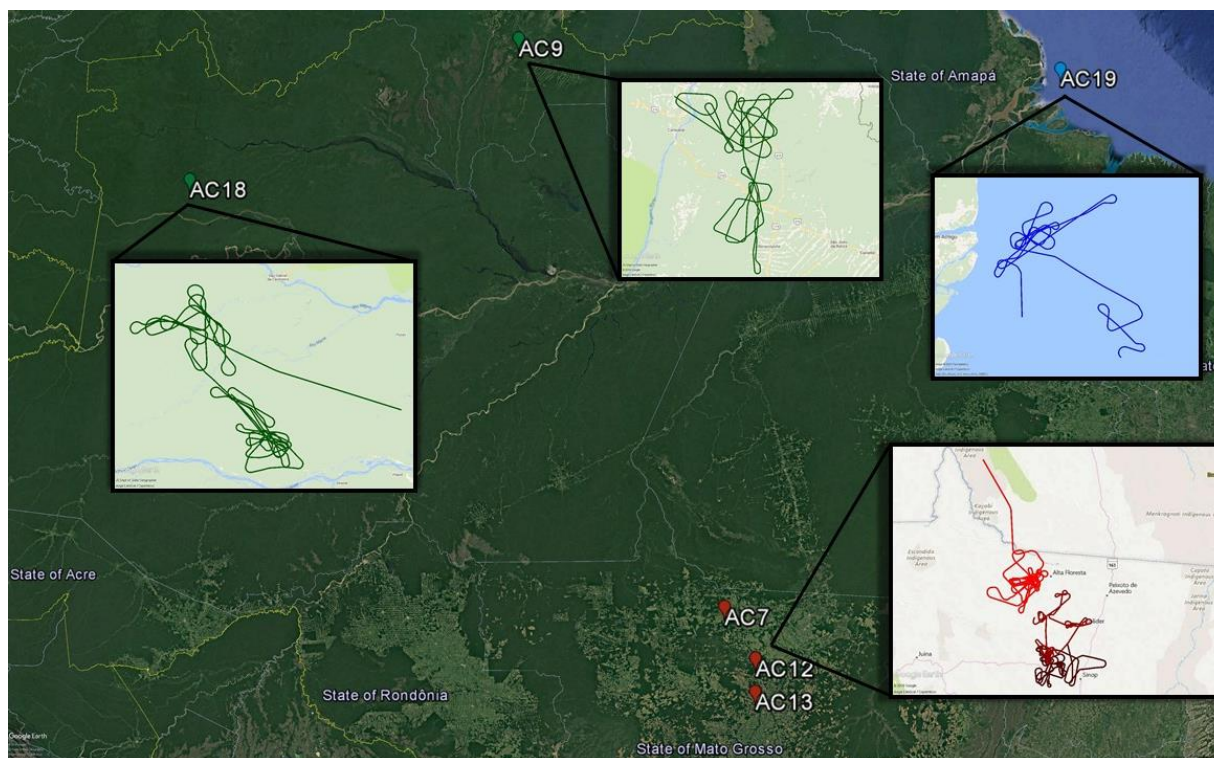
For the representation of hydrometeor size distributions in two-moment bulk schemes, one of the three Gamma parameters is either fixed or diagnosed based on thermodynamic or DSD properties (THOMPSON et al., 2004; MILBRANDT;

YAU, 2005; FORMENTON et al., 2013a, 2013b). This process may produce artificial trajectories in the phase space when comparing Gamma fittings to observations. This study herein analyzes cloud DSD data collected during the ACRIDICON-CHUVA campaign (WENDISCH et al., 2016) in the Gamma phase space. The Gamma phase space and its potential use for understanding cloud processes is introduced and explored. A specific focus is on the aerosol effect on the trajectories in the warm-layer phase-space and potential consequences for the mixed-phase formation.

6.2. Flight characterization

During September-October 2014, the German HALO (High Altitude and Long Range Research Aircraft) performed a total of 96 h of research flights over the Amazon. The 14 flights were part of the ACRIDICON-CHUVA campaign (MACHADO et al., 2014; WENDISCH et al., 2016) that took place during the second intensive operation period (IOP2) of the GoAmazon2014/5 experiment (MARTIN et al., 2016). Here we focus on cloud profiling sections during six flights that occurred in different regions in the Amazon (Figure 6.1). The research flights of the ACRIDICON-CHUVA were named chronologically from AC7 to AC20; the six flight missions focusing on the profiling of cloud microphysical properties (AC7, AC9, AC12, AC13, AC18 and AC19) accumulated 16.8 h of data (in or out of clouds), of which 50 min were inside the lower 6 km of the clouds. We concentrate on these flights for the DSD analysis in order to capture both warm-phase characteristics and early mixed-layer formation. The time-frame of the campaign corresponds to the local dry-to-wet season transition, when biomass burning is active in the southern Amazon (ARTAXO et al., 2002; ANDREAE et al., 2015).

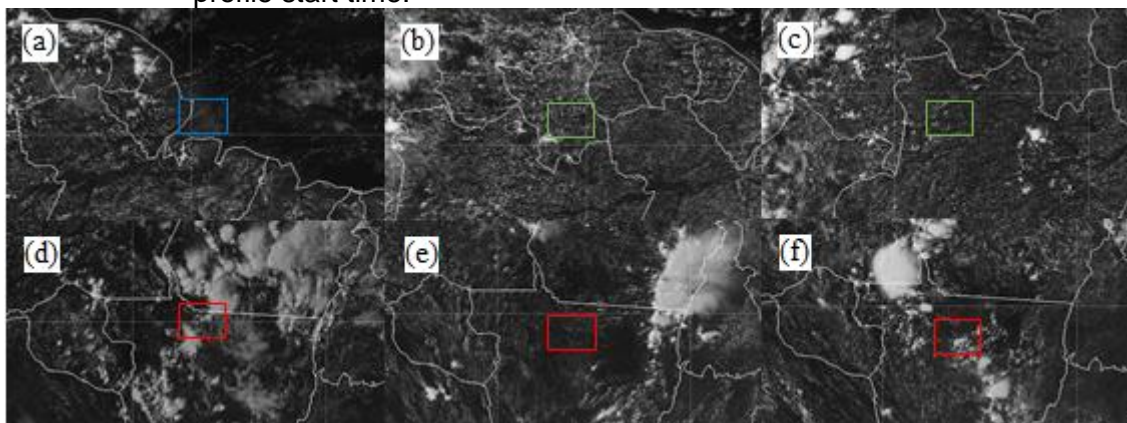
Figure 6.1 - Profile locations and trajectories of interest to this study. ACRIDICON-CHUVA research flights were labeled chronologically from AC7 to AC20. The labels in the figure reflect the respective flights where the cloud profiling section took place. The colors represent the different regions: green for remote Amazon, blue for near the Atlantic coast and red for Arc of Deforestation (different shades for clarity).



The flight paths followed a regular three-stage pattern: (i) Sampling of the air below clouds for aerosol characterization, (ii) Measurements of DSDs at cloud base, and (iii) Sampling of growing convective cloud tops (BRAGA et al., 2016; WENDISCH et al., 2016). Surface and thermodynamic conditions were different for the various flights (see Figure 6.1 and 6.4) with high contrasts in the north-south direction. Logging, agriculture and livestock activities management involve burning extended vegetated areas in the region, which emit large quantities of particles that serve as CCN in the atmosphere (ARTAXO et al., 2002; ROBERTS et al., 2003). Because of this, this region is known as the “Arc of Deforestation,” and its thermodynamic properties tend toward pasture-like characteristics. The energy partitioning over pasture-like areas is different compared to regions over

the rainforest (FISCH et al., 2004), favoring sensible heat and higher cloud base heights (see Table 6.1).

Figure 6.2 - GOES-13 visible images for flights (a) AC19, (b) AC9, (c) AC18, (d) AC7, (e) AC12, and (f) AC13. Images are approximately one hour after the profile start time.



The cloud profiling missions were mostly characterized by cumulus fields, with some developed convection in two flights over the Arc of Deforestation (Figure 6.2d, f). For flight AC7 some precipitation-sized droplets were observed (not shown); the clouds sampled during AC12 and AC13 presented almost no droplets having $D > 100 \mu\text{m}$. The precipitation during AC7 might be explained by the lower aerosol particle number concentrations compared to flights AC12 and AC13, later start of the profile and the presence of deep convection nearby (Table 6.1 and Figure 6.2).

The results to be presented in this chapter are based on the five HALO sensors described in Section 3.2.2. For the DSD measurements, we applied Gamma fits as explained in Section 3.3.

Table 6.1 - General characteristics of the cloud profiling missions of interest to this study: condensation nuclei (N_{CN}) and CCN concentrations (N_{CCN} , with $S = 0.48\% \pm 0.03\%$), cloud base and 0 °C isotherm altitude (H_{base} and $H_{0^\circ C}$, respectively), start and end time and total number of DSDs collected. The data are limited to the lower 6 km of the clouds. Profile start and end are given in local time. Cloud base altitude is calculated as the lower measurement where LWC is higher than 0.01 g m^{-3} .

Region	Flight	N_{CN} (cm^{-3})	N_{CCN} (cm^{-3})	H_{base} (m)	$H_{0^\circ C}$ (m)	Start	End	# DSDs
Atlantic Coast	AC19	465	119	550	4651	13:17	14:57	630
Remote	AC9	821	372	1125	4823	11:30	14:21	665
Amazon	AC18	744	408	1650	4757	12:32	14:14	397
Arc of Deforestation	AC7	2498	1579	1850	4848	13:49	17:16	674
	AC12	3057	2017	2140	4938	12:55	15:16	381
	AC13	4093	2263	2135	4865	12:46	15:36	204

6.3. Introducing the Gamma phase space

The fitted to Gamma parameters can be plotted in a 3D subspace where each parameter (N_0 , μ and Λ) represents one dimension. Each point in this 3D Gamma phase space is defined by one (N_0 , μ and Λ) triplet and thus represents one fitted DSD. This space includes all possible combinations of Gamma parameters of the theoretical variability of the DSDs.

The 3D Gamma phase space is illustrated in Figure 6.3. There are two points in this figure defined by two location vectors \vec{P}_1 and \vec{P}_2 , each one representing a fit to a specific DSD (see the insert in the left side of Figure 6.3) at different times (t_1 and t_2 for $t_2 > t_1$). If we consider that \vec{P}_1 and \vec{P}_2 represent the same population of droplets evolving in the time (i.e. a Lagrangian case), we can link the two points by a displacement vector $\vec{P} = \vec{P}_2 - \vec{P}_1$, which can be associated to a pseudo-force

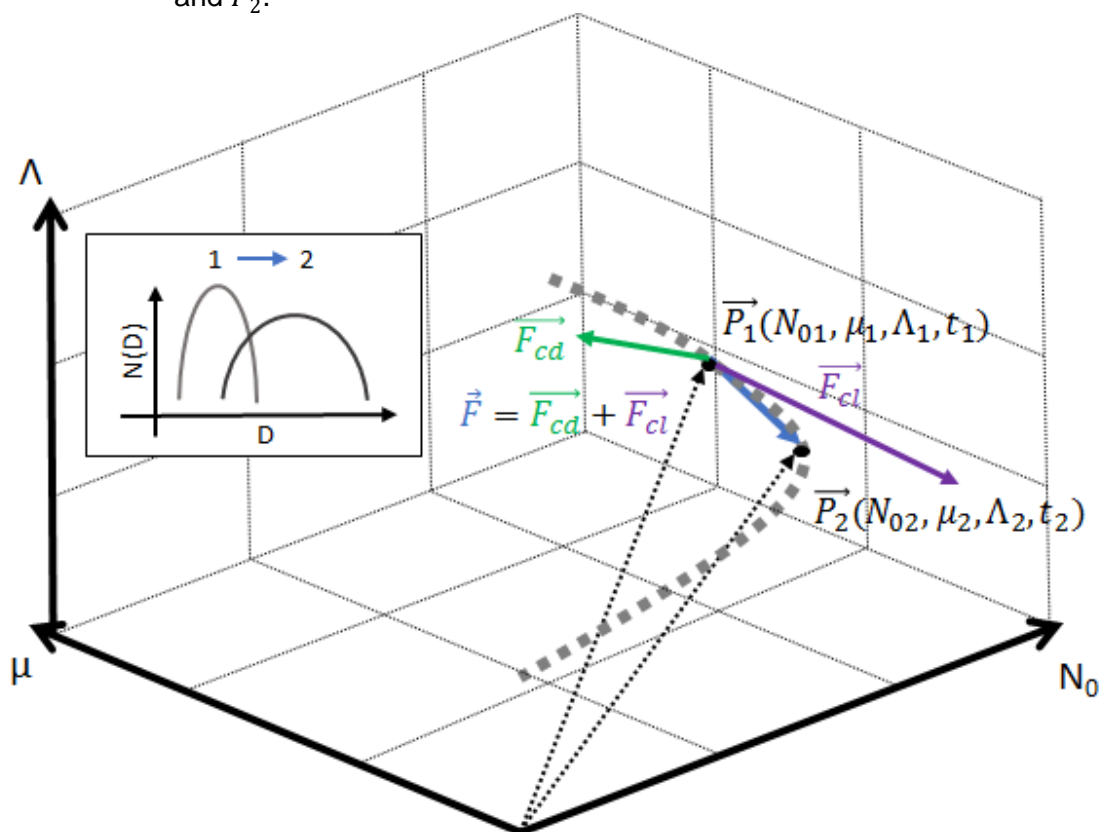
\vec{F} (blue arrow in Figure 6.3). We use the term pseudo-force in order to illustrate that the growth processes produce displacements in the phase space. Alternatively, displacements in the phase space can also be understood as phase transitions, in which case each phase is related to a DSD. The pseudo-force \vec{F} can be decomposed into two components, one related to condensational growth and the other to the collision-coalescence (collection) process. The respective pseudo-forces are illustrated as \vec{F}_{cd} and \vec{F}_{cl} in Figure 6.3, respectively. This approach can be applied to multiple points, defining a trajectory through the phase space (gray dotted line). The change of the DSD results in modified Gamma parameters, which determine the trajectory through the Gamma phase space. The direction and speed of the displacements forming the trajectory are determined by the direction and intensity of the underlying physical processes that modify the DSD (condensation and collection). Those pseudo-forces are defined by properties such as the initial DSD, N_{CCM} , updraft speed and supersaturation. Of course, this generalization considers only condensation and collision-coalescence. The pseudo-forces can be represented with more sophistication in models, including the several processes involved in the DSD changes such as evaporation, turbulence, melting from the layer above, breakup, sedimentation, etc. Therefore, these two processes can be replaced by a number of pseudo-forces as function of the level of sophistication of the model. We should remember that this approach does not consider contributions from other levels because advection is not directly addressed. To describe the whole process of DSD evolution during all cloud life cycle the contribution from other layers should be considered.

The direction of the \vec{F}_{cd} pseudo-force in Figure 6.3 represents the transition of the DSD during the condensation process, which favors high values of μ while slightly increasing Λ . This induces both the narrowing and a slight increase in the effective droplet diameter (see equations in Section 3.3) of the DSD, which is expected from conventional condensation growth theory. Because of the DSD narrowing, the intercept parameter (N_0) is also reduced. Condensational growth

may cause a broadening of the DSD in specific situations such as at the cloud base of polluted systems. However, this is an exception and most of the time condensational growth leads to DSD narrowing. The collision-coalescence pseudo-force acts in a significantly different way in the phase-space. From theory and precise numerical simulations that solve the stochastic collection equation, it is known that this process leads to DSD broadening (given the collection of small droplets and breakup of bigger ones) and faster droplet growth in size (compared to condensation). In the Gamma phase space, it should reflect in lower values of Λ and μ , the former decreasing at a faster pace. The intercept parameter N_0 should remain relatively constant, given that the effects of increased mean diameter and DSD broadening balance each other. With N_0 almost constant, lower values of Λ and μ result in reduced droplet number concentration, which is consistent with theory (see Figure 6.9).

In Section 6.5 we show Gamma parameters fitted to real DSD observations. It is not feasible to follow certain populations of droplets in a Lagrangian way with an aircraft. Therefore, the evolutions we analyze in the Gamma space are not strictly over time. As a compromise, we use the altitude above cloud base (H) of the measurements instead of time evolution, given the conditions of the measurements and our data handling. The cloud profiling missions were planned to capture growing convective elements before reaching their mature state, which is the reason why they usually started at around 12:00 local time. Additionally, we only consider DSD measurements where updraft speed $w > 0$ in order to focus on the ascending part of the growing clouds.

Figure 6.3 - Conceptual drawing of the properties of the Gamma phase-space in the warm-layer of the clouds. The dotted gray line represents one trajectory through the phase-space, representing the DSD evolution. \vec{P}_1 is one DSD that grows by condensation and collision-coalescence to reach \vec{P}_2 . The displacement represented by the pseudo-force \vec{F} is decomposed into two components - \vec{F}_{cd} (condensational pseudo-force) and \vec{F}_{cl} (collisional pseudo-force). Also shown are the two DSDs representative of points \vec{P}_1 and \vec{P}_2 .



6.4. Aerosol and thermodynamic conditions in different Amazonian regions

The HALO flights are classified according to the region they covered and the respective aerosol and CCN number concentrations (Table 6.1). Note the close link between region of the measurements and the aerosol concentrations. From the most pristine clouds in the coast to the most polluted cases in the Arc of Deforestation, there is a ten-fold increase in N_{CN} . Remote regions in the Amazon have aerosol particle concentrations slightly higher than over the coast, which is one of the reasons for the denomination “Green Ocean” (MARTIN et al., 2016).

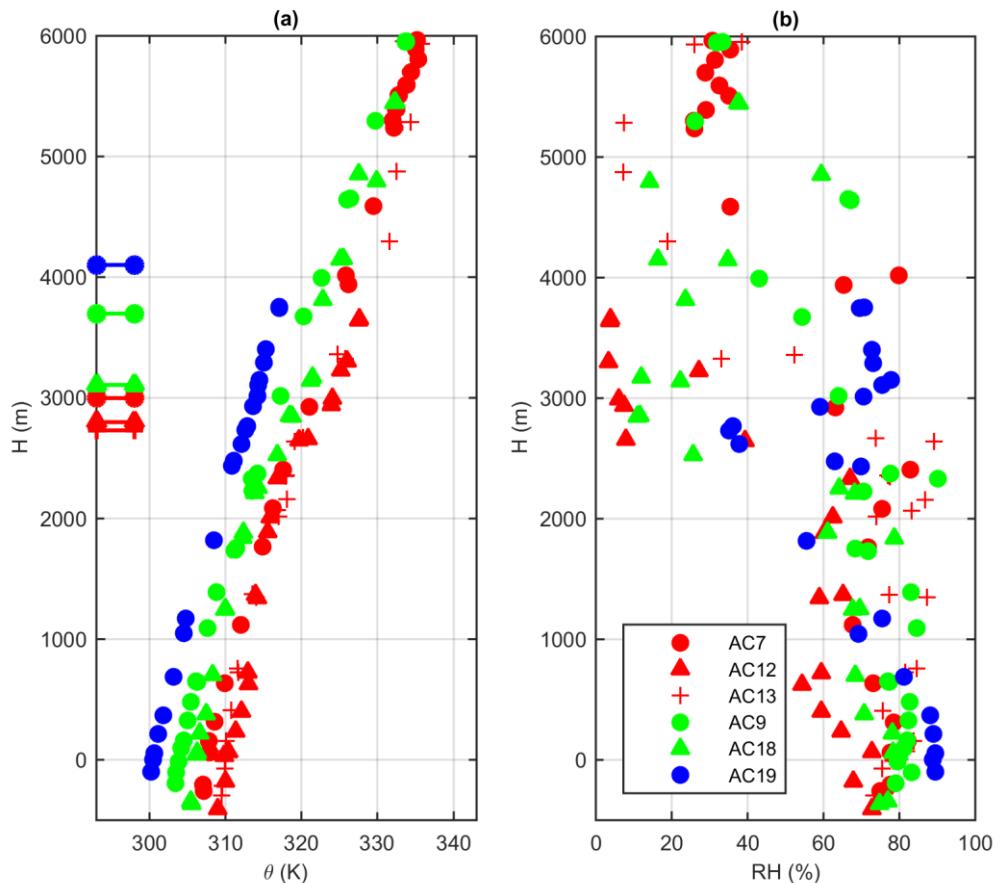
Flights AC7, AC12 and AC13 present flight patterns progressively shifted to the south, which are accompanied by increasing values of N_{CN} and N_{CCN} . The farther away the flights take place from the forest, and consequently closer to urbanized regions, the higher are the pollution levels.

Cloud profiles started late in the morning or at early afternoon. The flights were specifically planned for this time period because the convective systems are usually in their developing stages at this time. The freezing level varied between 4500 and 5000 m, while cloud base altitudes were more variable (500 to 2000 m), which resulted from the regional meteorological conditions (Figure 6.4), and which affects the characteristics of the cloud layers. Clouds in the Arc of Deforestation are subject to drier air, given the diminished evapotranspiration rate, and form higher in the atmosphere. As a result, there are thinner warm layers in the polluted clouds that limit the time available for droplets to grow by collision-coalescence. Flight AC18 was characterized by a just slightly higher depth of the warm layer compared to the polluted clouds, partly due to the lower altitude of the freezing level. Nevertheless, cleaner clouds can present warm layers 1000 m thicker than clouds affected by human pollution.

The vertical profile of the relative humidity (RH) should also be taken into account when comparing clouds formed over different regions. Figure 6.4b shows that all clouds measured formed in an environment with RH between 60 % and 90 % for their lower 2500 m layer, being higher for forested areas compared to the Arc of Deforestation. For 2500 m and above, there was a significant drying of the atmosphere for the flights AC19, AC18 and AC12. It is unsure if the other flights presented similar behavior given the relatively low data coverage for this layer. Regardless, surrounding dry air can significantly enhance the entrainment mixing process (KOROLEV et al., 2016). As pointed out by Freud et al. (2008), the mixing in Amazonian convective clouds (and also in other regions – FREUD et al., 2011) tends toward the extreme inhomogeneous mixing case, where the effective droplet diameter D_{eff} presents almost no sensitivity to the entrainment. Our result largely corroborates this finding (see Figure 6.11). It should be pointed

out, however, that the recent studies of Korolev et al. (2016), Pinsky et al. (2016a) and Pinsky et al. (2016b) show that homogeneous and inhomogeneous mixing can be indistinguishable depending on meteorological conditions and DSD characteristics when considering the time-dependent characteristics of the entrainment process. Mixing processes may have an impact in the shape of the DSDs measured, thus affecting displacements in the Gamma phase space. The specific type of mixing responsible for it, however, is beyond the scope of this work.

Figure 6.4 - Average vertical profiles of (a) potential temperature and (b) relative humidity for flights over the Atlantic coast, remote Amazon and Arc of Deforestation. The markers in the left vertical axis in (a) represent the altitude of the 0 °C isotherm for the different flights. Altitudes are relative to cloud base (H , negative values are below clouds). θ and RH are calculated as averages of level flight legs outside clouds.



6.5. Observed trajectories in the Gamma phase space

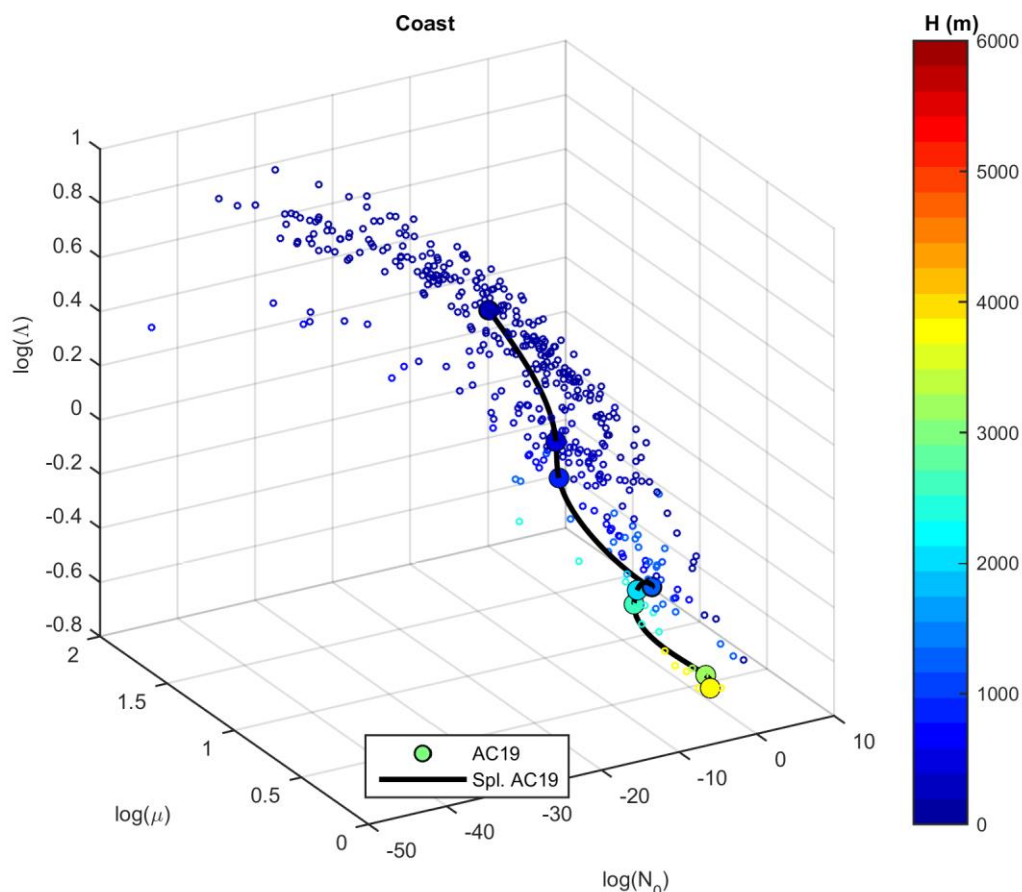
In this study, we use the Gamma phase space as a means to study DSD variability. As described in Section 6.3, this space is obtained when the DSD measurements are fitted to Equation 3.3.1 and N_0 , μ and Λ are used as the dimensions of the 3D subspace. In this space, each point represents one DSD. As the different DSDs were obtained close to the cloud top at the time of the cloud development, the ensemble of position in the Gamma phase-space can be hypothesized as the evolution of the DSDs of a typical cloud through stages of its life cycle. The sequential connection of points (here we use cubic spline fits for illustrating purposes) can be considered as trajectories describing multiple processes responsible for the DSD variability observed. The advantage of using this space is that this variability can be readily observed and compared between different cloud life cycles with different properties. Given the relations between Gamma parameters and DSD properties (Section 3.3), the variability of all cloud microphysical properties can also be inferred from the points in the trajectories. The analysis regarding cloud DSDs and the Gamma phase-space is limited to the regions in which $w > 0$ in order to capture the developing parts of the growing convective elements.

Figures 6.5 to 6.7 show the Gamma phase-space for all profiles considered in this study, grouped by region. The coloring represents the altitude above cloud base (H), with the 1 Hz measurements in small markers. Bigger markers represent averages at every 200-m vertical interval with information available. Curves (or trajectories) represent cubic spline fits to the averaged points. At first glance, it is possible to see significant overall differences between the trajectories in the different regions, while internal variations are much weaker. Aerosol concentrations seem to be a key factor controlling warm-phase properties in the Amazon, so the internal similarities can be attributed to similar pollution conditions. On the other hand, differences between the regions stem from the different weights of growth processes. Pristine clouds, like the ones found over the remote Amazon and the coast of the Atlantic Ocean, are characterized by

faster droplet growth with altitude associated with enhanced collisional growth. In the Gamma space, this is seen as diagonally-tilted trajectories in Figures 6.5 and 6.6, contrasting with the more vertical trajectories found in polluted clouds (Figure 6.7).

The differences of the DSD variability in each region highlight the relation of growth processes and trajectories in the Gamma phase-space. From the theory described in Section 6.3, it is expected that collisional growth results in diagonal trajectories where the droplets get progressively bigger with DSD broadening. Pristine clouds over the coast and remote Amazon show such tilting (Figures 6.5-6), indicating that this process is effective in those systems. The more vertically-oriented trajectories of polluted clouds (Figure 6.7) show that there is a different balance between condensational and collisional growth. In terms of the Gamma phase-space characteristics, this can be understood as weaker $\overrightarrow{F_{cl}}$ that is a result of smaller droplets and narrower DSDs. This highlights that the interaction between aerosols and collisional growth occurs mainly through changes in the initial DSD (i.e. $\overrightarrow{P_1}$ in Figure 6.3). For each point in the Gamma phase space the collisional pseudo-forces have different intensities and directions, suggesting that a vector field can be constructed. This could only be achieved by idealized model experiments, however, where the updraft speeds can also be prescribed.

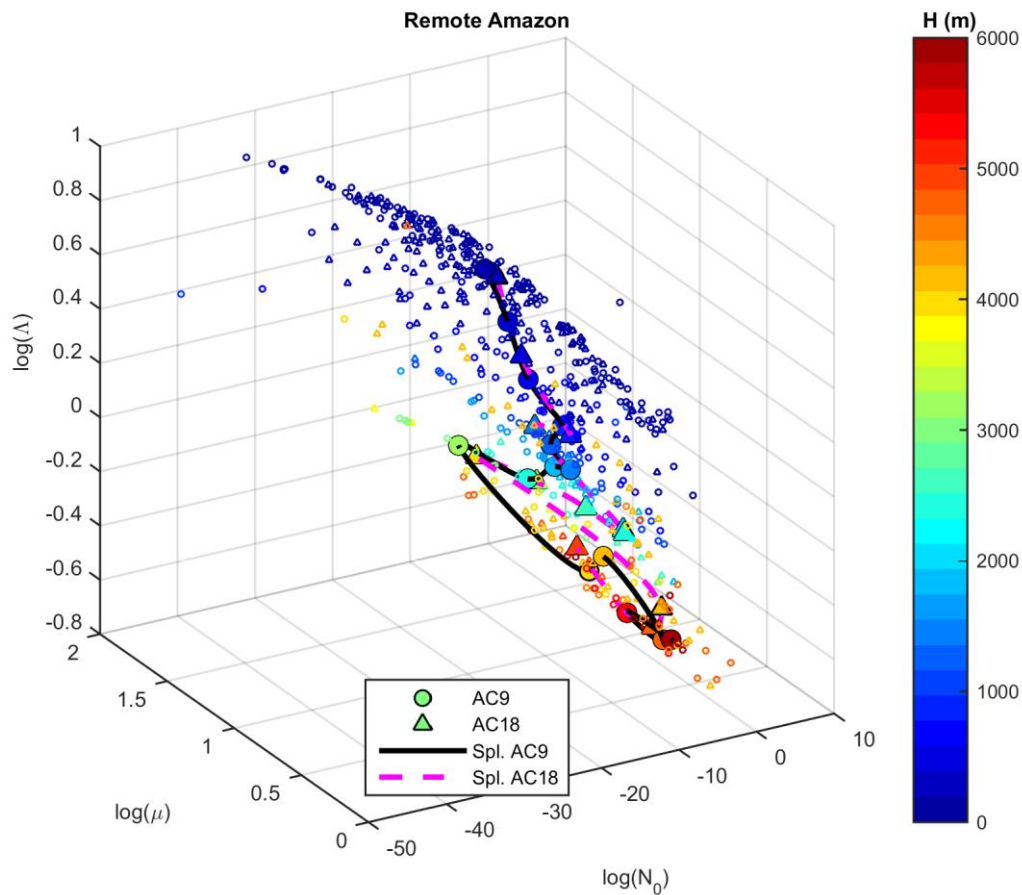
Figure 6.5 - Gamma phase space for flight AC19 over the coastal region. Small markers represent 1 Hz data, while bigger ones are averages for 200 m vertical intervals. The continuous black line represents a cubic spline fit for the averaged DSDs to illustrate its mean evolution. Altitudes are relative to cloud base (H).



Condensational growth can also be illustrated by some points in Figures 6.6 and 6.7. Under polluted conditions, this type of growth is expected to be dominant close to cloud base where the droplets are too small to trigger collision-coalescence. In Figure 6.7, this is seen in the first two or three points in the trajectories (dark blue colors), where the points evolve to higher μ values with altitude. This results in DSD narrowing and almost opposite displacement in the Gamma space compared to collisional growth. This trend is shifted when the altitude where collection processes start to become relevant is reached. Another example of condensational growth can be seen in Figure 6.6 at 3000 m. At this point, which is close to the freezing level, there is a sudden increase in the

updrafts (see Tables 6.2-3) and consequently increased condensation rates. The rapid increase in condensational growth, with no significant changes in collision-coalescence, tilts the trajectories to a direction similar to the observed close to cloud base in polluted systems. The displacement is closer to the horizontal direction (i.e. the plane $N_0 \times \mu$), because droplets are growing concomitantly by collision-coalescence in the cleaner clouds.

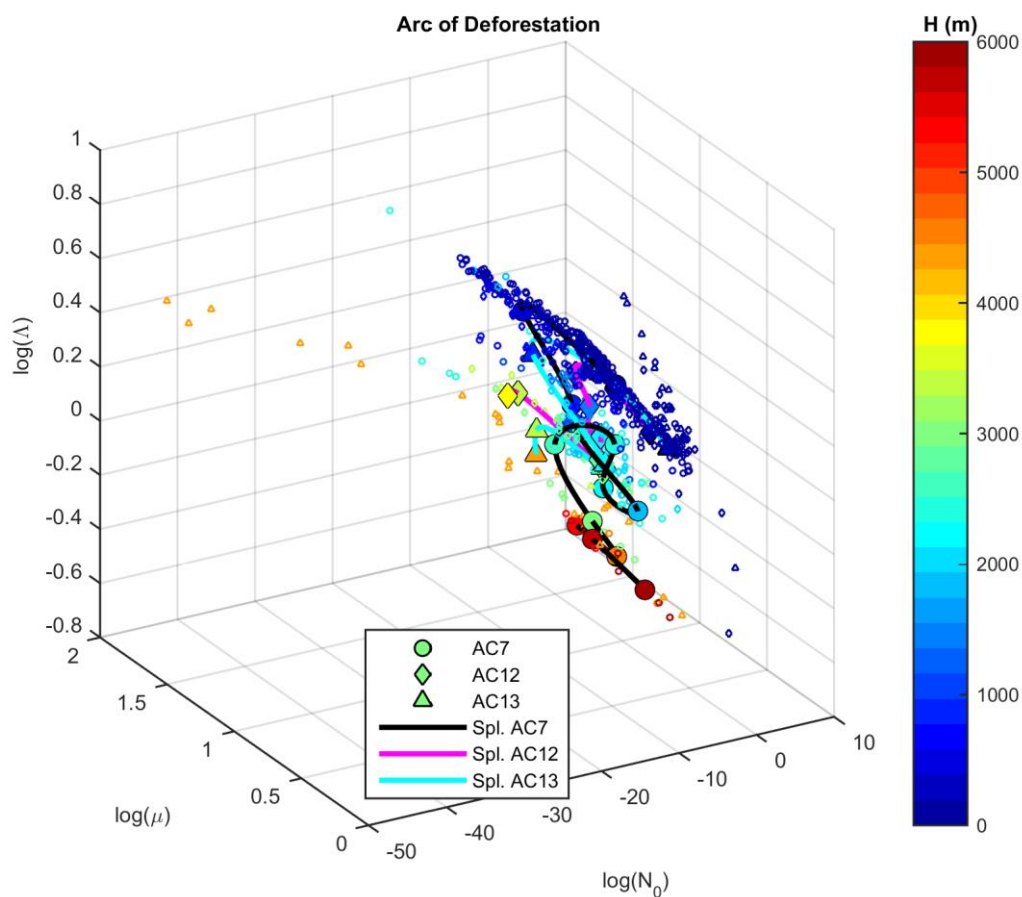
Figure 6.6 - Similar to Figure 6.5, but for flights AC9 and AC18 over the remote Amazon.



The magnitude of the condensational pseudo-force ($\overrightarrow{F_{cd}}$ in Figure 6.3) also depends on initial DSD characteristics ($\overrightarrow{P_1}$). Condensational growth rates are inversely proportional to droplet size, meaning that it gets weaker higher in the cloud. The different dependences of $\overrightarrow{F_{cd}}$ and $\overrightarrow{F_{cl}}$ on $\overrightarrow{P_1}$ and their balance throughout the warm-phase life cycle ultimately define the cloud trajectory in the

phase-space. If they can be mapped with sufficient resolution, covering different updraft and supersaturation conditions, trajectories may be forecast from a single DSD at cloud base and the evolving thermodynamic conditions. Aerosols are a key aspect in that regard because they significantly change the cloud-base-DSD in the Gamma space (Figures 6.5-7) and also affect cloud thermodynamics, impacting condensation rates and consequently latent heat release. Note that clouds subject to similar aerosol conditions have similarities in their trajectories represented by small variability along the trajectories of the respective flights (Figures 6.6-7).

Figure 6.7 - Similar to Figure 6.5, but for flights AC7, AC12 and AC13 over the Arc of Deforestation.



The $\overrightarrow{F_{cd}}$ and $\overrightarrow{F_{cl}}$ tabulation over the Gamma space can potentially be achieved with the help of Lagrangian large eddy simulation bin microphysics models that

precisely solve the condensation and collection equations for varying input DSDs and updraft conditions. Initial DSDs can be obtained from observations and analytical considerations. For instance, Pinsky et al. (2012) show an analytical way to obtain the maximum supersaturation (which is usually a few meters above cloud base) and the relative droplet concentration. If D_{eff} behaves adiabatically (FREUD et al., 2008; FREUD et al., 2011) and is linearly correlated to the mean volumetric diameter (FREUD; ROSENFELD, 2012), it is possible to estimate the initial DSD based on Gamma-DSD equations and adiabatic theory given that the aerosol population is known. The advantage of such approach is that all DSD characteristics, most notably its shape, would be realistically represented and there would be no need for fixing or diagnosing (THOMPSON et al., 2004; MILBRANDT; YAU, 2005; FORMENTON et al., 2013a, 2013b) Gamma parameters for various hydrometeor types – which works for specific applications but may be lacking in the physical representation of the processes. This study focuses on introducing the Gamma phase-space and its characteristics and further work is needed if new parameterizations are to be developed.

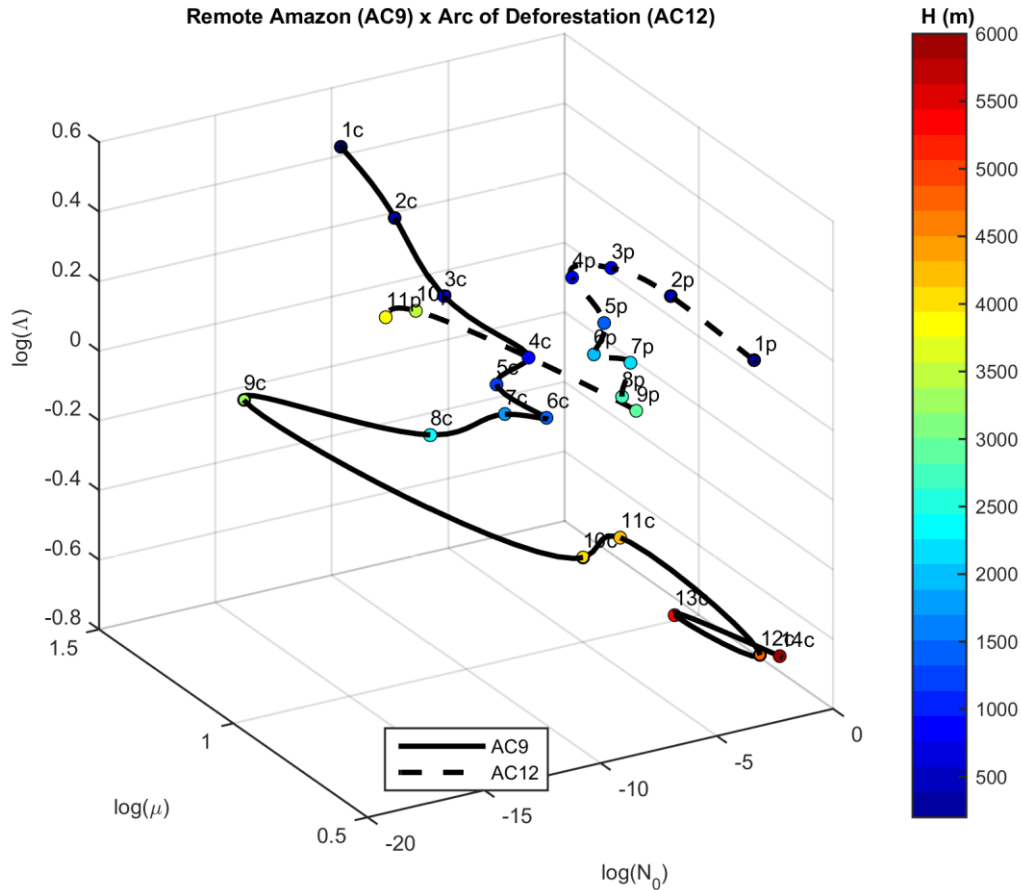
6.6. Contrasts between clean and polluted trajectories

In this section, we focus on flights AC9 and AC12 in order to study the differences of natural and human-affected clouds in the Gamma space. Figure 6.8 shows the trajectories of the clouds measured during those flights, where the points related to the averaged DSDs are numbered and the corresponding properties are shown in Tables 6.2-3. The numbers start at 1 close to cloud base and grow with altitude (“p” stands for “polluted”, while “c” is for “clean”). Also presented in Tables 6.2-3 are the adiabatic fractions which correspond to the ratio between the observed and adiabatic LWC . Some observed and the respective Gamma DSDs are shown in Figure 6.9, highlighting different growth processes.

It is clear from Figure 6.8 that clean and polluted clouds cover different regions of the Gamma phase-space. Nevertheless, it is possible to see that the trajectories can evolve almost in parallel depending on the dominant growth

process. Polluted clouds have wider DSDs at cloud base because of the tail to lower diameters (Figure 6.9), which brings down the value of μ (see Equation 3.3.9). Given the lower droplet size (Table 6.3), condensation is efficient and the trajectory evolve in the overall direction of \vec{F}_{cd} illustrated in Figure 6.3. From point 1p to 2p, N_d and LWC are approximately doubled. Condensational growth seems to be the dominant growth process in the polluted clouds up to the point 3p, corresponding to a cloud depth of 600 m. A similar layer is nonexistent in cleaner clouds, where there are enough big droplets to readily activate the collision-coalescence growth. Collisional growth dominates the DSD shape evolution between points 1c and 6c for flight AC9 and between 4p and 7p for AC12. Note that the trajectories are almost parallel in that region. Condensation is still active in that period given the increasing LWC , but collision-coalescence have a comparatively bigger impact on the overall DSD shape. Both sections of the trajectories represent 1400 m-thick layers, but droplet growth and DSD broadening is more efficient in the cleaner clouds (Figure 6.9). This explains the pronounced tilting of its trajectory, consistent with stronger \vec{F}_{cl} pseudo-force.

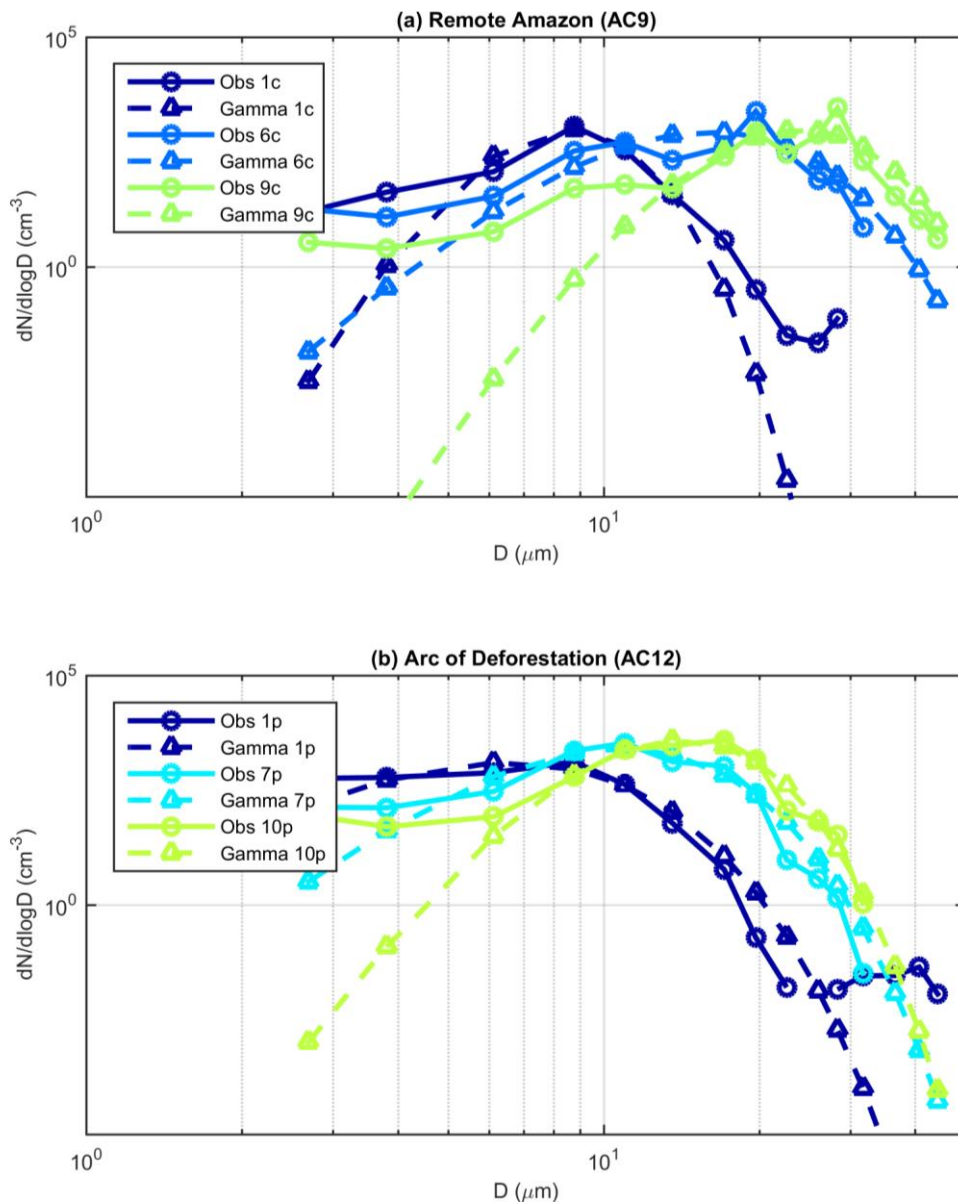
Figure 6.8 - Observed trajectories for the clouds measured over the remote Amazon during flight AC9 (continuous line) and over the Arc of Deforestation during flight AC12 (dashed line). The numbers shown close to the observed trajectories start at 1 at cloud base and grow with altitude (the respective markers are colored according do altitude above cloud base, H). Their respective properties are presented in Tables 6.2-3.



Eventually, the trajectories reach a point close to the 0 °C isotherm where the updrafts are enhanced given the continued latent heat release. This w -enhanced layer can be several hundred meters thick and culminates in narrower DSDs. This is exemplified between points 7c and 9c and between 8p and 10p. Although droplets are still growing by collision-coalescence, the enhanced updrafts increase condensational growth sufficiently to produce observable effects on the DSDs. Both trajectories evolve in the condensational growth direction, but with slightly different tilting. The tilting is less pronounced in the cleaner clouds given the stronger $\overline{F_{cl}}$ component. The way in which the DSDs evolve in this region is

important for the mixed-phase initiation, given that both primary and secondary ice generation depend on the characteristics of the liquid droplets. The different properties of the polluted and clean DSDs (see Tables 6.2-3, Figures 6.8 and 6.9) indicate that ice formation may follow distinct pathways.

Figure 6.9 - Averaged DSDs and their respective Gamma fittings for some points in the trajectories of clouds measured over (a) the remote Amazon (flight AC9) and (b) the Arc of Deforestation (flight AC12).



Previous studies suggest that droplets bigger than 23 μm at concentrations higher than 1 cm^{-3} favor secondary ice generation, which was identified as the main mechanism for cloud glaciation (MOSSOP 1978; SAUNDERS; HOSSEINI 2001; HEYMSFIELD; WILLIS, 2014; LAWSON et al., 2015). In order to visualize those conditions in the Gamma phase-space, it is interesting to consider constant N_d surfaces. Those surfaces are defined when N_d is fixed in Equation 3.3.6, resulting in a relation of the form $\Lambda = f(N_o, \mu)$ when inverted. Examples are shown in Figure 6.10, where $N_d = \{10, 100, 1000\} \text{cm}^{-3}$ (axes are rotated for clarity). The surfaces are evidently parallel and are stacked in relatively close proximity (at the scale used here). The trajectories evolve through the surfaces depending on their N_d , where polluted clouds tend toward higher droplet concentration (i. e. closer to the red surface). The surfaces can be used to delimit specific regions of interest. Additionally, further DSD properties can be analyzed along those surfaces. Figure 6.10 highlights the region of $23 \mu\text{m} < D_{\text{eff}} < 50 \mu\text{m}$ with black lines along the surface of $N_d = 10 \text{cm}^{-3}$. Regarding cloud DSDs (drizzle droplets are not analyzed here, although they also contribute for ice formation), the region delimited by the black lines for the different surfaces of constant N_d can be interpreted as the most favorable for secondary ice generation, thus indicating a quick glaciation process. Note that the trajectory of the cleaner clouds enters this region while in the w -enhanced layer mentioned previously, which corresponds to the transition to temperatures below 0 °C. Polluted clouds are able to produce high droplet number concentrations, but their lower size mean that they are out of the delimited region. More details about the transition to the mixed-phase are given in the next section.

Figure 6.10 - Surfaces of constant N_d as calculated by the inversion of Equation 3.3.6. The trajectories for the clouds measured during flights AC9 (blue) and AC12 (red) are also shown. Note that the axes are rotated for clarity.

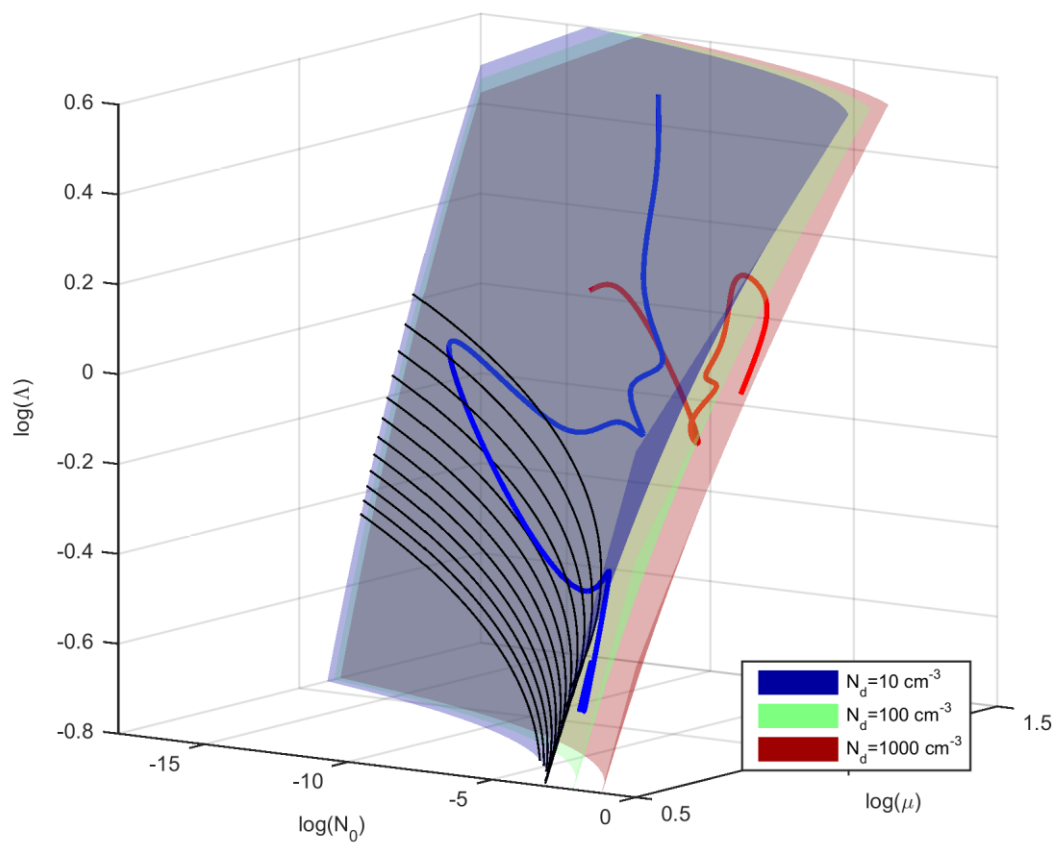


Table 6.2 - Properties of the points highlighted in Figure 6.8 for flight AC9. H is shown as the average of each of the 200-m vertical bin. The adiabatic fraction is defined as the ratio between the observed and adiabatic LWC . Adiabatic values for N_d , LWC and ε are shown below the respective observed quantities.

Point	H (m)	N_d (cm^{-3})	LWC ($g\ m^{-3}$)	ε	D_{eff} (μm)	T ($^{\circ}C$)	UR (%)	w ($m\ s^{-1}$)	Adiabatic fraction
1c	100	214	0.079	0.19	9.2	19.9	81	0.84	0.31
2c	300	238	0.15	0.22	11.1	18.6	82	0.91	0.22
3c	500	218	0.25	0.24	13.8	17.5	83	1.43	0.30
4c	700	227	0.34	0.28	15.2	16.6	77	1.41	0.28
5c	1100	245	0.61	0.27	18.0	13.6	85	1.13	0.31
6c	1300	284	0.79	0.29	18.9	12.0	80	1.03	0.34
7c	1700	231	0.79	0.28	20.1	10.6	71	1.49	0.28
8c	2300	187	1.21	0.27	24.7	7.1	78	1.66	0.34
9c	3100	233	1.95	0.22	26.4	3.5	64	2.79	0.47
10c	3900	54	0.61	0.34	30.9	-1.2	39	1.08	0.13
11c	4100	49	0.31	0.36	25.6	-1.8	61	0.31	0.065
12c	4700	36	0.26	0.47	28.6	-4.8	67	1.30	0.053
13c	5300	39	0.42	0.40	31.4	-8.1	26	2.39	0.083
14c	5900	30	0.16	0.48	26.4	-11.4	33	3.27	0.032

The observation of constant N_d surfaces poses an interesting question for parameterizations. In existing two moment schemes, both N_d and LWC are predicted. For each pair of such properties, it is possible to define two surfaces (with constant N_d and LWC , respectively) based on Equations 3.3.6 and 3.3.7. Those surfaces intersect, defining a curve where both properties are conserved.

In this curve, the mean volumetric diameter (proportional to the ratio between LWC and N_d) is also constant. Based on the limited information provided by the model (only two moments for three Gamma parameters), this curve represents the infinite DSD solutions for the undetermined equation system. A good parameterization scheme should be able to choose one of the DSDs that best fits observations. Given the undetermined equation system, other considerations have to be made.

One parameter that varies along the infinite DSD solution curve is the relative dispersion ε . If ε is calculated from theoretical considerations or provided by observations, it should be possible to obtain the full Gamma DSD – which is the point in the intersection curve that presents the given ε . The advantage of relying in ε is that it has low variability between clean and polluted clouds and its average is almost constant with altitude. Tas et al. (2015) studied the relative dispersion parameter in detail, noting that averaged values for ε were independent of N_d , LWC or height but its variability is significantly lower for the most adiabatic portions of the cloud (notably its updraft core). For precise parameterizations, ε variability should be taken into account at regions with relatively low N_d and LWC , but for the updraft cores averaged values may be considered. Our observations show that ε is slightly higher in polluted Amazonian clouds compared to the ones measured over remote regions mainly because of their reduced droplet size (Tables 6.2-3). This can be considered to produce slight corrections to ε based on CCN concentrations.

Table 6.3 - Properties of the points highlighted in Figure 6.8 for flight AC12. H is shown as the average of each of the 200-m vertical bin. The adiabatic fraction is defined as the ratio between the observed and adiabatic LWC . Adiabatic values for N_d , LWC and ε are shown below the respective observed quantities.

Point	H (m)	N_d (cm⁻³)	LWC (g m⁻³)	ε	D_{eff} (μm)	T (°C)	UR (%)	w (m s⁻¹)	Adiabatic fraction
1p	100	528	0.11	0.37	8.4	16.3	72	1.17	0.59
2p	300	960	0.27	0.31	8.8	15.5	64	1.02	0.72
3p	500	634	0.21	0.28	9.2	14.7	58	1.28	0.29
4p	700	597	0.29	0.27	10.4	12.4	59	0.57	0.24
5p	1300	543	0.34	0.29	11.5	6.9	65	1.13	0.15
6p	1900	1066	1.12	0.29	13.7	2.6	69	0.74	0.38
7p	2100	874	0.75	0.31	12.8	2.4	62	2.89	0.26
8p	2700	477	0.62	0.32	14.8	0.4	8	1.62	0.17
9p	2900	1271	1.95	0.32	15.7	0.2	5	9.36	0.52
10p	3300	1024	1.78	0.24	15.7	-1.5	3	5.68	0.44
11p	3700	137	0.25	0.24	16.0	-3.6	4	0.26	0.06

6.7. Observations of the mixed-phase formation

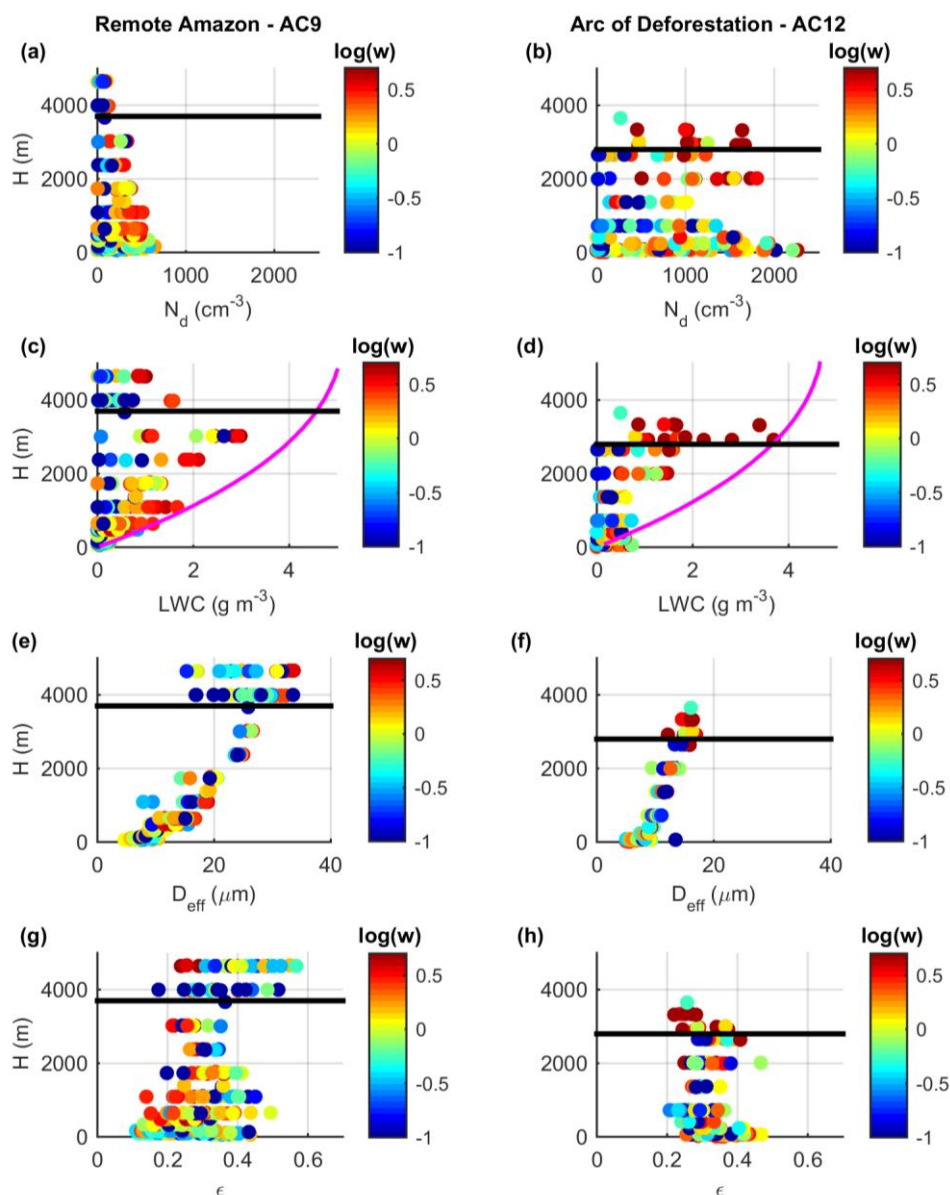
The Gamma phase-space provides an insightful way to study the formation of the mixed-phase by providing the history of the warm-phase development as a trajectory. Liquid cloud droplet properties are important for the glaciation process because they determine the probability of contacting ice nuclei (IN) and the conditions for secondary generation. As shown in the previous sections, different aerosol and thermodynamic conditions alter warm-phase characteristics and can thus impact the early formation of ice in the clouds.

Figure 6.11 shows vertical profiles of N_d , LWC , D_{eff} and ε for clouds subject to background and polluted conditions (flights AC9 and AC12, respectively). It shows the different microphysical properties (1 Hz) of the clouds associated to the trajectories presented in Figures 6.8 and 6.10 ($w > 0$). It shows that droplet concentrations are much higher in polluted clouds, which are not depleted with altitude as much as in cleaner clouds (Figure 6.11a, b). The lower effective diameter for clouds over the Arc of Deforestation may contribute to enhanced evaporation, leading to lower adiabatic fractions. As commented in the previous section, ε shows small variation between the flights and do not change much with altitude.

The properties of the DSDs around the 0 °C level in Figure 6.11 are a significant feature regarding the mixed-phase formation. Note that cleaner clouds have a sudden change in behavior right above the freezing level. At this point, there is a fast decrease in LWC , with higher variability in both D_{eff} and ε . This suggests that ice processes have been triggered, disrupting the smooth evolution observed in the warm-phase. In polluted clouds, this transition takes place for considerably different DSD properties. Averaged N_d reach values above 1000 cm^{-3} (compared to 50 cm^{-3} in cleaner clouds) with very strong updrafts, bringing LWC closer to adiabaticity. However, no significant variability was observed for D_{eff} suggesting that most of the water is still in condensed state.

In order to further detail the characteristics of the hydrometeors in the transition from warm- to mixed-phase, we analyzed the sphericity criteria obtained by the NIXE-CAPS probe (COSTA et al., 2017). The methodology developed by Costa et al. (2017) indicates whether each individual 1 Hz measurement contained or not some aspherical hydrometeors. This criterion can be used to indicate whether the hydrometeors are liquid (spherical), mixed (spherical and aspherical) or frozen (aspherical). By combining all measurements for clouds over remote Amazon (AC9 and AC18) and the Arc of Deforestation (AC7, AC12 and AC13), we obtained the results shown in Figure 6.12.

Figure 6.11 - Vertical profiles of the 1 Hz measurements of N_d , LWC , D_{eff} and ϵ for background clouds over the remote Amazon (a, c, e, g) and polluted clouds over the Arc of Deforestation (b, d, f, h). Updraft speeds are colored in log scale, corresponding to $0.1 \leq w \leq 5 \text{ m s}^{-1}$. Horizontal black lines mark the 0°C level. Magenta curves in (c) and (d) are the adiabatic water content profiles. H is relative to cloud base altitude.



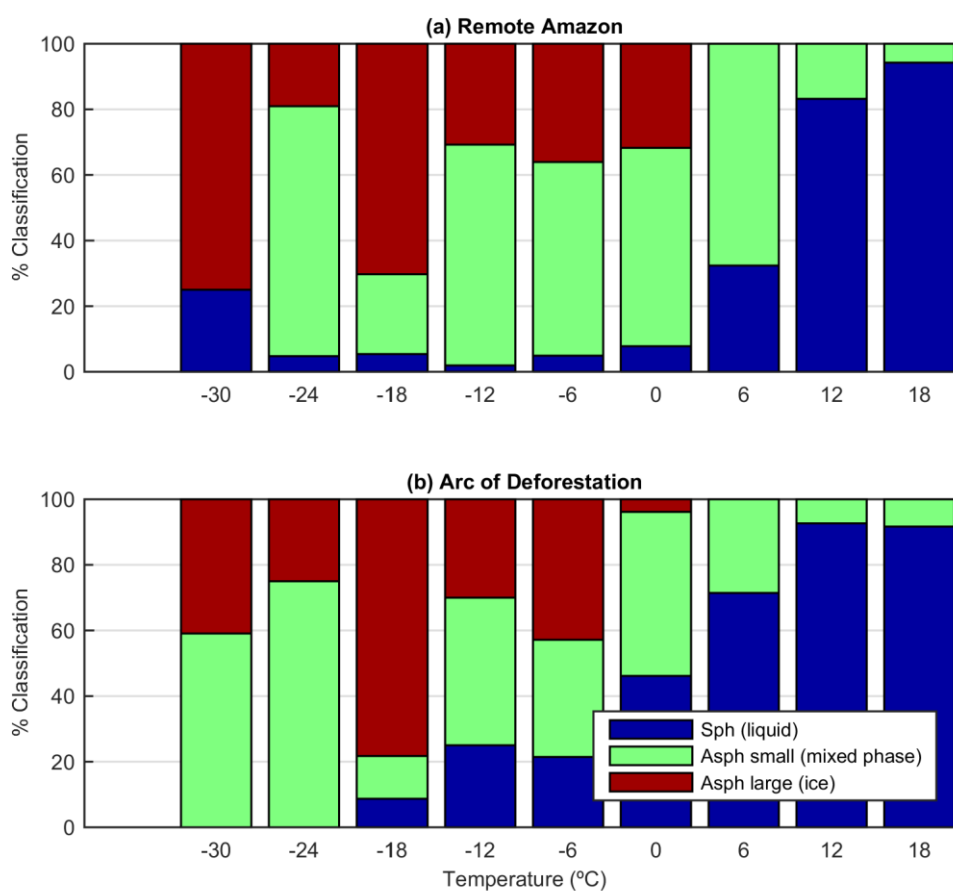
The classifications shown in Figure 6.12 separates the volumes probed as: (i) containing many ($> 1 \text{ cm}^{-3}$) spherical, liquid droplets only – “Sph (liquid)”; (ii) containing many ($> 3 \text{ cm}^{-3}$) predominantly spherical but also some aspherical (most likely ice) hydrometeors for $D < 50 \mu\text{m}$ and only aspherical hydrometeors

for $D > 50 \mu\text{m}$ – “Asph small (mixed phase)”; (iii) containing very few ($< 1 \text{ cm}^{-3}$) aspherical hydrometeors for $D < 50 \mu\text{m}$ and only aspherical hydrometeors for $D > 50 \mu\text{m}$ – “Asph large (ice)”. It is possible to observe that close to cloud base most of the hydrometeors were detected as spherical for both regions, which is expected given that it is the warmest layer of the cloud. However, higher in the clouds the distribution of the classifications become different. The amount of measurements with aspherical particles increases relatively fast for the cleaner clouds, being higher than 90% at the layer around $0 \text{ }^\circ\text{C}$. For polluted clouds, on the other hand, almost half of the measurements contained exclusively spherical hydrometeors at this level. Exclusively spherical hydrometeors persisted with a frequency of $\sim 20 \%$ down to temperatures of $-15 \text{ }^\circ\text{C}$. This is in line with previous studies that found supercooled droplets high into continental convective systems (ROSENFELD; WOODLEY, 2000; ROSENFELD et al., 2008). Our results show that the persistence of supercooled droplets in continental clouds are more likely under polluted conditions.

The characteristics of the cloud warm layer determine the properties of the liquid DSDs close to the $0 \text{ }^\circ\text{C}$ level and should have a determinant role in the glaciation initiation. Our measurements show that clean clouds can produce droplets roughly twice the size of the ones found in polluted systems at this layer, with 95 % lower concentrations (Tables 6.2-3). Bigger droplets are not only more likely to interact with IN and glaciate by immersion or contact freezing, but may also trigger a cascading effect through secondary ice generation (HEYMSFIELD; WILLIS, 2014; LAWSON et al., 2015). This process is able to quickly glaciate the cloud, which fits the results shown in Figure 6.12. Beyond the DSD bulk properties, the Gamma phase-space can also provide more information regarding the kind of DSD that enables or hampers the glaciation process. In the present study, we have only a few examples to compare warm- and mixed-phase characteristics, but it is clear that it is possible to correlate some regions of the phase-space with the characteristics of the ice initiation. Detailed model experiments would greatly enrich this discussion by providing control over the

liquid DSD properties and the resulting formation of the mixed layer. More specifically, it would be invaluable to study the impacts of the properties of cloud-base- and 0 °C-isotherm-DSDs on the primary and secondary ice production.

Figure 6.12 - Frequency of occurrence of NIXE-CAPS sphericity classifications for (a) the remote Amazon and (b) the Arc of Deforestation. “Sph (liquid)” stands for many only spherical ($D < 50 \mu\text{m}$) and predominantly spherical ($D > 50 \mu\text{m}$) hydrometeors, “Asph small (mixed phase)” for many predominantly spherical ($D < 50 \mu\text{m}$) and only aspherical ($D > 50 \mu\text{m}$) hydrometeors, and “Asph large (ice)” for only very few aspherical ($D < 50 \mu\text{m}$) and only aspherical ($D > 50 \mu\text{m}$) hydrometeors. Temperatures shown on x-axis are the center for 6 °C intervals, which corresponds to roughly 1-km-thick layers.



6.8. Closing remarks

In this study, the visualization of the Gamma DSD phase space was introduced, defined when the cloud DSDs are parameterized by conserving the moments of order zero, two and three. It was shown that trajectories in the space are related to DSD evolution and are linked to microphysical processes taking place inside the cloud. As such, those processes can be understood as pseudo-forces in the phase space. Measurements over the Amazon during the ACRIDICON-CHUVA and GoAmazon2014/5 campaigns show that it is possible to relate the direction of the pseudo-forces to different DSD growth processes. Cloud layers with strong updrafts and consequently relatively strong condensational growth showed that this process induces displacements in the direction of high shape and curvature parameters. This tendency is accompanied by DSD narrowing, consistent with condensational growth theory. On the other hand, collision-coalescence, observable in clean clouds over the Amazon, favors displacements in roughly the opposite direction. Observed displacements in the warm phase may be interpreted as a combination of both pseudo-forces.

Previous studies have identified cloud conditions that favor rapid secondary ice generation, which can be translated into the phase space. It was shown that clean clouds over the Amazon evolve into the region that favors secondary ice generation because of the enhanced collisional growth. Droplets in polluted clouds take much longer to grow by warm processes and they cross 0 °C before reaching the region favorable for glaciation. This leads to the persistence of supercooled droplets higher in the clouds that interact with other ice processes, including sublimating to produce big ice particles through the Wegener-Bergeron-Findeisen mechanism.

It is proposed that the Gamma space can be used to both evaluate current parameterization and steer the development of new ones. The results presented here show that different types of clouds have different trajectories through the Gamma phase-space. The aerosol effect seems to play a major role in the

trajectories of the warm layer. The ability of current parameterizations to reproduce such aspects can be tested in the phase space, where artificially produced DSDs would be apparent. For new two-moment parameterizations, the Gamma space can be used to constrain the DSD from the given droplet concentration and liquid water content. For each pair of those properties, the possible DSD solutions lie on a curve in the Gamma space where the main differentiating factor is the distribution relative dispersion. Observations such as the ones shown here and in previous studies can be used to find the appropriate relative dispersion value to find the optimal solution. Additionally, precise bin microphysics simulations can be used in order to produce full condensational and collisional pseudo-force fields in the space. The fields would be dependent on the evolution of properties such as aerosol concentration, updraft speed and supersaturation conditions. If such tabulation is achieved, bulk microphysical models would only need to predict the initial DSD close to cloud base and the rest would be determined by the pseudo-force fields.

7 CONCLUSIONS

This work had the goal of analyzing the aerosol-cloud interactions with a new dataset acquired by recent experimental campaigns in the Amazon. The study was divided into three sections focused on different aspects of the aerosol-cloud interactions. Firstly, the local aspects of Manaus pollution plume in the properties of surrounding clouds were inspected with data collected by the G-1 aircraft. This proved to be an interesting way to study aerosol-cloud interactions given that the thermodynamic conditions do not change much between the plume-affected and plume-free regions. The HALO aircraft also allowed larger-scale studies, where a sensitivity methodology was needed in order to compare the aerosol and thermodynamic effects on clouds. Finally, the use of the Gamma DSD was discussed in the context of the aerosol-cloud interactions in the Amazon. It was shown that it is possible to understand several characteristics of the aerosol-cloud interactions by studying the Gamma phase space, which can potentially also be used in the development of new microphysics parameterizations. The specific conclusions from each study will be discussed below.

The first study focused on the analysis of microphysics of warm-phase clouds in Amazonia during the wet season, with a specific emphasis on interactions with the pollution emitted by Manaus city. A statistical approach was used to compare several clouds probed in different flights on different days. Concerning the effects of the pollution plume on the cloud DSDs bulk properties, there are two processes to consider. A polluted environment with high particle count presents a high total area for the condensation, favoring higher bulk liquid water on the DSDs. Additionally, the total amount of condensed water scales with updraft speed in the plume-affected clouds, which is not the case for background clouds. The growth processes under background aerosol levels are much more effective even with lower bulk liquid water contents. Despite the lower amount of water condensed in background DSDs, bigger droplets readily form given the early start of the collision-coalescence process (which does not increase LWC). Polluted

clouds had droplets 10%-40% smaller on average and more numerous droplets (as high as 1000% difference) in the same vertical layers inside the cloud.

The averaged DSDs in different layers of warm clouds show droplets grow with altitude overall, with bigger droplets acquiring mass from the smaller ones. However, the growth rates with altitude are much slower for plume-affected clouds (almost half of the clean growth rate) due to the enhanced water vapor competition and the lack of bigger droplets at the onset of the systems. Background clouds present relatively high concentrations of droplets greater than 20 μm near cloud base that contributed to the growth rates, especially taking into account the non-linear nature of the collection process. With respect to warm-phase cloud DSDs, the updraft strength does not seem to be the major driving force for effective droplet growth, especially beyond the 20 μm range. The most important features to produce such big droplets are weak water vapor competition (usually observed in background clouds) and the existence of bi-modality at the lower levels of the cloud. The weak water vapor competition favors the formation of big droplets ($> 20 \mu\text{m}$) required for the collision-coalescence process, while the bi-modality favors the efficiency of the collision-coalescence process due to the large terminal velocity differences between the modes. However, the thermodynamic role of the updraft speeds should not be underestimated. It is responsible for transporting hydrometeors beyond the freezing level, activating the cold processes. Those processes are known to be associated to thunderstorms and intense precipitation. Nevertheless, the main feature that determines warm-phase DSD shapes seems to be the aerosol conditions, with the vertical velocities playing a role in the modulation of the distributions.

Similar results were obtained at larger scale in the Amazon, when the sensitivity methodology was applied. In that regard, the ACRIDICON-CHUVA campaign and the capabilities of the HALO aircraft allowed, for the first time, analyzing the sensitivities of Amazon tropical convective clouds to aerosol number concentrations and updraft speed while also considering cloud evolution. The sensitivity formulation identified that aerosol number concentrations play a

primary role in the formation of the warm phase of convective clouds, determining not only droplet concentration but also diameter and overall DSD shape. On the other hand, the thermodynamic conditions, as represented by the updraft intensity, affect primarily DSD bulk properties such as water content and droplet concentration. It was shown that the altitude above cloud base is critical when analyzing aerosol and updraft impacts on clouds, given that the DSD properties evolve with further processing in the system.

It was observed that an increase of 100% in aerosol concentration results in an 84% increase in droplet number concentration on average, while the same relative increase in updraft wind speed results in only 43% change. Regarding mean droplet size, we found it to be effectively independent of the updraft speed. Roughly, the effective droplet diameter decreases 25% when aerosol concentration doubles. The comparison between the aerosol and the thermodynamic effects shows that the aerosol concentration is the primary driver for DSD, whereas the updrafts mainly affect droplet number concentration and liquid water content. During cloud evolution, droplet number concentration is depleted while the diameter sensitivity to the growth processes is quantitatively similar to the aerosol effect. Additionally, the aerosol effect on DSD shape inverts in sign with altitude, favoring broader droplet distributions close to cloud base but narrower higher in the clouds. This highlights the importance of differentiating the analysis by altitude above cloud base, which is an appropriate proxy for DSD lifetime for our measurements.

The results presented in this section can potentially be used to derive new parameterizations in numerical models. They pointed out the specific roles of aerosol particles, updraft speed, and cloud evolution on warm-phase microphysical properties, which can help evaluate the ability of numerical models to reproduce tropical convective clouds. For instance, the sensitivities can be calculated by the models and then compared to the quantifications shown here. Additionally, the behavior of the relative dispersion parameter was shown to change in altitude, which is often not considered in models.

Another way to evaluate the representation of the microphysical processes in clouds is to consider the Gamma DSD distribution. Despite being widely adopted in many modeling and remote sensing applications, there is almost no study analyzing the evolution of cloud droplet size distributions in Gamma phase space. Herein, this visualization in phase space was introduced, defined when the cloud DSDs are parameterized by conserving the moments of order zero, two and three. It was shown that trajectories in the space are related to DSD evolution and are linked to microphysical processes taking place inside the cloud. As such, those processes can be understood as pseudo-forces in the phase space. Measurements over the Amazon during the ACRIDICON-CHUVA and GoAmazon2014/5 campaigns show that it is possible to relate the direction of the pseudo-forces to different DSD growth processes. Cloud layers with strong updrafts and consequently relatively strong condensational growth showed that this process induces displacements in the direction of high shape and curvature parameters. This tendency is accompanied by DSD narrowing, consistent with condensational growth theory. On the other hand, collision-coalescence, observable in clean clouds over the Amazon, favors displacements in roughly the opposite direction. Observed displacements in the warm phase may be interpreted as a combination of both pseudo-forces.

The Gamma phase space can also be used as a diagnostic tool for cloud evolution. By studying the displacements in the warm phase, it is possible to determine regions that favor, for instance, cloud glaciation. Previous studies have identified cloud conditions that favor rapid secondary ice generation, which can be translated into the phase space. It was shown that clean clouds over the Amazon evolve into the region that favors secondary ice generation because of the enhanced collisional growth. Droplets in polluted clouds take much longer to grow by warm processes and they cross 0 °C before reaching the region favorable for glaciation. This leads to the persistence of supercooled droplets higher in the clouds that interact with other ice processes, including sublimating to produce big ice particles through the Wegener-Bergeron-Findeisen

mechanism. In this regard, the Gamma phase-space approach proved to be an interesting tool to analyze the relation between warm microphysics and the evolution of the mixed-phase. More studies are encouraged in that direction, especially in modeling scenarios given the difficulties in the prediction of mixed-phase processes.

It is proposed that the Gamma space can be used to both evaluate current parameterization and steer the development of new ones. The results presented here show that different types of clouds have different trajectories through the Gamma phase-space. The aerosol effect seems to play a major role in the trajectories of the warm layer. The ability of current parameterizations to reproduce such aspects can be tested in the phase space, where artificially produced DSDs would be apparent. For new two-moment parameterizations, the Gamma space can be used to constrain the DSD from the given droplet concentration and liquid water content. For each pair of those properties, the possible DSD solutions lie on a curve in the Gamma space where the main differentiating factor is the distribution relative dispersion. Observations such as the ones shown here and in previous studies can be used to find the appropriate relative dispersion value to find the optimal solution. Additionally, precise bin microphysics simulations can be used in order to produce full condensational and collisional pseudo-force fields in the space. The fields would be dependent on the evolution of properties such as aerosol concentration, updraft speed and supersaturation conditions. If such tabulation is achieved, bulk microphysical models would only need to predict the initial DSD close to cloud base and the rest would be determined by the pseudo-force fields.

Overall, the three studies developed showed that the aerosols have a primary role in determining Amazonian clouds microphysical properties. As pointed out in Section 2.3, the Amazon has thermodynamic conditions that favor convection invigoration by aerosols, where the low vertical wind shear, high humidity, and high CAPE are highlighted. Therefore, the primary role of the aerosols in determining cloud microphysics can also be translated into significant macroscale

effects. By changing clouds macroscale characteristics, there will be effects on their interactions with radiation, the vertical profile of latent heat release, and the energy and hydrological budgets, which will impact the mesoscale circulation and potentially the South America or global climate. There are many more aspects and feedback mechanisms to consider between the anthropogenic aerosol emissions and the net effects on climate. Nonetheless, given the determinant role of the aerosols, studies in this direction are needed in order to understand and model tropical clouds and their effects on climate.

7.1. Future perspectives

The Gamma phase space introduced in Chapter 6 proved to be not only a good tool to analyze the aerosol effect, but also a simple way to study cloud evolution. As such, it may have uses on the evaluation and development of microphysical schemes in cloud-resolving models. For instance, it can be used in order to compare different schemes by providing a common framework. Additionally, the patterns observed in the phase space can be used to propose new parameterizations. In that regard, new parameterizations can be developed with the aim of reproducing the patterns observed by actual measurements such as the ones shown here.

Future efforts with the Gamma phase space methodology will be on testing its applicability in radar measurements focused on thunderstorm nowcasting in Southeast Brazil. By studying radar volumetric scans of thunderstorm clouds, it is possible to estimate the Gamma DSD spatial variability in the systems. By iterating this process, the evolution of the DSD spatial distribution can be followed during the cloud lifecycle. The evolution can be visualized in the Gamma phase space, where it should be possible to infer patterns shared by clouds that develop into thunderstorms. Therefore, if a developing cloud presents Gamma phase space patterns consistent with the thunderstorm case, it may be possible to generate warnings beforehand.

REFERENCES

- ACKERMAN, A. S.; TOON, O. B.; STEVENS, D. E.; HEYMSFIELD, A. J.; RAMANATHAN, V.; WELTON, E. J. Reduction of tropical cloudiness by soot. **Science**, v. 288, p. 1042–1047, 2000. doi:10.1126/science.288.5468.1042.
- ALBRECHT, B.A. Aerosols, cloud microphysics, and fractional cloudiness. **Science**, v. 245, p. 1227–1230, 1989.
- ALTARATZ, O.; KOREN, I.; YAIR, Y.; PRICE, C. Lightning response to smoke from Amazonian fires. **Geophys. Res. Lett.**, v. 37, n. L07801, 2010. doi:10.1029/2010gl042679.
- ALTARATZ, O.; KOREN, I.; REMER, L. A.; HIRSCH, E. Review: cloud invigoration by aerosols-Coupling between microphysics and dynamics. **Atmos. Res.**, v.140–141, p. 38–60, 2014.
- ANDERSON, N. F.; GRAINGER, C. A.; STITH, J. L. Characteristics of strong updrafts in precipitation systems over the central tropical Pacific Ocean and in the Amazon. **J. Appl. Meteor.**, v. 44, p. 731–738, 2005.
- ANDREAE, M. O.; ARTAXO, P.; FISCHER, H.; FREITAS, S. R.; GREGOIRE, J. M.; HANSEL, A.; HOOR, P.; KORMANN, R.; KREJCI, R.; LANGE, L.; LELIEVELD, J.; LINDINGER, W.; LONGO, K.; PETERS, W.; DE REUS, M.; SCHEEREN, B.; DIAS, M.; STROM, J.; VAN VELTHOVEN, P. F. J.; WILLIAMS, J.: Transport of biomass burning smoke to the upper troposphere by deep convection in the equatorial region. **Geophys. Res. Lett.**, v. 28, p. 951–954, 2001.
- ANDREAE, M. O.; ROSENFELD, D.; ARTAXO, P.; COSTA, A. A.; FRANK, G. P.; LONGO, K. M.; SILVA-DIAS, M. A. F. Smoking rain clouds over the Amazon. **Science**, v. 303, p. 1337-1342, 2004.
- ANDREAE, M. O. Aerosols before pollution. **Science**, v. 315, p. 50–51, 2007.
- ANDREAE, M.O.; ROSENFELD, D. Aerosol–cloud–precipitation interactions. Part 1. The nature and sources of cloud-active aerosols. **Earth-Science Reviews**, v. 89, n. 1–2, p.13-41, 2008.
- ANDREAE, M. O.; ACEVEDO, O. C.; ARAÚJO, A.; ARTAXO, P.; BARBOSA, C. G. G.; BARBOSA, H. M. J.; BRITO, J.; CARBONE, S.; CHI, X.; CINTRA, B. B. L.; DA SILVA, N. F.; DIAS, N. L.; DIAS-JÚNIOR, C. Q.; DITAS, F.; DITZ, R.; GODOI, A. F. L.; GODOI, R. H. M.; HEIMANN, M.; HOFFMANN, T.; KESSELMEIER, J.; KÖNEMANN, T.; KRÜGER, M. L.; LAVRIC, J. V.; MANZI, A. O.; LOPES, A. P.; MARTINS, D. L.; MIKHAILOV, E. F.; MORAN-ZULOAGA, D.; NELSON, B. W.; NÖLSCHER, A. C.; SANTOS NOGUEIRA, D.; PIEDADE,

M. T. F.; PÖHLKER, C.; PÖSCHL, U.; QUESADA, C. A.; RIZZO, L. V.; RO, C.-U.; RUCKTESCHLER, N.; SÁ, L. D. A.; DE OLIVEIRA SÁ, M.; SALES, C. B.; DOS SANTOS, R. M. N.; SATURNO, J.; SCHÖNGART, J.; SÖRGE, M.; DE SOUZA, C. M.; DE SOUZA, R. A. F.; SU, H.; TARGHETTA, N.; TÓTA, J.; TREBS, I.; TRUMBORE, S.; VAN EIJCK, A.; WALTER, D.; WANG, Z.; WEBER, B.; WILLIAMS, J.; WINDERLICH, J.; WITTMANN, F.; WOLFF, S.; YÁÑEZ-SERRANO, A. M. The Amazon Tall Tower Observatory (ATTO): overview of pilot measurements on ecosystem ecology, meteorology, trace gases, and aerosols. **Atmos. Chem. Phys.**, v. 15, p. 10723-10776, 2015. doi:10.5194/acp-15-10723-2015.

ARAKAWA, A. The cumulus parameterization problem: past, present, and future. **J. Climate**, v. 17, p. 2493–2525, 2004.

ARTAXO, P.; MARTINS, J. V.; YAMASOE, M. A.; PROCÓPIO, A. S.; PAULIQUEVIS, T. M.; ANDREAE, M. O.; GUYON, P.; GATTI, L. V.; LEAL, A. M. C. Physical and chemical properties of aerosols in the wet and dry seasons in Rondônia, Amazonia. **J. Geophys. Res. Atmos.**, v.107, n. D20, 8081, 2002. doi:10.1029/2001JD000666.

ARTAXO, P.; RIZZO, L. V.; BRITO, J. F.; BARBOSA, H. M. J.; ARANA, A.; SENA, E. T.; CIRINO, G. G.; BASTOS, W.; MARTIN, S. T.; ANDREAE, M. O. Atmospheric aerosols in Amazonia and land use change: from natural biogenic to biomass burning conditions. **Faraday Discuss.**, v.165, p. 203–235, 2013.

BERG, L. K.; BERKOWITZ, C. M.; BARNARD, J. C.; SENUM, G.; SPRINGSTON, S. R. Observations of the first aerosol indirect effect in shallow cumuli. **Geophys. Res. Lett.**, v. 38, n. 3, L03809, 2011. doi:10.1029/2010GL046047.

BERGERON, T. On the physics of clouds and precipitation. In: **Proces Verbaux de l'Association de Météorologie**, n. 5, 1933, Lisbon, Portugal. International Union of Geodesy and Geophysics, 156–178, 1935.

BESWICK, K. M.; GALLAGHER, M. W.; WEBB, A. R.; NORTON, E. G.; AND PERRY, F. Application of the Aventech AIMMS20AQ airborne probe for turbulence measurements during the convective storm initiation project. **Atmos. Chem. Phys.**, v. 8, p. 5449-5463, 2008. doi:10.5194/acp-8-5449-2008.

BETTS, A. K.: Evaluation of the diurnal cycle of precipitation, surface thermodynamics, and surface fluxes in the ECMWF model using LBA data. **J. Geophys. Res. Atmos.**, v.107, 8045, 2002. doi:10.1029/2001jd000427.

BETTS, R. A.; COX, P. M.; COLLINS, M.; HARRIS, P. P.; HUNTINGFORD, C.; JONES, C. D. The role of ecosystem-atmosphere interactions in simulated Amazonian precipitation decrease and forest dieback under global climate warming. **Theo. Appl. Clim.**, v.78, p. 157–175, 2004.

BIESENTHAL, T. A.; WU, Q.; SHEPSON, P. B.; WIEBE, H. A.; ANLAUF, K. G.; MACKAY, G. I. A study of relationships between isoprene, its oxidation products, and ozone, in the Lower Fraser Valley, BC. **Atmos. Environ.**, v.31, p. 2049–2058, 1997.

BOISIER, J. P.; CIAIS, P.; DUCHARNE, A.; GUIMBERTEAU, M. Projected strengthening of Amazonian dry season by constrained climate model simulations. **Nature Climate Change**, v. 5, p. 656–660, 2015.

BOWMAN, D.; BALCH, J.; ARTAXO, P.; BOND, W.; COCHRANE, M.; D'ANTONIO, C.; DEFRIES, R.; JOHNSTON, F.; KEELEY, J.; KRAWCHUK, M.; KULL, C.; MACK, M.; MORITZ, M.; PYNE, S.; ROOS, C.; SCOTT, A.; SODHI N.; SWETNAM, T. The human dimension of fire regimes on Earth. **J. Biogeogr.**, v. 38, p. 2223–2236, 2011.

BRAGA, R. C.; ROSENFELD, D.; WEIGEL, R.; JURKAT, T.; ANDREAE, M. O.; WENDISCH, M.; PÖHLKER, M. L.; KLIMACH, T.; PÖSCHL, U.; PÖHLKER, C.; VOIGT, C.; MAHNKE, C.; BORRMANN, S.; ALBRECHT, R. I.; MOLLEKER, S.; VILA, D. A.; MACHADO, L. A. T.; ARTAXO, P. Comparing calculated microphysical properties of tropical convective clouds at cloud base with measurements during the ACRIDICON-CHUVA campaign. **Atmos. Chem. Phys. Discuss.**, doi:10.5194/acp-2016-872, in review, 2016.

BRÉON, F.; TANRÉ, D.; GENEROSO, S. Aerosol effect on cloud droplet size monitored from satellite. **Science**, v. 295, p. 834–838, 2002. doi:10.1126/science.1066434.

BULGIN, C. E.; PALMER, P. I.; THOMAS, G. E.; ARNOLD, C. P. G.; CAMPMANY, E.; CARBONI, E.; GRAINGER, R. G.; POULSEN, C.; SIDDANS, R.; LAWRENCE, B. N. Regional and seasonal variations of the Twomey indirect effect as observed by the ATSR-2 satellite instrument. **Geophys. Res. Lett.**, v. 35, L02811, 2008. doi:10.1029/2007GL031394.

CAMPONOGARA, G.; SILVA DIAS, M. A. F.; CARRIÓ, G. G. Relationship between Amazon biomass burning aerosols and rainfall over the La Plata Basin. **Atmos. Chem. Phys.**, v.14, p. 4397-4407, 2014. doi:10.5194/acp-14-4397-2014.

CECCHINI, M. A.; MACHADO, L. A. T.; COMSTOCK, J. M.; MEI, F.; WANG, J., FAN, J.; TOMLINSON, J. M.; SCHMID, B.; ALBRECHT, R. I.; MARTIN, S. T.; ARTAXO, P. Impacts of the Manaus pollution plume on the microphysical properties of Amazonian warm-phase clouds in the wet season. **Atmos. Chem. Phys.**, v. 16, p. 7029-7041, 2016. doi:10.5194/acp-16-7029-2016.

CHAMEIDES, W. L.; FEHSENFELD, F.; RODGERS, M. O.; CARDELINO, C.; MARTINEZ, J.; PARRISH, D.; LONNEMAN, W.; LAWSON, D. R.; RASMUSSEN, R. A.; ZIMMERMAN, P.; GREENBERG, J.; MIDDLETON, P.;

- WANG, T. Ozone precursor relationships in the ambient atmosphere. **J. Geophys. Res. Atmos.**, v. 97, n. D5, p. 6037–6055, 1992.
- CHANG, D.; CHENG, Y.; REUTTER, P.; TRENTMANN, J.; BURROWS, S. M.; SPICHTINGER, P.; NORDMANN, S.; ANDREA, M. O.; PÖSCHL, U.; SU, H. Comprehensive mapping and characteristic regimes of aerosol effects on the formation and evolution of pyro-convective clouds. **Atmos. Chem. Phys.**, v. 15, 10325-10348, 2015. doi:10.5194/acp-15-10325-2015.
- CHEN, S.-H.; LIU, Y.-C.; NATHAN, T. R.; DAVIS, C.; TORN, R.; SOWA, N.; CHENG, C.-T.; CHEN, J.-P. Modeling the effects of dust-radiative forcing on the movement of Hurricane *Helene* (2006). **Q.J.R. Meteorol. Soc.**, v.141, p. 2563–2570, 2015. doi:10.1002/qj.2542.
- CHENG, C.-T.; WANG, W.-C.; CHEN, J.-P. A modeling study of aerosol impacts on cloud microphysics and radiative properties. **Q. J. R. Meteorol. Soc.**, v. 133, p. 283–297, 2007. doi:10.1002/qj.25.
- CHENG, C.-T.; WANG, W.-C.; CHEN, J.-P. Simulation of the effects of increasing cloud condensation nuclei on mixed-phase clouds and precipitation of a front system. **Atmos. Res.**, v. 96, n. 2–3, p. 461–476, 2010.
- CHRISTENSEN, M. W.; STEPHENS, G. L. Microphysical and macrophysical responses of marine stratocumulus polluted by underlying ships: Evidence of cloud deepening. **J. Geophys. Res. Atmos.**, v. 116, D03201, 2011. doi:[10.1029/2010JD014638](https://doi.org/10.1029/2010JD014638).
- COOPER, W.A. A possible mechanism for contact nucleation. **J. Atmos. Sci.**, v. 31, p. 1832-1837, 1974.
- COSTA, A.; MEYER, J.; AFCHINE, A.; LUEBKE, A.; GÜNTHER, G. DORSEY, J. R.; GALLAGHER, M. W.; EHRlich, A. WENDISCH, M.; BAUMGARDNER, D.; WEX, H.; KRÄMER, M. Classification of Arctic, Mid-Latitude and Tropical Clouds in the Mixed-Phase Temperature Regime. **Atmos. Chem. Phys. Discuss.**, doi:10.5194/acp-2017-226, in review, 2017.
- CRUTZEN, P. J.; ANDREA, M. O. Biomass burning in the tropics: Impact on atmospheric chemistry and biogeochemical cycles. **Science**, v. 250, p. 1669–1678, 1990.
- DAI, A. Precipitation characteristics in eighteen coupled climate models. **J. Climate**, v.19, p. 4605–4630, 2006.
- DAVIDSON, E. A.; DE ARAÚJO, A. C.; ARTAXO, P.; BALCH, J. K.; BROWN, I. F.; BUSTAMANTE, M. M. DA C.; COE, M. T.; DEFRIES, R. S.; KELLER, M.; LONGO, M.; MUNGER, J. W.; SCHROEDER, W.; SOARES-FILHO, B. S.;

SOUZA JR., C. M.; WOFSY, S. C. The Amazon Basin in Transition. **Nature**, v. 481, p. 321–328, 2012.

DEMOTT, P. J.; PRENNI, A. J.; LIU, X.; KREIDENWEIS, S. M.; PETTERS, M. D.; TWOHY, C. H.; RICHARDSON, M. S.; EIDHAMMER, T.; ROGERS, D. C. Predicting global atmospheric ice nuclei distributions and their impacts on climate. **Proc. Natl. Acad. Sci. U. S. A.**, v.107, p. 11,217–11,222, 2010. doi:10.1073/pnas.0910818107.

FAN, J.; ZHANG, R.; LI, G.; TAO, W.-K.; LI, X.: Simulations of cumulus clouds using a spectral bin microphysics in a cloud resolving model. **J. Geophys. Res. Atmos.**, v.112, D04201, 2007. <http://dx.doi.org/10.1029/2006JD007688>.

FAN, J.; YUAN, T.; COMSTOCK, J. M.; GHAN, S.; KHAIN, A.; LEUNG, L. R.; LI, Z.; MARTINS, V. J.; OVCHINNIKOV, M. Dominant role by vertical wind shear in regulating aerosol effects on deep convective clouds. **J. Geophys. Res. Atmos.**, v.114, D22206, 2009. doi:[10.1029/2009JD012352](http://dx.doi.org/10.1029/2009JD012352).

FAN, J.; COMSTOCK, J. M.; OVCHINNIKOV, M. Tropical anvil characteristics and water vapor of the tropical tropopause layer: Impact of heterogeneous and homogeneous freezing parameterizations. **J. Geophys. Res. Atmos.**, v.115, D12201, 2010a. doi:10.1029/2009JD012696.

FAN, J.; GHAN, S.; OVCHINNIKOV, M.; LIU, X.; RASCH, P. J.; KOROLEV, A.: Representation of Arctic mixed-phase clouds and the Wegener-Bergeron-Findeisen process in climate models: Perspectives from a cloud-resolving study. **J. Geophys. Res. Atmos.**, v.116, D00T07, 2011. doi:10.1029/2010JD015375.

FAN, J.; LEUNG, L. R.; LI, Z.; MORRISON, H.; CHEN, H.; ZHOU, Y.; QIAN, Y.; WANG, Y.: Aerosol impacts on clouds and precipitation in eastern China: Results from bin and bulk microphysics. **J. Geophys. Res. Atmos.**, v.117, D00K36, 2012a. doi:10.1029/2011JD016537.

FAN, J.; ROSENFELD, D.; DING, Y.; LEUNG, L. R.; LI, Z. Potential aerosol indirect effects on atmospheric circulation and radiative forcing through deep convection. **Geophys. Res. Lett.**, v.39, L09806, 2012b. doi:10.1029/2012GL051851.

FAN, J.; LEUNG, L. R.; ROSENFELD, D.; CHEN, Q.; LI, Z.; ZHANG, J.; YAN, H.: Microphysical effects determine macrophysical response for aerosol impacts on deep convective clouds. **Proc. Natl. Acad. Sci. U. S. A.**, v. 110, E4581–E4590, 2013. doi:10.1073/pnas.1316830110.

FAN, J.; WANG, Y.; ROSENFELD, D.; LIU, X.: Review of aerosol-cloud interactions: mechanisms, significance and challenges. **Journal of the**

Atmospheric Sciences, v. 73, p. 4221-4525, 2016. doi:10.1175/JAS-D-16-0037.1.

FEINGOLD, G. Modeling of the first indirect effect: analysis of measurement requirements. **Geophys. Res. Lett.**, v. 30, n. 19, 2003. doi:10.1029/2003GL017967.

FEINGOLD, G.; COTTON, W. R.; KREIDENWEIS, S. M.; DAVIS, J. T. The impact of giant cloud condensation nuclei on drizzle formation in stratocumulus: Implication for cloud radiative properties. **J. Atmos. Sci.**, v. 56, p. 4100–4117, 1999. doi:10.1175/1520-0469(1999)056<4100:TIOGCC>2.0.CO;2.

FIELD, P. R.; LAWSON, R. P.; BROWN, P. A.; LLOYD, G. G.; WESTBROOK, C. C.; MOISSEEV, D. D.; MILTENBERGER, A. A.; NENES, A. A.; BLYTH, A. A.; CHOULARTON, T. T.; CONNOLLY, P. P.; BUEHL, J. J.; CROSIER, J. J.; CUI, Z. Z.; DEARDEN, C. C.; DEMOTT, P. P.; FLOSSMANN, A. A.; HEYMSFIELD, A. A.; HUANG, Y. Y.; KALESSE, H. H.; KANJI, Z. A.; KOROLEV, A. A.; KIRCHGAESSNER, A. A.; LASHER-TRAPP, S. S.; LEISNER, T. T.; MCFARQUHAR, G. G.; PHILLIPS, V. V.; STITH, J. J.; SULLIVAN, S.S. Secondary Ice Production: Current State of the Science and Recommendations for the Future. **Meteorological Monographs**, v. 58, p. 7.1–7.20, 2017. doi: 10.1175/AMSMONOGRAPHS-D-16-0014.1.

FIERRO, A. O.; SIMPSON, J.; LEMONE, M. A.; STRAKA, J. M.; SMULL, B. F. On how hot towers fuel the Hadley cell: an observational and modeling study of line-organized convection in the equatorial trough from TOGA COARE. **J. Atmos. Sci.**, v. 66, p. 2730–2746, 2009.

FIERRO, A. O.; ZIPSER, E. J.; LEMONE, M. A.; STRAKA, J. M.; SIMPSON, J. M. Tropical oceanic hot towers: need they be undilute to transport energy from the boundary layer to the upper troposphere effectively? An answer based on trajectory analysis of a simulation of a TOGA COARE convective system. **J. Atmos. Sci.**, v. 69, p. 195–213, 2012.

FINDEISEN, W.: Kolloid-meteorologische Vorgänge bei Neiderschlagsbildung. **Meteor. Z.**, 55, 121–133, 1938.

FISCH, G.; TOTA, J.; MACHADO, L. A. T.; DIAS, M.; LYRA, R. F. D.; NOBRE, C. A.; DOLMAN, A. J.; GASH, J. H. C. The convective boundary layer over pasture and forest in Amazonia. **Theor. Appl. Climatol.**, v. 78, p. 47–59, 2004.

FORMENTON, M.; PHILLIPS, V. T. J.; LIENERT, B.: A new snow microphysics parameterization applied to a cloud electrification model: Framework and preliminary results. **93rd AMS Annual Meeting**, Austin, Tex., 6–10 Jan, 2013a.

FORMENTON, M.; PANEGROSSI, G.; CASELLA, D.; DIETRICH, S.; MUGNAI, A.; SANO, P.; DI PAOLA, F.; BETZ, H.-D.; PRICE, C.; YAIR, Y. Using a cloud

electrification model to study relationships between lightning activity and cloud microphysical structure. **Nat. Hazards Earth Syst. Sci.**, v.13, p. 1085–1104, 2013b. doi:10.5194/nhess-13-1085-2013.

FREUD, E.; ROSENFELD, D.; ANDREAE, M. O.; COSTA, A. A.; ARTAXO, P. Robust relations between CCN and the vertical evolution of cloud drop size distribution in deep convective clouds. **Atmos. Chem. Phys.**, v. 8, p. 1661–1675, 2008. doi:10.5194/acp-8-1661-2008.

FREUD, E.; ROSENFELD, D.; KULKARNI, J. R. Resolving both entrainment-mixing and number of activated CCN in deep convective clouds. **Atmos. Chem. Phys.**, v. 11, p. 12887-12900, 2011. doi:10.5194/acp-11-12887-2011.

FREUD, E.; ROSENFELD, D. Linear relation between convective cloud drop number concentration and depth for rain initiation. **J. Geophys. Res. Atmos.**, v. 117, D02207, 2012. doi:10.1029/2011JD016457.

FUZZI, S.; DECESARI, S.; FACCHINI, M. C.; CAVALLI, F.; EMBLICO, L.; MIRCEA, M.; ANDREAE, M. O.; TREBS, I.; HOFFER, A.; GUYON, P.; ARTAXO, P.; RIZZO, L. V.; LARA, L. L.; PAULIQUEVIS, T.; MAENHAUT, W.; RAES, N.; CHI, X. G.; MAYOL-BRACERO, O. L.; SOTO-GARCIA, L. L.; CLAEYS, M.; KOURTCHEV, I.; RISSLER, J.; SWIETLICKI, E.; TAGLIAVINI, E.; SCHKOLNIK, G.; FALKOVICH, A. H.; RUDICH, Y.; FISCH G.; GATTI, L. V. Overview of the inorganic and organic composition of size-segregated aerosol in Rondonia, Brazil, from the biomass-burning period to the onset of the wet season. **J. Geophys. Res.**, v. 112, D01201, 2007.

GERKEN, T.; WEI, D.; CHASE, R. J.; FUENTES, J. D.; SCHUMACHER, C.; MACHADO, L. A.; ANDREOLI, R. V.; CHAMECKI, M.; DE SOUZA, R. A. F.; FREIRE, L. S.; JARDINE, A. B.; MANZI, A. O.; DOS SANTOS, R. M. N.; VON RANDOW, C.; DOS SANTOS COSTA, P.; STOY, P. C.; TÓTA, J.; TROWBRIDGE, A. M. Downward transport of ozone rich air and implications for atmospheric chemistry in the amazon rainforest. **Atmospheric Environment**, v. 124, Part A, p. 64 – 76, 2016.

GIANGRANDE, S. E.; TOTO, T.; JENSEN, M. P.; BARTHOLOMEW, M. J.; FENG, Z.; PROTAT, A.; WILLIAMS, C. R.; SCHUMACHER, C.; MACHADO, L. A. T. Convective cloud vertical velocity and mass-flux characteristics from radar wind profiler observations during GoAmazon2014/5. **J. Geophys. Res. Atmos.**, v. 121, n. 12, p. 891–12, 913, 2016. doi:10.1002/2016JD025303.

GONÇALVES, W. A.; MACHADO, L. A. T.; KIRSTETTER, P.-E. Influence of biomass aerosol on precipitation over the Central Amazon: an observational study. **Atmos. Chem. Phys.**, v. 15, p. 6789-6800, 2015. doi:10.5194/acp-15-6789-2015.

GUNTHER, S. S.; KING, S. M.; ROSE, D.; CHEN, Q.; ROLDIN, P.; FARMER, D. K.; JIMENEZ, J. L.; ARTAXO, P.; ANDREA, M. O.; MARTIN, S. T.; PÖSCHL, U. Cloud condensation nuclei in pristine tropical rainforest air of Amazonia: size-resolved measurements and modeling of atmospheric aerosol composition and CCN activity. **Atmos. Chem. Phys.**, v. 9, p. 7551-7575, 2009. doi:10.5194/acp-9-7551-2009.

GUO, J.; DENG, M.; FAN, J.; LI, Z.; CHEN, Q.; ZHAI, P.; DAI, Z.; LI, X. Precipitation and air pollution at mountain and plain stations in northern China: insights gained from observations and modeling. **J. Geophys. Res. Atmos.**, v. 119, p. 4793–4807, 2014. doi:10.1002/2013JD021161.

HALLET, J.; MOSSOP, S.C. Production of secondary ice particles during the riming process. **Nature**, v. 249, p. 26–28, 1974.

HALLQUIST, M.; WENGER, J. C.; BALTENSPERGER, U.; RUDICH, Y.; SIMPSON, D.; CLAEYS, M.; DOMMEN, J.; DONAHUE, N. M.; GEORGE, C.; GOLDSTEIN, A. H.; HAMILTON, J. F.; HERRMANN, H.; HOFFMANN, T.; IINUMA, Y.; JANG, M.; JENKIN, M. E.; JIMENEZ, J. L.; KIENDLER-SCHARR, A.; MAENHAUT, W.; MCFIGGANS, G.; MENDEL, TH. F.; MONOD, A.; PRÉVÔT, A. S. H.; SEINFELD, J. H.; SURRATT, J. D.; SZMIGIELSKI, R.; WILDT, J. The formation, properties and impact of secondary organic aerosols: Current and emerging issues. **Atmos. Chem. Phys.**, v. 9, p. 5155–5236, 2009. doi:10.5194/acp-9-5155-2009.

HEIBLUM, R. H.; ALTARATZ, O.; KOREN, I.; FEINGOLD, G.; KOSTINSKI, A. B.; KHAIN, A. P.; OVCHINNIKOV, M.; FREDJ, E.; DAGAN, G.; PINTO, L.; YAISH, R.; CHEN, Q. Characterization of cumulus cloud fields using trajectories in the center-of-gravity vs. water mass phase space: 1. Cloud tracking and phase space description. **J. Geophys. Res. Atmos.**, v.121, n. 11, 2016a. doi:10.1002/2015JD024186.

HEIBLUM, R. H.; ALTARATZ, O.; KOREN, I.; FEINGOLD, G.; KOSTINSKI, A. B.; KHAIN, A. P.; OVCHINNIKOV, M.; FREDJ, E.; DAGAN, G.; PINTO, L.; YAISH, R.; CHEN, Q. Characterization of cumulus cloud fields using trajectories in the center of gravity versus water mass phase space: 2. Aerosol effects on warm convective clouds. **J. Geophys. Res. Atmos.**, v.121, n. 11, p. 6356–6373, 2016b. doi:10.1002/2015JD024193.

HEYMSFIELD, A. J.; BANSEMER, A.; FIELD, P. R.; DURDEN, S. L.; STITH, J.; DYE, J. E.; HALL, W.; GRAINGER, A. Observations and parameterizations of particle size distributions in deep tropical cirrus and stratiform clouds: Results from in situ observations in TRMM field campaigns. **J. Atmos. Sci.**, v. 59, 3457–3491, 2002.

HEYMSFIELD, A. J.; BANSEMER, A.; HEYMSFIELD, G.; FIERRO, A. O. Microphysics of maritime tropical convective updrafts at temperatures from -

20°C to -60°C. **J. Atmos. Sci.**, v. 66, p. 3530–3562, 2009. doi:10.1175/2009JAS3107.1.

HEYMSFIELD, A.; WILLIS, P. Cloud conditions favoring secondary ice particle production in tropical maritime convection. **J. Atmos. Sci.**, v. 71, p. 4500–4525, 2014.

HOBBS, P.V.; RANGNO, A.L. Ice particle concentrations in clouds. **J. Atmos. Sci.**, v. 42, p. 2523-2449, 1985.

HOFFMANN, F.; RAASCH, S.; NOH, Y. Entrainment of aerosols and their activation in a shallow cumulus cloud studied with a coupled LCM–LES approach. **Atmospheric Research**, v. 156, p. 43-57, 2015.
<http://dx.doi.org/10.1016/j.atmosres.2014.12.008>.

HUANG, Y.; BLYTH, A.; BROWN, P.; CHOULARTON, T.; CONNOLLY, P.; GADIAN, A.; JONES, H.; LATHAM, J.; CUI, Z.; CARSLAW, K. The development of ice in a cumulus cloud over southwest England. **New J. Phys.**, v. 10, 105021, 2008.

HUNTINGFORD, C.; ZELAZOWSKI, P.; GALBRAITH, D.; MERCADO, L. M.; SITCH, S.; FISHER, R.; LOMAS, M.; WALKER, A. P.; JONES, C. D.; BOOTH, B. B. B.; MALHI, Y.; HEMMING, D.; KAY, G.; GOOD, P.; LEWIS, S. L.; PHILLIPS, O. L.; ATKIN, O. K.; LLOYD, J.; GLOOR, E.; ZARAGOZA-CASTELLS, J.; MEIR, P.; BETTS, R.; HARRIS, P. P.; NOBRE, C.; MARENGO, J.; COX, P. M. Simulated resilience of tropical rainforests to CO₂-induced climate change. **Nat. Geosci.**, v. 6, p. 268–273, 2013.

INSTITUTO BRASILEIRO DE GEOGRAFIA E ESTATÍSTICA (IBGE). Cidades, available at: <http://cidades.ibge.gov.br/v3/cidades/municipio/1302603>, last access: 6 April 2017.

JOHNSON, D. B. The role of giant and ultra-giant aerosol particles in warm rain initiation. **J. Atmos. Sci.**, v.39, p. 448–460, 1982. doi:10.1175/1520-0469(1982)039<0448:TROGAU>2.0.CO;2.

KANAKIDOU, M.; TSIGARIDIS, K.; DENTENER, F. J.; CRUTZEN, P. J.: Human-activity-enhanced formation of organic aerosols by biogenic hydrocarbon oxidation. **J. Geophys. Res. Atmos.**, v. 105, n. D7, p. 9243–9254, 2000.

KARYDIS, V. A.; CAPPS, S. L.; RUSSELL, A. G.; NENES, A. Adjoint sensitivity of global cloud droplet number to aerosol and dynamical parameters. **Atmos. Chem. Phys.**, v.12, p. 9041–9055, 2012. doi:10.5194/acp-12-9041-2012.

KAY, J. E.; WOOD, R. Timescale analysis of aerosol sensitivity during homogeneous freezing and implications for upper tropospheric water vapor

budgets. **Geophys. Res. Lett.**, v. 35, L10809, 2008.
doi:10.1029/2007gl032628.

KELLER, M.; BUSTAMANTE, M.; GASH, J.; DIAS, P. **Amazonia and global change**. Washington, DC: Wiley, 2009. v. 186, American Geophysical Union, Wiley, Washington, DC, 2009.

KHAIN, A.; ROSENFELD, D.; POKROVSKY, A. Aerosol impact on the dynamics and microphysics of convective clouds. **Q. J. R. Meteorol. Soc.**, v.131, p. 2639–2663, 2005. doi:10.1256/qj.04.62.

KHAIN, A. P.; BENMOSHE, N.; POKROVSKY, A. Factors determining the impact of aerosols on surface precipitation from clouds: An attempt at classification. **J. Atmos. Sci.**, v. 65, p. 1721–1748, 2008.
doi:10.1175/2007JAS2515.1.

KHAIN, A. P. Notes on state of the art investigations of aerosol effects on precipitation: A critical review. **Environ. Res. Lett.**, v. 4, 015004, 2009.
doi:10.1088/1748-9326/4/1/015004.

KHAIN, A. P.; BEHENG, K. D.; HEYMSFIELD, A.; KOROLEV, A.; KRICHAK, S. O.; LEVIN, Z.; PINSKY, M.; PHILLIPS, V.; PRABHAKARAN, T.; TELLER, A.; VAN DEN HEEVER, S. C.; YANO, J.-I. Representation of microphysical processes in cloud-resolving models: spectral (bin) microphysics versus bulk parameterization. **Rev. Geophys.**, v. 53, n. 2, p. 247–322, 2015. Doi: 10.1002/2014RG000468.

KIDD, C.; DAWKINS, E.; HUFFMAN, G. Comparison of precipitation derived from the ECMWF operational forecast model and satellite precipitation datasets. **J. Hydrometeor.**, v. 14, p. 1463–1482, 2013. doi:10.1175/JHM-D-12-0182.1.

KLINGEBIEL, M.; DE LOZAR, A.; MOLLEKER, S.; WEIGEL, R.; ROTH, A.; SCHMIDT, L.; MEYER, J.; EHRlich, A.; NEUBER, R.; WENDISCH, M.; BORRMANN, S. Arctic low-level boundary layer clouds: In-situ measurements and simulations of mono- and bimodal supercooled droplet size distributions at the cloud top layer. **Atmos. Chem. Phys.**, v.15, p. 617–631, 2015.
doi:10.5194/acp-15-617-2015.

KÖHLER, H. The nucleus in and the growth of hygroscopic droplets. **Trans. Faraday Soc.**, v. 32, p. 1152–1161, 1936.

KOREN, I.; MARTINS, J. V.; REMER, L. A.; AFARGAN, H. Smoke invigoration versus inhibition of clouds over the Amazon. **Science**, v. 321, p. 946–949, 2008. doi:10.1126/science.1159185.

KOREN, I.; FEINGOLD, G.; REMER, L. A. The invigoration of deep convective clouds over the Atlantic: Aerosol effect, meteorology or retrieval artifact?

Atmos. Chem. Phys., v. 10, p. 8855–8872, 2010. doi:10.5194/acp-10-8855-2010a.

KOREN, I.; ALTARATZ, O.; REMER, L. A.; FEINGOLD, G.; MARTINS, J. V.; HEIBLUM, R. H. Aerosol-induced intensification of rain from the tropics to the mid-latitudes. **Nat. Geosci.**, v. 5, p. 118–122, 2012. doi:10.1038/ngeo1364.

KOREN, I.; DAGAN, G.; ALTARATZ O. From aerosol-limited to invigoration of warm convective clouds. **Science**, v. 344, p. 1143–6, 2014.

KOROLEV, A. Reconstruction of the sizes of spherical particles from their shadow images. part i: theoretical considerations. **J. Atmos. Oceanic Technol.**, v. 24, p. 376-389, 2007. doi:10.1175/JTECH1980.1, 2007.

KOROLEV, A.; KHAIN, A.; PINSKY, M.; FRENCH, J. Theoretical study of mixing in liquid clouds – part 1: classical concepts. **Atmos. Chem. Phys.**, v.16, p. 9235-9254, 2016. doi:10.5194/acp-16-9235-2016.

KUHN, U.; GANZVELD, L.; THIELMANN, A.; DINDORF, T.; SCHEBESKE, G.; WELLING, M.; SCIARE, J.; ROBERTS, G.; MEIXNER, F. X.; KESSELMEIER, J.; LELIEVELD, J.; KOLLE, O.; CICCIOLI, P.; LLOYD, J.; TRENTMANN, J.; ARTAXO, P.; ANDREAE, M. O. Impact of Manaus City on the Amazon Green Ocean atmosphere: ozone production, precursor sensitivity and aerosol load. **Atmos. Chem. Phys.**, v.10, p. 9251-9282, 2010. doi:10.5194/acp-10-9251-2010.

KUMAR, V. A.; PANDITHURAI, G.; LEENA, P. P.; DANI, K. K.; MURUGAVEL, P.; SONBAWNE, S. M.; PATIL, R. D.; MAHESKUMAR, R. S. Investigation of aerosol indirect effects on monsoon clouds using ground-based measurements over a high-altitude site in Western Ghats. **Atmos. Chem. Phys.**, v.16, p. 8423-8430, 2016. doi:10.5194/acp-16-8423-2016.

LAMB, D.; HALLETT, J.; SAX, R.I. Mechanistic limitations to the release of latent heat during the natural and artificial glaciation of deep convective clouds. **Q.J.R. Meteorol. Soc.**, v. 107, p. 935-954, 1981.

LANCE, S.; BROCK, C. A.; ROGERS, D.; GORDON, J. A. Water droplet calibration of the Cloud Droplet Probe (CDP) and inflight performance in liquid, ice and mixed-phase clouds during ARCPAC. **Atmos. Meas. Tech.**, v.3, p. 1683-1706, 2010. doi:10.5194/amt-3-1683-2010.

LAU, K. M.; WU, H. T. Warm rain processes over tropical oceans and climate implications. **Geophys. Res. Lett.**, v. 30, n. 24, 2003. doi:[10.1029/2003GL018567](https://doi.org/10.1029/2003GL018567).

- LAWSON, R. P.; WOODS, S.; MORRISON, H. The microphysics of ice and precipitation development in tropical cumulus clouds. **J. Atmos. Sci.**, v. 72, p. 2429–2445, 2015. doi:10.1175/JAS-D-14-0274.1.
- LEBO, Z. J.; SEINFELD, J. H. Theoretical basis for convective invigoration due to increased aerosol concentration. **Atmos. Chem. Phys.**, v. 11, p. 5407–5429, 2011. doi:10.5194/acp-11-5407-2011.
- LEE, S. S.; DONNER, L. J.; PHILLIPS, V. T. J.; MING, Y. Examination of aerosol effects on precipitation in deep convective clouds during the 1997 ARM summer experiment. **Q. J. R. Meteorol. Soc.**, v. 134, n. 634, p. 1201–1220, 2008. doi:10.1002/qj.287.
- LELIEVELD, J.; BUTLER, T. M.; CROWLEY, J. N.; DILLON, T. J.; FISCHER, H.; GANZEVELD, L.; HARDER, H.; LAWRENCE, M. G.; MARTINEZ, M.; TARABORRELLI, D.; WILLIAMS, J. Atmospheric oxidation capacity sustained by a tropical forest. **Nature**, v. 452, p. 737–740, 2008.
- LI, Z.; NIU, F.; FAN, J.; LIU, Y.; ROSENFELD, D.; DING, Y. Long-term impacts of aerosols on the vertical development of clouds and precipitation. **Nat. Geosci.**, v. 4, p. 888–894, 2011. doi:10.1038/ngeo1313.
- LI, Z.; NIU, F.; FAN, J.; LIU, Y.; ROSENFELD, D.; DING, Y. Long-term impacts of aerosols on the vertical development of clouds and precipitation. **Nat. Geosci.**, v. 4, p. 888–894, 2012. doi:10.1038/ngeo1313.
- LIN, J. C.; MATSUI, T.; PIELKE, R. A.; AND KUMMEROW, C. Effects of biomass-burning-derived aerosols on precipitation and clouds in the Amazon basin: a satellite-based empirical study. **J. Geophys. Res. Atmos.**, v.111, D19204, 2006. doi:10.1029/2005JD006884.
- LIU, Y.; DAUM, P. H. Anthropogenic aerosols: Indirect warming effect from dispersion forcing. **Nature**, v. 419, p. 580–581, 2002. doi:10.1038/419580a.
- LIU, G.; SHAO, H.; COAKLEY JR., J. A.; CURRY, J. A.; HAGGERTY, J. A.; TSCHUDI, M. A. Retrieval of cloud droplet size from visible and microwave radiometric measurements during INDOEX: implication to aerosols' indirect radioactive effect. **J. Geophys. Res. Atmos.**, v. 108, n. D1, p. 4006, 2003. doi:10.1029/2001JD001395.
- LIU, C. Rainfall contributions from precipitation systems with different sizes, convective intensities, and durations over the tropics and subtropics. **J. Hydrometeorol.**, v.12, p. 394–412, 2011.
- LOGAN, J. A.; PRATHER, M. J.; WOFSY, S. C.; MCELROY, M. B. Tropospheric chemistry: a global perspective. **J. Geophys. Res. Atmos.**, v. 86, p. 7210–7254, 1981.

LOHMANN, U.; FEICHTER, J. Global indirect aerosol effects: a review. **Atmos. Chem. Phys.**, v. 5, p. 715-737, 2005. doi:10.5194/acp-5-715-2005.

LOHMANN, U.; HOOSE, C. Sensitivity studies of different aerosol indirect effects in mixed-phase clouds. **Atmos. Chem. Phys.**, v. 9, p. 8917-8934, 2009. doi:10.5194/acp-9-8917-2009.

LUEBKE, A. E.; AFCHINE, A.; COSTA, A.; GROOß, J.-U.; MEYER, J.; ROLF, C.; SPELTEN, N.; AVALLONE, L. M.; BAUMGARDNER, D.; KRÄMER, M. The origin of midlatitude ice clouds and the resulting influence on their microphysical properties. **Atmos. Chem. Phys.**, v.16, p. 5793-5809, 2016. doi:10.5194/acp-16-5793-2016.

MACHADO, L. A. T.; FISCH, G.; TOTA, J.; SILVA DIAS, M. A. F.; LYRA, F.; NOBRE, C. Seasonal and diurnal variability of convection over the Amazonia: A comparison of different vegetation types and large scale forcing. **Theoretical and Applied Climatology**, v. 78, n.1-3, p. 61, 2004. doi 10.1007/s00704-004-0044-9.

MACHADO, L.A.T.; SILVA DIAS, M. A. F.; MORALES, C.; FISCH, G.; VILA, D.; ALBRECHT, R. I.; GOODMAN, S. J.; CALHEIROS, A. J. P.; BISCARO, T.; KUMMEROW, C.; COHEN, J.; FITZJARRALD, D.; NASCIMENTO, E. L.; SAKAMOTO, M. S.; CUNNINGHAM, C.; CHABOUREAU, J.-P.; PETERSEN, W. A.; ADAMS, D. K.; BALDINI, L.; ANGELIS, C. F.; SAPUCCI, L. F.; SALIO, P.; BARBOSA, H. M. J.; LANDULFO, E.; SOUZA, R. A. F.; BLAKESLEE, R. J.; BAILEY, J.; FREITAS, S.; LIMA, W. F. A.; TOKAY, A. The Chuva Project: How Does Convection Vary across Brazil? **Bull. Amer. Meteor. Soc.**, v.95, p.1365–1380, 2014.

MALHI, Y.; ROBERTS, J. T.; BETTS, R. A.; KILLEEN, T. J.; LI, W. H.; NOBRE, C. A. Climate change, deforestation, and the fate of the Amazon. **Science**, v. 319, p. 169–172, 2008.

MALLAUN, C.; GIEZ, A.; BAUMANN, R. Calibration of 3-D wind measurements on a single-engine research aircraft. **Atmos. Meas. Tech.**, v. 8, n. 8, p. 3177–3196, 2015. doi:10.5194/amt-8-3177-2015.

MARENGO, J. A.; NOBRE, C. A.; TOMASELLA, J.; CARDOSO, M. F.; OYAMA, M. D.: Hydroclimatic and ecological behaviour of the drought of Amazonia in 2005. **Philos. Trans. R. Soc. London**, Ser. B, v. 363, p. 1773–1778, 2008.

MARENGO, J. A.; TOMASELLA, J.; ALVES, L. M.; SOARES, W. R.; RODRIGUEZ, D. A. The drought of 2010 in the context of historical droughts in the Amazon region. **Geophys. Res. Lett.**, v. 38, L12703, 2011.

MARTIN, G. M.; JOHNSON, D. W.; SPICE, A. The measurement and parameterization of effective radius of droplets in warm stratocumulus clouds. **J.**

Atmos. Sci., v. 51, p. 1823–1842, 1994. doi:10.1175/1520-0469(1994)051,1823:TMAPOE.2.0.CO;2.

MARTIN, S. T.; ANDREAE, M. O.; ARTAXO, P.; BAUMGARDNER, D.; CHEN, Q.; GOLDSTEIN, A. H.; GUENTHER, A.; HEALD, C. L.; MAYOL-BRACERO, O. L.; MCMURRY, P. H.; PAULIQUEVIS, T.; PÖSCHL, U.; PRATHER, K. A.; ROBERTS, G. C.; SALESKA, S. R.; SILVA DIAS, M. A.; SPRACKLEN, D. V.; SWIETLICKI, E.; TREBS, I. Sources and properties of Amazonian aerosol particles. **Rev. Geophys.**, v. 48, RG2002, 2010.

MARTIN, S. T.; ARTAXO, P.; MACHADO, L. A. T.; MANZI, A. O.; SOUZA, R. A. F.; SCHUMACHER, C.; WANG, J.; ANDREAE, M. O.; BARBOSA, H. M. J.; FAN, J.; FISCH, G.; GOLDSTEIN, A. H.; GUENTHER, A.; JIMENEZ, J. L.; PÖSCHL, U.; SILVA DIAS, M. A.; SMITH, J. N.; WENDISCH, M. Introduction: Observations and Modeling of the Green Ocean Amazon (GoAmazon2014/5). **Atmos. Chem. Phys.**, v. 16, p. 4785-4797, 2016. doi:10.5194/acp-16-4785-2016.

MARTINS, J. A.; SILVA DIAS, M. A. F. The impact of smoke from forest fires on the spectral dispersion of cloud droplet size distributions in the Amazonian region. **Environmental Research Letters**, v. 4, p. 015002, 2009.

MCFARQUHAR, G. M.; HSIEH, T.; FREER, M.; MASCIIO, J.; JEWETT, B. F. The characterization of ice hydrometeor gamma size distributions as volumes in N_0 - λ - μ phase space: Implications for microphysical process modeling. **J. Atmos. Sci.**, v. 72, p. 892–909, 2015. doi:10.1175/JAS-D-14-0011.1.

MCFIGGANS, G.; ARTAXO, P.; BALTENSPERGER, U.; COE, H.; FACCHINI, M. C.; FEINGOLD, G.; FUZZI, S.; GYSEL, M.; LAAKSONEN, A.; LOHMANN, U.; MENTEL, T. F.; MURPHY, D. M.; O'DOWD, C. D.; SNIDER, J. R.; WEINGARTNER, E.: The effect of physical and chemical aerosol properties on warm cloud droplet activation. **Atmos. Chem. Phys.**, v. 6, p. 2593–2649, 2006. doi:10.5194/acp-6-2593-2006.

MILBRANDT, J. A.; YAU, M. K. A multimoment bulk microphysics parameterization. Part I: Analysis of the role of the spectral shape parameter. **J. Atmos. Sci.**, v. 62, p. 3051–3064, 2005.

MÖHLER, O.; DEMOTT, P. J.; VALI, G.; LEVIN, Z. Microbiology and atmospheric processes: the role of biological particles in cloud physics. **Biogeosciences**, v. 4, p. 1059-1071, 2007. doi:10.5194/bg-4-1059-2007.

MOLLEKER, S.; BORRMANN, S.; SCHLAGER, H.; LUO, B.; FREY, W.; KLINGEBIEL, M.; WEIGEL, R.; EBERT, M.; MITEV, V.; MATTHEY, R.; WOIWODE, W.; OELHAF, H.; DÖRNBRACK, A.; STRATMANN, G.; GROOß, J.-U.; GÜNTHER, G.; VOGEL, B.; MÜLLER, R.; KRÄMER, M.; MEYER, J.; CAIRO, F. Microphysical properties of synoptic scale polar stratospheric clouds:

in situ measurements of unexpectedly large HNO₃ containing particles in the Arctic vortex. **Atmos. Chem. Phys.**, v. 14, p. 10785-10801, 2014. doi:10.5194/acp-14-10785-2014.

MORRIS, C. E.; GEORGAKOPOULOS, D. G.; SANDS, D. C.: Ice nucleation active bacteria and their potential role in precipitation. **Journal de Physique IV**, v. 121, 87–103, 2004. doi:10.1051/jp4:2004121004.

MOSSOP, S.C. The influence of drop size distribution on the production of secondary ice particles during graupel growth. **Q. J. R. Meteorol. Soc.**, v. 104, p. 323–330, 1978.

NOBRE, C.; MARENGO, J.; ARTAXO, P.: Understanding the climate of Amazonia: Progress from LBA. In: KELLER, M.; BUSTAMANTE, M.; GASH, J.; DIAS, P. S. (eds.). **Amazonia and global change**. Washington, DC: Wiley, 2009., v. 186, p. 147–150, 2009. ISBN: 978-0-87590-449-8. American Geophysical Union, Geophysical Monograph.

O'DOWD, C. D.; SMITH, M. H.; CONSTERDINE, I. E.; LOWE, J. A.: Marine aerosol, sea-salt, and the marine sulphur cycle: A short review. **Atmos. Environ.**, 31, 73–80, doi:10.1016/S1352-2310(96)00106-9, 1997.

OMETTO, J. P.; NOBRE, A. D.; ROCHA, H. R.; ARTAXO, P.; MARTINELLI, L. A. Amazonia and the modern carbon cycle: lessons learned. **Oecologia**, v. 143, n. 4, p. 483–500, 2005.

PANDITHURAI, G.; DIPU, S.; PRABHA, T. V.; MAHESKUMAR, R. S.; KULKARNI, J. R.; GOSWAMI, B. N. Aerosol effect on droplet spectral dispersion in warm continental cumuli. **J. Geophys. Res. Atmos.**, v.117, D16202, 2012.

PETTERS, M. D.; KREIDENWEIS, S. M. A single parameter representation of hygroscopic growth and cloud condensation nucleus activity. **Atmos. Chem. Phys.**, 7, 1961-1971, doi:10.5194/acp-7-1961-2007, 2007.

PETTERS, M. D.; KREIDENWEIS, S. M.: A single parameter representation of hygroscopic growth and cloud condensation nucleus activity – Part 2: Including solubility. **Atmos. Chem. Phys.**, v. 8, p. 6273-6279, 2008. doi:10.5194/acp-8-6273-2008.

PETTERS, M. D.; KREIDENWEIS, S. M.: A single parameter representation of hygroscopic growth and cloud condensation nucleus activity – Part 3: Including surfactant partitioning. **Atmos. Chem. Phys.**, v. 13, p. 1081-1091, 2013. doi:10.5194/acp-13-1081-2013.

- PINSKY, M.; KHAIN, A.; MAZIN, I.; KOROLEV, A.: Analytical estimation of droplet concentration at cloud base. **J. Geophys. Res. Atmos.**, v. 117, D18211, 2012. doi:10.1029/2012JD017753.
- PINSKY, M.; KHAIN, A.; KOROLEV, A.; MAGARITZ-RONEN, L.: Theoretical investigation of mixing in warm clouds – Part 2: Homogeneous mixing. **Atmos. Chem. Phys.**, v. 16, p. 9255-9272, 2016a. doi:10.5194/acp-16-9255-2016.
- PINSKY, M.; KHAIN, A.; KOROLEV, A.: Theoretical analysis of mixing in liquid clouds – Part 3: Inhomogeneous mixing. **Atmos. Chem. Phys.**, v.16, p. 9273-9297, 2016b. doi:10.5194/acp-16-9273-2016.
- PÖSCHL, U.; MARTIN, S. T.; SINHA, B.; CHEN, Q.; GUNTHER, S. S.; HUFFMAN, J. A.; BORRMANN, S.; FARMER, D. K.; GARLAND, R. M.; HELAS, G.; JIMENEZ, J. L.; KING, S. M.; MANZI, A.; MIKHAILOV, E.; PAULIQUEVIS, T.; PETTERS, M. D.; PRENNI, A. J.; ROLDIN, P.; ROSE, D.; SCHNEIDER, J.; SU, H.; ZORN, S. R.; ARTAXO, P.; ANDREAE, M. O. Rainforest aerosols as biogenic nuclei of clouds and precipitation in the Amazon. **Science**, v. 329, n. 5998, p. 1513-1516, 2010.
- PRENNI, A. J.; PETTERS, M. D.; KREIDENWEIS, S. M.; HEALD, C. L.; MARTIN, S. T.; ARTAXO, P.; GARLAND, R. M.; WOLLNY, A. G.; PÖSCHL, U. Relative roles of biogenic emissions and Saharan dust as ice nuclei in the Amazon Basin. **Nat. Geosci.**, v. 2, p. 402–405, 2009. doi:10.1038/ngeo517.
- QIAN, Y.; GONG, D.; FAN, J.; LEUNG, L. R.; BENNARTZ, R.; CHEN, D.; WANG, W. Heavy pollution suppresses light rain in China: observations and modeling. **J. Geophys. Res. Atmos.**, v. 114, D00K02, 2009. doi:10.1029/2008JD011575.
- QUAAS, J.; BOUCHER, O.; BREON, F. Aerosol indirect effects in POLDER satellite data and the Laboratoire de Meteorologie Dynamique-Zoom (LMDZ) general circulation model. **J. Geophys. Res. Atmos.**, v. 109, D08205, 2004. doi:10.1029/2003JD004317.
- RAMANATHAN, V.; CRUTZEN, P. J.; KIEHL, J. T.; ROSENFELD, D. Aerosols, climate, and the hydrological cycle. **Science**, v. 294, p. 2119–2124, 2001. doi:10.1126/science.1064034.
- REUTTER, P.; SU, H.; TRENTMANN, J.; SIMMEL, M.; ROSE, D.; GUNTHER, S. S.; WERNLI, H.; ANDREAE, M. O.; PÖSCHL, U. Aerosol- and updraft-limited regimes of cloud droplet formation: influence of particle number, size and hygroscopicity on the activation of cloud condensation nuclei (CCN). **Atmos. Chem. Phys.**, v. 9, p. 7067-7080, 2009. doi:10.5194/acp-9-7067-2009.
- RIEHL, H.; MALKUS, J. S. On the heat balance in the equatorial trough zone. **Geophysica**, v. 6, p. 503–538, 1958.

RIEHL, H.; SIMPSON, J. S. On the heat balance in the equatorial trough zone, revisited. **Contrib. Atmos. Phys.**, v. 52, p. 287–305, 1979.

ROBERTS, J. M.; WILLIAMS, J.; BAUMANN, K.; BUHR, M. P.; GOLDAN, P. D.; HOLLOWAY, J.; HUBLER, G.; KUSTER, W. C.; MCKEEN, S. A.; RYERSON, T. B.; TRAINER, M.; WILLIAMS, E. J.; FEHSENFELD, F. C.; BERTMAN, S. B.; NOUAIME, G.; SEAVER, C.; GRODZINSKY, G.; RODGERS, M.; YOUNG, V. L. Measurements of PAN, PPN, and MPAN made during the 1994 and 1995 Nashville Intensives of the Southern Oxidant Study: Implications for regional ozone production from biogenic hydrocarbons. **J. Geophys. Res. Atmos.**, v. 103, n. D17, p. 22473–22490, 1998.

ROBERTS, G. C.; ANDREAE, M. O.; ZHOU, J. C.; ARTAXO, P. Cloud condensation nuclei in the Amazon Basin: “Marine” conditions over a continent? **Geophys. Res. Lett.**, v. 28, p. 2807–2810, 2001. doi:10.1029/2000GL012585.

ROBERTS, G. C.; ARTAXO, P.; ZHOU, J. C.; SWIETLICKI, E.; ANDREAE, M. O. Sensitivity of CCN spectra on chemical and physical properties of aerosol: A case study from the Amazon Basin. **J. Geophys. Res. Atmos.**, v. 107, n. D20, 8070, 2002. doi:10.1029/2001JD000583.

ROBERTS, G. C.; NENES, A.; SEINFELD, J. H.; ANDREAE, M. O. Impact of biomass burning on cloud properties in the Amazon Basin. **J. Geophys. Res. Atmos.**, v. 108, n. D2, 4062, 2003. doi:10.1029/2001JD000985.

ROBERTS, G. C.; NENES, A. A continuous-flow streamwise thermal-gradient CCN chamber for atmospheric measurements. **Aerosol Sci. Technol.**, v. 39, n. 3, p. 206–221, 2005. doi:10.1080/027868290913988.

ROSE, D.; GUNTHER, S. S.; MIKHAILOV, E.; FRANK, G. P.; DUSEK, U.; ANDREAE, M. O.; PÖSCHL, U.: Calibration and measurement uncertainties of a continuous-flow cloud condensation nuclei counter (DMT-CCNC): CCN activation of ammonium sulfate and sodium chloride aerosol particles in theory and experiment. **Atmos. Chem. Phys.**, v. 8, p. 1153–1179, 2008. doi:10.5194/acp-8-1153-2008.

ROSENFELD, D.; LENSKY, I. M. Satellite-based insights into precipitation formation processes in continental and maritime convective clouds. **B. Am. Meteorol. Soc.**, v. 79, p. 2457–2476, 1998.

ROSENFELD, D. TRMM observed first direct evidence of smoke from forest fires inhibiting rainfall. **Geophys. Res. Lett.**, v. 26, p. 3105–3108, 1999. doi:10.1029/1999GL006066.

ROSENFELD, D.; WOODLEY, W. L. Deep convective clouds with sustained supercooled liquid water down to $-37.5\text{ }^{\circ}\text{C}$. **Nature**, v. 405, p. 440-442, 2000. DOI:10.1038/35013030.

ROSENFELD, D.; LOHMANN, U.; RAGA, G. B.; O'DOWD, C. D.; KULMALA, M.; FUZZI, S.; REISELL, A.; ANDREAE, M. O. Flood or drought: how do aerosols affect precipitation? **Science**, v. 321, p. 1309–1313, 2008.

ROSENFELD, D.; WANG, H.; RASCH, P. J. The roles of cloud drop effective radius and LWP in determining rain properties in marine stratocumulus. **Geophys. Res. Lett.**, v. 39, L13801, 2012. doi:[10.1029/2012GL052028](https://doi.org/10.1029/2012GL052028).

ROSENFELD, D.; ANDREAE, M. O.; ASMI, A.; CHIN, M.; DE LEEUW, G.; DONOVAN, D. P.; KAHN, R.; KINNE, S.; KIVEKÄS, N.; KULMALA, M.; LAU, W.; SCHMIDT, K. S.; SUNI, T.; WAGNER, T.; WILD, M.; QUAAS, J.: Global observations of aerosol-cloud-precipitation-climate interactions. **Rev. Geophys.**, v. 52, p. 750–808, 2014. doi:10.1002/2013RG000441.

ROSENFELD, D.; ZHENG, Y.; HASHIMSHONI, E.; PÖHLKER, M. L.; JEFFERSON, A.; PÖHLKER, C.; YU, X.; ZHU, Y.; LIU, G.; YUE, Z.; FISCHMAN, B.; LI, Z.; GIGUZIN, D.; GOREN, T.; ARTAXO, P.; BARBOSA, H. M. J.; PÖSCHL, U.; ANDREAE, M. O. Satellite retrieval of cloud condensation nuclei concentrations by using clouds as CCN chambers. **Proc. Natl. Acad. Sci. U. S. A.**, v. 113, p. 5828–5834, 2016.

SAUNDERS, C. P. R.; HOSSEINI, A. S. A laboratory study of the effect of velocity on Hallett–Mossop ice crystal multiplication. **Atmos. Res.**, v. 59–60, p. 3–14, 2001.

SCHMID, B.; TOMLINSON, J. M.; HUBBE, J. M.; COMSTOCK, J. M.; MEI, F.; CHAND, D.; PEKOUR, M. S.; KLUZEK, C. D.; ANDREWS, E.; BIRAUD, S.C.; McFARQUHAR, G. M. The DOE ARM aerial facility. **Bull. Amer. Meteor. Soc.**, v. 95, n. 5, p. 723–742, 2014. doi: 10.1175/BAMS-D-13-00040.1.

SCHMIDT, J.; ANSMANN, A.; BÜHL, J.; WANDINGER, U.: Strong aerosol–cloud interaction in altocumulus during updraft periods: lidar observations over central Europe. **Atmos. Chem. Phys.**, v.15, p. 10687-10700, 2015. doi:10.5194/acp-15-10687-2015.

SEIFERT, A.; BEHENG, K. D. A two-moment cloud microphysics parameterization for mixed-phase clouds. Part 2: Maritime vs. continental deep convective storms. **Meteorol. Atmos. Phys.**, v. 92, p. 67–82, 2006.

SEINFELD, J. H.; BRETHERTON, C.; CARSLAW, K. S.; COE, H.; DEMOTT, P. J.; DUNLEA, E. J.; FEINGOLD, G.; GHAN, S.; GUENTHER, A. B.; KAHN, R.; KRAUCUNAS, I.; KREIDENWEIS, S. M.; MOLINA, M. J.; NENES, A.;

PENNER, J. E.; PRATHER, K. A.; RAMANATHAN, V.; RAMASWAMY, V.; RASCH, P. J.; RAVISHANKARA, A. R.; ROSENFELD, D.; STEPHENS, G.; WOOD, R. Improving our fundamental understanding of the role of aerosol-cloud interactions in the climate system. **Proc. Natl. Acad. Sci. U. S. A.**, v. 113, p. 5781-5790, 2016.

SHRIVASTAVA, M.; BERG, L. K.; FAST, J.; EASTER, R.; LASKIN, A.; CHAPMAN, E.; GUSTAFSON JR., W. I.; LIU, Y.; BERKOWITZ, C. Modeling aerosols and their interactions with shallow cumuli during the 2007 CHAPS field study. **J. Geophys. Res. Atmos.**, v. 118, p. 1343–1360, 2013. doi:[10.1029/2012JD018218](https://doi.org/10.1029/2012JD018218).

SILVA DIAS, M. A. F.; RUTLEDGE, S.; KABAT, P.; SILVA DIAS, P. L.; NOBRE, C.; FISCH, G.; DOLMAN, A. J.; ZIPSER, E.; GARSTANG, M.; MANZI, A.; FUENTES, J. D.; ROCHA, H.; MARENGO, J.; PLANA-FATTORI, A.; SÁ, L.; ALVALÁ, R.; ANDREAE, M. O.; ARTAXO, P.; GIELOW, R.; GATTI, L. V.: Clouds and rain processes in a biosphere atmosphere interaction context in the Amazon Region. **J. Geophys. Res. Atmos.**, v. 107, n. D20, p. 8072–8092, 2002.

SOARES-FILHO, B. S.; NEPSTAD, D. C.; CURRAN, L. M.; CERQUEIRA, G. C.; GARCIA, R. A.; RAMOS, C. A.; VOLL, E.; MCDONALD, A.; LEFEBVRE, P.; SCHLESINGER, P.: Modeling conservation in the Amazon Basin. **Nature**, v. 440, p. 520–523, 2006.

SOROOSHIAN, A.; FEINGOLD, G.; LEBSOCK, M. D.; JIANG, H. L.; STEPHENS, G. L. On the precipitation susceptibility of clouds to aerosol perturbations. **Geophys. Res. Lett.**, v. 36, L13803, 2009. doi:10.1029/2009gl038993.

STARN, T. K.; SHEPSON, P. B.; BERTMAN, S. B.; WHITE, J. S.; SPLAWN, B. G.; RIEMER, D. D.; ZIKA, R. G.; OLSZYNA, K. Observations of isoprene chemistry and its role in ozone production at a semirural site during the 1995 Southern Oxidants Study. **J. Geophys. Res. Atmos.**, v. 103, n. D17, p. 22425–22435, 1998.

STEVENS, B.; FEINGOLD, G. Untangling aerosol effects on clouds and precipitation in a buffered system. **Nature**, v. 461, p. 607–613, 2009. doi:10.1038/nature08281.

STITH, J. L.; DYE, J. E.; BANSEMER, A. A.; HEYMSFIELD, A. J. Microphysical observations of tropical clouds. **J. Appl. Meteor.**, 41, 97–117, 2002.

STITH, J. L.; HAGGERTY, J. A.; HEYMSFIELD, A.; GRAINGER, C. A. Microphysical characteristics of tropical updrafts in clean conditions. **J. Appl. Meteorol.**, v. 43, p. 779–794, 2004. doi:10.1175/2104.1.

STITH, J. L.; HAGGERTY, J.; GRAINGER, C.; DETWILER, A. A comparison of the microphysical and kinematic characteristics of midlatitude and tropical convective updrafts and downdrafts. **Atmos. Res.**, v. 82, p. 350–366, 2006.

STORER, R.L.; VAN DEN HEEVER, S.C.; STEPHENS, G.L. Modeling aerosol impacts on convective storms in different environments. **J. Atmos. Sci.**, v. 67, n. 12, p. 3904–3915, 2010.

STORER, R. L.; VAN DEN HEEVER, S. C. Microphysical processes evident in aerosol forcing of tropical deep convective clouds. **J. Atmos. Sci.**, v. 70, p. 430–446, 2013. doi:10.1175/JAS-D-12-076.1.

SULLIVAN, S. C.; LEE, D.; OREOPOULOS, L.; NENES, A. Role of updraft velocity in temporal variability of global cloud hydrometeor number. **Proc. Natl. Acad. Sci. U. S. A.**, v. 113, p. 5791–5796, 2016.

SUN, J.; PARISA, A.; ARIYA, H.; LEIGHTON, G.; YAU, M.K. Modeling study of ice formation in warm-based precipitating shallow cumulus clouds. **J. Atmos. Sci.**, v. 69, p. 3315–3335, 2012.

TAO, W.-K.; LI, X.; KHAIN, A.; MATSUI, T.; LANG, S.; SIMPSON, J. Role of atmospheric aerosol concentration on deep convective precipitation: Cloud-resolving model simulations. **J. Geophys. Res. Atmos.**, v. 112, D24S18, 2007. doi:10.1029/2007JD008728.

TAO, W.-K.; CHEN, J.-P.; LI, Z.; WANG, C.; ZHANG, C. Impact of aerosols on convective clouds and precipitation, **Rev. Geophys.**, v. 50, RG2001, 2012. doi:10.1029/2011RG000369.

TAS, E.; TELLER, A.; ALTARATZ, O.; AXISA, D.; BRUINTJES, R.; LEVIN, Z.; KOREN, I. The relative dispersion of cloud droplets: its robustness with respect to key cloud properties. **Atmos. Chem. Phys.**, v. 15, p. 2009–2017, 2015. doi:10.5194/acp-15-2009-2015.

THOMPSON, A. M. The oxidizing capacity of the Earth's atmosphere: Probable past and future changes. **Science**, v. 256, p. 1157–1165, 1992.

THOMPSON, G.; RASMUSSEN, R. M.; MANNING, K. Explicit forecasts of winter precipitation using an improved bulk microphysics scheme. Part I: Description and sensitivity analysis. **Mon. Weather Rev.**, v. 132, p. 519–542, 2004.

TRAINER, M.; WILLIAMS, E. J.; PARRISH, D. D.; BUHR, M. P.; ALLWINE, E. J.; WESTBERG, H. H.; FEHSENFELD, F. C.; LIU, S. C. Models and observations of the impact of natural hydrocarbons on rural ozone. **Nature**, v. 329, p. 705–707, 1987.

TWOMEY, S. The nuclei of natural cloud formation part II: The supersaturation in natural clouds and the variation of cloud droplet concentration. **Geofis. Pura Appl.**, v. 43, p. 243-249, 1959.

TWOMEY, S. Pollution and the planetary albedo. **Atmos. Environ.**, v. 8, p. 1251–1256, 1974. doi:10.1016/0004-6981(74)90004-3.

TWOMEY, S. Influence of pollution on shortwave albedo of clouds. **J. Atmos. Sci.**, v. 34, p. 1149–1152, 1977. doi:10.1175/1520-0469(1977)034,1149:TIOBOT.2.0.CO;2.

ULBRICH, C. W. Natural variations in the analytical form of the raindrop size distribution. **J. Climate Appl. Meteor.**, v. 22, p. 1764–1775, 1983.

VAN DEN HEEVER, S. C.; CARRIÓ, G. G.; COTTON, W. R.; DEMOTT, P. J.; PRENNI, A. J. Impacts of nucleating aerosol on Florida storms. Part I: Mesoscale simulations. **J. Atmos. Sci.**, v. 63, p. 1752–1775, 2006. doi:10.1175/JAS3713.1.

VAN DEN HEEVER, S. C.; COTTON, W. R.: Urban aerosol impacts on downwind convective storms. **J. Appl. Meteorol. Climatol.**, 46, 828–850, 2007.

VAN DEN HEEVER, S. C.; STEPHENS, G. L.; WOOD, N. B. Aerosol indirect effects on tropical convection characteristics under conditions of radiative-convective equilibrium. **J. Atmos. Sci.**, v. 68, p. 699–718, 2011. doi:10.1175/2010JAS3603.1.

VERA, C.; HIGGINS, W.; AMADOR, J.; AMBRIZZI, T.; GARREAUD, R.; GOCHIS, D.; GUTZLER, D.; LETTENMAIER, D.; MARENGO, J.; MECHOSO, C. R.; NOGUES-PAEGLE, J.; SILVA DIAZ, P. L.; ZHANG, C. Towards a unified view of the American Monsoon System. **J. Climate**, v. 19, p. 4977–5000, 2006.

WANG, J.; KREJCI, R.; GIANGRANDE, S.; KUANG, C.; BARBOSA, H. M. J.; BRITO, J.; CARBONE, S.; CHI, X.; COMSTOCK, J.; DITAS, F.; LAVRIC, J.; MANNINEN, H. E.; MEI, F.; MORAN-ZULOAGA, D.; PÖHLKER, C.; PÖHLKER, M. L.; SATURNO, J.; SCHMID, B.; SOUZA, R. A. F.; SPRINGSTON, S. R.; TOMLINSON, J. M.; TOTO, T.; WALTER, D.; WIMMER, D.; SMITH, J. N.; KULMALA, M.; MACHADO, L. A. T.; ARTAXO, P.; ANDREAE, M. O.; PETÄJÄ, T.; MARTIN, S. T. Vertical transport during rainfall sustains aerosol concentration in Amazon boundary layer. **Nature**, v. 539, n. 7629, p. 416-419. doi:10.1038/nature19819.

WEGENER, A. **Thermodynamik der atmosphäre**. Leipzig: J. A. Barth, 1911. 331 p.

WEIGEL, R.; SPICHTINGER, P.; MAHNKE, C.; KLINGEBIEL, M.; AFCHINE, A.; PETZOLD, A.; KRÄMER, M.; COSTA, A.; MOLLEKER, S.; REUTTER, P.;

SZAKÁLL, M.; PORT, M.; GRULICH, L.; JURKAT, T.; MINIKIN, A.; BORRMANN, S. Thermodynamic correction of particle concentrations measured by underwing probes on fast-flying aircraft. **Atmos. Meas. Tech.**, v. 9, p. 5135-5162, 2016. doi:10.5194/amt-9-5135-2016.

WENDISCH, M.; J.-L. BRENGUIER (Eds.). **Airborne measurements for environmental research: methods and instruments**. KGaA, Weinheim, Germany: Wiley-VCH Verlag GmbH & Co, 2013. 655p. ISBN: 978-3-527-40996-9. doi:10.1002/9783527653218.

WENDISCH, M.; PÖSCHL, U.; ANDREAE, M. O.; MACHADO, L. A. T.; ALBRECHT, R.; SCHLAGER, H.; ROSENFELD, D.; MARTIN, S. T.; ABDELMONEM, A.; AFCHINE, A.; ARAÚJO, A.; ARTAXO, P.; AUFMHOFF, H.; BARBOSA, H. M. J.; BORRMANN, S.; BRAGA, R.; BUCHHOLZ, B.; CECCHINI, M. A.; COSTA, A.; CURTIUS, J.; DOLLNER, M.; DORF, M.; DREILING, V.; EBERT, V.; EHRlich, A.; EWALD, F.; FISCH, G.; FIX, A.; FRANK, F.; FÜTTERER, D.; HECKL, C.; HEIDELBERG, F.; HÜNEKE, T.; JÄKEL, E.; JÄRVINEN, E.; JURKAT, T.; KANTER, S.; KÄSTNER, U.; KENNTNER, M.; KESSELMEIER, J.; KLIMACH, T.; KNECHT, M.; KOHL, R.; KÖLLING, T.; KRÄMER, M.; KRÜGER, M.; KRISNA, T. C.; LAVRIC, J. V.; LONGO, K.; MAHNKE, C.; MANZI, A. O.; MAYER, B.; MERTES, S.; MINIKIN, A.; MOLLEKER, S.; MÜNCH, S.; NILLIUS, B.; PFEILSTICKER, K.; PÖHLKER, C.; ROIGER, A.; ROSE, D.; ROSENOW, D.; SAUER, D.; SCHNAITER, M.; SCHNEIDER, J.; SCHULZ, C.; DE SOUZA, R. A. F.; SPANU, A.; STOCK, P.; VILA, D.; VOIGT, C.; WALSER, A.; WALTER, D.; WEIGEL, R.; WEINZIERL, B.; WERNER, F.; YAMASOE, M. A.; ZIEREIS, H.; ZINNER, T.; ZÖGER, M. The ACRIDICON-CHUVA campaign: studying tropical deep convective clouds and precipitation over Amazonia using the new German research aircraft HALO. **B. Am. Meteorol. Soc.**, doi:10.1175/BAMS-D-14-00255.1, 2016. Disponível em: <<http://dx.doi.org/10.1175/BAMS-D-14-00255.1>>.

WERNER, F.; DITAS, F.; SIEBERT, H.; SIMMEL, M.; WEHNER, B.; PILEWSKIE, P.; SCHMEISSNER, T.; SHAW, R. A.; HARTMANN, S.; WEX, H.; ROBERTS, G. C.; WENDISCH, M. Twomey effect observed from collocated microphysical and remote sensing measurements over shallow cumulus. **J. Geophys. Res. Atmos.**, v. 119, p. 1534-1545, 2014. doi:10.1002/2013JD020131.

WIEDINMYER, C.; FRIEDFELD, S.; BAUGH, W.; GREENBERG, J.; GUENTHER, A.; FRASER, M.; ALLEN, D. Measurement and analysis of atmospheric concentrations of isoprene and its reaction products in central Texas. **Atmos. Environ.**, v. 35, p. 1001–1013, 2001.

XIE, X.; ZHANG, H.; LIU, X.; PENG, Y.; LIU, Y. New cloud parameterization with relative dispersion in CAM5.1: model evaluation and impacts on aerosol indirect effects. **Atmos. Chem. Phys. Discuss.**, doi:10.5194/acp-2016-1172, in review, 2017.

XUE, H.; FEINGOLD, G. Large-eddy simulations of trade wind cumuli: Investigation of aerosol indirect effects. **J. Atmos. Sci.**, v. 63, p. 1605–1622, 2006. doi:10.1175/JAS3706.1.

YOUNG, K.C. The role of contact nucleation in ice phase initiation in clouds. **J. Atmos. Sci.**, v. 31, p. 768-776, 1974.

YUAN, T.; REMER, L. A.; YU, H. Microphysical, macrophysical and radiative signatures of volcanic aerosols in trade wind cumulus observed by the A-Train. **Atmos. Chem. Phys.**, v. 11, p. 7119-7132, 2011. doi:10.5194/acp-11-7119-2011.

ZHOU, J.; LAU, K. M. Does a monsoon climate exist over South America? **Journal of Climate**, v. 11, p. 1020 – 1040, 1998.

APPENDIX A – SUPPLEMENT MATERIAL TO CHAPTER 5

Sensitivities for individual intervals

By fixing two dimensions in the 3D matrices and varying the third, we can obtain individual sensitivities in the form of the Equation 5.3.1. As an example, we can fix both w and H and obtain the sensitivities of DSD parameters to varying N_{CN} . By using the natural logarithm scale and applying a linear fit, we obtain the sensitivity as the angular coefficient and the R^2 parameter is a measure of the significance of the relation. By calculating every possible combination, we obtain Tables A.1-15 shown below. The amount of 1 Hz data for each sensitivity are shown in Tables A.16-18.

Table A.1 - sensitivities of D_{eff} to N_{CN} - $S_{D_{eff}}(N_{CN}) = \frac{\partial \ln D_{eff}}{\partial \ln N_{CN}} \Big|_{w,H}$. Intervals upper limits are highlighted in bold letters.

w (m s ⁻¹) \ H (m)	200	500	950	1625	2637.5	4156.25
0.5	-0.11 $R^2 = 0.85$	-0.27 $R^2 = 0.96$	-0.25 $R^2 = 0.99$	-0.23 $R^2 = 0.94$	-0.38 $R^2 = 0.97$	-0.47 $R^2 = 0.71$
1	-0.13 $R^2 = 0.84$	-0.26 $R^2 = 0.93$	-0.30 $R^2 = 0.99$	-0.18 $R^2 = 0.86$	-0.25 $R^2 = 1.00$	-0.26 $R^2 = 0.96$
2	-0.16 $R^2 = 0.79$	-0.26 $R^2 = 0.98$	-0.28 $R^2 = 0.91$	-0.17 $R^2 = 0.64$	-0.31 $R^2 = 0.98$	-0.16 $R^2 = 0.53$
4	-0.18 $R^2 = 0.82$	-0.28 $R^2 = 0.95$	-0.25 $R^2 = 0.96$	-0.25 $R^2 = 0.95$	-0.31 $R^2 = 0.95$	-0.28 $R^2 = 0.99$
8	-	-	-	-	-0.26 $R^2 = 0.80$	-0.33 $R^2 = 0.98$

Table A.2 - sensitivities of D_{eff} to w - $S_{D_{eff}}(w) = \frac{\partial \ln D_{eff}}{\partial \ln w} \Big|_{N_{CN}, H}$. Intervals upper limits are highlighted in bold letters.

N_{CN} (cm ⁻³) \ H (m)	200	500	950	1625	2637.5	4156.25
500	0.020 R ² = 0.63	0.049 R ² = 0.61	0.048 R ² = 0.90	-0.018 R ² = 0.034	0.032 R ² = 0.77	-
1000	0.018 R ² = 0.17	0.031 R ² = 0.57	0.0072 R ² = 0.029	0.046 R ² = 0.71	0.0032 R ² = 0.0040	0.0034 R ² = 0.0010
3000	0.031 R ² = 0.90	0.044 R ² = 0.69	-	-0.011 R ² = 0.055	0.13 R ² = 0.93	0.18 R ² = 0.72
4500	-0.085 R ² = 0.97	0.013 R ² = 0.57	0.046 R ² = 0.62	-0.0063 R ² = 0.23	0.021 R ² = 0.44	0.024 R ² = 0.48

Table A.3 - sensitivities of D_{eff} to H - $S_{D_{eff}}(H) = \frac{\partial \ln D_{eff}}{\partial \ln H} \Big|_{N_{CN}, w}$. Intervals upper limits are highlighted in bold letters.

N_{CN} (cm ⁻³) \ w (m s ⁻¹)	0.5	1	2	4	8
500	0.33 R ² = 0.98	0.27 R ² = 0.92	0.31 R ² = 0.85	0.32 R ² = 0.92	-
1000	0.35 R ² = 0.98	0.32 R ² = 0.99	0.30 R ² = 0.95	0.32 R ² = 1.00	0.41 R ² = 0.94
3000	0.14 R ² = 0.62	0.23 R ² = 0.90	0.28 R ² = 0.96	0.26 R ² = 0.97	0.27 R ² = 0.96
4500	0.19 R ² = 0.95	0.24 R ² = 0.98	0.24 R ² = 0.99	0.26 R ² = 0.97	-

Table A.4 - sensitivities of N_d to N_{CN} - $S_{N_d}(N_{CN}) = \frac{\partial \ln N_d}{\partial \ln N_{CN}} \Big|_{w,H}$. Intervals upper limits are highlighted in bold letters.

w (m s ⁻¹) \ H (m)	200	500	950	1625	2637.5	4156.25	
0.5	0.69	0.75	1.23	0.64	-0.069	1.24	
	R ²	= R ²	= R ²	= R ²	= R ²	= R ²	=
	0.97	0.82	0.89	0.86	0.011	0.83	
1	0.67	0.79	0.90	0.87	0.70	1.11	
	R ²	= R ²	= R ²	= R ²	= R ² = 1.00	R ²	=
	0.90	0.87	1.00	0.88		0.95	
2	0.72	0.89	1.049	0.87	0.90	1.40	
	R ²	= R ²	= R ²	= R ²	= R ² = 0.92	R ²	=
	0.84	0.98	0.94	0.92		0.96	
4	0.54	0.85	0.79	0.49	0.72	1.22	
	R ²	= R ²	= R ²	= R ²	= R ² = 0.92	R ²	=
	0.62	0.95	0.99	0.37		0.98	
8	-	-	-	-	0.94	0.83	
					R ² = 1.00	R ²	=
						0.98	

Table A.5 - sensitivities of N_d to w - $S_{N_d}(w) = \frac{\partial \ln N_d}{\partial \ln w} \Big|_{N_{CN},H}$. Intervals upper limits are highlighted in bold letters.

N_{CN} (cm ⁻³) \ H (m)	200	500	950	1625	2637.5	4156.25	
500	0.57	0.46	0.86	-0.12	0.40		
	R ²	= R ²	= R ²	= R ²	= R ²	= -	
	1.00	0.89	0.97	0.070	0.76		
1000	0.45	0.44	0.34	0.32	0.29	0.64	
	R ²	= R ²	= R ²	= R ² = 0.89	R ²	= R ²	=
	0.91	0.99	0.47		0.91	0.89	
3000	0.61	0.85	-	0.37	0.39	0.65	
	R ²	= R ²	= -	R ² = 0.82	R ²	= R ²	=
	0.94	0.96			0.95	0.92	
4500	0.24	0.30	0.41	-0.37	1.034	0.38	
	R ²	= R ²	= R ²	= R ² = 0.46	R ²	= R ²	=
	0.91	0.89	0.67		0.70	0.90	

Table A.6 - sensitivities of N_d to H - $S_{N_d}(H) = \frac{\partial \ln N_d}{\partial \ln H} \Big|_{N_{CN}, w}$. Intervals upper limits are highlighted in bold letters.

N_{CN} (cm ⁻³) \ w (m s ⁻¹)	0.5	1	2	4	8
500	0.20 R ² = 0.11	-0.29 R ² = 0.97	-0.084 R ² = 0.20	-0.094 R ² = 0.080	-
1000	-0.24 R ² = 0.36	-0.21 R ² = 0.24	-0.22 R ² = 0.21	-0.26 R ² = 0.54	-0.15 R ² = 0.64
3000	-0.11 R ² = 0.97	-0.14 R ² = 0.26	-0.22 R ² = 0.94	-0.32 R ² = 0.89	-0.26 R ² = 0.85
4500	-0.26 R ² = 0.094	0.068 R ² = 0.14	0.075 R ² = 0.056	0.081 R ² = 0.022	-

Table A.7 - sensitivities of LWC to N_{CN} - $S_{LWC}(N_{CN}) = \frac{\partial \ln LWC}{\partial \ln N_{CN}} \Big|_{w, H}$. Intervals upper limits are highlighted in bold letters.

w (m s ⁻¹) \ H (m)	200	500	950	1625	2637.5	4156.25
0.5	0.30 R ² = 0.97	-0.11 R ² = 0.070	0.48 R ² = 0.66	-0.022 R ² = 0.013	-1.11 R ² = 0.82	0.058 R ² = 0.0052
1	0.24 R ² = 0.40	-0.030 R ² = 0.0072	0.055 R ² = 0.42	0.43 R ² = 0.50	0.024 R ² = 0.12	0.62 R ² = 0.90
2	0.22 R ² = 0.26	0.021 R ² = 0.019	0.23 R ² = 0.21	0.41 R ² = 0.34	-0.043 R ² = 0.097	0.60 R ² = 0.41
4	0.032 R ² = 0.0033	-0.025 R ² = 0.0067	0.015 R ² = 0.054	-0.42 R ² = 0.25	-0.12 R ² = 0.29	0.20 R ² = 0.98
8	-	-	-	-	0.15 R ² = 0.17	-0.20 R ² = 0.90

Table A.8 - sensitivities of LWC to w - $S_{LWC}(w) = \frac{\partial \ln LWC}{\partial \ln w} \Big|_{N_{CN}, H}$. Intervals upper limits are highlighted in bold letters.

N_{CN} (cm^{-3}) \ H (m)	200	500	950	1625	2637.5	4156.25
500	0.62	0.60	1.024	0.060	0.34	
	$R^2 = 1.00$	$R^2 = 0.85$	$R^2 = 0.98$	$R^2 = 0.0047$	$R^2 = 0.91$	$R^2 = -$
1000	0.50	0.42	0.37	0.42	0.31	0.69
	$R^2 = 0.87$	$R^2 = 0.90$	$R^2 = 0.43$	$R^2 = 0.88$	$R^2 = 0.85$	$R^2 = 0.75$
3000	0.70	0.94		0.33	0.70	0.89
	$R^2 = 0.97$	$R^2 = 0.94$	$R^2 = -$	$R^2 = 0.72$	$R^2 = 0.96$	$R^2 = 0.87$
4500	0.10	0.33	0.53	-0.47	1.00	0.42
	$R^2 = 0.44$	$R^2 = 0.84$	$R^2 = 0.70$	$R^2 = 0.64$	$R^2 = 0.66$	$R^2 = 0.81$

Table A.9 - sensitivities of LWC to H - $S_{LWC}(H) = \frac{\partial \ln LWC}{\partial \ln H} \Big|_{N_{CN}, w}$. Intervals upper limits are highlighted in bold letters.

N_{CN} (cm^{-3}) \ w (m s^{-1})	0.5	1	2	4	8
500	1.14	0.27	0.74	0.80	
	$R^2 = 0.83$	$R^2 = 0.45$	$R^2 = 0.62$	$R^2 = 0.84$	$R^2 = -$
1000	0.73	0.69	0.65	0.71	1.062
	$R^2 = 0.92$	$R^2 = 0.90$	$R^2 = 0.65$	$R^2 = 0.92$	$R^2 = 0.79$
3000	0.51	0.58	0.64	0.48	0.52
	$R^2 = 0.61$	$R^2 = 0.76$	$R^2 = 0.95$	$R^2 = 0.92$	$R^2 = 0.86$
4500	0.36	0.77	0.70	0.76	
	$R^2 = 0.16$	$R^2 = 0.98$	$R^2 = 0.83$	$R^2 = 0.62$	$R^2 = -$

Table A.10 - sensitivities of Λ to N_{CN} - $S_{\Lambda}(N_{CN}) = \frac{\partial \ln \Lambda}{\partial \ln N_{CN}} \Big|_{w,H}$. Intervals upper limits are highlighted in bold letters.

w (m s ⁻¹) \ H (m)	200	500	950	1625	2637.5	4156.25
0.5	-0.25 R ² = 0.50	0.20 R ² = 0.50	0.51 R ² = 0.70	0.43 R ² = 0.74	0.53 R ² = 0.87	0.54 R ² = 0.40
1	-0.33 R ² = 0.76	0.12 R ² = 0.17	0.62 R ² = 0.87	0.37 R ² = 0.87	0.37 R ² = 0.62	0.74 R ² = 0.86
2	-0.42 R ² = 0.93	0.11 R ² = 0.28	0.40 R ² = 0.91	0.40 R ² = 0.66	0.51 R ² = 0.86	0.069 R ² = 0.13
4	-0.54 R ² = 0.97	-0.15 R ² = 0.39	0.062 R ² = 0.20	0.29 R ² = 0.36	0.56 R ² = 0.88	0.14 R ² = 0.18
8	-	-	-	-	0.52 R ² = 0.99	0.090 R ² = 0.93

Table A.11 - sensitivities of Λ to w - $S_{\Lambda}(w) = \frac{\partial \ln \Lambda}{\partial \ln w} \Big|_{N_{CN},H}$. Intervals upper limits are highlighted in bold letters.

N_{CN} (cm ⁻³) \ H (m)	200	500	950	1625	2637.5	4156.25
500	0.35 R ² = 0.98	0.35 R ² = 0.65	0.41 R ² = 0.66	0.049 R ² = 0.14	-0.090 R ² = 0.98	-
1000	0.061 R ² = 0.24	0.0043 R ² = 0.0037	-0.062 R ² = 0.11	0.19 R ² = 0.67	-0.11 R ² = 0.75	0.24 R ² = 0.82
3000	-0.062 R ² = 0.31	0.13 R ² = 0.55	-	0.015 R ² = 0.045	-0.14 R ² = 0.83	-0.15 R ² = 0.42
4500	-0.0064 R ² = 0.13	-0.11 R ² = 0.91	-0.097 R ² = 0.82	-0.18 R ² = 0.23	0.0068 R ² = 0.0089	0.049 R ² = 0.56

Table A.12 - sensitivities of Λ to H - $S_{\Lambda}(H) = \frac{\partial \ln \Lambda}{\partial \ln H} \Big|_{N_{CN}, w}$. Intervals upper limits are highlighted in bold letters.

N_{CN} (cm ⁻³) \ w (m s ⁻¹)	0.5	1	2	4	8
500	-0.75 R ² = 0.96	-0.84 R ² = 0.94	-0.94 R ² = 0.98	-1.11 R ² = 0.97	-
1000	-0.61 R ² = 0.98	-0.63 R ² = 0.96	-0.47 R ² = 0.87	-0.54 R ² = 0.86	-0.25 R ² = 0.073
3000	-0.10 R ² = 0.088	-0.17 R ² = 0.48	-0.25 R ² = 0.54	-0.21 R ² = 0.34	-0.26 R ² = 0.38
4500	-0.17 R ² = 0.47	-0.15 R ² = 0.43	-0.15 R ² = 0.50	-0.14 R ² = 0.62	-

Table A.13 - sensitivities of ε to N_{CN} - $S_{\varepsilon}(N_{CN}) = \frac{\partial \ln \varepsilon}{\partial \ln N_{CN}} \Big|_{w, H}$. Intervals upper limits are highlighted in bold letters.

w (m s ⁻¹) \ H (m)	200	500	950	1625	2637.5	4156.25
0.5	0.17 R ² = 0.81	0.013 R ² = 0.014	-0.17 R ² = 0.45	-0.12 R ² = 0.66	-0.097 R ² = 0.56	-0.097 R ² = 0.36
1	0.21 R ² = 0.93	0.066 R ² = 0.21	-0.19 R ² = 0.75	-0.11 R ² = 0.80	-0.080 R ² = 0.38	-0.24 R ² = 0.77
2	0.30 R ² = 0.95	0.027 R ² = 0.068	-0.12 R ² = 0.98	-0.14 R ² = 0.50	-0.14 R ² = 0.72	0.036 R ² = 0.090
4	0.44 R ² = 1.00	0.091 R ² = 0.24	0.0092 R ² = 0.018	-0.072 R ² = 0.12	-0.17 R ² = 0.70	0.0031 R ² = 0.0012
8	-	-	-	-	-0.18 R ² = 0.94	0.16 R ² = 0.95

Table A.14 - sensitivities of ε to w - $S_{\varepsilon}(w) = \frac{\partial \ln \varepsilon}{\partial \ln w} \Big|_{N_{CN}, H}$. Intervals upper limits are highlighted in bold letters.

N_{CN} (cm ⁻³) \ H (m)	200	500	950	1625	2637.5	4156.25
500	-0.29 R ² = 0.95	-0.11 R ² = 0.60	-0.19 R ² = 0.80	0.015 R ² = 0.057	0.063 R ² = 1.00	-
1000	-0.080 R ² = 0.41	-0.016 R ² = 0.71	0.076 R ² = 0.34	-0.12 R ² = 0.78	0.049 R ² = 0.53	-0.14 R ² = 0.86
3000	0.037 R ² = 0.31	-0.17 R ² = 0.76	-	0.00013 R ² = 0.000024	0.0024 R ² = 0.0019	-0.035 R ² = 0.22
4500	0.027 R ² = 0.51	0.037 R ² = 0.61	0.024 R ² = 0.53	0.018 R ² = 0.30	-0.025 R ² = 0.27	-0.023 R ² = 0.28

Table A.15 - sensitivities of ε to H - $S_{\varepsilon}(H) = \frac{\partial \ln \varepsilon}{\partial \ln H} \Big|_{N_{CN}, w}$. Intervals upper limits are highlighted in bold letters.

N_{CN} (cm ⁻³) \ w (m s ⁻¹)	0.5	1	2	4	8
500	0.22 R ² = 0.85	0.30 R ² = 0.73	0.36 R ² = 0.94	0.48 R ² = 0.99	-
1000	0.15 R ² = 0.79	0.16 R ² = 0.82	0.094 R ² = 0.63	0.16 R ² = 0.74	-0.16 R ² = 0.084
3000	0.0066 R ² = 0.0045	0.0093 R ² = 0.030	0.017 R ² = 0.046	0.028 R ² = 0.032	0.010 R ² = 0.0024
4500	-0.022 R ² = 0.062	-0.037 R ² = 0.20	-0.036 R ² = 0.17	-0.046 R ² = 0.29	-

Table A.16. number of 1 Hz DSD data for the sensitivities to N_{CN} .

w (m s ⁻¹) \ H (m)	200	500	950	1625	2637.5	4156.25
0.5	289	89	21	32	36	45
1	247	82	20	24	22	45
2	223	87	26	34	28	49
4	111	47	30	37	29	38
8	0	0	0	0	18	27

Table A.17 - number of 1 Hz DSD data for the sensitivities to w .

$N_{CN} (\text{cm}^{-3}) \setminus H (\text{m})$	200	500	950	1625	2637.5	4156.25
500	259	84	28	27	11	0
1000	234	84	38	40	56	81
3000	265	91	0	61	43	75
4500	125	55	25	16	23	44

Table A.18 - number of 1 Hz DSD data for the sensitivities to H .

$N_{CN} (\text{cm}^{-3}) \setminus w (\text{m s}^{-1})$	0.5	1	2	4	8
500	169	119	90	35	0
1000	137	136	146	94	20
3000	142	100	138	110	51
4500	64	85	73	53	0